TECHNISCHE UNIVERSITÄT MÜNCHEN
Lehrstuhl für Werkstoffkunde und Werkstoffmechanik

Thermomechanical Behaviour of Two Heterogeneous Tungsten Materials via 2D and 3D Image-Based FEM

Alessandro Zivelonghi

Vollständiger Abdruck der von der Fakultät für Maschinenwesen der Technischen Universität München zur Erlangung des akademischen Grades eines

Doktor-Ingenieurs (Dr.-Ing)

genehmigten Dissertation.

Vorsitzender: Univ.-Prof. Dr. mont. habil. E. Werner

Prüfer der Dissertation:

1. Hon.-Prof. Dr.-Ing., Dr.-Eng. (Japan) H. H. Bolt
2. Univ.- Prof. Dr.-Ing. H. Baier

Die Dissertation wurde am 02.12.2010 bei der Technischen Universität München eingereicht und durch die Fakultät für Maschinenwesen am 11.04.2011 angenommen.

Kurzfassung

Ein fortgeschrittenes numerisches Verfahren, basierend auf der Abbildung der Mikrostruktur (*Image-Based Finite Element Method*, Abk. *Image-Based FEM*), wurde für die Modellierung des thermo-mechanischen Materialverhaltens neuer Fusionswerkstoffe weiterentwickelt. Zwei auf Wolfram als Hauptbestandteil basierende heterogene Materialien mit unterschiedlichen, zufälligen Morphologien auf mehreren Längenskalen wurden als Fallstudien ausgewählt: 1) gemischte duktil-spröde W/CuCr1Zr-Verbundwerkstoffe und 2) vacuum plasma-sprayed tungsten (VPS-W 75 vol.%), ein plasmagespritztes poröses Beschichtungssystem mit einer zweiskaligen Mikrostruktur. Beide Materialien sind für den Einsatz in dem zukünftigen Fusionsreaktor DEMO geplant: W/CuCr1Zr-Verbundwerkstoff als Hauptbestandteil eines Gradienten-Übergangs und VPS-W als mögliche Lösung für die Beschichtung der ersten Reaktorwand mit unmittelbarem Plasmakontakt.

Hauptziel der vorliegenden Arbeit war die numerische Modellierung von Materialversagen und Wärmetransport in Werkstoffen mit zufälliger Mikrostruktur durch Untersuchung des mesoskopischen und makroskopischen Werkstoffverhaltens. Besondere Beachtung wurde dabei der experimentellen Validierung von Simulationsergebnissen geschenkt. Direkte Simulation auf der realen Mikrostruktur ergab wichtige Erkenntnisse über den komplexen Versagensmechanismus beider Materialien. Für den W/CuCr1Zr Werkstoff wurde die gesamte Spannungs-Dehnungs-Kurve (inklusiv des Entfestigungs- und Versagensteils) bei unterschiedlichen Temperaturen berechnet und dabei eine gute Übereinstimmung mit experimentellen Daten gefunden. Darüber hinaus konnten neue Möglichkeiten zur Bestimmung von meso- und mikroskaligen Material-Parametern aus dem experimentell ermittelten makroskopischen Verhalten hinsichtlich plastischer Verformung bzw. Versagen aufgezeigt werden.

Sowohl die Wärmeleitung als auch das elastische Verhalten von VPS-W wurden umfassend untersucht. Neue mögliche Anwendungen des *Image-Based FEM* wurden hier damit gezeigt: quantitative Dekomposition des Beitrages der einzelnen morphologischen Phasen zur Behinderung der Wärmeübertragung und Abschätzung der reduzierten Steifigkeit an den interlamellaren Grenzflächen.

Die Mikrostruktur realer VPS-W-Proben wurde sowohl bei der Entwicklung der planaren als auch der dreidimensionalen Modelle berücksichtigt. Um Zugang zu der realen dreidimensionalen Mikrostruktur zu gewinnen war eine Synchrotron-Mikrotomographie des Beschichtungssystems erforderlich. Wegen der starken Absorption von Röntgenstrahlung durch Wolfram war die tomographische Messung eine technische Herausforderung. Die Tomographie eines heterogenen Materials mit Wolfram als Hauptanteil erforderte die Entwicklung einer speziellen Probengeometrie sowie die Optimierung mehrerer experimenteller Parameter an einer Hochenergetischen Beamline des European Synchrotron Radiation Facility in Grenoble.

Abstract

An advanced numerical procedure based on imaging of the material microstructure (*Image-Based Finite Element Method* or *Image-Based FEM*) was extended and applied to model the thermomechanical behaviour of novel materials for fusion applications. Two tungsten based heterogeneous materials with different random morphologies have been chosen as challenging case studies: 1) a two-phase mixed ductile-brittle W/CuCr1Zr composite and 2) vacuum plasma-sprayed tungsten (VPS-W 75 vol.%), a porous coating system with complex dual-scale microstructure. Both materials are designed for the future fusion reactor DEMO: W/CuCr1Zr as main constituent of a layered functionally graded joint between plasma-facing armor and heat sink whereas VPS-W for covering the first wall of the reactor vessel in direct contact with the plasma.

The primary focus of this work was to investigate the mesoscopic material behaviour and the linkage to the macroscopic response in modeling failure and heat-transfer. Particular care was taken in validating and integrating simulation findings with experimental inputs. The solution of the local thermomechanical behaviour directly on the real material microstructure enabled meaningful insights into the complex failure mechanism of both materials. For W/CuCr1Zr full macroscopic stress-strain curves including the softening and failure part could be simulated and compared with experimental ones at different temperatures, finding an overall good agreement. The comparison of simulated and experimental macroscopic behaviour of plastic deformation and rupture also showed the possibility to indirectly estimate micro- and mesoscale material parameters.

Both heat conduction and elastic behaviour of VPS-W have been extensively investigated. New capabilities of the *Image-Based FEM* could be shown: decomposition of the heat transfer reduction as due to the individual morphological phases and back-fitting of the reduced stiffness at interlamellar boundaries.

The microstructure of VPS-W was included in planar as well as in three-dimensional models. In order to image the three-dimensional microstructure of the coating a synchrotron microtomography was necessary. Because of the strong X-rays absorption from W, the measurement was a technical challenge. The tomographic reconstruction of a heterogeneous material where W has the main volume fraction required the design of a special sample geometry and the optimization of several beam parameters at a high-energy beamline of the European Synchrotron Radiation Facility in Grenoble.

"Random numbers should not be generated with a method chosen at random."

Donald Knuth (Prof. Emeritus at Stanford University)

Contents

Notation

σ_{ij}	Stress tensor component
ε_{ij}	Strain tensor component
ϕ_i	Heat-flux vector component
λ_i	Thermal conductivity vector component
α_i	Thermal diffusivity vector component
$\alpha^{app}/\alpha^{eff}$	Apparent and effective diffusivity
x, y, z	Indexes of orthogonal spatial components
ρ	Mass density
C_p	Specific heat
σ^{ult}	Ultimate (tensile) strength
ϵ^{ult}	Ultimate (tensile) strain
$\langle \, \rangle$	Volume average of a tensorial/vectorial component on a single unit cell[1]
$\Omega \{\Omega_i\}$	Ensemble Ω made of n unit cells $\Omega_{i=1,..,n}$
$\langle\langle \, \rangle\rangle_\Omega$	Ensemble average over multiple unit cells belonging to the ensemble Ω
V	Volume or area of a unit cell
V_i	Volume or area of unit cells belonging to the set Ω^{V_i}
$D^2_Z(V_i)$	Variance of the average quantity Z over an ensemble of sample size V_i
A_i	Area of the element i of a unit cell mesh

---

[1] Unit Cell or Simulation Cell indicates a finite spatial domain representing the material microstructure where the single phases have been unambiguously identified and discretized (meshed).

List of Abbreviations

IB	Image Based
FE	Finite Element
IB-FEM	Image-Based Finite Element Method
CZ	Contact Zone
HR	High (spatial) Resolution
2D/3D	Two-Dimensional / Three-Dimensional
IBHR	Image Based High Resolution (2D mesh)
IBHR-CZ	Image Based High Resolution with Contact Zone (2D mesh)
IBS	Image Based Smooth (3D mesh)
IBL	Image Based Lego (3D mesh)
RT	Room Temperature
RVE	Representative Volume Element
YS	Yield Stress
US	Ultimate (tensile) Stress
UE	Ultimate (tensile) Strain
MAXPS	Maximum Principal Stress
MAXPE	Maximum Principal Strain
PEEQ	Equivalent Plastic Strain
PEEQ-th	Equivalent Plastic Strain Threshold

Chapter 1

Introduction

1.1 Motivation

A wide range of materials used in engineering and industry are heterogeneous and multi component, possessing a rich and complicated internal structure. This structure, which may also differ at different scales, strongly influences their particular response in specific applications.

Nowadays, advances in manufacturing, characterization and modeling of complex material structures allow us to overcome the most demanding problems in engineering applications. Some of these challenges arise from a demanding field of research known as Nuclear Fusion.

The ultimate goal of nuclear fusion research is to provide a sustainable alternative to large scale power generation. First attempts of controlled thermonuclear fusion date back to the 1950s[1]. Since then, several fusion experiments have been attempted world wide with a steady rise in performance over the decades.

Due to the very hot and radiative plasma inside a fusion reactor, the materials in direct contact with the plasma, so called *plasma facing materials* (PFM) are affected by extreme and unique thermo-physical conditions. In particular ion bombardment and radiation emitted from the plasma core results in very high power densities (up to 20 $\mathrm{MW/m^2}$) hitting the PFM. The huge heat flux must be removed in a efficient and reliable way in order to prevent material failure and in order to allow a sustainable fusion power generation. Plasma contamination from PFM also affects the performance of a fusion plasma [3] eventually leading to break-down of the plasma itself. The complex interaction mechanisms between plasma and first wall materials include material erosion by ions and neutrals, physical spattering and chemical erosion, arcing, melting and desorption [2, 3].

These facts firstly restrict the choice of suitable physical elements for the PFM [4, 5]. Among them, tungsten (W) gained favour over the years because of its excellent thermomechanical properties [6, 9, 8] (good conductivity, high strength, refractory nature and the highest melting point among all elements) and good plasma compatibility (low sputtering yield and no chemical erosion by hydrogen) [12, 8].

1.1.1 Heterogeneous W-Materials for Fusion

Due to their high melting point and low vapor pressure, W and W-alloys are generally well suited for all kind of high temperature/high vacuum applications. Nowadays a spectrum of suitable tungsten based materials is available or under development. Some of them possess a particular *heterogeneous* microstructure.

Arranging W in heterogeneous microstructures (porous mono-component or dense multi-component) can add new properties to the resulting material and extend the spectrum of possible applications.

Two promising microstructured materials for fusion applications are plasma-sprayed tungsten and W/CuCrZr Functionally Graded Materials (FGM). Both these materials are planned to be employed in DEMO, the first prototype fusion power plant, scheduled for 2040-45 [17].

Plasma-Sprayed Tungsten

One way to generate heterogeneous microstructures with tungsten also deals with plasma: plasma-sprayed tungsten (PS-W) is produced from cumulative deposition of tungsten droplets, partially molten in a plasma gun and deposited at high impact speed on a substrate [11, 99]. The resulting inhomogeneous material is a porous coating made of a solid phase with random porous inclusions (Fig. 1.1). Compared to homogeneous tungsten coatings deposited by classic PVD and CVD processes, PS-W reaches a much higher coating thickness (up to some mm) whilst keeping a satisfactory adhesion to the substrate (depending on substrate type) [8].

Residual stresses, generated from the high processing temperature of VPS-W and from the strong mismatch in the coefficient of thermal expansion (CTE) between W-coating and substrates (usually steel [15], carbon [14] or copper [8]) limit the adhesion between coatings and substrate, causing delamination[15]. With a further plasma sprayed interlayer made of W and substrate material (usually steel) and by actively cooling the substrate during deposition, it is possible to improve adhesion, reducing interfacial stress sources leading to coating detachment or internal cracking [15, 16]. This coating solution, while retaining the advantages of tungsten as plasma facing material, improves its performance under extensive cyclic thermomechanical load [13]. PS-W has been successfully tested to withstand cycled heat load up to 2.5 MW/m^2 (actively water-cooled) on low activation steels designed for fusion applications (EUROFER97 and F82H [15]) and 10 MW/m^2 on carbon fiber composites and graphite (not actively cooled) [14]. Thermomechanical performances of the coating are mainly influenced by morphology, type of substrate and interlayer. Morphology itself depends on substrate material, interlayer and several other manufacturing parameters [15, 103]. Because of the complexity of the microstructure, the local mechanisms of coating deformation and failure, while phenomenologically well characterized in the literature [96, 16, 15]are not very well understood from a theoretical point of view (in particular the relation between failure mode, coating system configuration and thermomechanical load). Since the coating microstructure is clearly the most challenging part of the whole coating system to be modeled and since it can be controlled to some extent during

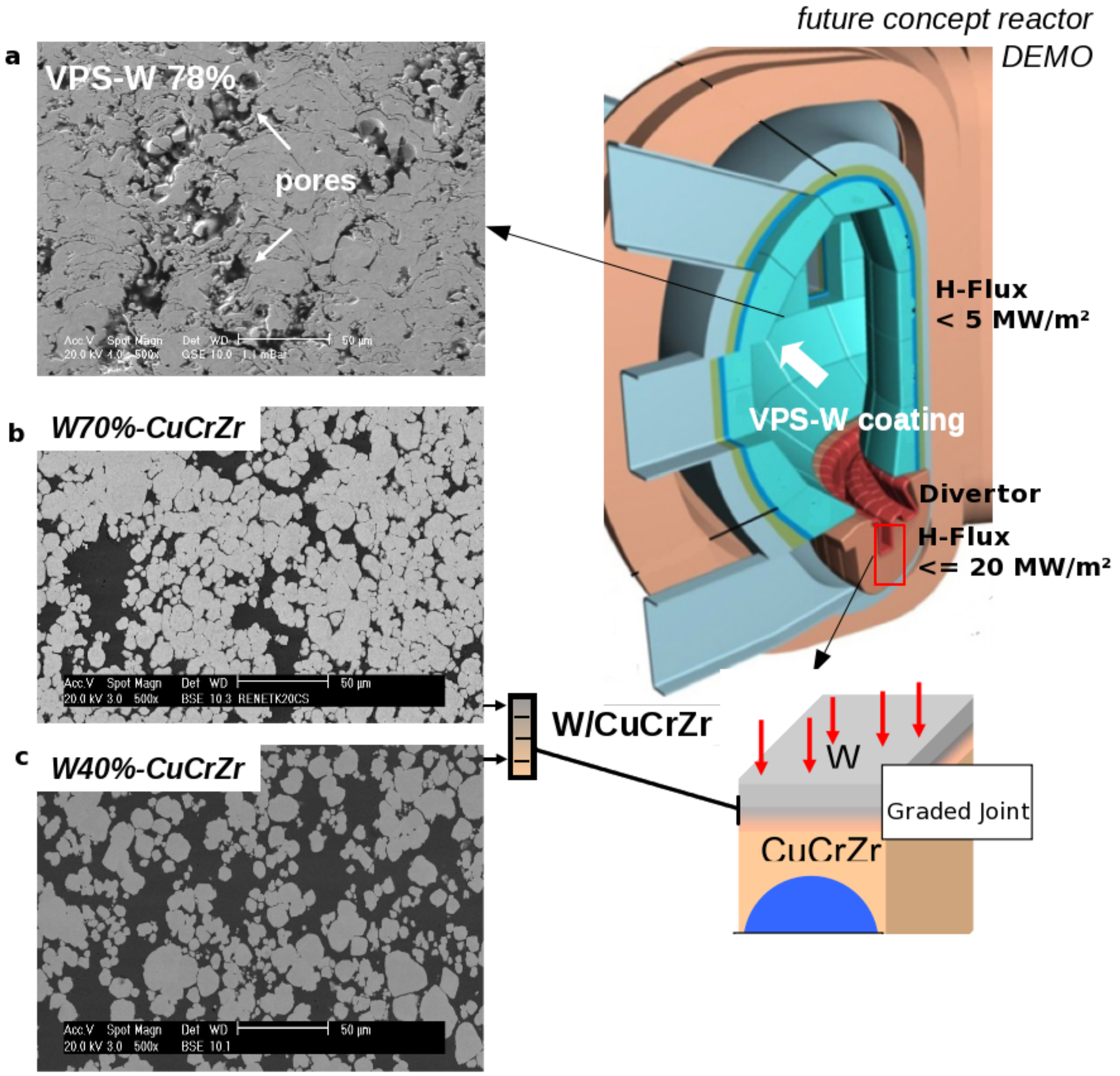

Figure 1.1: *Left: cross-sections of the two heterogeneous materials in scope. Right - their possible locations in the fusion concept reactor DEMO (image revised from [7]). a) PS-W coating, designed for armoring moderate heat-flux regions of the reactor vessel. b) and c) W/CuCrZr particulate composites (courtesy of Luis Renner GmbH, Germany). These are the constituents of the multi-layer structure of a functionally graded joint between tungsten coating and CuCrZr heat-sink (the flat tile concept is shown).*

manufacturing, there is a first need to calculate the internal arrangement of *local* fields (stress, strain, heat-flux and temperature) and to investigate the link between local fields, coating microstructure and average thermomechanical properties.

W/CuCrZr Functionally Graded Materials

Coatings are not the only group of heterogeneous materials which find application in fusion engineering. The demanding requirement of combining high thermal conductivity with high temperature strength, fatigue resistance and low plasma contamination, is difficult to be properly fulfilled by a single component homogeneous medium [26]. W has a good thermal conductivity, but insufficient to satisfy alone the very high requirement of heat removal in the most thermally loaded region in reactor: the *divertor*. Here W must be coupled with other more conductive and ductile elements, like copper or copper alloys. The divertor system, located at the bottom of the reactor, is responsible for heat removal, as well as for exhausting the He-ash, unburned D and T and other impurities [19]. Very high heat fluxes between 15 and 20 MW/m^2 are expected in the divertor of DEMO [17]. For efficient energy production, the temperature of the water-cooled heat sink, made of CuCrZr (a copper alloy with improved conductivity and strength [27]), should be maintained at 300 °C. This thermal constraint, combined with the high incoming heat flux values, induces temperatures of up to 550°C (in steady-state conditions) at the interface between the PFM (W) and the copper alloy .

Due to a mismatch of about factor four in the CTEs, high stresses can develop at the interface of these two materials. It has been calculated [20] that internal stress in W would range from compressive stress at room temperature (-800MPa) to tensile stress at 550 °C (500MPa). Under such conditions the adhesion of the joint would degrade and the component fail after a low number of thermal cycles. A valuable alternative which may overcome the limitation of brazed joint, is offered by Functionally Graded Materials (FGM) [25]. FGM are inhomogeneous composites where certain material properties exhibit a continuous (in general non-linear) change from one boundary surface to the next, by gradually varying the volume fraction and the arrangement of constituent materials. In practice, however, stepwise FGM are often encountered [35, 26].

As explained in [35, 36] for the first time, the adoption of a stepwise FGM for joining W and Cu notably improved the performance under moderate cyclic thermal load (no macroscopic interfacial crack developed due to mismatch of CTE). Improvements in the fabrication process of W/Cu FGM [37] allowed the specimens to survive up to 140 cycles with power density of 10 MW/m^2 without interfacial crack. First experiments in manufacturing prototypes of the W/CuCrZr FGM joint [28] indicate the multilayer design (Fig. 2.6) as the most viable solution for the metallurgical process, which allows full infiltration of the copper alloy in a tungsten skeleton with low residual porosity. However, further improvements in the design of the FGM-layers requires to model the link between overall thermomechanical properties and the particular heterogeneous microstructure. The ultimate goal of design optimization of the whole FGM-joint with respect to conductivity and failure constraints requires also to investigate the relationship between the layers structure and the macroscopic response at component level.

It now appears clear that for both heterogeneous materials, PS-W and W/CuCrZr composites, there is a common need for reliable predictions of their global and local thermomechanical behavior. In the coming section we will explain the reasons why standard modeling approaches are not suitable to this scope and why an advanced numerical method based on imaging of the real morphology appears to be the most appropriate approach.

1.1.2 Modeling with Direct Mapping of Morphology

Modeling the thermomechanics of PS-W and W/CuCrZr at a macroscopic and microstructural level is a challenging task for theoretical micromechanics. This fact is primarily ascribed to an extremely irregular random morphology of both materials.

This statement can be better understood after briefly reviewing conventional analytical and semi-analytical micromechanical approaches, which fall in two major groups (following Böhm [38]): Variational Bounding Methods (VBMs) and Mean Field Approaches (MFAs).

Classical variational bounds (Wiener [41], Voigt and Reuss [40, 42], Hill [45], Hashin and Shtrikman [43]) give universal ranges for macroscopic properties of composites, without containing any information on the micro geometry of the material except for the volume fractions. VBM are powerful tools in assessing other models but not accurate enough for practical purposes. Improved bounds are significantly tighter than classical ones, but at the price of high level of sophistication in the analytical formulation [46], which requires information on the phase arrangement in the form of n-point correlation functions, difficult to identify in complex morphologies. Furthermore, they are restricted to morphologies with inclusions of elementary shapes (for an extensive review, see Torquato [47]). Some analytical attempts were also made to model the effective thermal conductivity of plasma sprayed coatings using the electrical series and parallel equivalents [76, 77]. However, such models are based on a simplified assumption of the porous network made of elementary inclusions regularly distributed and do not provide bounds but single estimations of average thermal properties.

The Mean Field Approaches on the other hand, such as Eshelby [49] or Eshelby-like [50, 51] models (for dilute matrix-inclusion composite) and classical [52] or extended [55, 56, 53, 54] Mori-Tanaka methods (which account for non dilute composite and intra–phase interactions, also in elastoplastic regime), suffer from two major limitations:

1. They only predict the overall material response approximating the micro fields within each constituent by spatially constant phase averages. In other words, the micro fields are not resolved locally. They are therefore not suitable for modeling damage and failure mechanisms which require a strong interaction between micro fields and morphology to account for stress/strain localization phenomena.

2. MFAs are mostly designed for highly symmetric morphologies with inclusions of elementary shape (spherical or elliptical), in most cases uniformly distributed (as for regular fiber arrangements in fiber composites).

Analytical and semi analytical methods therefore appear unsuitable for modeling complex heterogeneous materials with random distributions of inclusions of irregular shape, like those of PS-W and W/CuCrZr. One is forced to include more details of the complex microstructure and to move from analytical to numerical modeling, usually based on the finite element method (FEM).

In numerical approaches for random micro-geometries without periodic arrangement (also known as “windowing approaches” [38]), the material is approximated by one or many finite

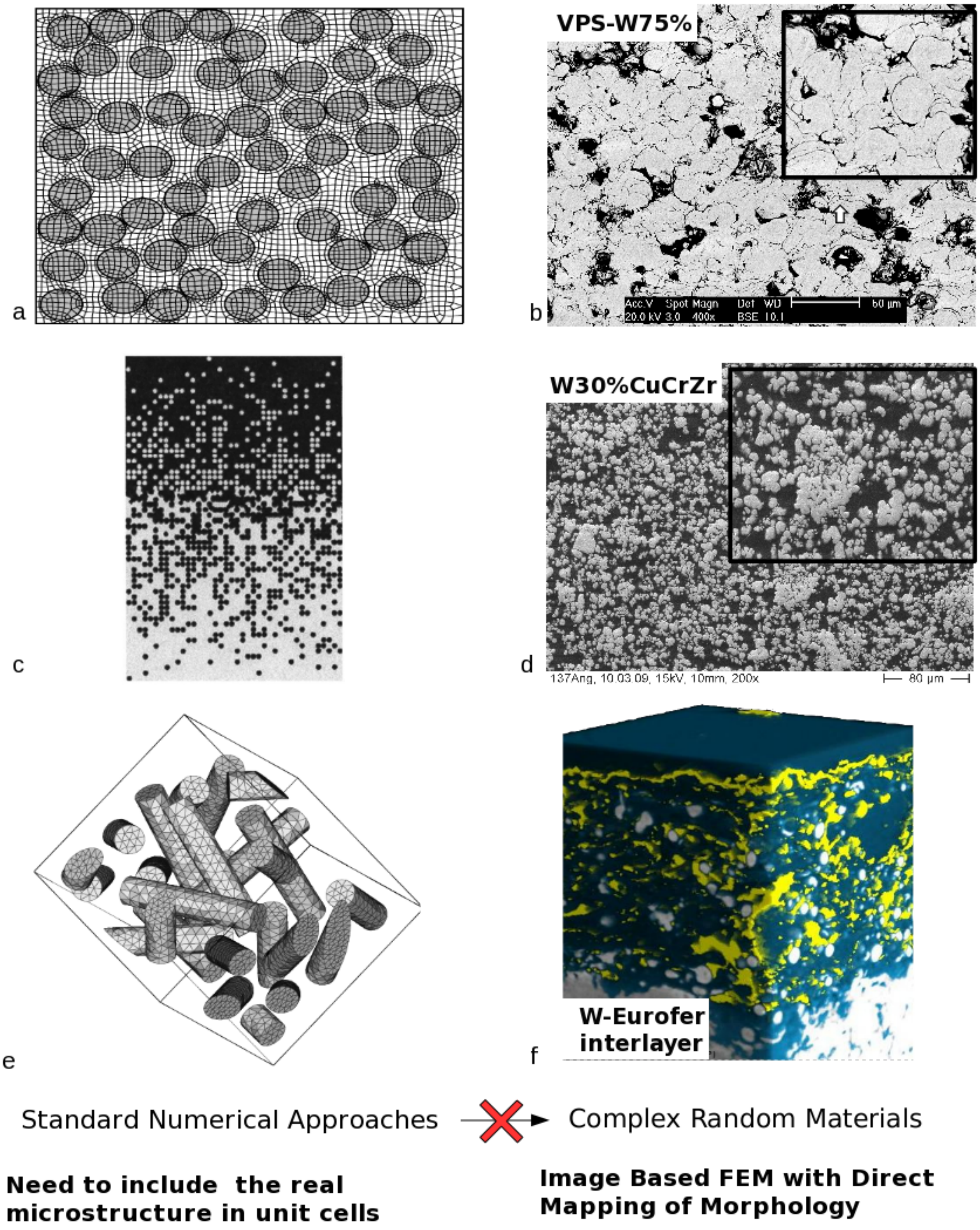

Figure 1.2: *On the left column: examples of unit cells generated via random distributions of inclusions of elementary shapes - a) planar distribution of disks representing a section of MMC with aligned fibers [39]; c) planar distribution of disks with vertical gradient of density representing a Functionally Graded Material [24]; e) 3D distribution of cylinders at random positions and orientations representing a random fiber composite[38]. In some cases this semi-analytical approach (based on random generator functions) cannot be used to properly model real microstructures. The three examples on the right column are much more complex random structures showing multiple scales (b), clustering (d) and non-stationarity of the random process (f). Unit-cells generated via direct mapping of the real morphology can easily and very accurately represent these microstructures.*

subvolumes (called “realizations of the random set” in the theory of random media [59]) supposed to be representative of the whole inhomogeneous material[1]. Classical windowing models are based on different (random) algorithms to distribute inclusions of elementary shapes (like polygons or polyhedrons: see, for instance, the popular Voronoi space tessellation scheme [57] widely used to model polycrystals [106] and foams [58]). For the specific case of FGM, a number of models can be found in literature [62, 25, 61, 60, 65, 66], mainly focused on general analytical and semi-analytical homogenization techniques (adapting the previously mentioned Eshelby and MTM - for an extended review of modeling works, the reader is referred to Birman [63]). Most of them, however, are based on the simplifying assumption of ideal FGM, with continuous variation of volume fraction. Sub-modeling of the microstructure (when present[2]) has been always performed distributing inclusions of elementary shapes (Fig. 1.2).

The current state of the art technique in numerical approaches for inhomogeneous materials is actually based on imaging of the real morphology, obtained either from cross-sectional microscopy (2D) or computer tomography (3D). Some recent works are [87, 67] and [71, 70, 69, 68] respectively.

This method, called here image-based finite element method (IB-FEM) but often found in the literature as “Object-Oriented FEM”, is based on a convenient discretization (meshing) of scanned 2D or 3D images of the real microstructure, used as geometrical input for the “direct” numerical calculation of *local* fields through the Finite-Element approach. This method is applied to a wide range of micromechanical problems, implemented through different possible boundary and initial conditions on the representative domain (prescribed temperature, heat-flux, traction or strain). The numerical solution is directly obtained on the mapped geometry, considered “as it is”. The only limitations in matching the model geometry with the real microstructure are given by the spatial resolution of the source image and the level of selected mesh refinement.

The main advantage of the IB-FEM compared to other conventional windowing approaches (based on the generation of unit-cells distributing inclusions of pre-defined geometrical shape) is the possibility to include into the model any possible real phase arrangement without the need to approximate the geometry of inclusions and without the need to guess their random distribution with complex (and always approximate) random multivariate generation functions.

The IB-FEM approach has already been proven successful in several works, most of them based on OOF2, a two dimensional mesh generator and FE solver [81, 80]. The tool is capable to generate mesh well adapted on a given cross-sectional image (taken from optical or electron microscopy) and to numerically estimate local solutions of *thermoelastic* problems for any possible two-dimensional phase arrangement (limited only in image spatial resolution). A

---

[1] According to one of the most recent and accepted quantitative definition of Representative Volume Element (RVE), as given in [106, 107], when one or an *ensemble* of such realizations spans a sufficiently large total volume, this can be statistically representative of the whole inhomogeneous material, for a given accuracy and a certain thermomechanical property.

[2] As stated from Birman in [63] (2007) “it is noted that the models most often used in the recent papers are the Mori–Tanaka method and the self-consistent method, i.e., the locally heterogeneous nature of FGM is usually disregarded”.

general good agreement with analytical and numerical solutions has been shown for various time-independent thermoelastic problems [83, 82, 84, 85, 88]. A quantitative good matching with experimental data has been shown for thermal properties of plasma-sprayed zirconia (with single-scale porosity) in [91] and for elastic properties of particulate-reinforced MMCs in [88], while qualitative agreement with experimental indentation measurements has been recently reported for crack propagation studies on brittle composites [86, 90]. As for 3D, some authors tried to correlate tomographic analysis with results from the extended finite element method (X-FEM) for simulating crack propagation but always modeling the material as homogeneous during simulation [69, 68].

To the author's knowledge, however, no published work to date based on object-oriented FEM explored the full *thermoelastoplastic* regime of random heterogeneous microstructures with ductile matrix (like sections of W30[%vol]/CuCrZr) explicitly accounting for ductile damage evolution up to failure. Furthermore, there is a need to predict via IB-FEM full macroscopic stress-strain curves (which include besides yielding also the softening and failure part) for the direct comparison with experimental ones. As for model generation, the meshes usually adopted, while accurate enough for their purposes, had limits in spatial resolution and size which were insufficient for the purpose of mapping large regions of a dual-scale random microstructure like that of VPS-W, including internal interfaces.

It appears therefore justified to adopt and extend the Image-Based FEM approach to model PS-W and W/CuCrZr as fusion relevant heterogeneous materials and as formidable case studies for numerical micromechanics.

The specific modeling objectives and strategies for each material are explained in the coming sections.

1.2 Purpose

The goal of this thesis is the extension of a general simulation procedure based on image-based FEM for modeling both the linear and non-linear thermomechanical behavior of W/CuCrZr and PS-W.

For the first random heterogeneous material in scope, W/CuCrZr, the general purpose was to investigate the influence of the complex microstructure of the macroscopic mechanical response as the basis for further material optimization at the level of the FGM joint. Because of the discontinuous variation of the microstructure in the layered design, the global joint response follows a hierarchical homogenization schema made of two levels. The first one is the mesoscale homogenization, i.e. the estimation of the average behaviour of the individual layers as dictated by the unique microstructure underlying each of them. The second one, based on the output of the first homogenization level, is the component level homogenization, i.e. the relationship between the multilayer structure (as the layers were homogeneous), and the overall response of the whole joint. This work only addresses the first homogenization level, which directly deals with the complex microstructure and is the fundamental one in the computational hierarchy.

More precisely, such investigation should cover the full thermoelastoplastic response of different concentrations (and morphologies) of W/CuCrZr MMC, for the temperature range which is relevant for reactor operation in steady-state (RT-550 °C).

As for PS-W, the specific purpose was firstly to investigate the influence of the random morphology, including interlamellar crack-like porosity in the heat transfer problem, which is critical for the coating. In order to get accurate results, the morphology of PS-W needed to be mapped with such a level of detail that it was necessary to overcome the resolution limit of the current state of the art techniques in IB-FEM. Furthermore, in order to include in the same simulation domain porous inclusions with large size differences (macro pores up to hundreds of micrometers and thin interlamellar voids at the lower boundary of the micrometer scale) large models were required. Finally, because of the morphological complexity of PS-W, the need for a 3D model of the real microstructure will also be addressed, in order to make comparison between predictions from 2D and 3D models and assess the quality of the 2D approximation.

1.3 Strategy

Because of its high accuracy and the possibility to calculate local fields, we adopted the image-based FEM approach to simulate the thermomechanical response of both materials. After an introduction on basic concepts of micromechanics in chapter 3, details on this method are provided in chapter 4. Special care has been taken in the choice of local material models (discussed in section 3.3).

The simulation of elastoplastic deformation and failure in W/CuCrZr has been implemented combining IB-FEM and the damage modeling capability of the FEM-Solver ABAQUS (Section 3.3.1). To simulate the complex crack initiation phenomenon across the random brittle/ductile phases, a continuum local damage model has been applied in combination with micrograph stress-concentration analysis. These results are discussed in chapter 5.

As for PS-W, the challenges of keeping the simulation domains large enough and the spatial resolution high enough required one to map 2D images with unprecedented resolution (0.2µm/px) and size (~0.1 mm^2). Besides a 2D model from Scanning Electron Microscopy, further efforts have been made into developing a tomographic 3D model. High resolution synchrotron tomography, which had to overcome the high absorption of tungsten while measuring large material volumes, was successfully carried out at the European Synchrotron Radiation Facility. It produced the first 3D reconstructions of the complex porous morphology suitable for FEM simulations. Details of this measurement are explained in chapter 6.

Results of 2D thermal- and 2D/3D mechanical modeling of PS-W are finally given in chapter 7. In order to address the issue of statistical representativity of simulation results, a quantitative estimation of the Representative Volume Element (RVE) will also be presented in section 3.4 and 7.3.3.

Chapter 2

Material Properties and Manufacturing

2.1 Tungsten[1]

Tungsten is a metallic transition element. Its most stable crystalline form is body-centered cubic (bbc). Besides amorphous tungsten, three crystalline modifications are known (α, β, γ), the most stable one being α-tungsten.

Tungsten has the highest cohesive energy[2] among all elements (including carbon in diamond) as indicated from ab-initio calculations [10]. This is the main reason behind its exceptional tensile strength (up to several GPa of theoretical strength for single crystal W at low temperature) and its capability to retain high strength values also at high temperatures (up to 800°C). Unfortunately, due to segregation of interstitials at grain boundaries, the cohesion between the single crystals (grain boundary strength) is much lower than the internal crystalline strength causing the well known high brittleness in polycrystalline tungsten.

As for elastic properties of the bulk form, tungsten behaves nearly isotropically up to room temperature with Young's modulus ranging from 390 to 410 GPa and shear modulus ranging from 156 to 177 GPa (for polycrystalline and single crystal forms respectively) [9].

Ultimate strength and yield stress are strongly dependent from grain size and grain shape which are strongly influenced by thermal history and extent of cold-working. Fig.2.2 shows the wide range of variation for the tungsten ultimate tensile strength. Ultimate elongation and extent of ductility can also vary considerably depending on purity and thermomechanical history (Fig. 2.1) .

For fusion applications the most important properties of W are thermal conductivity, tensile strength, thermal shock, creep and thermal fatigue resistance, structural stability at elevated temperature and stability of the properties under neutron irradiation [6].

Polycrystalline tungsten has an high ductile to brittle transition temperature (DBTT) which lies between RT and 800°C (depending on thermomechanical treatment) and an high recrystal-

---

[1] Here only some basic thermomechanical properties (of interest for the present contribution) are briefly presented. For an extended review of all the physical and chemical properties, the reader is referred to the first chapter of [9].

[2] defined as the difference between the crystalline bulk equilibrium energy and the energy of the free atoms

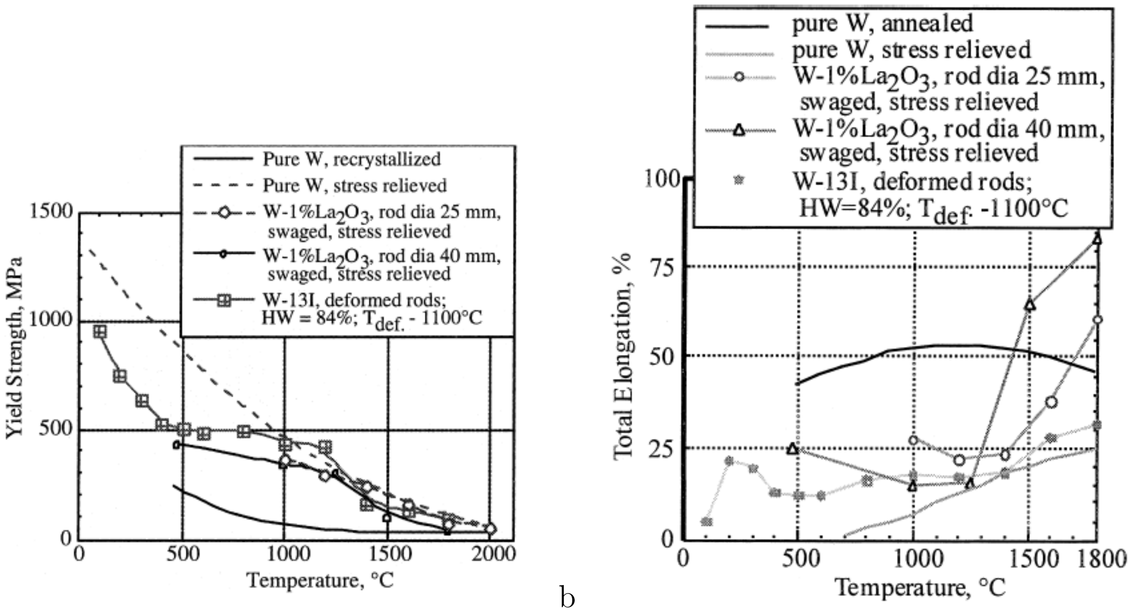

a b

Figure 2.1: *Yield strenght and ultimate elongation as function of temperature for different forms of dense W. Graphs taken from [115].*

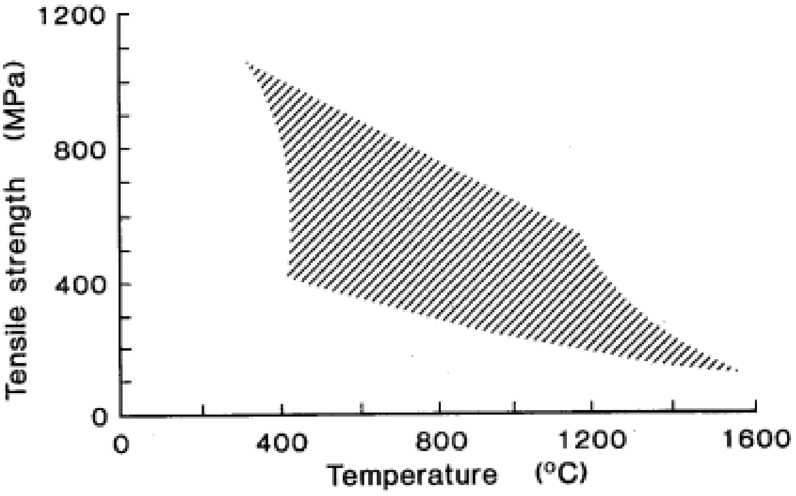

Figure 2.2: *Range of variation of ultimate tensile strength of tungsten sheets. The upper limit correspond to stress-relieved sheets, the lower limit to recrystallized sheets. Image courtesy of PLANSEE [116].*

lization temperature (1200-1350°C). DBTT can be lowered down considerably by cold working and doping with elements like rhenium [6] (improved ductility and reduction of crack formation during heat flux tests on W-Re[26%wt] has been reported in [8]). Depending upon deformation history, purity, thermal and stress-state, fracture in polycrystalline tungsten can be intergranular (developing along grain boundaries) or transgranular (cleavage) or most commonly a mixture of both modes [9].

Tungsten and tungsten alloys are commercially available in many forms. The most common manufacturing route is powder metallurgy (PM). Other manufacturing techniques are casting, chemical vapor deposition (CVD), physical vapor deposition (PVD) and plasma-spraying (PS)

[9]. Production of dense tungsten via powder metallurgy comprises two steps: compaction and sintering. Compaction is usually done via *cold isostatic pressing* with pressure in the range of 200 to 400 MPa. Sintering is a high temperature thermal treatment (commonly performed between 2000 and 2700 °C in hydrogen atmosphere[3]) necessary to increase the strength of green compacts through lowering of the surface energy by diffusional flow into pores under the action of capillary forces (shrinkage). Besides this, other phenomena occurring during sintering like recovery (change of sub-grain structures and strain relief), recrystallization and grain growth also contribute to the minimization of the free energy [9].

2.1.1 (Vacuum) Plasma-Sprayed Tungsten

The plasma spraying technique, developed in the 1970s, uses a high-temperature plasma jet to partially melt and accelerate metal particles on a substrate. Very high temperatures are reached within the plasma flame which is generated by arc discharge (plasma flame temperature is guessed to be higher than 15000 K [102] but modeling the complex plasma-spray physics is still an active research field[99]). This makes it possible to spray even tungsten, the metal with the highest melting point.

Vacuum plasma-sprayed tungsten (VPS-W) is produced from cumulative deposition of tungsten droplets with an Ar/H_2 plasma torch in a low oxygen environment (usually between $10^{-3}$and 10^{-4} mbar) [15]. Since the spraying atmosphere has a strong influence on coating performance[78] a controlled atmosphere can improve thermal diffusivity (due to reduced oxidization and reduced number of entrapped gas molecules at inter-splats boundaries or inside macropores). The tungsten droplets are from a much coarser starting powder than those used for sintering [9]. The plasma jet flame accelerates and partially melts the solid particles which hit the substrate at high speed. Estimated impact velocity ranges from 100 to 500 m/s for low Z-metals like aluminum and nickel [98, 99] (depending on several plasma-gun parameters), while estimations for W are missing in the literature. Once the partially molten tungsten droplets impinge the actively cooled substrate, they "splat" upon each other and solidify under fast cooling rate (up to 10^6K/s [102]). The chosen substrate and the plasma torch parameters (voltage, current, gas velocity, strike angle, etc) strongly affect porosity and coating morphology. Average porosity typically ranges from 5 to 40 %, while for a given porosity value different morphologies can be obtained [9, 11]. We measured on our coating a porosity of 22.5% +-1% (with microbalance and assuming literature value for the tungsten density at RT).

PS, and thermal spraying techniques in general, usually generate residual stress in the coating system. Quenching stress and mismatch stress are two major contributions to the residual stress[23, 97]. The so-called quenching stress is generated by rapid cooling of hot-sprayed molten splats striking the substrate whereas the mismatch stress sets up due to the mismatch of thermal contraction during the final cooling (cooling from the steady state deposition temperature to ambient temperature).

---

[3] to remove oxygen layers from the tungsten particles

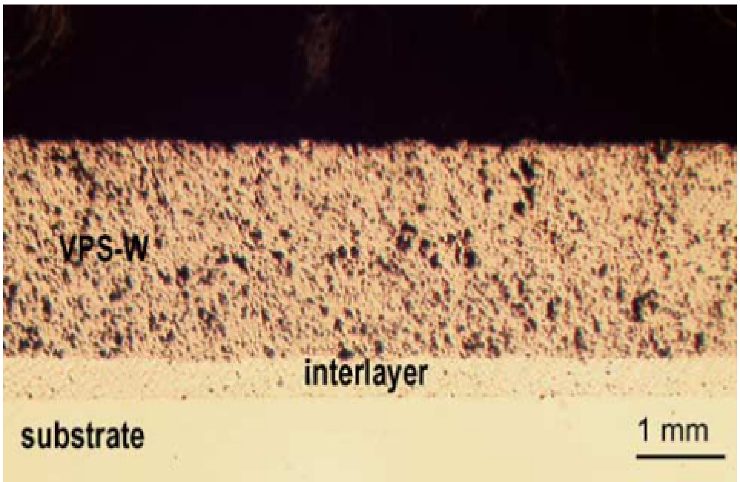

Figure 2.3: *Cross-sectional optical micrograph of the VPS-W coating system: coating, W/steel interlayer and steel substrate (EUROFER) [15].*

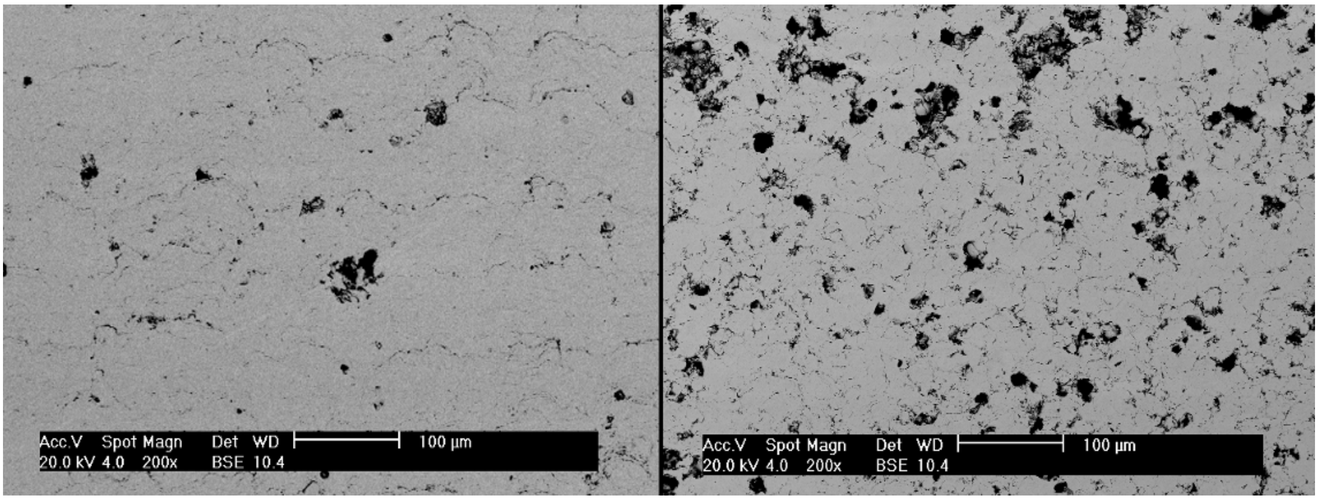

Figure 2.4: *SEM images showing the different morphologies of low and high porosity (left and right respectively) VPS-W deposited on steel.*

More details about the plasma spraying technology can be found in [103].

2.2 W/CuCrZr FGM Composites

W/CuCrZr Functionally Graded Materials (FGMs) are a recent development of the most common W/Cu FGMs, obtained using CuCrZr-alloy (see next section) instead of pure copper [28]. W/Cu composites are mostly fabricated by powder metallurgical routes [30, 29] whereas plasma spraying is also possible [31]. The most popular way to produce W/Cu FGMs is by forming a tungsten skeleton with graded open pores and subsequent infiltration [36, 32, 28]. Two important manufacturing requirements are a penetration microstructure which allows solidification of a continuous percolating ductile network and low residual porosity (to maximize thermal conductivity and reduce failure spots) [30, 28, 34].

Manufacturing of W/CuCrZr-composites was performed at Dresden Technical University, Institut für Werkstoffwissenschaft. The generation of a W/CuCrZr FGM consisted of two main

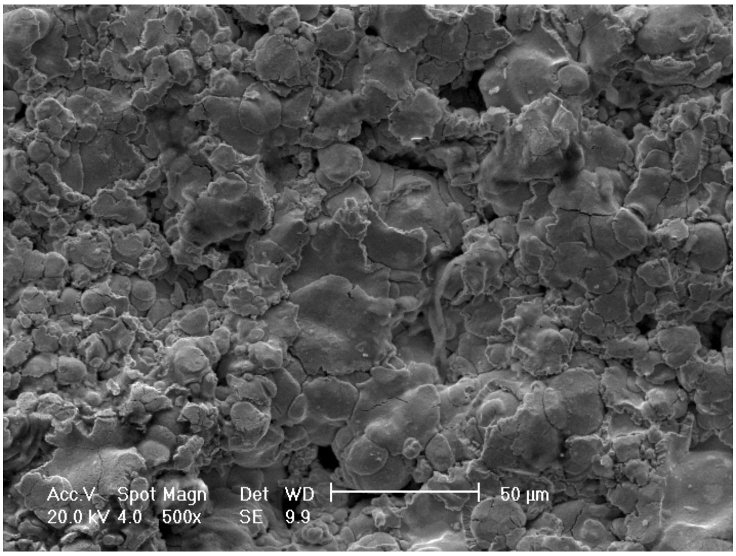

Figure 2.5: *Top view of the surface morphology of a 15% porous VPS-W coating. One can notice the boundaries of the solidified W-droplets.*

steps:

1. Assembly of a graded tungsten skeleton with a multi-layer structure (Fig. 2.6)
2. Infiltration of the tungsten skeleton with CuCrZr

For the preparation of a graded tungsten skeleton (1) several kinds of methods are available such as using different size W powders, space holders, centrifugal powder forming (CPF), electrochemical gradation and powder segregation [30, 29, 33, 32, 35]. The chosen method was based on amid wax as space holder and subsequent sintering of the three different layers (with 30, 55 and 70 [%vol] amount of W respectively).

The tungsten skeleton was assembled from powder metallurgical tungsten (provided by PLANSEE Metall, Austria.), with average particle size of 4 µm for W and 12 µm for the amid wax (provided by Hoechst, Germany). The tungsten powder and the amid wax were mixed together and ground in a mortar for 30min to increase the homogeneity of the mixture. Next, green compacts were uniaxially pressed at different pressures and debinded/sintered in hydrogen at 450°C for 30min and 1200°C for 60min respectively. For the production of a porous graded tungsten skeleton with three layers the mixed powders were pressed layer by layer and then debinded/sintered.

In the second step (2) CuCrZr sheets provided by Thyssen Duro Metall (Germany) with a composition of CuCr0,8Zr0,08[%wt] were placed on top of the tungsten samples and heated at 1200°C for 30min. The molten CuCrZr filled the pores of the tungsten skeleton solidifying during cooling down to RT. Infiltration experiments under different atmospheres revealed that only under vacuum condition (p~10^{-3} mbar) it was possible to produce completely infiltrated, dense W/CuCrZr-composites with a homogeneous distribution of the ductile alloy.

The copper alloy in composite was then precipitation hardened by solution annealing in

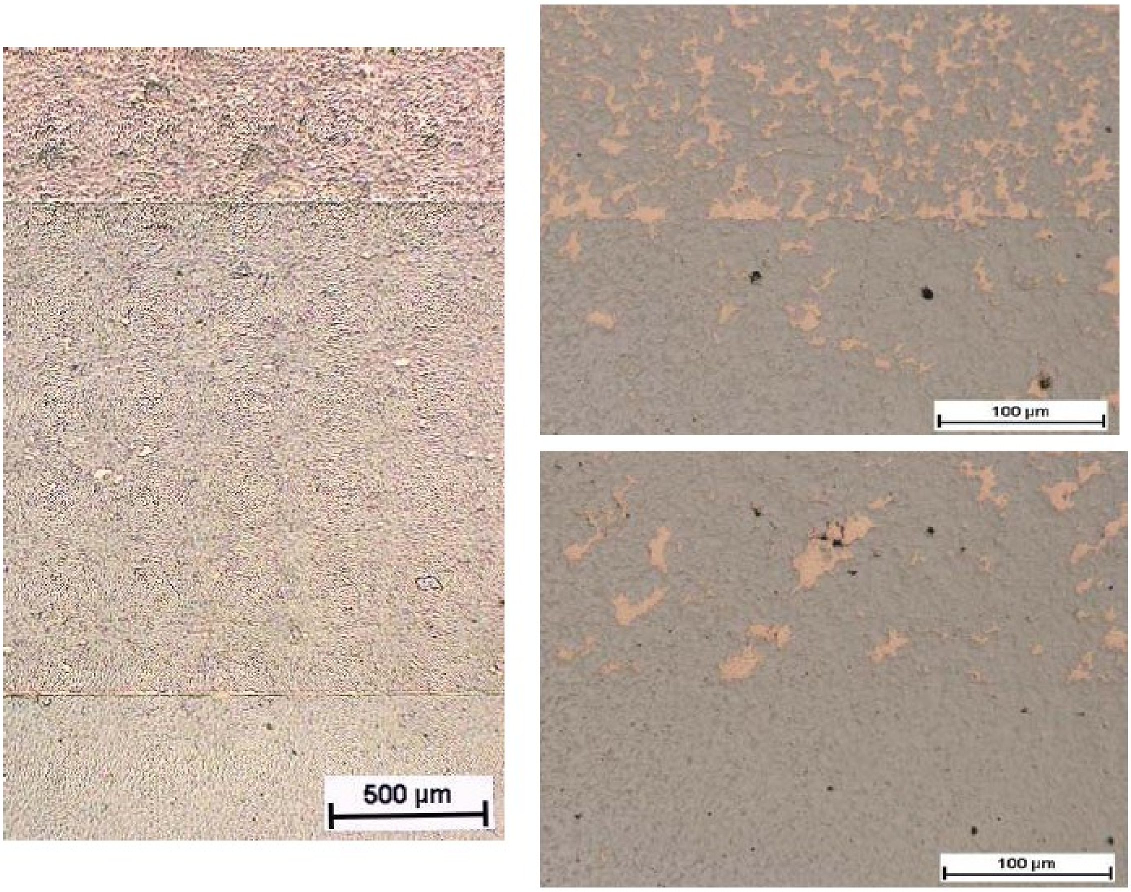

Figure 2.6: *Prototype of a W/CuCrZr multilayer gradient structure (30, 55 and 70 %vol. of W respectively) [28]. Top-right: the transition zone W30[%vol]-W55[%vol]. Bottom-right: the transition zone W55[%vol]-W70[%vol]. Images were taken with optical microscope causing the CuCrZr phase to be barely visible in the lowest layer.*

high vacuum at 970°C for 30min[4] and by aging in argon atmosphere at 480°C for 60min (at this stage the composite is assumed to be stress relieved). The final step was air cooling out of the furnace. The last thermal transition from 480°C to RT was considered for the calculation of residual stress in W/CuCrZr as we will see in section 5.3.

A more detailed description of the complex metallurgical route for manufacturing of W/CuCrZr FGM can be found in [28].

2.2.1 CuCrZr

Cu alloys, are usually selected for fusion applications due to higher yield stress and fracture toughness at high temperatures compared to standard copper [120]. Copper-chromium-zirconium (CuCrZr) is a precipitation-strengthened alloy whose typical composition is Zr 0.03 - 0.3%, Cr 0.5 - 1.2%, rest Cu [119]. It exhibits an α-structure in the solution-annealed state and crystallizes in a face-centered cubic (fcc) body like pure copper. Precipitation hardening considerably increases strength and yield stress . Through aging under the solubility temperature,

---

[4] together with oil quenching treatment without breaking the vacuum

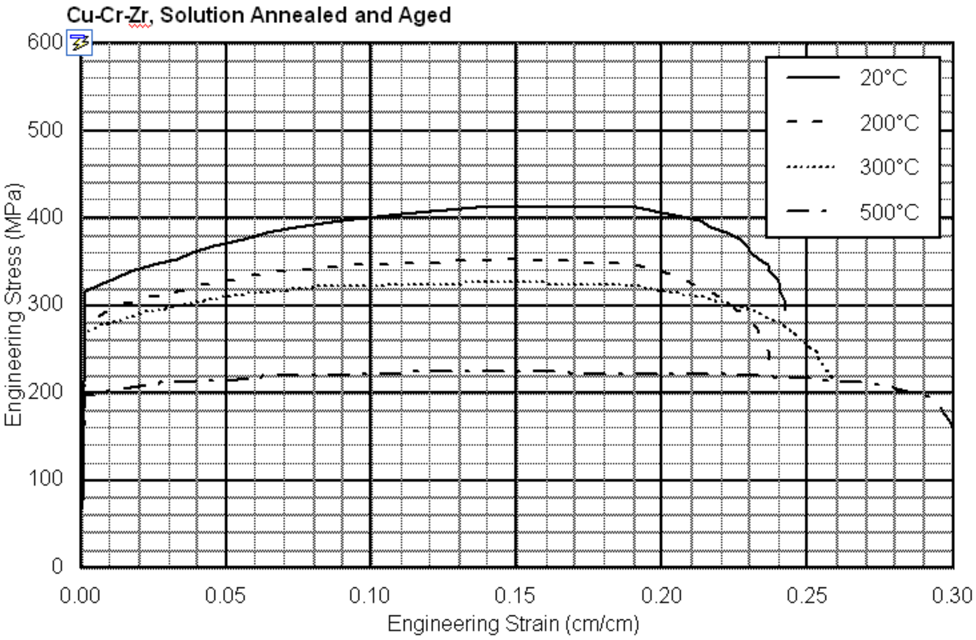

Figure 2.7: *Experimental stress-strain curves of CuCrZr (solution annealed for 1h at 980°C, water quenched and aged at 475°C for 2h). Graph taken from [117].*

Cr and Cr2-Zr phases precipitate out of the over-saturated matrix. The precipitates are homogeneously dispersed at 450°C before dissolving. This Cu-alloy can therefore be used within temperature ranges up to the precipitation temperature [27]. Fig. 2.7 shows stress-strain curves at different temperatures of precipitation hardened and aged CuCrZr. A combination of thermomechanical treatments can be adopted to target specific material properties optimization (like radiation resistance, for instance [120]). Cold working before aging further improves the yield strength [117] and provides for better homogeneity of the precipitate distribution through the structure, while retaining good ductility. For obvious reasons however, the CuCrZr employed in W/CuCrZr FGM could not be cold-worked. Fig. 2.7 shows stress strain curves of solution-annealed, oil quenched and aged CuCrZr as taken from the ITER MPH [117] (of the same kind of the CuCrZr used for manufacturing W/CuCrZr FGM).

Chapter 3

General Micromechanical Framework

The main purpuse of this work was to develop numerical micromechanical models of random heterogeneous materials with complex microstructure. In this chapter the necessary theoretical background is briefly presented in order to understand the general framework behind the modeling strategy adopted. An extended description of the specific image-based Finite Element technique (mostly concerning mesh generation) is left to the next chapter.

The vast subject of micromechanics is just shortly revised here. After an explanation of the fundamental multiscale approach and basic numerical homogenization technique we will focus on the description of the local models used for the phase constituents (tungsten and copper alloy). An advanced constitutive model based on Continuum Damage Mechanics for modeling ductile damage evolution in CuCrZr is discussed in a dedicated section (3.3.1). The last section introduces some notions of statistical characterization of random media (as both materials in scope belong to this category) and focus in particular on a rigorous definition of the Representative Volume Element (RVE).

For a more formal treatment of the concepts and methods discussed in what follows the reader is referred to dedicated micromechanical textbooks like e.g. those of Böhm [38] and Torquato [47].

3.1 Microscale, Mesoscale and Macroscale

A fundamental aim of *continuum micromechanics* lies in deducing overall *effective* properties of multiphase heterogeneous materials from the corresponding material behavior of the constituents and from their geometrical phase arrangement. Depending on the specific material microstructure and on the goal of investigation, a micromechanical approach implies different levels of material description. In the literature one usually distinguish three levels (here qualitatively described because limits between the scales can change slightly, depending on the material and modeling approach chosen):

- microscale: the bottom limit of continuum models. It include micro and sub-micron structures. At the microscale the solids can be described with their grain-boundary structure and plastic deformation can be described in terms of dislocation density[1].

- mesoscale: usually the level of phase arrangement and inclusions in heterogeneous composites. The range of the mesoscale can be extremely wide as the inclusions can range from few micrometers up to several millimeters.

- macroscale: the level where materials can be described as homogeneous. It usually ranges from millimeters to large length scales.

Continuum micromechanics usually aims at linking mesoscale with macroscale. With this convention the terms "micromechanics" and "microstructure" are sometime misleading and they are replaced by *mesomechanics* and *mesostructure* respectively.

Anyway, what really distinguishes a micromechanical approach from that of classical continuum mechanics is a defined modeling hierarchy. This usually consists of two levels: a *bottom level* (defined at the micro-scale or at the mesoscale or at both scales), where the material micro- or mesostructure is described explicitly and a *top-level* (which defines the macro-scale), where the material is described as homogeneous with effective properties.

The bottom-up linkage between the two levels is generally referred as *homogenization*, while the top-down connection is called *localization.* General homogenization approaches assume a marked separation between scales, so that a macrofield as $A(\mathbf{x})$ (function of the position vector$\mathbf{x}$; it could be stress or strain or whatever thermomechanical field) can be split into two components, a slow and a fast one:

$$A(\mathbf{x}) = \langle a \rangle + a'(\mathbf{x}) \tag{3.1}$$

where $\langle a \rangle$ is the slow macroscopic field, whereas $a'(\mathbf{x})$ represents the fast field (microscopic fluctuations). However, the extent of such separation is usually not well defined and rather arbitrary.

For inhomogeneous materials that show sufficient separation between the length scales the relation:

$$\int_\Omega \widetilde{\sigma}(\mathbf{x})\widetilde{\varepsilon}(\mathbf{x})d\Omega = \int_\Omega \widetilde{\sigma}(\mathbf{x})d\Omega \int_\Omega \widetilde{\varepsilon}(\mathbf{x})d\Omega \tag{3.2}$$

can be shown to hold for general statically admissible stress fields $\widetilde{\sigma}$ and kinematically admissible strain fields $\widetilde{\varepsilon}$, (see [45]). This equation is known as Hill's macro homogeneity condition, the Mandel–Hill condition or the energy equivalence condition.

3.2 Numerical Homogenization

Two general approaches can be pursued in homogenization: *analytical* and *numerical.* The first one aims at finding macroscopic constitutive equations in closed form through an analytical

---

[1] this is the case of crystal plasticity models

description of the microstructure (usually simplified, with inclusions represented with ideal geometrical shapes). [2]

On the other hand, *numerical* (or *computational*) approaches aim at finding effective properties at the macroscale (and eventually also approximate constitutive relations[3]) from a direct numerical solution of basic equilibrium equations at the microscale. Here the microstructural information is not simplified by inclusions of elementary shape and can be in principle any phase arrangement.

Numerical homogenization methods usually operate on *unit cells* (also called *simulation domains* or improperly RVE) which are models of the material microstructure. This can be represented in a more or less accurate way depending also on the material in scope. For the complex random morphologies of PS-W and W/CuCrZr composites, the image-based method adopted in this work generates unit cells from real images of the material microstructure, i.e. the microstructure is represented in a very accurate way[4]. Since the particular morphologies under investigation span a quite large interval of scales (from submicrometric interlamellar gaps in PS-W to inclusion clusters of hundreds of micrometers in W/CuCrZr) we refer to our unit cells simply as *mesoscale unit cells* (implicitly including also the microscale) and to the homogenization level as *meso-macro* homogenization.

In numerical homogenization applied to random structures the concept of Representative Volume Element (RVE) is of paramount importance as it sets the limit between micro/meso and macroscale. The RVE is qualitatively defined as the minimum volume that is *sufficiently large* to be statistically representative of the whole material while remaining small enough to be considered as an elementary (ideally infinitesimal) volume element in a macroscopic description of the material as homogeneous medium (macroscale). Later in section 3.4.1 we will return more extensively on the RVE concept introducing a more rigorous statistical definition.

In this work the numerical approach is based on the finite element method (FEM) and numerical *homogenization* means “averaging” a certain microfield over the unit cell. Here it is important to distinguish the concept of RVE from that of unit cell: the RVE is a particular unit cell (or a set of unit cells) which satisfies the requirement of sufficiently large total size to achieve a predefined statistical accuracy in prediction of macroscale properties. In other words, a unit cells of size V becomes an RVE once the statistical accuracy associated with that particular volume size is known and is sufficiently low.

In mathematical form, homogenization refers to an operation (indicated by the symbol $\langle\rangle$ or $\langle\langle\rangle\rangle$) which transforms a general tensorial microscopic field $a_{ij}(\mathbf{x})$ into a corresponding macroscopic field $\mathbf{A} = A_{ij} = \langle a_{ij}(\mathbf{x})\rangle$. For the micro fields of stress $\sigma_{ij}(\mathbf{x})$, strain $\varepsilon_{ij}(\mathbf{x})$ and heat-flux $\phi_i(\mathbf{x})$ within a unit cell models of sufficiently large volume V, this operation is by

---

[2] The analytical methods fall into further two categories: variational estimates (bounds) or direct estimates.

[3] A more general aim of computational homogenization is to find not only effective properties but also macroscopic *constitutive equations* through a dynamic linkage between top and bottom level which assures convergence during an iterative multiscale numerical procedure. This is not the case of the present contribution which focuses on the meso-macro linkage through a single homogenization step.

[4] limited only by the resolution of the imaging technique and computational power

definition the volume average of the micro fields across the cell:

$$\langle \sigma_{ij} \rangle = \frac{1}{V} \int_V \sigma_{ij}(\mathbf{x}) dV \tag{3.3}$$

$$\langle \varepsilon_{ij} \rangle = \frac{1}{V} \int_V \varepsilon_{ij}(\mathbf{x}) dV \tag{3.4}$$

$$\langle \phi_i \rangle = \frac{1}{V} \int_V \phi_i(\mathbf{x}) dV \tag{3.5}$$

Computational homogenization takes as input the numerical solution obtained in a simulation cell and outputs estimations of the macroscopic quantities through equations 3.3,3.4 and 3.5.

When using a finite element grid or mesh, equations 3.8 and 3.5 can therefore be estimated through the following formulas:

$$\langle \sigma_{ij} \rangle \approx \frac{1}{V} \sum_n \sigma_{ij}^{FE}(\mathbf{x}_\mathrm{n}) V_n \tag{3.6}$$

$$\langle \varepsilon_{ij} \rangle \approx \frac{1}{V} \sum_n \varepsilon_{ij}^{FE}(\mathbf{x}_\mathrm{n}) V_n \tag{3.7}$$

$$\langle \phi_i \rangle \approx \frac{1}{V} \sum_n \phi_i^{FE}(\mathbf{x}_\mathrm{n}) V_n \tag{3.8}$$

Where $\sigma_{ij}^{FE}(\mathbf{x}_\mathrm{n})$and $\varepsilon_{ij}^{FE}(\mathbf{x}_\mathrm{n})$ are the approximate solutions of the micro fields of stress and strain at the integration point $\mathbf{x}_\mathrm{n}$ as obtained by the finite element method and V_n is the volume associated with that integration point. For planar and volumetric meshes based on triangles and tetrahedrons respectively, $\mathbf{x}_\mathrm{n}$ is usually taken as the centroid of the element n and the field value linearly interpolated there. The reduction of the previous equations for the planar case is trivial.

Thanks to the Gauss's theorem it is possible to demonstrate the equivalence between volume integrals and surface integrals when the condition of continuity is satisfied for internal fields. For the most symmetric uniaxial loading cases (like most of the cases handled here), it is therefore convenient to calculate the macroscopic fields of strain and stress from the displacement at master nodes or from stress components at master edges of the simulation cell[5].

3.2.1 Equilibrium and Constitutive Equations

For a material region subjected to external thermomechanical load and for all its subvolumes a state of equilibrium of forces, momenta and heat-fluxes is to be found (at both micro and macrolevel). The microfield equations to be solved numerically concern the theory of elasto-

---

[5] master nodes and master edges are respectively the grid nodes or element faces where the boundary conditions have been prescribed.

plastic solids, on the one hand, and that of heat transfer, on the other hand. The associated governing equations for a body of volume V are the balance of momentum and the heat equation respectively:

$$\sigma_{ij,j}(\mathbf{x}) = 0 \tag{3.9}$$

$$\phi_{i,i}(\mathbf{x}) = 0 \tag{3.10}$$

They must be fulfilled at any regular material point $\mathbf{x} \in V$ of components x_i in a Cartesian orthonormal coordinate system.

The comma, i denotes partial derivation with respect to the coordinate x_i. The symbols $\sigma_{ij}$and ϕ_i denote the stress tensor and the heat flux vector components respectively. Sources terms, such as body forces and heat production, are not considered in this work. Dynamical effects and transient thermal conduction are also excluded.

In order to solve equations 3.9 and 3.10 further relations are required which relate the micro fields of stress, strain and temperature. These are the so called “constitutive equations”, supposed to govern the *local* behavior at the microscale of phase constituents i.e. the behaviour of small (ideally infinitesimal) volumes of homogeneous phase constituents.

Basic constitutive equations describing heat transfer, thermoelasticity and metal plasticity are postponed in Appendix A. The choice of appropriate constitutive equations for modeling the phase constituents of W/CuCrZr and VPS-W is discussed in section 3.3

3.2.2 Boundary Conditions

A volume element V made of a heterogeneous material is considered. Conditions are prescribed at its boundary ∂V in order to estimate its overall properties. For mechanical problems, two types of boundary conditions (BC) are classically used in computational homogenization([34]): kinematic uniform (KUBC) or stress uniform (SUBC).

KUBC are defined imposing a displacement vector $\mathbf{u}$ at any point$\overline{\mathbf{x}}$ belonging to the boundary ∂V of the unit cell, such that:

$$\mathbf{u} = \langle \varepsilon_{ij} \rangle \, \overline{\mathbf{x}} \quad \forall \overline{\mathbf{x}} \in \partial V \tag{3.11}$$

In case of a simple tension test and a unit cell of height H the previous equations implies:

$$\mathrm{u}_{2,3}(n_i) = \bar{\varepsilon}\, H;\ \forall \mathrm{n_i} \in \mathit{TOP\,nodes} \qquad \mathrm{u}_{2,3}(n_i) = 0;\ \forall \mathrm{n_i} \in \mathit{BOTTOM\,nodes} \tag{3.12}$$

Where $\bar{\varepsilon}$is the prescribed macroscopic strain and the indexes 2 and 3 refer to 2D and 3D cases respectively.

SUBC are defined imposing the traction vector at the boundary∂V (with normal vector $\mathbf{n}$) such that: $\sigma_{ij}(\overline{\mathbf{x}})n_j = \langle \sigma_{ij} \rangle \, n_j; \; \forall \overline{\mathbf{x}} \in \partial V$. SUBC were not used in this work.

For the thermal problem in steady-state one can usually impose either Uniform Heat Flux (UHF) or Uniform Gradient of Temperature (UGT) at the boundary. We used UGT with fixed temperatures at the TOP and BOTTOM nodes of the micrograph.

In both the mechanical and thermal cases one can also set periodic boundary conditions (PBC) and combine the fundamental BC into Mixed Uniform Boundary Conditions (MUBC). PBC however, were not considered here since they are problematic to implement on image-based unit cells without geometrical periodicity. Furthermore, they require a considerable amount of additional memory [107]).

For the two special cases of KUBC and SUBC the Hill's condition (equation 3.2) can be shown to hold by transforming the volume integrals into surface integrals, to which the fluctuations σ and ε give zero contributions. This is referred to as Hill's lemma.

3.3 Modeling the Phase Constituents

Results of a micromechanical simulation are obviously affected from the material data and the constitutive equations assigned to the single phases of the microstructured composite. We discuss here how we modeled the solid phases (W and CuCrZr in W/CuCrZr and W in VPS-W) in FE simulations. Since their properties are function of the manufacturing process we provide first a short description of their metallurgical history.

In W/CuCrZr composites, a local thermoelastoplastic behaviour with progressive damage evolution has been assumed for the ductile phase. For modeling W in W/CuCrZr composites and in VPS-W coating, linear thermoelasticity have been adopted and criteria for the crack onset have been defined.

A general assumption for all the microscale constitutive models adopted in this work was *isotropic response* for all the phase constituents.

3.3.1 Continuum Damage Model for Ductile Failure in CuCrZr

A ductile damage evolution model for modeling ductile damage and failure in W/CuCrZr was included within the image-based FEM simulation scheme. Ductile damage evolution models are usually based on continuum damage mechanics (CDM). CDM is a vast research area which has been widely developed over the past years both phenomenologically and theoretically (see for instance [124] and [122]). Main scope of CDM is to investigate the conditions of material degradation leading to failure within the framework of continuum mechanics. The main differences with the fracture mechanics (FM) approach is that FM investigates the conditions for crack stability and propagation once a “macroscopic” crack front has already been initiated while CDM focuses on the pre-conditions of failure as determined by the overall effect of damage processes occurring at a lower scale.

From the microscopic point of view the key role played by microvoids in ductile fracture has been pointed out by Rice and Tracy already in 1969 [125]. Microvoids start at the interface of the ductile matrix with brittle inclusions and precipitates as soon as the local stress field is strong enough either to debond or to break the inclusions. Subsequently, voids growth until they link by coalescence. Gurson, Needlemann and Tverrgaard [126, 127] proposed a porosity based analytical model (the GNT model) where the yield function for ductile materials is modified by growth and coalescence of voids: when the void volume fraction f, considered as a local parameter, starts to increase material softens and progressively looses its capability to carry loads. The GNT approach incorporates the micro-meso connection in its analytical formulation, but for mascroscale predictions it should be usually incorporated within unit-cell homogenization schemes.

Homogenization on unit-cells which include portions of the real material microstructure was the approach considered in this work for model ling ductile failure in W/CuCrZr composites, with two main differences with respect to classical homogenization schemes which incorporates

GNT models. First, an intermediate mesostructure is necessarily introduced (the mesoscale arrangement of random inclusions) where the ductile phase (CuCrZr) is itself one of the two random phases. In the IB-FEM simulation scheme the ductile phase is then further substructured into smaller domains (the elements of an IB-mesh). Second, the chosen damage evolution parameter for the numerical constitutive model is here the *accumulated plastic strain* (instead of the void volume fraction) with the assumption that this parameter incorporates the average effect of the mentioned ductile damage processes supposed to occur at a lower scale (the *microscale*).

In this section we will briefly describe the general CDM-approach (limited to the case of isotropic ductile metals) and the damage evolution model which was used in our simulations as implemented in ABAQUS [92].

General CDM Approach

Following Lemaitre and Chaboche [123], the CDM approach is based on the concept of effective stress and equivalent strain, assuming degradation of stiffness and a parameter (D) which quantifies this degradation. The degradation of elastic capability of the material is considered the result of a number of microcracks and voids which progressively reduce the available surface able to transmit stress and ultimately reduces the stiffness of the damaged material considered as homogeneous. When the damage phenomenon occurs isotropically only a scalar D is needed to model it. Two important stages should be identified in a CDM-model (Fig. 3.1): the stage of damage initiation (corresponding to $D = 0$) and the stage of total material failure (usually corresponding to $D = 1$, while experimental measurements). The stress value resulting from measuring the same strain on a undamaged specimen (equivalent stress $\overline{\sigma}$) is therefore reduced by a factor (1-D). For the general multiaxial the effective (measured) stress for the damaged specimen is:

$$\sigma = \overline{\sigma}(1 - D) \tag{3.13}$$

Consider now the simple monoxial loading case (Fig. 3.1).We can measure the total equivalent strain and isolate the elastic contribution $\bar{\varepsilon}^{el}$ as:

$$\bar{\varepsilon}^{el} = \frac{\overline{\sigma}}{E} = \frac{\sigma}{(1 - D)E} \tag{3.14}$$

From which it follows the stiffness degradation (from E to E*(1-D)) of our material in the “softening” part of the stress-strain curve.

The damage parameter can be measured in different ways, the most common one is to measure the stiffness during unloading. By repeating load/unload cycles for increasing total strain it is also possible to track the evolution of D.

Basically a CDM-model consists then of three parts:

- a suitable elastoplastic material model for the undamaged case

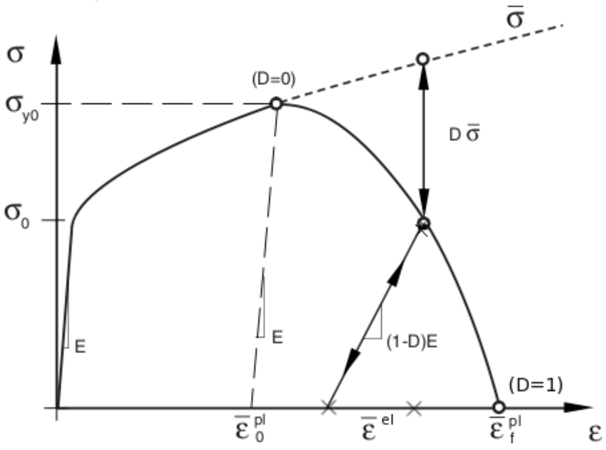

Figure 3.1: *Reference stress-strain curve under monoaxial tension to explain the CDM-approach for modeling progressive damage degradation (from D=0 to D=1). Image reprinted by permission from Dassault Systèmes (Abaqus Analysis User's Manual) [92].*

- a single or multiple damage initiation criteria (usually based on effective plastic strain or dissipated plastic energy)

- a damage evolution law

CDM-models have been developed for metals, concrete and rocks using different damage initiation criteria (isotropic or anisotropic, monoaxial or multiaxial) and different damage evolution laws (based on stress or energy) [123]. In complex models more than one initiation criterion can be used each with an associated parameter d_i and the maximum of such set (or a function of them) is the actual damage parameter. Since convergence of the FE solution was not easy to get due to the geometrical complexity of image-based models (non-linearity of the solution domain) only isotropic CDM-models with a single initiation criterion were assumed (mixed mode initiation criteria are not considered here).

Initiation Criteria for Ductile Metals

Two main mechanisms can cause the fracture of a ductile metal: ductile fracture due to the nucleation, growth, and coalescence of voids; and shear fracture due to shear band localization. Based on phenomenological observations, these two mechanisms call for different forms of the criteria for the onset of damage [121], namely the Ductile Criterion and the Shear Criterion.

The Ductile Criterion is a phenomenological criterion based on strain for predicting the onset of damage due to nucleation, growth, and coalescence of voids in ductile metals. The model assumes that the equivalent plastic strain at the onset of damage, $\bar{\varepsilon}_{pl}^{D}$, is a function of stress triaxiality $\eta = -p/q$ (where p is the isostatic pressure and q the Mises equivalent stress) and equivalent plastic strain rate $\dot{\bar{\varepsilon}}_{pl}$:

$$\bar{\varepsilon}_{D}^{pl} = f(\eta, \dot{\bar{\varepsilon}}_{pl}, T) \tag{3.15}$$

The criterion for damage initiation is met when the following condition is satisfied:

$$\omega_D = \int_0^{\varepsilon^{pl}} \frac{d\bar{\varepsilon}^{pl}}{f(\eta, \dot{\bar{\varepsilon}}_{pl}, T)} = 1 \tag{3.16}$$

where ω_D is a state variable which increases monotonically with plastic deformation.

The shear criterion is a phenomenological model for predicting the onset of damage due to shear band localization. The model assumes that the limit value $\bar{\varepsilon}^S_{pl}$ is here a function of the shear stress ratio θ and strain rate:

$$\bar{\varepsilon}^S_{pl} = g(\theta, \dot{\bar{\varepsilon}}_{pl}, T) \tag{3.17}$$

$$\omega_S = \int_0^{\varepsilon^{pl}} \frac{d\bar{\varepsilon}_{pl}}{g(\theta, \dot{\bar{\varepsilon}}_{pl}, T)} = 1 \tag{3.18}$$

where $\theta = (q + kp)/\tau_{max}$, $\tau_{max}$is the maximum shear stress, and k is a material parameter. The shear criterion however appears indicated for situations where the average finite element size is large enough to include the band localization phenomenon within it. This is certainly not the case for the our W/CuCrZr meshes, where, as wil will see bands develop at the mesoscale involving many elements. For this reason a ductile criterion appeared more indicated.

However, in case of our CuCrZr neither for f nor for g the exact dependence from their parameters is known, but what really counts in the end is the ratio between the total equivalent plastic strain[6] $\bar{\varepsilon}^{tot}_{pl} = \int_0^{\bar{\varepsilon}_{pl}} d\bar{\varepsilon}_{pl}$ and a certain plastic strain threshold $\bar{\varepsilon}^D_{pl}$. It appeared therefore a reasonable approximation to assume f or g as constant functions.

For this reasons we assumed a simplified form of the damage initiation criterionω_D:

$$\omega_D = \frac{\int_0^{\varepsilon^{pl}} d\bar{\varepsilon}_{pl}}{\bar{\varepsilon}^D_{pl}(T)} = 1 \tag{3.19}$$

with $\bar{\varepsilon}^D_{pl}(T)$ increasing with temperatures (as suggested from the temperature dependence of the ultimate tensile strain for homogeneous CuCrZr as shown in Fig. 2.7.)

Damage Evolution

Several damage evolution laws which describe the evolution of the damage variable D under increasing load can be adopted. They are usually based either on plastic displacement at failure $\bar{u}^f_{pl}$ or ductile fracture energy $G^f = \int_o^{\bar{u}^f_{pl}} \sigma_y d\bar{u}_{pl}$ (dissipated during the softening process). Here only an evolution law based on relative plastic displacement will be considered to avoid further computational costs when computing G^f at each step and each integration point (remember the geometry is already complex and the equations non-linear). Because of an intrinsic mesh dependency problem in damage evolution models Hillerborg (1976) proposed to base the evolution laws (both displacement and energy based) on the effective plastic displacement and not on the plastic strain, by introducing the characteristic length of the element $L = \bar{u}_{pl}/\bar{\varepsilon}_{pl}$ (which is calculated automatically by ABAQUS).

---

[6] the variable PEEQ in ABAQUS

Once the damage initiation criterion has been reached, the effective plastic displacement, $\bar{u}^{pl}$, is defined through the evolution equation:

$$\dot{\bar{\varepsilon}}_{pl} = L\dot{\bar{u}}_{pl} \tag{3.20}$$

where L is the characteristic length of the element. The characteristic length of the element is introduced in the model to alleviate mesh dependency of the results.

The evolution law of the variable D can then assume either a linear form:

$$\dot{D} = \frac{L\dot{\bar{\varepsilon}}_{pl}}{\bar{u}^{f}_{pl}} = \frac{\dot{\bar{u}}_{pl}}{\bar{u}^{f}_{pl}} \tag{3.21}$$

or an exponential form (where a further parameter α is introduced:

$$D = \frac{1 - exp[-\alpha(\bar{u}^{pl}/\bar{u}^{f}_{pl})]}{1 - exp(-\alpha)} \tag{3.22}$$

For copper a linear damage evolution has been verified to be quite a good approximation for the real material response [122] (with negligible non-linearity confined to small regions of threshold and failure strains).

Element Removal

Both definitions ensure that when the effective plastic displacement $\bar{u}_{pl}$ reaches the value $\bar{u}^{f}_{pl}$, the material stiffness will be fully degraded ($D = 1$) and the corresponding element can be removed from the mesh. However, one can independently set a lower limit $D_{max} < 1$. In our model we always assumed $D_{max} = 1$.

In ABAQUS a degraded stiffness is equally applied to all components. At each step and for every mesh element the damage variable D is calculated and the element removed if D reaches the value D_{max} at all of the section points at any integration point of that element.

Material Data for CuCrZr

Elastic properties like Young's modulus and hardness have been first measured via nanoindentation in composite. Since the measurements could only be performed at room temperature, values at higher temperatures have been extrapolated from the reference literature data [117], assuming the same temperature dependence.

For the ductile copper alloy in W/CuCrZr, temperature dependent isotropic work hardening (with decreasing yield thresholds by increasing temperatures) has been assumed. This choice is supported by numerous literature data on bulk CuCrZr. However exact values of the yield stress at a given temperature considerably change depending on composition and metallurgical history. Furthermore we cannot exclude that yield-stress values measured for bulk specimens could slightly differ in composite.

For the determination of proper yield stress values of CuCrZr to be used in our simulation, we started from material data taken from an ITER Document of the ITER Material Property Handbook (IMPH) [117] (shown in Fig. 2.7) since they referred to a CuCrZr alloy with a similar metallurgical treatment. A complete description of the test procedure shown in the IMPH can be found in [118]. Yield stress values has been also parametrically changed during simulation of the W30[%vol] composition at 300°C in order to show the effect on the whole composite (see section 5.6.3). As for damage parameters, we assumed the initiation threshold $\bar{\varepsilon}_{pl}^{D}(T)$ to be 0.8, 1, 1.5 for the three temperatures considered during tensile test (RT, 300°C and 550°C). The plastic displacement at failure $\bar{u}_{pl}^{f}$ (required for the evolution law) was assumed to be temperature independent and guessed combining material data from [117] (Fig.2.7) for estimating $\bar{\varepsilon}_{pl}^{D}$ and an estimation of the average element size <L>. However, since the extracted $\bar{\varepsilon}_{pl}^{D}$ refers to homogeneous macro samples of CuCrZr but the derived $\bar{u}_{pl}^{f}$ is used as local parameter for removal of single elements representing a much more limited material region (in the order of 0.5-1 μm^2), a parametrical test has been performed in order to assess the impact on the homogenized stress-strain curve of the whole composite (Fig. 5.16). It resulted that varying $\bar{u}_{pl}^{f}$ of some orders of magnitude has a negligible impact at the macroscale.

3.3.2 Modeling W and the Onset of Failure

Linear thermoelasticity have been assumed below DBTT. Elastic properties like Young's modulus and hardness have been measured locally via nanoindentation. Simple criteria for the crack onset have been defined considering both brittle and ductile behaviour (above DBTT). We remark here that calculating the condition for crack onset does not mean to know how cracks later propagate across the material. While for the ductile CuCrZr phase crack propagation has been included in the FEM simulation through the element removal criterion, an equivalent implementation for the tungsten brittle phase was not possible. The main reasons were:

a. the complex random mesoscale morphology excludes a classical approach based on stress intensity factors or Griffith's criterion. This because both approaches assume a symmetric pre-crack of ideal shape and a naturally defined crack-length a but the plasma-sprayed structure makes it hard to properly define a locally, e.g at the boundary between lamellas where "crack-like" gaps has already developed with irregular curvatures. Furthermore, the surface energy required in the Griffith's criterion should be also a local value difficult to get experimentally and certainly dependent on the local grain structure.

b. brittle crack propagation requires to model the case of a crack developing through the elements of the mesh. This cannot be simulated with an element removal criterion (as for the ductile case). It implies either adaptive re-meshing (expensive) or a redefinition of the finite elements properties as in the Extended Finite Element (XFEM) approach.

c. even within the XFEM framework, brittle crack propagation in VPS-W and W/CuCrZr is problematic to implement. Preliminary attempts on VPS-W grids turned into serious convergence problem in both 2D and 3D models. At least 4 elements of the same phase should be used in each section to get reliable crack propagation results. This further requirement implies very high computational costs, since the mesh refinement must further be increased, and e.g. 2D-HRDM models with 3-400.000 elements already needed about 30h each to be generated.

For these reasons we limited to investigate crack initiation across VPS-W. We also extrapolated conditions on total failure based on the analysis of stress distribution before cracking. This method is proposed in section 7.2.2.

Criteria for Brittle Crack Onset

Among the initiation criteria for modeling brittle cracking one can choose between displacement-based criteria, stress-based criteria or energy criteria []. We consider here only the first two criteria because they are relatively easy to implement and widely accepted. The first criterion is based on the principal stress and is formulated as:

$$max(\sigma_{ii}^{p})_{T} > \sigma_{T}^{ult} \tag{3.23}$$

where $max(\sigma_{ii}^{p})_{T}$ is the maximum between the principal stress components at a given temperature and σ_{T}^{ult} is the ultimate strength of the material at a given temperature.

The same criterion based on strain reads:

$$max(\varepsilon_{ii}^{p})_{T} > \varepsilon_{T}^{ult} \tag{3.24}$$

where $max(\varepsilon_{ii}^{p})_{T}$ is the maximum between the principal strain components at a given temperature and ε_{T}^{ult} the ultimate strain at a given temperature.

Below DBTT tungsten is one of the most brittle metals. For the bulk case, this means that once initiated, cracks tend to propagate rapidly leading to total failure of the material. This implies an ultimate strain limited to some fraction of percentage (such very low strain is also difficult to measure on standard specimens).

When temperature increase above DBTT it is better to set the onset criterion on displacement, since considerable plastic deformation can occur. Both criteria are relatively easy to check during post-processing, since principal stresses or strains are computed from the corresponding local tensor, which is a direct output of the simulation. During tensile tests on W/CuCrZr at 550 °C, tungsten could have crossed its ductile to brittle transition temperature (DBTT). However, DBTT itself and accurate data about the ductile behaviour of tungsten above DBTT are difficult to be measured or to be found in the literature (in particular, hardening parameters for the polycrystalline tungsten). For these reasons we performed some tests simplifying the tungsten ductile behaviour above DBTT assuming isotropic yielding and perfect plasticity with an upper limit for the total elongation, deuced from experimental data on polycrystalline tungsten.

As for the effective values of ultimate strain and stress to be chosen, a bride range can be found in the literature as shown in Fig. 2.1, depending on level of purity and thermomechanical

Table 3.1: *Ultimate tensile strength and strain values for polycrystalline tungsten at 500°C as measured by PLANSEE.*

Material (T=500°C)	State	Test-Direction	Max. Stress [MPa]	Max. Strain [%]
W Stab Ø 25 mm	Forged	Axial	450 - 480	3 - 5
W Stab Ø 25 mm	Recrystall.	Axial	330 - 350	28 - 39
W Blech # 1mm	Recrystall.	Longitudinal	600 - 700	40 - 46

history. One can also notice the strong dependence on temperature (Fig. 2.1 and 2.2).

For the local ultimate strength of W at RT in VPS-W we could expect values below the limit for stress-relieved W (1350MPa), since the W in coating was not stress-relieved. That means in the range 1000-1200 MPa. At higher temperatures (interesting for the tensile test of W/CuCrZr) we used material data from PLANSEE as reference.

An indication of limit values in tension at high temperatures were taken from measurements performed on polycrystalline, non recrystallized tungsten (Table 3.1). Since the measurement was performed at 500°C and high values in tensile ultimate strain were shown, a ductile behaviour already at such temperature must be assumed for the measured bulk-specimens. The values of ultimate tensile strength and maximum elongation of the first raw of Table 3.1 were used as reference during discussion about the tungsten-DBTT in W/CuCrZr composite.phase in composite was supposed to be above DBTT (Section 5.7).

3.3.3 The Contact-Zone Model in VPS-W

We define the Contact Zone (CZ) as the morphological region where thin interlamellar gaps are closed or partially closed (Fig. 3.2). In the real case both thermal and mechanical contact at the CZ are degraded compared to the bulk case. Since the CZ is distributed *quasi-homogeneously* across the material, we should expect a strong influence on the overall mechanical and thermal behaviour of the coating. A CZ-model should therefore be introduced to take into account for the influence of the CZ. The model as implemented here is purely numerical and consists of two parts:

1. Identification of the CZ as geometrical information to be included in the FE-mesh
2. Assignment of proper material properties to the CZ-elements

While morphological information can be extracted with high precision from SEM pictures and included into FE-grids thanks to the image-based technique, estimating the local CZ properties is a much more difficult task. First, the CZ at the microscale looks as a further heterogeneous “material”, made of secondary phases like gases, oxides and nitrides irregularly distributed along interlamellar boundaries [109]. This immediately forces one to look at the average properties of the CZ instead of local ones.

If one would think to experimentally measure the average extent, e.g. of stiffness and conductivity degradation at the CZ, this would require to use close to 100% dense plasma-spray specimens in order to isolate the CZ contribution. Unfortunately this looks quite unfeasible since the highest density known for plasma-sprayed tungsten is around 97%. Even if one would be able to produce plasma-sprayed specimens close to bulk ones, the results from this particular case could not be easily generalized for the specimen with medium and high porosity (those interesting for real applications). This because the CZ local properties in these cases certainly correlate with the porous network (e.g. one should expect the amount of oxides accumulated at interlamellar interfaces to be higher for higher porosity levels). Isolating the CZ contribution for porous specimens through experiments only, seems unfeasible since it is not possible to produce porous PS-specimen without CZ (to be measured as reference). All these reasons further motivate a parametric numerical model for the CZ integrated in the general IB-FEM simulation procedure in order to quantitatively assess the CZ contribution.

The numerical model is parametric since it does not uniquely solve issue n.2. Once a material property at the CZ has been identified, we assigned to it different values *parametrically* (with reference to the balk case) exploring quantitatively their effect on the overall response. Since the main uncertainty in the overall VPS-W model is limited to the value of CZ-properties and not on the CZ morphological arrangement, we can evaluate "numerical bounds" for a certain overall material property, exploring a wide range of values for the local property at the CZ.

The CZ-properties which have been defined parametrically are those necessary for the estimation of basic thermomechanical properties like overall stiffness and conductivity. For simplicity's sake we assume the local property as isotropic along the CZ and we consider these properties as homogenized along the CZ-phase. Through the parameters q and k we introduce reduced stiffness E_{cz} and reduced conductivity λ_{cz}in the CZ as:

$$E_{cz} = \langle E \rangle_{\,cz} = q \cdot E_W \tag{3.25}$$

$$\lambda_{cz} = \langle \lambda \rangle_{\,cz} = k \cdot \lambda_W \tag{3.26}$$

Both parameters were explored until saturation effects were recognizable.

For the calculation of thermal diffusivity from thermal conductivity (but also for simulating a thermal transient) average CZ-density and CZ-specific heat would be required too. In these cases the CZ substructure should be looked more closer since it contains a mixture of gas and solid phase and the gas phase could in principle affect density and specific heat[7]. These quantities however are not variable in strict sense and their range of variation can be fairly estimated through a guess on the gas phase properties and simple homogenization based on image analysis (see Fig. 3.2). The procedure is briefly described. For VPS-W, due to the controlled atmosphere during deposition, we only considered the presence of residual Argon gas in the CZ, which has a fixed Cp at room temperature (we only consider here the RT case for all the analysis of PS-W). Since a certain amount of solid tungsten is also included in the virtual CZ region and Cp homogenization is to be done by mass, we can neglect the gas contribution and have$\langle Cp \rangle_{\,cz} \approx Cp_w$. As for CZ-density, the gas phase volume at the CZ can be segmented

---

[7] in order to segment the CZ from SEM picture and include this information into a FE-mesh we must introduce an artificial CZ-thickness, since we were limited by the smallest element size. This means that in any CZ mesh elements a certain amount of gas and solid phase coexists (Fig. 3.2).

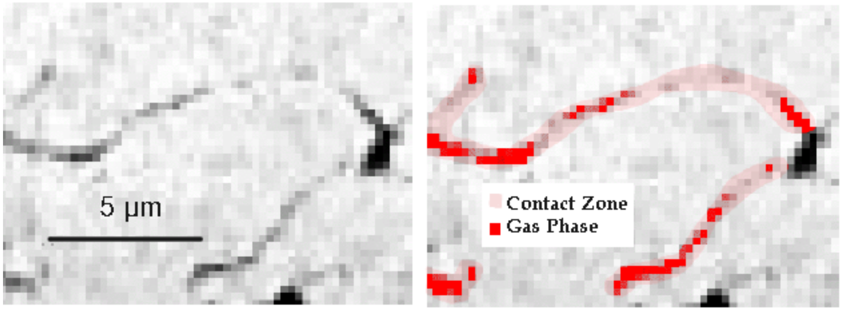

Figure 3.2: *Magnification of partially closed gaps (Contact-Zone, CZ) in the VPS-W morphology: the dark red pixels indicate the CZ sub-region where gas thermal properties (Cp and* ρ*) have been assigned in order to estimate average thermal properties to be assigned during simulation.*

and quantified in pixels, since gas pixels have intensity values close to black. Assuming an ideal gas behaviour we reduce the unknown parameter of the gas phase to one (the pressure, linked to the gas density). Since the Ar-density at 10 bar is still more than 1000 times lower than solid W (at RT), we could basically neglect the gas density at all pressures and the average CZ-density turned to be determined only by the gas volume fraction. The resulting estimation range for$\langle \rho \rangle_{cz}$was 13.5-14 g/cm^3, 25% lower than in the tungsten case.

3.4 Statistical Characterization of Random Media

3.4.1 RVE and The Problem of Statistical Representativity

As we have seen in section 3.1, in micromechanics of random heterogeneous media one important goal is to derive effective properties from the knowledge of local constitutive laws and spatial arrangement of components. To this end, homogenization methods (Section 3.2) have been designed. On the one hand we find *analytical* homogenization techniques (variational ones like Hashin and Shtrikman's bounds or direct estimations like the Mori-Tanaka method) based on random composite media with an infinite extension. On the other hand, a different way to solve homogenization problems is based on numerical techniques and simulations on a finite number of realizations of the microstructure. This is the approach adopted with the image-based finite element method in this work (Chapter 4). Even during experimental estimation of average properties of a random heterogeneous material, one is forced to work on a limited number of samples, which are finite realizations of the ideally infinite random structure. In these cases, it is of great interest to investigate statistical representativity through the notion of *representative volume element (RVE)* of an heterogeneous medium. Several definitions of the RVE can be found in the literature (see [111] for an extended review). However, most of them are qualitative definition like the following one[59]:

The RVE is that minimum volume V of an heterogeneous material that is sufficiently large to be statistically representative of the whole material while remaining small enough to be con-

sidered as a volume element of continuum mechanics[8].

The concept of representative volume element (RVE) needs therefore to be precisely and *quantitatively* defined in order to assess statistical accuracy of the calculated average properties.

Quantitative Definition of RVE

In this work we follow the stochastic definition of RVE for random heterogeneous media as given in [106, 107]by Kanit and Jeulin (under ergodicity hypothesis of the random process):

Given a certain property Z, the RVE is that minimal unit cell volume V, which assures to estimate the mean value $\overline{Z}$ *of a certain property Z with a prescribed relative error* $\varepsilon(V) = \frac{2D_Z(V)}{\overline{Z}}$ *, where* $D_Z^2(V)$ *is the variance of Z over different unit cells having the same volume V.*[9]

The above definition assumes the RVE being a single cell. A more general definition is that for the case of multiple realizations of the random media (n cells):

the RVE is the set of n unit cells (each of minimal volume V), which assures to estimate the mean value $\overline{Z}$ *of a certain property Z (after satisfying convergence of an estimator of Z over V) with a prescribed relative error* $\varepsilon(V) = \frac{2D_Z(V)}{\overline{Z}\sqrt{n}}$.

The estimation of the RVE is based on the second general definition. Once$\varepsilon(V)$ is known for the general case, the reduction for the case n=1 is trivial.

The method proposed is based on the estimation of the variance function $D_Z^2(V)$ of a micromechanical property Z as function of the volume size V. Such estimation is achieved through different numerical approximations of D_Z^2 at different volume sizes V_i, fitted with a given analytical function derived from the theory of random processes:

$$D_Z^2(V) = \bar{D}_Z^2 \cdot \left(\frac{A_n}{V}\right)^{\gamma} \sim \frac{\xi}{V} \tag{3.27}$$

where A_n is the integral range (a complex morphological parameter difficult to be estimated analytically [105], introduced for the first time in geostatistics from G.Matheron [104]) and $\bar{D}_Z^2$ is the point variance. Since $\bar{D}_Z^2$ and $A_n$are constant one can first fit their product ξ in 3.27). In 2 dimensions A_n=A_2 and V is the area of the region considered.

Once ξ is known, the quantitative estimation of the RVE is finally given combining equation 3.27 with the formula for the relative error ε of a measured property Z from n independent realizations (as taken from the theory of sampling). The result reads [107]:

$$V^{RVE} = \frac{4\,\xi}{\overline{Z}^2\,\varepsilon^2 n} \tag{3.28}$$

---

[8] *or, in equivalent terms (see section 3.1) to allow separation of meso- and macroscale fields.*

[9] the exact mean value $\overline{Z}$ is to be distinguished from estimation of it on limited volumes ($\langle Z\rangle_V$). Usually $\overline{Z}$ can be well approximated extrapolating$\langle Z\rangle_V$ for sufficiently large volumes V.

where $\overline{Z}$ is the exact mean value of the property Z (which is a priori unknown but can be well approximated from converging values of the ensemble averages $\langle Z\rangle_{V_i}$ taken at sufficiently large volume size, see for instance Fig. 7.12). The RVE-Volume corresponds to the smallest volume (or area in two-dimensions) necessary and sufficient for the estimation of the effective property Z with a given relative error ε and n unit cells.

The practical determination of the RVE can be summarized as follows (in 2D we still use the variable V to indicate the unit cell area):

1. Generate i ensembles having each n_i different realizations of the random media with unit cell size V_i. Each ensemble gives an estimation of the variance function $D_Z^2(V)$ in equation3.27 [10]

2. Compute the apparent property $\langle Z\rangle_{S_i}$ (first homogenizing local values over a micrograph and then averaging over the ensemble). Compute the corresponding variance $D_Z^2(V_i)$ of the property Z for each ensemble. Extrapolate $\overline{Z}$ for $V \rightarrow \infty$.

3. Set the desired precision (relative error ϵ). Good values for reaching stabilization are usually lower than 5%.

4. Use 3.27 to fit the data and get an estimation for ξ. Use then equation 7.11 to estimate the RVE size as function of the number of realization n.

An important remark is that the size of the RVE depends in general on the specific property investigated and on the specific boundary conditions adopted , while only in the ideal case an RVE should be property-independent[106].

Because of the high computational effort required in estimating the general relation of an RVE, we will perform only one RVE calculation limited to the less expensive case (thermal conductivity of VPS-W, shown in section 7.3.3).

3.4.2 Covariograms of a Random Set

Fig.3.3 shows *covariograms* calculated on segmented planar images of VPS-W in the two principal directions (Oy parallel to coating deposition and Ox parallel to substrate). Covariograms are used in theory of random structures [59] as fingerprints to characterize a particular random morphology and provide useful morphological parameters. They are calculated from the auto-covariance (usually indicated as C(h)) of binarized pictures along one particular direction whose linear coordinate is h.They can provide, for instance, a direct estimation of the average

---

[10] three is the minimum numbers of points to fit the hyperbolic function in equation 3.27. The higher the number of points, the more accurate is the fit.

length of the random inclusions in one particular direction. This is given by the *sill of covariance* h*, which satisfies $C(h^*) = C(0)^2$. They are also an useful indicator to show anisotropy of the random structure (and quantify it).

Covariograms of VPS-W were dominated by the isotropic distribution of globular macro pores. We also calculated covariograms on the interlamellar microgaps isolated as independent morphological phase (and dilated in order for the thin structures to be better detected). These covariograms could show a small difference between the main orientations (Fig3.3b). anisotropy was actually expected because the deposition process has a well defined orientation (perpendicular to the substrate), but it is interesting to notice that the extent of such anisotropy remains low for this particular plasma-sprayed morphology. This is probably due to the high number of rounded interlamellar gaps which elongate also in the vertical direction during the solidification process.

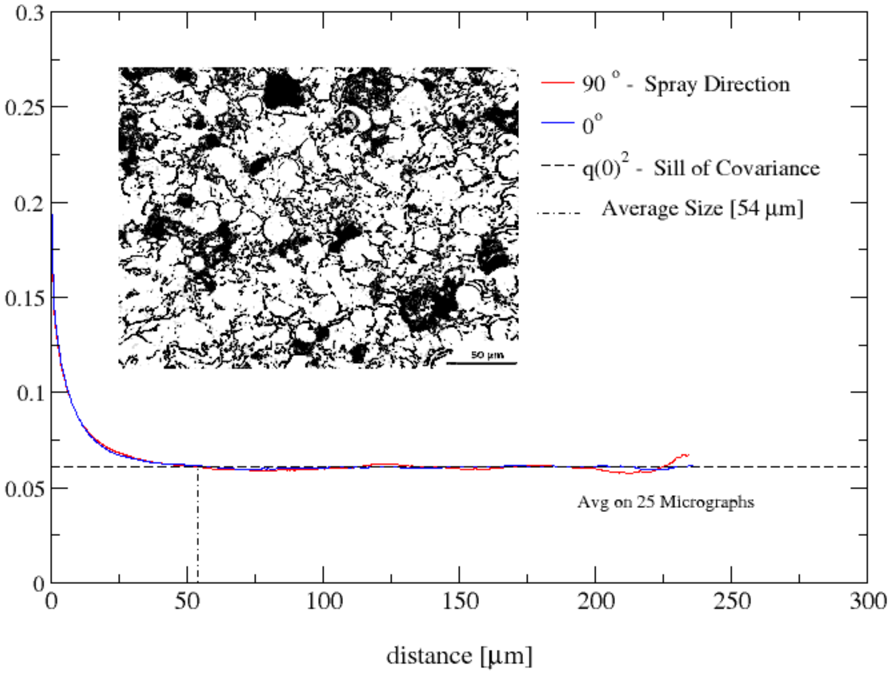

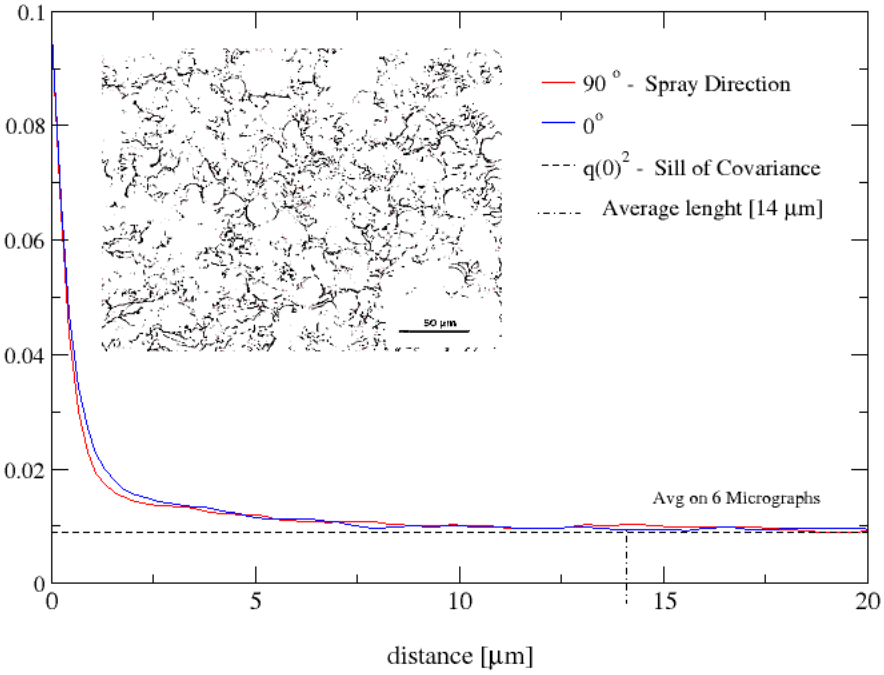

Figure 3.3: *Covariograms in the two principal directions of binarized images of VPS-W (25% porous). Top: covariograms of the full porous network (macro pores and interlamellar gaps). Bottom: covariograms of isolated interlamellar gaps.*

Chapter 4

Image-Based Finite Element Method

The general meaning of “Image-based FEM” (also referred in the literature as “Object-Oriented FEM” or ”Direct Mapping FEM”) refers to the generation of finite element models from images representing the real structure of an object and the solution of continuum mechanics problems on these models through the finite element method.

Conventional mesh[1] generation tools require as input a numerical representation of the model geometry in terms of simple building blocks to be meshed with standard techniques. The boundaries of such domains are described by points, straight lines, planes, and simple curves resulting into a model which is usually called CAD-model, meaning Computer Aided Design model. In materials science, especially when dealing with inhomogeneous materials, the starting point is a micrograph of the real microstructure which cannot be translated into a CAD model by means of geometrical building blocks of elementary shapes. The models shown in Fig. 4.1 help to understand this point.

In this particular context the objects to be modeled are regions of heterogeneous materials with complex morphological features. The corresponding images are usually taken either from Optical Microscopy (OM) or Scanning Electron Microscopy (SEM) or Computed Tomography (CT). In the first two cases the image is planar, while tomographic reconstructions are three-dimensional.

An image-based finite element model usually consists of:

a. one or more regions of interest or micrographs selected from images of that material

b. a mesh which discretizes each region of interest into a simulation unit cell (usually square or cubic, as the original images)

c. a logical structure which links mesh-subparts with the phase constituents of the material as close as possible to the phase arrangement in the original picture (in other words, the mesh has the same internal boundaries of the real material)

d. material data to be assigned to each phase constituents

A general requirement for generating FE-models from images is that these have been previously “segmented”, i.e. that the spatial domains of the phase constituents (morphological

---

[1] in text the terms “mesh” and “grid” are synonym referring to the same concept: discretization of a planar or volumetric structure by means of polygons or polyhedra respectively.

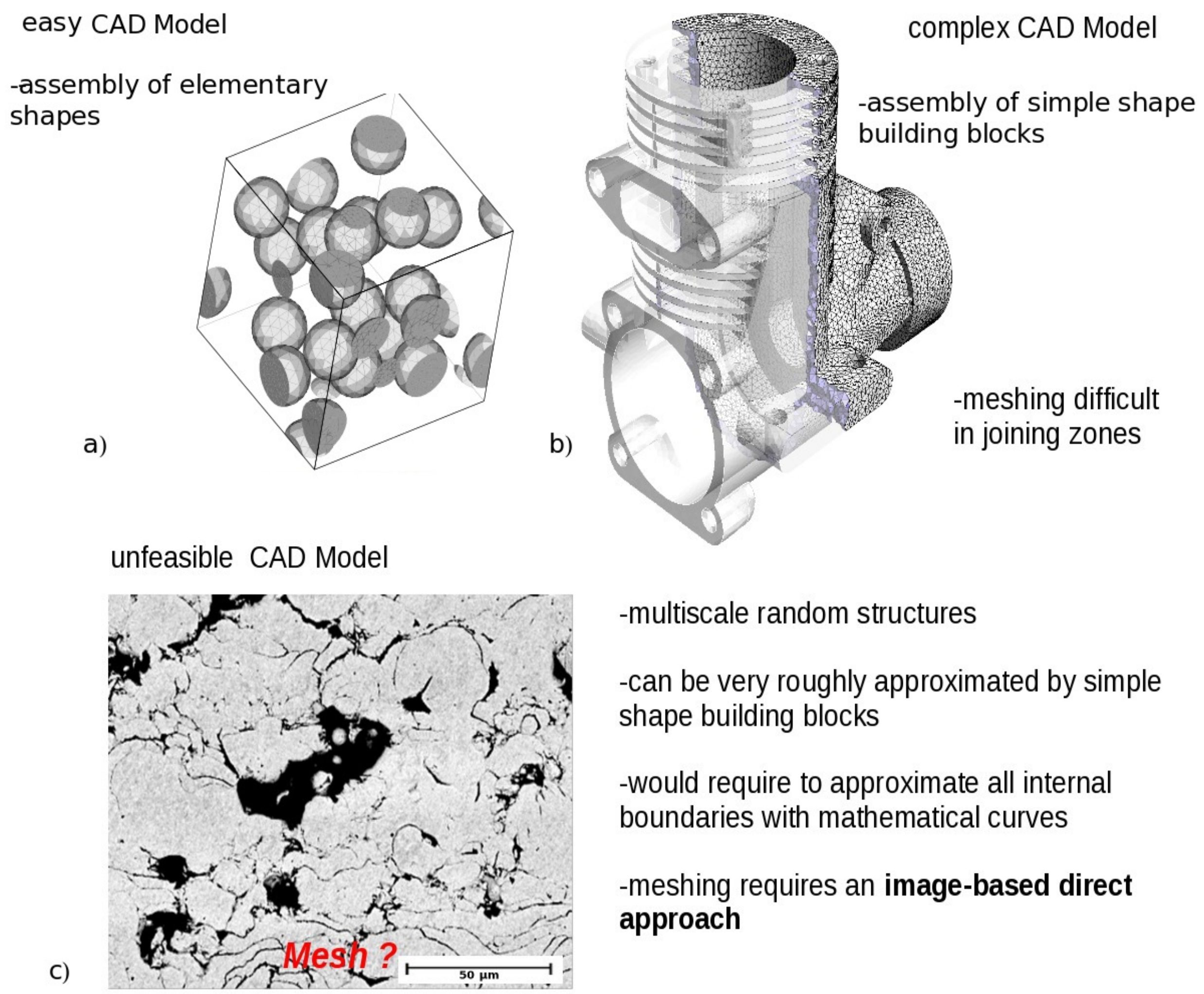

Figure 4.1: *Overview of FE-models and related meshes. a) unit cell for a particle reinforced MMC [100], b) meshed CAD-model of a cylinder block as generated from Gmsh [101]. For the complex random structure of VPS-W (c) conventional mesh generation on CAD-like models made of elementary building blocks of simple shape was not feasible. An alternative approach was used, which is based on direct mesh adaptation on the photographic input (SEM image).*

phases) have been unambiguously identified. This operation corresponds to the link between points a. and b. in the list above. In practical terms “segmentation” means that a unique numerical value (usually an integer), corresponding to a certain phase, has been assigned to each pixel (in 2D) or voxel (in 3D) of that phase. Pixels and voxels are the basic image structures (corresponding to a first discretization of space before meshing) to which a certain intensity value (color) has been assigned.

After segmentation is done, the “adaptive” mesh generation procedure can start, which is the core of the image-based FEM procedure. The primary aim is the generation of a new discrete structure corresponding as good as possible to the underlying image phase boundaries whilst keeping low the total number of discretization elements. At the same time good mapping quality should be combined with good mesh quality (roughly speaking, elements should not be excessively distorted) in order to get reliable results from subsequent Finite Element analysis.

Matching the pixel structure 1:1[2] is an example of bad mesh quality [81]. This is because the resulting "pixelized" structure shows "jagged edges" even where the boundaries of the real material are smooth , which can lead to artificial features such as stress concentrations at pixel corners.

Image-based FEM with OOF2 has already been proven successful in several previous works. Very good results in terms of agreement with experimental data and analytical models have been shown for various time-independent thermomechanical problems [83, 82, 84, 91, 90, 88, 89].

To author's knowledge, however, the image-based FEM approach has never been tried on a type of random morphology as that of VPS-W, with inclusions having a difference in size of up to two order of magnitudes (macropores up to 100 µm and microgaps even thinner than 1 µm). A sufficient number of inclusions must be incorporated into a single FE-model in order to produce meaningful results. To manage this, we started from large SEM-images (0.3*0.25 mm^2) with high spatial resolution (0.22 µm/px) for generating large and highly refined meshes (about half million elements with average element size of about 15 px).

As for FEM simulation itself, we preferred to import models into the FE simulation package ABAQUS, even though some linear problems could be solvable in OOF2 directly. This choice was justified by the necessity for including advanced non-linear constitutive models (like ductile damage in W/CuCrZr) and by the need for higher performance, parallel computing and solution stability. All these requirements were met by using the ABAQUS solver.

4.1 The Direct Mapping Technique with SEM Images

4.1.1 SEM Image Segmentation

Segmentation of SEM images of VPS-W aimed at the identification of three morphological phases: globular pores, thin "crack-like" interlamellar gaps and interlamellar surfaces in contact (Contact Zone). While identification of the first two phases together as a whole phase (Fig.4.2 top) can be achieved through standard thresholding, isolation of the three phases from each other is a non trivial segmentation task. Globular pores were separated from gaps applying first a Blur filter, then a selective Gaussian filter (whose effect is blurring only on the thin structures), then thresholding on the filtered image and finally applying image subtraction from the original image. The resulting image (Fig. 4.2 bottom) is a good approximation of the globular phase.

Segmentation of the Contact Zone was critical and eventually only feasible by hand (in a semi-automatic procedure, where the "net" contact zone was obtained subtracting background (black) pixels from the "gross" contact zone marked by hand). The problem is that partially closed interlamellar gaps share the same gray values of non negligible parts of the bulk-tungsten region, making impossible to filter the CZ-pixels alone operating on the gray-scale pixel distri-

---

[2] this process is also called "pixelization"

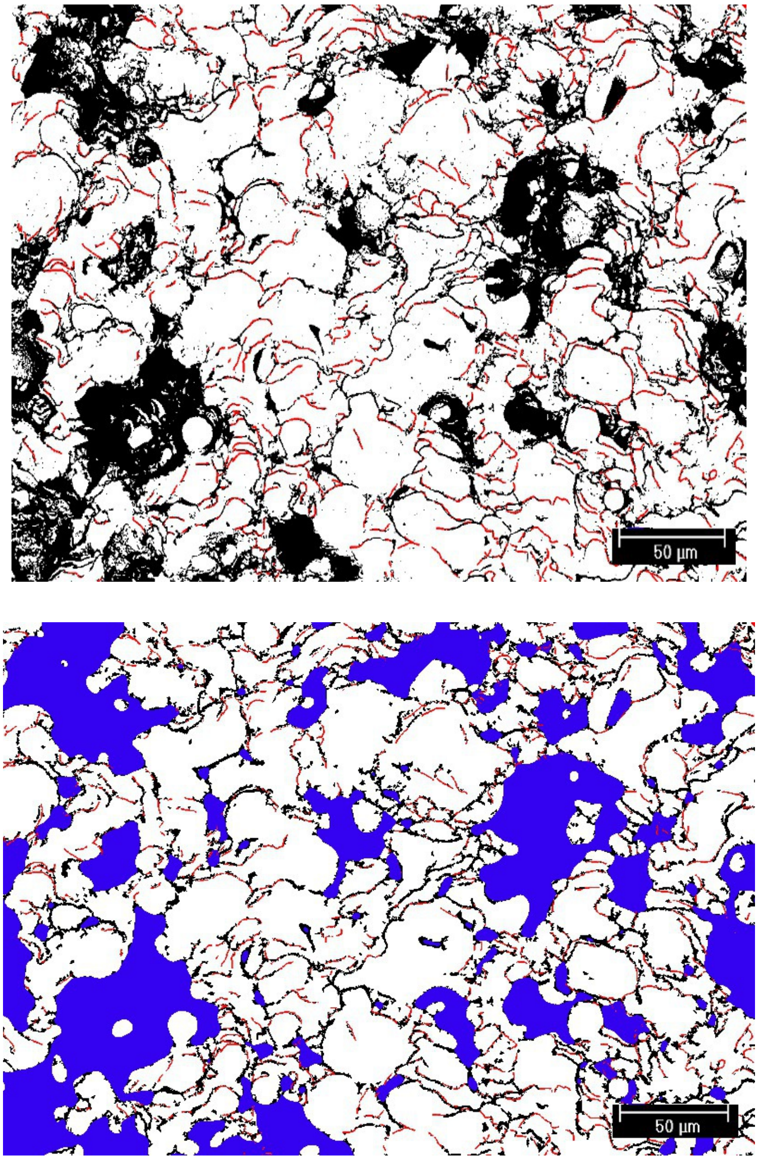

Figure 4.2: *Segmentation of planar images of PS-W for subsequent mesh generation. Top: example of segmented micrograph where the whole porous phase (in black) is distinguished from the contact zone (in red). This micrograph has been used for generating 2D-HRDM-CZ models. Bottom: isolation of globular pores for the generation of 2D-HRDM-GP models.*

bution. Edge detection algorithms like the Canny Filter have been also tried but they could not distinguish between open gaps and contact zone gaps.. A need for a tailor-made filter for the CZ was identified (whose development goes beyond the scope of this work).

4.1.2 Mesh Generation from Planar Images of Heterogeneous Media

This section, which explains the planar image-based mesh generation techniques follows Reid and Langer [80].

As stated in [80] “the software package OOF2 circumvents the difficulty of generating a CAD model of the microstructure by creating meshes directly from images, simultaneously

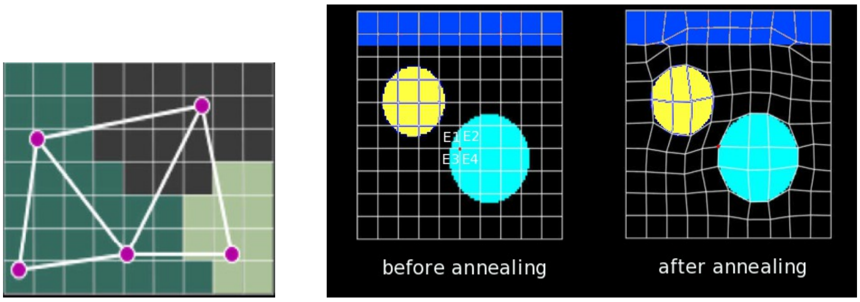

Figure 4.3: *Left: Linking mesh elements with the underlying pixel structure of an image (different colors indicates different material region, as results of segmentation). For each mesh element an homogeneity index HI (equation 4.2) is calculated, which indicates to which extent an element "covers" a certain material region. Right: example of mesh adaptation with OOF2 through "annealing" of a regular grid on a simple micrograph. Images taken and rearranged from [80].*

identifying boundaries in the image and bringing the finite element mesh into correspondence with these boundaries. Using this method, an explicit mathematical description of the image boundaries is not required, and is not explicitly constructed."

The OOF2 meshing scheme begins with a coarse, regular mesh on the image, and then brings that mesh into correspondence with the image by a series of mesh-modifying steps which try to preserve the space filling and well-formed character of the mesh.

The whole procedure is based on the definition of "mesh functionals" which quantitatively assess the mesh quality with respect to element shape and image adaptation. Such functionals are also called by OOF2 authors "energies" because some of mesh modification routines "move the mesh nodes as if they were physical particles with potential energies given by the shape and homogeneity functionals".

The "energy shape" functional measures the quality of the shape of an element assuming a value of one for degenerated elements (like triangle with a 0° angle) while ideal shape elements like equilateral triangles and squares, have a shape energy of zero. It is has different formulation depending on the element shape. For triangular elements of area A_i and side-lengths L_j it reads:

$$E_i^{shape} = 1 - 4\sqrt{3}\frac{A_i}{\sum_j L_j^2} \tag{4.1}$$

It is a figure of merit to keep the energy shape low since high- aspect-ratio elements can lead to slow convergence of the finite element solver.

The "homogeneity energy" functional is a measure of how well an element is adapted on the pixel phase boundaries within that element. It is defined by:

$$E_i^{hom} = 1 - H_i = 1 - \frac{max_j\,\{a_j\}}{A_i} \tag{4.2}$$

wherea_j are the area (in pixels) within the element i that belongs to material phase j. For elements having a single phase occupying the whole element area (homogeneous elements) E^{hom} is zero, while for increasing number of material phases within that element (increasing element heterogeneity) H tends to zero and E^{hom} to one.

These two measures can be combined into an effective element energy:

$$E_i = \alpha E_i^{hom} + (1-\alpha)E_i^{shape} \tag{4.3}$$

where $\alpha$is a tunable parameter. The sum over all mesh elements gives the global mesh element functional E_{tot}:

$$E_{tot} = \sum_{i=1}^{N} E_i = \alpha \sum_{i=1}^{N} E_i^{hom} + (1-\alpha)\sum_{i=1}^{N} E_i^{shape} \tag{4.4}$$

OOF2 tries to decrease the functional E_{tot}during all the available mesh modifications steps, while the parameter α is set by the user at each step.

The functional minimization problem described above corresponds to a parametrical optimization in a 2n configurational space (with n=number of nodes). It is therefore extremely difficult and eventually impossible to compute the absolute minimum valid for any kind of random microstructure. OOF2 is a powerful tool for exploring “paths” in the configurational space, offering several methods to decrease the effective mesh energy. Some mesh modifications like *annealing* and *snap nodes* can automatically find a local minimum. However, the most suitable combination of mesh modification steps must ultimately be found by the user, which is supposed to first judge parameters like maximum and minimum element size, mesh type (triangular, quadrilateral, mixed) and the acceptable level of mapping and mesh quality[3].

The entire sets of modification steps is accurately described in [80]. They can be classified into routines which move nodes preserving topology (e.g. Annealing, Snapping Nodes) or routines which modify topology by adding, removing, or reconnecting nodes (e.g. Refine, Snap Refine).

The most important routines are here briefly summarized:

-$Refinement$: elements are split into two, three or four sub-elements according to a given criterion. Refinement takes place locally, affecting for instance only those elements whose H index is lower than a given threshold (heterogeneous elements).

-*Annealing* : the nodes are “shacked” by randomly change their position with an acceptance criterion.

-$SnapNodes$: if an element edge crosses over different pixel regions, Snap Nodes tries to move one of the element corners to the crossing point. This routine improves elements homogeneity.

$-$*Rationalize* :it fixes badly shaped elements in a mesh by either removing them or modifying them and their immediate neighbors.

Some practical rules valid for the most common random structures in material science and a general strategy is proposed in [80].

---

[3] In other words, the user chooses directions for moving along the functional surface in the configurational space while the program calculates the states and sometime a part of the path towards an acceptable minimum of E_{tot}

The description of the *annealing* step is given in detail following [80]. Its computational interest arises from the fact that it implements concepts from statistical mechanics.

Mesh Annealing

The *annealing* modification routine moves nodes randomly from their original positions within a certain spatial range, accepting or rejecting node movements according to a given criterion. It is similar to a simulated annealing in statistical mechanics, from which it gets its name. As stated in [80] “Instead of minimizing the free energy of a system of particles, it minimizes the effective energy of a mesh.” The algorithm incorporate a type of Metropolis Monte Carlo method [128].

Precisely the Annealing step consists of:

- assigning to each nodes a random dx and dy from a Gaussian distribution of width $\triangle$ and zero mean.

- before making the move, computing the total effective energy of all the neighboring elements of the node (taking the red node of Fig. 4.3 as reference, these elements are E1, E2, E3,E4).

- discarding those moves which generate illegal elements.

- accepting those moves according to a user specified criterion. Usually this means to check whether the effective energy of the neighborhood ($\sum_{i=1}^{3\,or\,4} E_i$) has been decreased. Eventually additional constraints on homogeneity (H) and shape (E^{shape}) must be specified.

- if a non-zero T (annealing “Temperature”) has been specified, moves can still be accepted even if they cause an increase of the effective energy. This according to a Boltzmann probability distribution calculated as $exp(-\triangle E/T)$, where $\triangle E$ is the difference in the effective energies of the new and old element configurations.

In order to be effective, the annealing procedure must be repeated for a number of iterations (fixed or calculated by the program setting an acceptance rate).

If the change in energy or the acceptance rate gets too small, the annealing process has reached a point where it is no longer improving the mesh effectively. A local minimum of the global mesh energy functional (equation 4.4) has been reached.

Mesh Adaptation Sequence for VPS-W

While micrographs of W/CuCrZr composites did not pose a serious problem due to the approximately round nature of their inclusions, for the “dual-scale” random morphology of VPS-W with inclusions of large difference in size and shape, the optimal mesh generation sequence needed much more efforts and could eventually be found only after several attempts. Additional requirements about computational costs must be satisfied in this case. They arose from the particular microstructure and from the need for large micrographs (in order to investigate the RVE problem). A large number of elements pro grid was therefore required to cover large domains while simultaneously resolving the smallest morphological features. Hence, special care was taken in limiting the total number of modification steps (especially Annealing) and the number of elements involved in them. Applying an annealing[4], for instance, on more than half million elements could easily saturate the available memory (16 Gigabyte) and requiring several hours of computational time. To this regard, a critical parameter was the initial element size for the starting regular skeleton[5]. This influenced the total number of refinements (to get down to the scale of the smallest inclusions) and hence the total number of annealing steps (which followed each refinement).

The chosen mesh type was triangular. Triangles can better follow the boundaries of inclusions than quadrilaterals, especially when the inclusions had a small and highly variable curvature radius (like the "crack-like" porous structures). Triangles also adapt to round inclusions without needing excessive shape distortion. A mixed mesh structure was discarded since this would have implied further complications in post-processing analysis without producing substantial advantages in decreasing the total number of elements.

Furthermore, additional requirements had to be satisfied since the mesh ensemble of VPS-W should aim to be statistically representative. From one side the models had to be large enough to allow limited deviation of the average properties over the ensemble (or in other words the ensemble should be an RVE of the material within a certain tolerance). On the other side, the final model resolution (in terms of the inverse of the minimum finite element area in pixels) should be high enough to allow "mapping" of the most thin crack-like porous structures (critical for accurate calculation of thermal and mechanical properties of the coating).

For large micrographs at high resolution (~ 1.5 Mil pixels covering a region of 0.3*0.25 mm^2) best results were obtained for a starting element size of approximately 17 pixels The final mesh adaptation sequence for VPS-W micrographs including Contact Zone (CZ) is listed below:

- 1 * [Refinement + Annealing + Snap Nodes + Rationalize,α=0.8]
- 1 * [Refinement + Annealing + Snap Nodes + Rationalize,α=0.5]
- 1* [Rationalize, α=0.3]

With this sequence we were able to produce a good mapping mesh in about 24h on a 3GhZ Intel Xeon using approximately 10 Gbytes of RAM. Adding a further modification group (refinement,annealing,rationalize) would have resulted in additional computation time. It appears clear that there is a broad margin for future improvements in order to reduce the computational time (first of all, parallelization of the routines).

Other mesh modification sequences were tailored for models without CZ and for models with globular pores only, requiring increasingly less adaptation steps and computational time. Table 4.1 lists the properties of the most detailed type of planar mesh used.

---

[4] annealing and the other montecarlo-like routines are the most computationally expensive steps in OOF2

[5] a skeleton corresponds to a pre-stage of a mesh without material data assigned

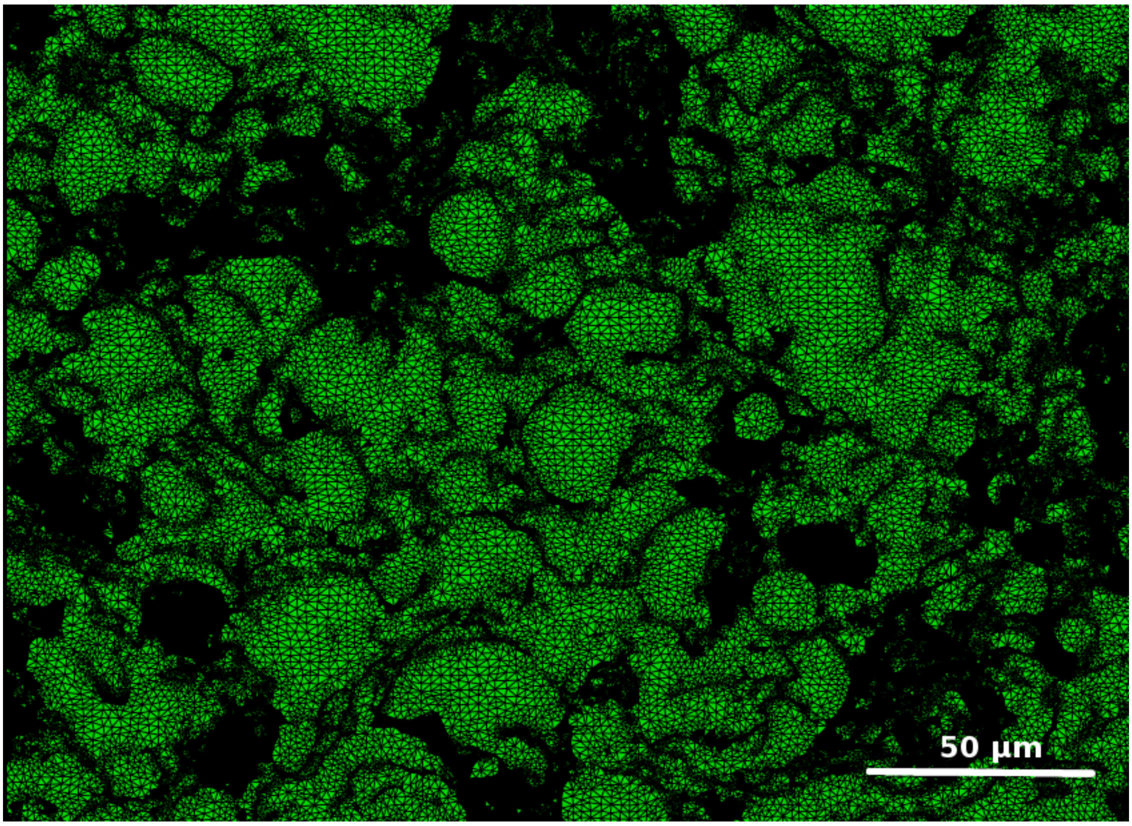

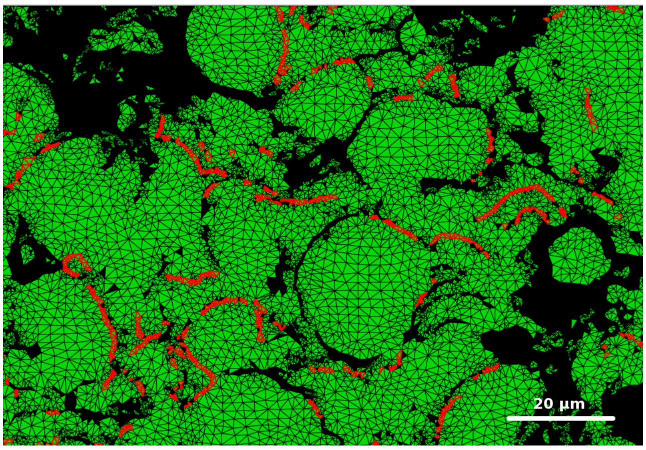

Figure 4.4: *The final result of a mesh adaptation procedure on a SEM micrograph of VPS-W at spatial resolution of 0.2µm/px. The big picture represents only one quarter of the whole grid which has in total about 400.000 triangular elements. Bottom: a zoomed micrograph region with red marked elements representing the Contact-Zone.*

Table 4.1: *Properties of a high resolution image-based (2D-HRIB) mesh. The minimal thickness (last column) refers to the smallest morphological feature (interlamellar gaps, the black elongated structure in Fig. 4.4) included.*

Mesh Type	Source Res.	N. of El.	Max./Min. El. Size	Avg. Size	Min. d.
2D-HRIB Triang.	0.2 µm/px	180350	1.53/0.07 µm^2	0.3 µm^2/el	0.4 µm

A study about the influence of local refinement on simulation results (limited to steady state heat-transfer simulations) will be discussed in section 7.3.1.

4.2 The Direct Mapping Technique with Tomographic Images

A procedure for the generation of simulation models from tomographic reconstructions (tomographs) of an heterogeneous material is shortly described here. Such procedure follows the same conceptual structure of the corresponding two-dimensional case: first the region of interest is scanned into a 3D image at the voxel[6] resolution (via computed tomography, for instance, but other suitable techniques were MRI scanners, ultrasound devices and 3D confocal microscopes), then the microstructural phases are quantitatively identified (image segmentation) and further discretized by larger elementary structures (finite element mesh or grid). Details of the complex tomographic segmentation of PS-W are postponed to section 6.3 within a chapter specifically dedicated to Computed Micro-Tomography (µCT). For further clarification we stress out the fact that starting image, segmented image and mesh, while strictly related each other, are three independent mathematical objects.

4.2.1 3D Mesh Generation from Tomographic Reconstructions of PS-W[7].

Without providing extensive details, this section briefly describes the generation of 3D meshes from tomographic reconstructions of VPS-W with the software package Amira v5.2 [129]. Mesh generation from tomographic images is an active research field of applied mathematics and a large dedicated literature is available (see e.g. [130]).

The first step for creating a three-dimensional grid is to segment the original tomographic scan, i.e. to univocally assign every voxel to a certain phase constituent. The next step is to generate a polygonal surface (a 2D object in a 3D space) well adapted on the phase boundaries of each segmented phase. In Amira a robust and fast surface reconstruction algorithm is used [132], which is based on the “marching cubes algorithm (MCA)” [131]for computing *isosurfaces* on a pre-existing regular grid (voxel image). What is an isosurface ? Firstly, we should consider the phase arrangement on the voxel structure. This can be seen as a three dimensional scalar field where each voxels gets a value corresponding to the morphological constituent (for instance 0 for tungsten voxels and 1 for void voxels). Given a regular grid sampling of a scalar field f and a scalar value σ (the threshold value also called isovalue, e.g. 0.5), the Marching Cubes algorithm constructs a piecewise linear approximation to the level set $\{x : f(x) = \sigma\}$. This is called *isosurface* and is the starting point for subsequent 3D grid generation. Another way to generate isosurfaces is to directly use the original 3D voxel structure and generating a mesh

---

[6] a “voxel” is, roughly speaking, a three dimensional pixel, i.e. the smallest element of a three dimensional digital image to which a color or gray scale value has been assigned. The voxel resolution is here by convention expressed as µm/vx where vx is the length of the voxel. The voxels shape meant in this work is always cubic.

[7] often in this section we will use the terms “surface density” and “mesh density”. These are respectively the total number of surface elements and the total number of mesh elements divided by the volume of the entire 3D region considered (calculated including the pores).

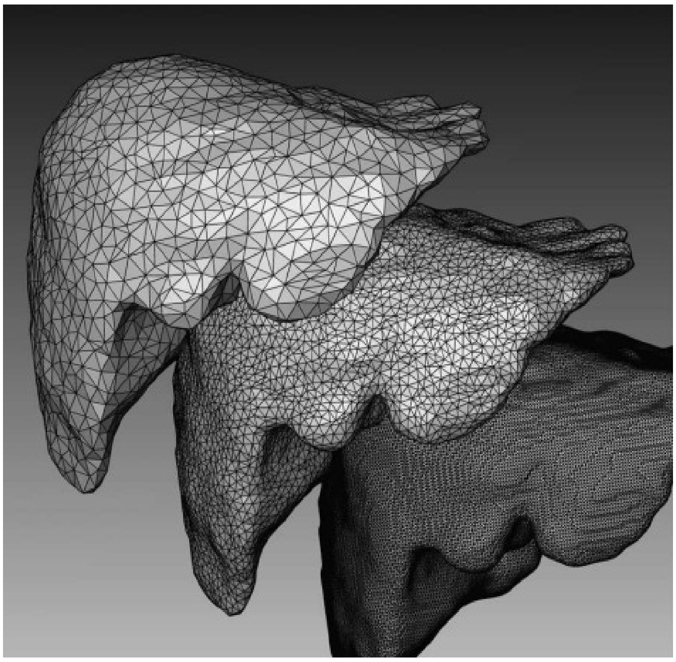

Figure 4.5: *Example illustrating the concept of surface simplification in Amira (image reprinted from [132]). A reconstructed model of a human liver is displayed at three different resolutions (1 cm maximum edge length, 0.5 cm maximum edge length, and "lego" surface with 0.125 cm voxel size). For increasing element size the surface becomes smoother and the number of surface elements drops.*

mapping exactly the voxel corners of each phase constituent. The resulting surface (also called "lego surface") will be made of quadrilateral elements whose size corresponds to the voxel length (or the half this value when splitting a voxel face into two triangles). This approach offers the highest mapping resolution but at the price of a very high surface density and final mesh density. As opposed to the computational strategy implemented in OOF2 for the 2D case, in Amira the mesh generation follows a bottom-up approach, i.e. it starts from the most accurate surface (a Lego surface or a surface as obtained from the MCA) which can get progressively simplified in further steps. Surface simplification (Fig. 4.5) is a procedure implemented in Amira which reduces the number of polygons needed to map a certain object surface (or an internal phase boundary).

The implemented algorithm for isosurface generation tries to avoid element intersection and bad element shapes [132]. An "intersection free surface" is the operative requirement for starting the subsequent full grid generation algorithm. Amira has several built-in tools for removing intersections. However, since the final surface on a tomograph of PS-W was containing several non convex domains and holes with large difference in size (representing open and closed porosity), it was extremely difficult to get the resulting surface intersection-free and some hand-corrections were needed.

Once the surface is completed, the 3D mesh generation algorithm can start, fulfilling the space with elements of about the same edge length (locally) of the surface elements. This is the most time consuming part of the whole computational process. The resulting total number of 3D-elements (N_{el}^{grid}) is obviously much higher than the starting number of surface elements

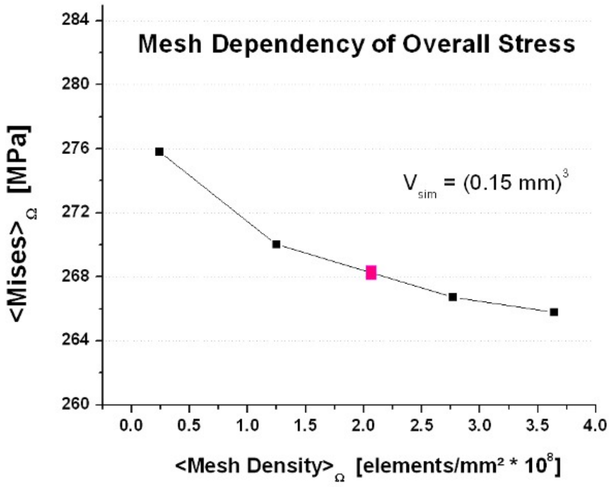

Figure 4.6: *Influence of mesh element density in smoothed 3D models on the volume-averaged von Mises stress. The first is an indicator of average refinement of a PS-W 3D grid and therefore an indicator of mapping quality, while the second is a possible indicator of overall stress. Prescribed strain during simulation: 0.02% at top-nodes. The red mark indicates a point where convergence is achieved within 1%. The minimum in the plot however, is supposed to be just local and not an absolute minimum, since non-negligible changes in the shape of inclusions are expected at much higher mesh density.*

N_{el}^{surf}. Since N_{el} strongly affects the total computational time (t_{tot}), it can easily escalate to intolerable levels. t_{tot} is the sum of the time required for surface generation, grid (=mesh) generation, FEM simulation and post-processing analysis [8]. t_{tot} obviously depends on the size of the model (in number of elements,N_{el}^{grid}) and the kind of simulation. For further study to come (for instance calculation of 3D RVE) we should also consider to simulate on multiple sets of 3D samples, a circumstance which would increase$t_{tot}$by a factor of n (number of samples). Referring to a fixed type of simulation, the critical factors influencing N_{el}^{grid}(and hence t_{tot}) are therefore the mesh density ($\rho^{grid} = N_{el}^{grid}/V$) and the total volume per simulation sample V. Limitations on both parameters during tomographic mesh generation were therefore required. These limitations were determined by the available RAM memory (8 Gbyte) and from a lower limit of acceptable mesh density as determined from a preliminary parametric study (Fig. 4.6). The first limit was about 3 millions of elements while the mesh dependency test led to set$\rho^{grid} \geqslant 2 * E08$ in order to get mesh independent results within 1% (however, as we will see soon, mesh Independence does not imply absolute quality of mapping).

Since the observed ratio $N_{el}^{grid}/N_{el}^{surf}$ was ranging from 7 to 10 (depending on element type and initial surface elements[9]), the previous limit on ρ^{grid} turned also into a lower limit for ρ^{surf} ($\geqslant 2 * E07$). The resulting maximum volume allowed was about 0.016 mm³ ($3Mil.el./\rho^{grid}$) corresponding to a cube of 0.25 mm in length, a value which was acceptable if compared to the RVE estimation for the 3D volume fraction.

Example grids are shown in Fig.4.7 and 4.8.

---

[8] averaging tensors over millions of elements in homogenization procedures requires a time comparable to short FEM simulations on the same model

[9] here such ratios were calculated for simplified isosufaces ranging from 150,000 to 200,000 elements

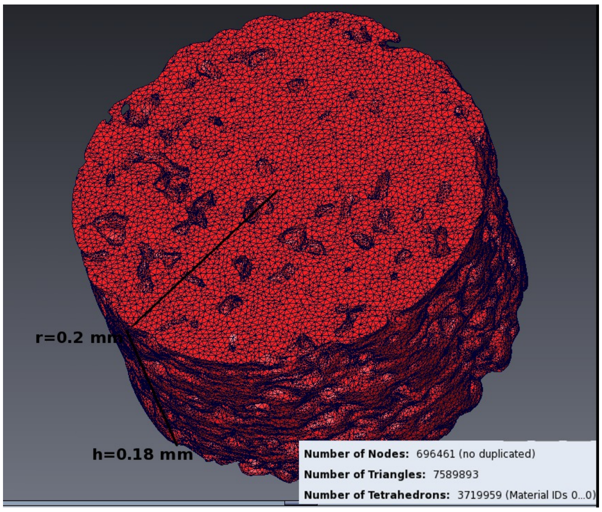

Number of Nodes: 696461 (no duplicated)
Number of Triangles: 7589893
Number of Tetrahedrons: 3719959 (Material IDs 0...0)

Figure 4.7: *A large tomographic mesh of PS-W (generated with Amira v5.3 [129]) spanning a volume of approximately one quarter of the total volume reconstructed during one scan (cropped reducing the height from 0.8 mm to 0.18 mm). The volume size is a volume fraction RVE with tolerance within 5%. The average mesh density here was 1.8*E08 elements/mm*^{3}.

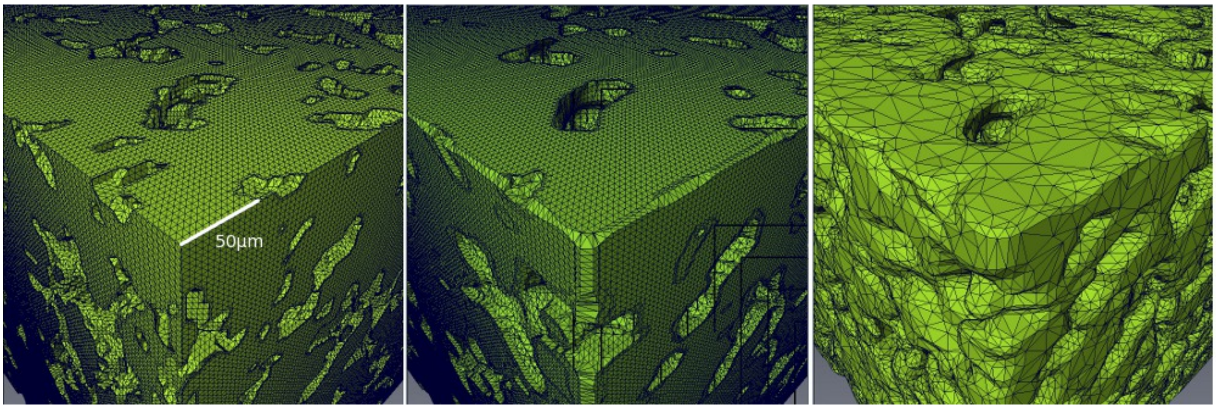

Figure 4.8: *Three different isosurfaces (generated with Amira v5.3[129]) of the same tomographic model of PS-W showing decreasing average element density (from left to right: 0.54, 0.34 and 0.06 tetrahedrons/voxel). The first two (left and center) are the original isosurfaces as generated from the Marching Cube Algorithm (MCA) with and without smoothing respectively. The right view with the lowest density was generated from MCA with smoothing and 2 further simplification steps. 3D-grids for FEM simulations were generated with the last isosurface type (together with lego-type isosurfaces, not shown here but in Fig. 4.9) capable of mapping significant regions of the coating with a limited number of grid elements.*

Due to the computational constraint, the final grids adopted for 3D FEM simulation in this work have contour shapes which look in between the middle and left grid of Fig. 4.8, with a final value of ρ^{grid} close to 2*E08 el/mm^3.

For our random morphology (as reconstructed by tomography) we could observe indeed a maximum average isosurface density[10] of about 0.3 triangles/voxel after smoothing and 0.5 tr/vx without smoothing. Generating a 3D-grid with such high starting densities had certainly improved the quality of mapping but it implied grids with N_{el}^{grid} getting quickly above 10 millions elements when coming close to RVE volumes: a totally unfeasible scenario.

---

[10] this is the starting density, before surface simplifications steps are done

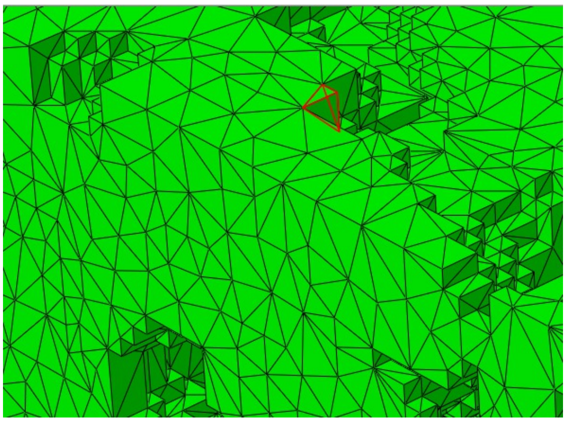

Figure 4.9: *Zoomed region of a "lego grid" with average mesh density of 1.25 tetrahedrons/voxel which approximately follows the tomographic voxel structure. The given density is about 3 times higher than that of the smoothed model used for simulations (0.5 el/vx corresponding to 2E08 el/mm^3).*

Mapping quality degradation for a wide range of mesh densities is shown in Fig.4.8. As to be expected the much lower values after smoothing and simplification steps ultimately affected results of FE calculations, since they substantially corrupted the morphological information (the convergence shown in Fig. 4.6was obtained only for smoothed and simplified meshes, i.e. within a closer interval of variation of mesh density. This means the minimum shown is not an absolute one).

For this reason, we restricted the use of 3D models for quantitative comparison with 2D models to "intrinsic" comparisons (cf. 2D/3D comparison of stress-fields in section 7.2.1). Computational limitations in handling good quality 3D-grids of the PS-W morphology is ultimately a consequence of the bottom-up approach for mesh generation in Amira. We could therefore expect improvements when a top-down refinement approach as that implemented in OOF2 would be also used for 3D mesh generation.

4.3 Homogenization on Image-Based FE-models

The link between mesoscale and macroscale follows a bottom-up schema based on volume or area average over the unit cell. This are further averaged over an ensemble of unit cells (also referred as micrographs or realizations). By convention, the first operation is referred as *micrograph homogenization* identified by a single bracket symbol $\langle\rangle$, while the second one as *ensemble homogenization* indicated with a double-bracket $\langle\langle\rangle\rangle$ (both with an index indicating the material, VPS-W or W/CuCrZr). ensemble homogenization defines our macroscale and, within its statistical error, is used for the quantitative comparison with experimental results. [11] For sufficiently large simulation volumes, even micrograph homogenization can be used for the comparison. In this case all the individual micrograph values are plotted in order to show the scatter of that particular quantity.

---

[11] When considering ensemble averaged, it is important to look not only at the average value but also at the variance of the set, as this is an indicator of representativeness (RVE, see chapter 1).

4.3.1 Mechanical Properties

As for VPS-W, stress has been computed from classical averaging techniques on discretized unit cells, integrating over the area (2D) or over the volume (3D):

$$\langle\sigma_{ij}\rangle_{2D}^{VPS-W} \approx \frac{1}{A}\sum_{n=1}^{N}\sigma_{ij}^{(n)} \cdot A^{el(n)} \tag{4.5}$$

$$\langle\sigma_{ij}\rangle_{3D}^{VPS-W} \approx \frac{1}{V}\sum_{n=1}^{N}\sigma_{ij}^{(n)} \cdot V^{el(n)} \tag{4.6}$$

where A and V are the total mesh area and volume respectively and the sum goes over all the N elements of the mesh. These are only tungsten elements in standard image-based planar models (2D-IB) and also contact-zone elements in 2D-IBCZ models (for which no changes are actually needed in the formulas). Equation 4.6 and 4.7 are valid for any stress component including equivalent Mises stress and principal stresses.

For W/CuCrZr composites the stress homogenization formula are the same, except that we should explicit the contributions of two solid phases (tungsten and the copper alloy). Since only planar simulation were performed the formula reads:

$$\langle\sigma_{ij}\rangle_{2D}^{W/CuCrZr} \approx \frac{1}{A}\sum_{n=1}^{N}\sigma_{ij}^{(n)} \cdot A^{el(n)} = \frac{1}{A_W}\sum_{n=1}^{N_W}\sigma_{ij}^{(n)} \cdot A_W^{el(n)} + \frac{1}{A_{CuCrZr}}\sum_{n=1}^{N_{CuCrZr}}\sigma_{ij}^{(n)} \cdot A_{CuCrZr}^{el(n)} \tag{4.7}$$

Strain has been estimated from the displacement at master nodes (under kinematic uniform boundary conditions). Considering for instance strain prescribed in vertical direction at the TOP nodes while BOTTOM nodes are fixed, and a unit cell of dimensions L_i, the formula used for the approximation of homogenized strain (intended as true strain in principal direction) is:

$$\langle\varepsilon_{2,3}\rangle_{2D,3D}^{VPS-W} \approx ln(1 + \frac{u_{2,3}^{TOP}}{L_{2,3}}) \tag{4.8}$$

were $u_2^{TOP}$is the displacement and the index 2,3 refer to the component in the 2D and 3D case respectively.

Macroscopic stress-strain curves have been derived from the formula above. Other parameters like the elastic modulus were calculated assuming a classical linear constitutive relation to be valid also at the macroscale:

$$\langle\sigma_{ij}\rangle = \langle E_{ijkl}\rangle\,\langle\varepsilon_{kl}\rangle \tag{4.9}$$

4.3.2 Thermal Properties

All the analysis focused on heat transfer in the vertical direction (parallel to deposition). Stationary states with fixed thermal gradient have been simulated (ΔT = 1°C). Only a direct estimation of conductivity (λ) is possible from the stationary solution, but we were actually interested into deriving diffusivity (α) since this is the parameter suitable for experimental comparison.

First we can calculate the average micrograph conductivity$\langle\lambda\rangle_\Omega$from the average flux $\langle\phi_2\rangle_\Omega$ through the Fourier's law:

$$\langle\lambda_2\rangle_\Omega = \frac{H\,\langle\phi_2\rangle_\Omega}{\Delta T} \tag{4.10}$$

The average flux $< \phi_2 >_\Omega$ is calculated homogenizing the vertical component $\phi_2(x,y)$ across a micrograph Ω_i :

$$\langle\phi_2\rangle\,_\Omega = \frac{1}{A_{tot}}\sum_{n=1}^{N}\phi_2^{el(n)}\cdot A^{el(n)} \tag{4.11}$$

where $A_{el(n)}$is the area of the element n in the mesh (non meshed region were assumed to be perfect thermal insulator).

After estimating the average conductivity $<\lambda>$ we can derive the average diffusivity $<\alpha>$ through the well known relation (valid in steady-state):

$$\langle\alpha\rangle_\Omega = \frac{\langle\lambda\rangle_\Omega}{\langle\rho\rangle_\Omega\,\langle C_p\rangle_\Omega} \tag{4.12}$$

In order to apply the previous formula we still need the homogenized specific heat and homogenized density. The first one is immediately obtained taking into account the porosity (and eventually considering the contribution of the contact-zone for a more precise calculation). For the specific heat we must average over the mass. One can immediately notice that $\langle C_p\rangle_\Omega$can be well approximated to the specific heat of tungsten[12] :

$$\langle C_p\rangle_\Omega = \frac{Cp^{cz}\rho^{cz}\sum_i A_{el(i)}^{cz} + Cp^W\rho^W\sum_i A_{el(i)}^W + Cp^{pores}\rho^{pores}\sum_i A_{el(i)}^{pores}}{\rho^{cz}\sum_i A_{el(i)}^{cz} + \rho^W\sum_i A_{el(i)}^W + \rho^{pores}\sum_i A_{el(i)}^{pores}} \approx Cp^W \tag{4.13}$$

---

[12] since $Cp^{cz}\to 0$ and $\rho^{pores}\to 0$

Chapter 5

Image-Based FEM on W/CuCrZr Composites

A deep characterization of deformation and failure behaviour of W/CuCrZr Composites trough application of the image-based FEM technique is the subject of this chapter. Both high and low W compositions have been investigated (W30[%vol]-CuCrZr70[%vol] and W70[%vol]-CuCrZr30[%vol]) at three different temperatures (for the sake of brevity we will refer to both compositions with the abbreviations W30% and W70% respectively). All the experimental samples of W/CuCrZr were provided by Dresden Technical University, Institut für Werkstoffwissenschaft (cf. previous section 2.2). Experimental tensile tests were performed at MTU Aero Engines Materials Laboratories.

The chapter is organized as follows: after a description of both numerical and real experiments, results are reported by subject (Residual Stress, Yielding and Failure) while result interpretation and discussion is postponed to the final section.

An important aspect of this numerical analysis was the validation through comparison with experimental results (stress-strain curves and fractographs). Within this approach, the mesoscale solution of stress-strain fields was an important instrument for the understanding of the local stress-deformation mechanisms of this material. To this end, efforts were made to reproduce similar experimental conditions during simulation, like morphological mapping performed on the same material used to generate experimental samples and the calculation of residual and thermal stress fields. It should be also noted that simulations were performed on small sub-domains of the real sample (as shown in Fig. 5.1), but sufficiently extended to capture the basic deformation phenomena interesting the whole material. A description of both experimental and simulated tensile tests follows.

5.1 Experimental Tensile Tests

Experimental tensile tests were carried out in cooperation with MTU Aero Engines, Germany at three different temperatures: 20, 300 and 550 °C. The tests were performed according to

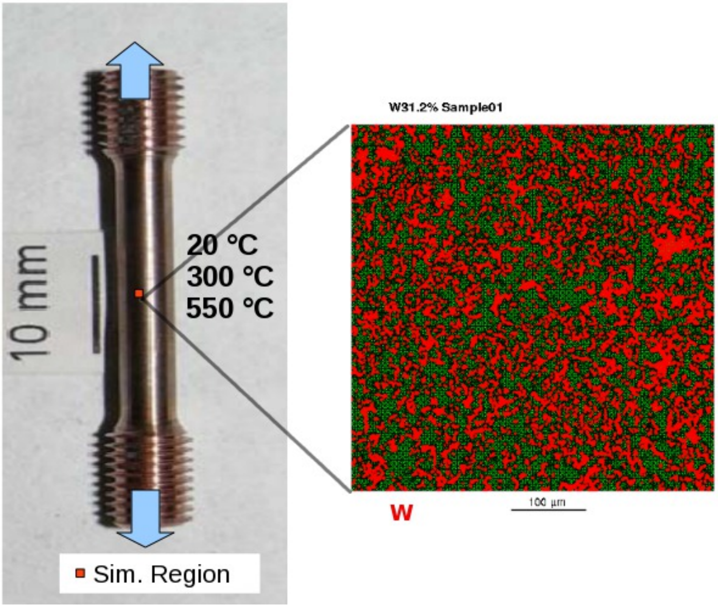

Figure 5.1: *A W-CuCrZr Specimen used for the experimental tensile test. The blue arrows indicate the loading direction. The small red square in the middle of the sample approximately indicates the domain of the FEM model, shown on the right side.*

the international standard regulation DIN EN 2002-002 for tensile test at high temperatures [94]. Fig. 5.2 shows the experimental setup. Cylindrical samples (length: 50 mm, diameter 3.5 mm) with thread-forming screw heads (Fig. 5.1) were cut out from sintered and infiltrated W/CuCrZr material at two different compositions: W30[%vol] and W70[%vol]. [1]

During the experiment the samples and the clumps were inductively heated at 20°C/s in air. Inductive heating allowed much higher heating rates and limited temperature overshooting than conventional heating in resistive furnaces. The relatively high heating rate was chosen in order to keep low the total exposure time at high temperatures, limited to 10-13 minutes only. A limited exposure time was necessary in order to make sure that no oxygen diffused to the inner part of the sample (since the sample were exposed to air), allowing to well support the assumption of perfect W/CuCrZr interfaces during simulation. Furthermore it allowed to neglect all possible creep effects. The exposure time was the sum of the time needed to perform the linear thermal transient (about 30s for the ramp RT-550°C), the time needed to adjust the temperature to the desired value within a prescribed tolerance (~ 7-10 min) and the time needed to perform the tensile test (~ 2 min). The 20°C/s is the average optimized value which comes out from the temperature controller (CTD) in order to get the temperature transient linear but with negligible overshooting effect (within a tolerance of 0.5% as dictated by the regulation). During the temperature ramp and temperature stabilization the samples were mechanically unconstrained (free to expand).

---

[1] The indicated estimations are based on density. During calculation of the volume fraction a mismatch (up to to 10% for the high tungsten composition) resulted between different methods, namely density based estimation through microbalance and SEM image analysis estimations. The second approach was necessary to qualify simulation results. However the mismatch did not prevent to clearly distinguish between high W and low W samples (both in experiments and simulations).

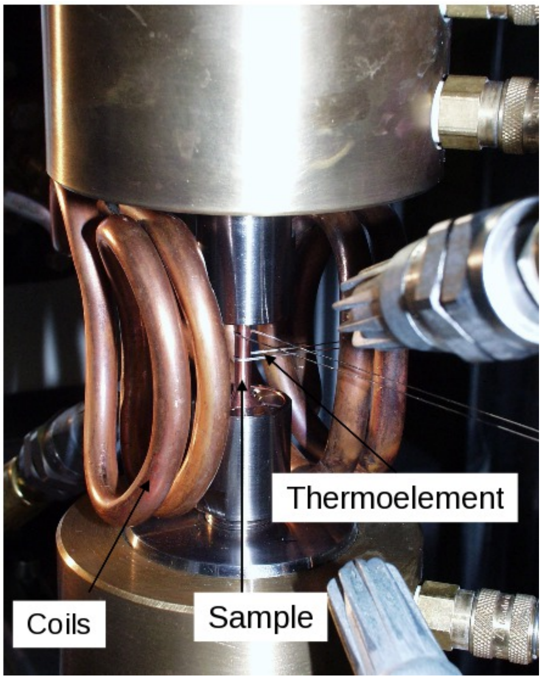

Figure 5.2: *The experimental setup for the tensile test at different temperatures (servo hydraulic test rig from MTU Aero Engines Materials Lab.). Coils inductively heated the clumps in contact with the sample.*

The specimens were then loaded along the cylinder axis at a low prescribed constant strain rate of $1.4e-03\,s^{-1}$. This allowed to reduce to negligible extent dissipative time depend phenomena like viscoelastic and viscoplastic effects which were not considered during calculation. The zero in the measured stress-strain curves were set when noise fluctuations became negligible and the induced stress could be measured.

5.1.1 Experimental Stress-strain Curves

Experimental stress-strain curves at different temperatures up to rupture are shown in Fig. 5.3

A strong monotonic temperature dependency of composite strength is immediately evident, with decreasing values for increasing temperatures. A rather strange temperature dependency is that of the ultimate strain of the composite: a first increase from RT to 300 °C is followed by a decrease from 300°C to 550 °C. Although the number of samples measured was limited to two per temperatures (and the related scatter quite high) this fact has been systematically observed in both compositions (W30% and W70%).

For the W30% case a general ductile behaviour is observed at all temperatures with large plastic strains (up to 12%!). The softening part is not as smooth as in the case of a ductile homogeneous media and is characterized by a rather abrupt (almost vertical) drop. At RT one sample failed outside the strain gauge resulting in a underestimation of the total elongation.

When the tungsten amount rises to 70[%vol] the total composite elongation at all temperatures becomes much lower, limited to some percents. The mixed deformation mode becomes clearly dominated by the tungsten phase (certainly brittle up to 300°C as proven by frac-

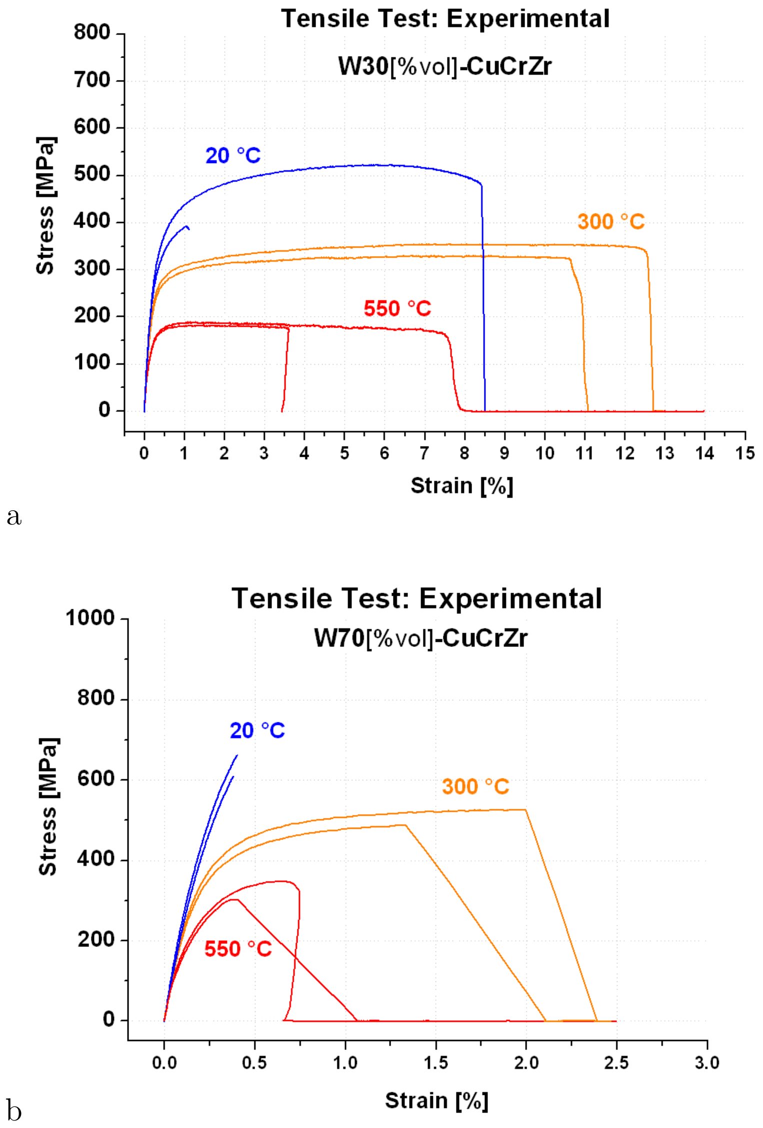

Figure 5.3: *Experimental stress-strain curves for the tensile test performed at RT, 300°C and 550°C. a) W30[vol%] b) W70[vol%]*

tographs, see 5.5). The whole composite shows then abrupt brittle failure at RT (with ultimate elongation limited to 0.4% for both samples) and a rather mixed failure behaviour at 300°C and 550°C with a large scatter between samples in ultimate elongation. Remarkably, one sample at 550°C behaved predominantly ductile with smoothed softening up to total failure.

5.2 Implementation of Simulated Tensile Tests

Simulated tensile tests have been performed at the same temperatures of the experimental measurements: 20 °C, 300 °C and 550°C. The solver ABAQUS takes temperature dependent material data (interpolated at the desired temperature, if necessary) and calculate intermediate thermomechanical equilibrium steps until the full prescribed load has been applied (in the form of prescribed total strain at the top boundary of the simulation cell). An extensive discussion about the local models adopted for tungsten and CuCrZr has been given in section 3.3. As for elastic constants material data, Young's modulus of both phases has been measured locally at room temperature and scaled at higher temperatures using reference material data from the ITER Material Property Handbook [117]. Data for the yield stress of the ductile phase have been taken from literature for solution annealed and aged CuCrZr [117], however, at 300°C the yield stress has been also varied parametrically to show the influence on the overall composite behaviour.

Except for the RT case, the simulated tensile tests at high temperature were implemented through three simulation steps:

1. Calculation of residual stress from 480°C to RT
2. Pre-heating to 300 or 550 °C and calculation of corresponding thermal stress
3. Tensile test at RT, 300, 550°C

Residual and thermal stress have been considered separately (as the first originates from the thermal treatment during manufacturing and the thermal stress during the heating ramps to 300 and 550 °C - see the dedicated section 5.3 for details).

This preliminary heating phase (before mechanical test was started) was implemented through a “Coupled Temperature-Displacement” simulation step.

Referring to Fig.5.4 the boundary conditions during the thermal transients 1 and 2 were :

- prescribed temperature field for all nodes of the model (linearly increasing from 20 to 300°C and from 20 to 550 °C).
- fixed vertical displacement at the bottom nodes.
- left, top and right boundaries planarly constrained (free to move in both vertical and horizontal directions, but forced to move “aligned” in each direction).

The last condition is justified since the simulated region is located ideally at half height of the real specimen, that is, far away from the external mechanical constraints. We can therefore assume that deformations at the boundaries of the FE-Model are planar, as they are surrounded by the remaining material.

After heating up to the desired temperature, the sample is maintained at the same temperature and mechanically loaded. Tensile loading (3) was implemented through the following boundary conditions:

1. prescribed strain at the top nodes varying from 0.5% up to 15 %
2. fixed vertical displacement for the bottom nodes
3. side nodes (left and right boundaries) planarly constrained (forced to move aligned in the horizontal direction).
4. RT, 300 and 550 °C assigned to all nodes and kept constant during the whole mechanical loading step.

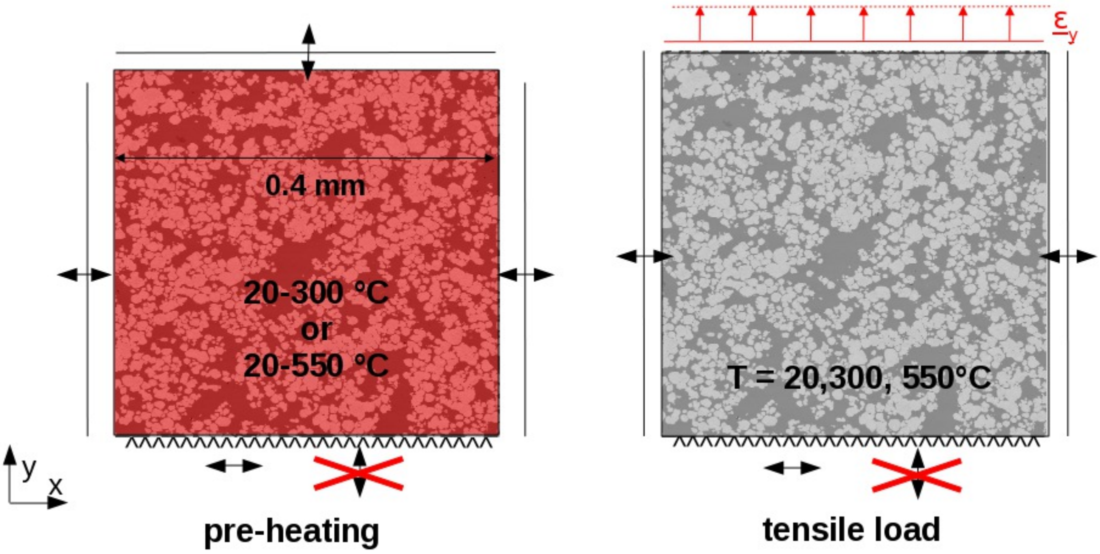

Figure 5.4: *Schematic representation of the boundary conditions used during pre-heating and tensile-load steps of the FEM simulation. Black arrows indicate unconstrained degrees of freedom. Black lines indicate that boundary nodes can move aligned along the allowed direction. The red arrows (right) indicate the prescribed vertical strain.*

Perfect internal W/CuCrZr interfaces were assumed during calculation. All models were meshed with planar triangular elements with active thermal and mechanical degrees of freedom (CPS3T or CPE3T elements in ABAQUS-Standard).

5.2.1 Calculation of Stress-Strain Curves

Stress-strain curves have been calculated during (3) by averaging stress on the whole area of the model and strain on master nodes (top boundary nodes). This homogenization approach (based on the equivalence of volume average and surface average for continuous fields) appeared to be the most suitable one for the comparison with experimental curves, since the strain is also measured on a virtual line from the strain-gauge. Average stress and strain were calculated at each increment of the simulated tensile test independently on two large unit cells of size [0.4 mm]^2 each.

The zero-point of the simulated stress-strain curve was adjusted to the same zero-point of experimental curves, since negligible non-zero average values (due to numerical artifacts) resulted from homogenization of residual and thermal stress before applying the load. The calculated curve could then be compared with the experimental ones.

5.3 Residual and Thermal Stress

In real samples of W/CuCrZr residual stress comes from manufacturing while thermal stress further developed after additional heating at 300°C and 550 °C. The thermal history of the sample was: 1- infiltration with molten CuCrZr at 1080 °C, 2 - solidification and cooling to

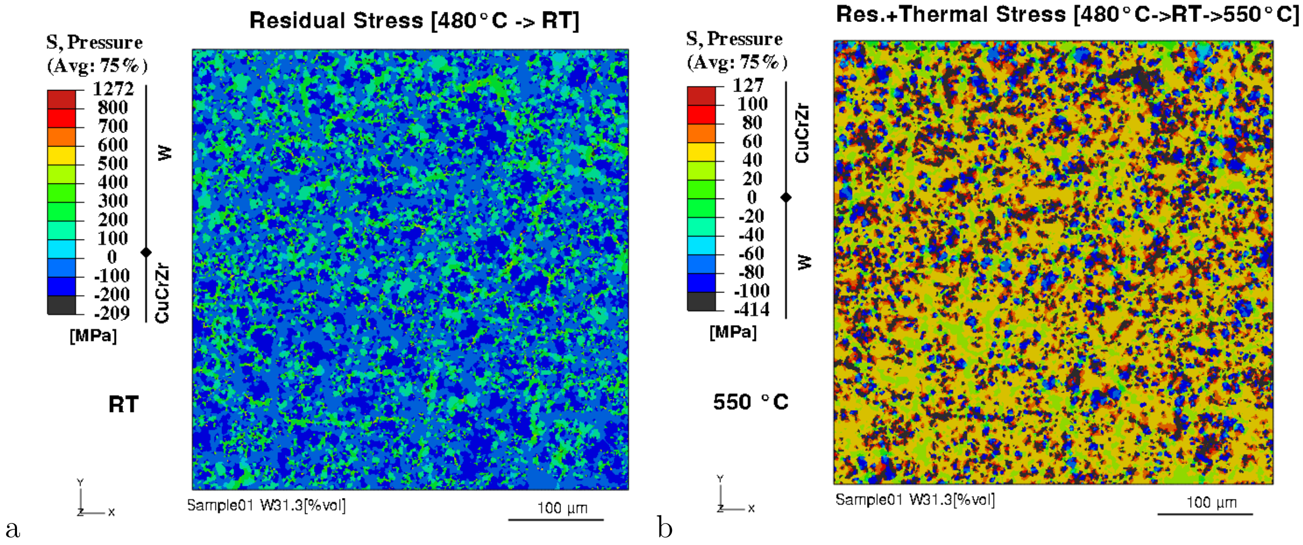

Figure 5.5: *a) Residual Stress as calculated after cooling from 480°C to RT (thermal treatment during manufacturing). b) The sum of Residual and Thermal Stress after subsequent heating from RT to 550 °C. Hydrostatic pressure has been chosen for representing the local stress status. One can notice the mutual change in stress status from compressive to tensile in the two phase constituent. The scales have been set in order to better show the average behaviour across the phases.*

room temperature, 3 - annealing of the whole composite at 970°C, 4 - aging at 480 °C and 5 - final cooling down to RT. This sequence has been simplified for the calculation of residual stress into a single cooling step from 480 °C to RT, since the sample is supposed to be stress-free after aging at 480 °C.

For the tensile tests at 300 °C and 550 °C an additional heating step from RT has been simulated for the calculation of thermal stress (supposed to be not relieved during a tensile test of about 10 minutes).[2]

Both stresses have been calculated with a coupled temperature-displacement simulation procedure in ABAQUS before mechanical loading was applied. During residual and thermal stress calculation, the sample was mechanically unconstrained (Fig 5.4), except for the condition of boundaries kept parallel during expansion/contraction, as it was supposed to be in the real configuration (Fig. 5.2, the clumps are free to expand and one can assume a perfect thermal contact between clumps and sample).

For such almost unconstrained thermal expansion the corresponding macroscopic (average) thermal stress ($< \sigma_{xx} >$) was negligible as expected, however high local stress concentration developed. The resulting internal stress fields (before starting the mechanical load) are shown in Fig. 5.5 for the RT and the 550 °C cases.

The internal stress arrangement changes considerably between the two extremal temperature paths (480°C-RT and 480°C-RT-550°C). In tungsten, tensile residual stress (developed during cooling to RT) turned into compressive thermal stress after heating to 550 °C with phase-average values ranging (in W30%) from 300 to -157 MPa. An opposite trend occurs in the

---

[2] although they are built from the same physical principle (CTEs mismatch) we distinguish here residual stress from thermal stress, since the first one is found at room temperature after a thermal cycle.

Table 5.1: *Estimations of Residual and Thermal Stress (RS and TS) at different temperatures homogenized along the phase constituents. The stress indicator used was the vertical stress component. Average on two samples with total area of 0.3 mm^2. CTE=Coefficient of Thermal Expansion.*

W30[%vol]	CTE at 20°C	RS 480-20°C	RS+TS 480-20-300°C	RS+TS 480-20-550°C
units	[1/°C]	[MPa]	[MPa]	[MPa]
W	4.4E-06	298 ± 3	-13 ± 1	-157 ± 2
CuCrZr	1.6E-05	-136 ± 5	6 ± 0	70 ± 2
W70[%vol]	-	-	-	-
W	4.4E-06	50 ±7	-23 ± 2	-33 ± 5
CuCrZr	1.6E-05	-269±1	19 ± 3	170 ± 1

Cu-alloy where an average compressive residual stress of about -136 MPa is turned at 550°C into tensile thermal stress of around70 MPa.

The equivalent plastic strain field (PEEQ) across the ductile phase has been also checked during all thermal transients and it remained fairly below the thresholds for damage initiation. We can therefore exclude that residual and thermal stress caused ductile fracture before mechanical load was applied.

On the other hand, we cannot exclude local failure initiation in tungsten caused by tensile peaks developed during cooling to room temperature. It is still unclear however, whether such high stress concentration (above 1200 MPa as indicated in Fig. 5.5-a) could be related or not to numerical artifacts, since it affects only a very small subregion of the model (whose size is in the order of fraction of mesh elements).

The calculated residual and thermal stress/strain fields at the end of each thermal history step were transferred as initial condition for the next simulation step: the simulated tensile test at RT, 300 °C and 550 °C respectively.

5.4 Plane Stress vs Plane Strain

Before looking in depth at the results we should briefly discuss our choice about the way a planar model approximates a real 3D mechanical object. This usually means to choose between the plane-stress ($\sigma_{zz} = 0$, for a model in xy plane) and the plane-strain ($\varepsilon_{zz} = 0$) approximation. The chosen element type determines the influence of the missing third dimensions in the planar model. While plane-stress elements correctly model thin objects under planar loads like plates, plane-strain elements are indicated for cross sections representing very thick structures like e.g. tunnels across mountains, where the object dimension perpendicular to load (length of the tunnel in this example), considerably exceeds the other two dimensions.

What is the most indicated choice for modeling a cylindrical sample of W-CuCrZr elongated parallel to tensile direction like that shown in Fig.5.1 ? A comparison between stress-strain curves calculated once with plane-stress elements (CPS3T) and then with plane-strain elements (CPE3T) is reported in Fig.5.6. Considering that the curves were calculated with the same

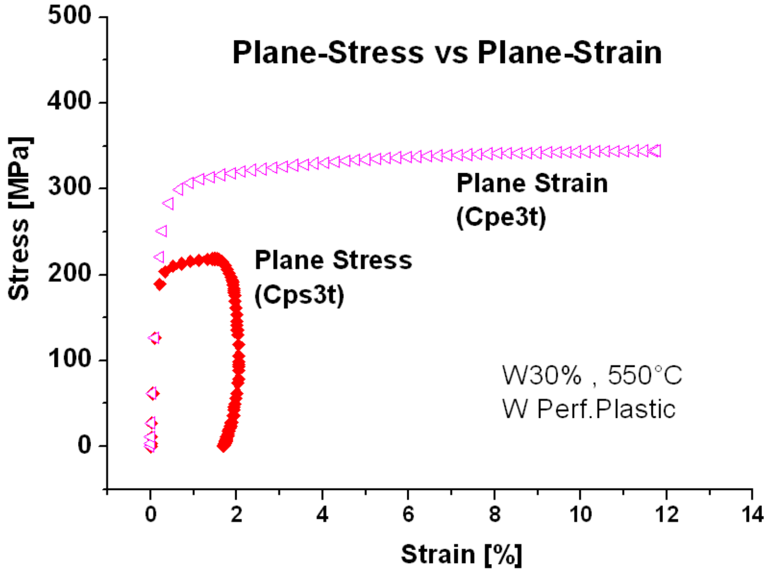

Figure 5.6: *Effect of the different planar assumptions on the homogenized stress-strain curve*

FE-Model, the mismatch is considerable (~30% on the yield stress values). We should then justify a proper choice.

If we look closer at the sample geometry, a planar section along the cylinder axis corresponds to a situation between the ideal plane-stress (plates) and the ideal plane-strain case (tunnel), because the specimen thickness is not negligible and the load is aligned with the symmetry axis. The results from the above mentioned comparison seems to confirm this view: the experimental curve lies between the two calculated approximations which behave like upper and lower bounds for the real solution.

Since the height of the sample is higher than its thickness (diameter of the cylinder) and since the specimen is loaded from top, the plane-stress approximation appears to be the right choice. We should not forget, however, that our specimen is not a bulk homogeneous one. Since both phases are randomly distributed but perfectly connected in 3D, a planar approximation can reduce the connectivity of the phases and therefore the average stiffness of the composite. This reduction, however, does not affect the plane-strain approximation since cross-sectional stresses in plane-strain cannot relax through deformation in normal direction and higher stress concentration develops causing higher average values. The global effect is therefore an overestimation for plane-strain and an underestimation for plane-stress (Fig.5.6). However, as evident later from the comparison with experimental curves , plane-strain overestimation case resulted quantitatively too far away from the real situation. Furthermore, it considerably overestimates the ultimate elongation, by retarding the localization effect (explained later in 5.6.2).

We will therefore assume plane-stress in the subsequent analysis, keeping in mind that this approximation slightly underestimates the average values of stress and strain for the real 3D case[3].

---

[3] We remark that modeling an unconstrained surface at the edge of the real sample with plane-stress elements can be regarded as non-approximation (since the stress on this surface must be planar at equilibrium). Since the length-scale of the simulated region is much smaller than the radius of the real specimen, we could regard

5.5 Fractography

Images of post-mortem fracture surfaces for both compositions are shown in Fig. 5.7, 5.8 and 5.9. An overview of the entire fracture surface is first given in Fig. 5.7. While in W70% the fracture surface looks almost planar, in W30% it shows irregular groove channels within a macroscopic fracture front propagating oblique to loading direction with a number of deviations from the initial direction. These images already indicate the main difference in macroscopic failure behaviour: pronounced ductility for high volume fraction of CuCrZr and macroscopic brittle failure for high volume fraction of W.

More detailed fractographs at higher magnification (Fig 5.8 and 5.9) are discussed separately in the following paragraph under the assumption that cooling down to observational temperature (RT) did not cause major morphological changes of the fracture surface.

W30%

The ductile failure mechanism is dominating in specimens with low tungsten volume fraction as evident from the formation of typical “cup and cone” structures on the rupture surface (Fig 5.8b and d). From room temperature to 300 °C an increase in ductility is noticed for the copper alloy phase so that this partly covers the tungsten skeleton after rupture. This covering effect is even more pronounced at 550 °C as the copper alloy becomes very weak and it seems to partly adapt its shape on the underlying W particles (Fig. 5.8f). The tungsten phase, on the other hand, shows typical traces of brittle failure (intergranular fracture mixed with transgranular cleavage) at RT and 300°C, while at 550°C the grain boundaries substantially changed from flat to curve. This could be an evidence of ductility, however more investigation were needed to demonstrate that the DBTT of this tungsten phase were below 550°C.

W70%

When the amount of tungsten arises to 80%, fractographs of Fig. 5.9 show how the mixed rupture mechanism across the composite is clearly dominated by brittle fracture of the tungsten phase at all temperatures (with transgranular cleavage also observed at room temperature). Intergranular fracture result as main failure mechanism from fractographs b and d which also show locations where internal surfaces in tungsten have been markedly detached (probably at the boundaries between poorly sintered tungsten particles). However some tungsten grains looks bended on the surface, as they had experienced a larger plastic deformation.

At 1000 times magnification (Fig 5.9 a,c,e) the almost planar surface from the overview images (Fig. 5.7) shows a more irregular three dimensional shape. This is the result of the random morphology of the composite microstructure, with the ductile phase completely surrounding the irregular structure of the tungsten skeleton. Local ductile failure in CuCrZr (clearly shown in Fig. 5.9 b and d) seems to cause small deviation of the crack front in the normal direction.

---

our planar model as a very good approximation when representing a piece of the external material surface.

For both compositions, interfacial debonding between phases seems to be excluded at RT, while at higher temperatures it could have partially occurred (black spots in Fig. 5.8 at low magnification). However, a further in-depth experimental characterization would be required to assess clearly this phenomenon.

5.6 From Yielding to Failure

Results of simulated tensile test (after pre-heating) are discussed here in detail at both scales: mesoscale (section 5.6.2) and macroscale (section 5.6.3).

The starting point is a preliminary discussion on the assumptions made for modeling the constituents behaviour during simulated yielding and failure. The choice to embed a damage evolution model within an image-based model offered the unique possibility to predict the *entire* composite stress-strain curve (through an explicit calculation of ductile crack *initiation* and *propagation*). In particular the *softening and failure parts of homogenized stress-strain curves,* could then be directly compared to experimental ones.

The comparison between calculated and experimental stress-strain curves is finally discussed in section 5.6.2 and 5.6.3. As we will see in detail in paragraphs 5.6.2and 5.6.3 the initial stress-strain configuration as effect of residual and thermal stress will have an important impact on simulation results together with the assumptions made on the behaviour of the single material constituents.

5.6.1 Starting Assumptions on the Constituents Behaviour

We discuss here briefly the starting assumptions which motivated the choice of constitutive equations and material data for CuCrZr and W. An isotropic local behaviour and perfect interfacial adhesion up to failure (for the temperatures considered) are the first assumptions on both constituents.

DBTT

While CuCrZr is obviously ductile in the whole temperature range considered, brittleness of the W-phase appears questionable at the highest temperature. Since DBTT cannot be measured locally, we need a guess based on literature values and the previous fractographical inspection. Because W-DBTT strongly depends on its metallurgical history and mostly on cold working, a wide interval of DBTT values is found in the literature (from RT to 800 °C [9]). Moreover, fractographs of Fig. 5.8 and 5.9 do not clearly and unambiguously show brittle failure at 550°C so that we may think that W-DBTT was probably not far away from 550°C. During the metallurgical route of W/CuCrZr, in particular during assembly of the W-skeleton, the extent of cold working is not precisely known and we cannot exclude a priori a ductile behaviour even at 300°C. However, fractographical evidences tend to exclude this, showing a rather brittle fracture surface of the W-phase at RT and 300°C (especially evident in W70%, Fig 5.9). Briefly, the

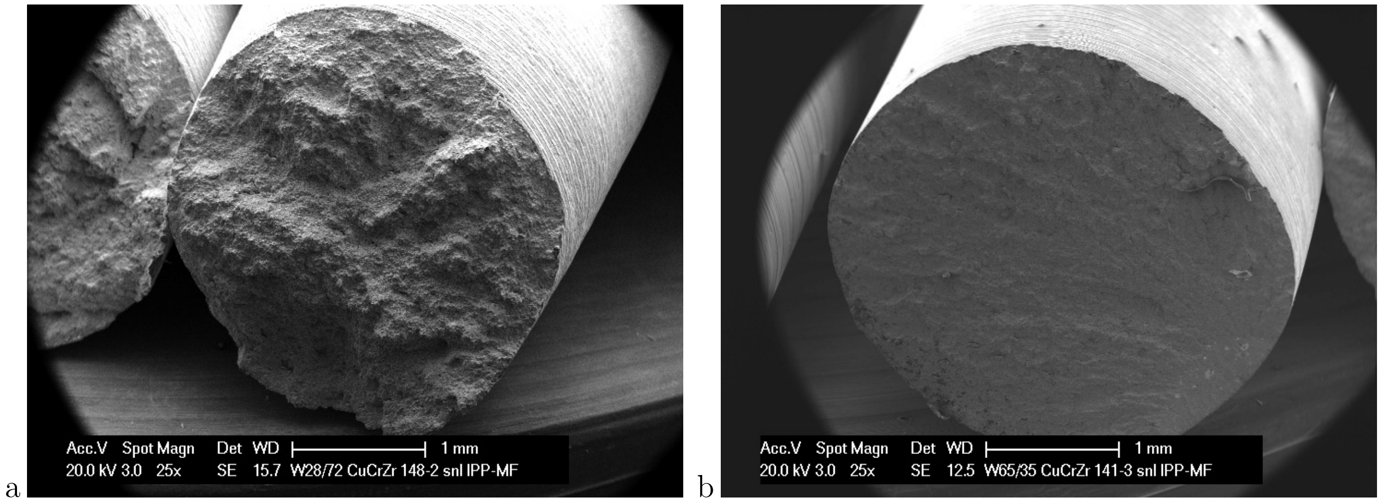

RT

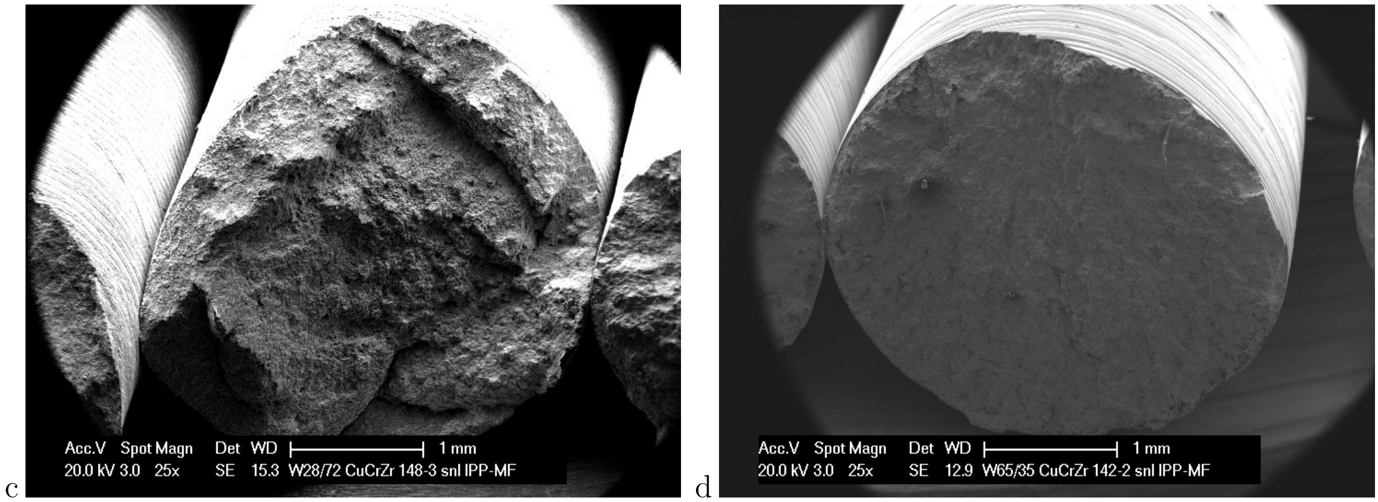

300°C

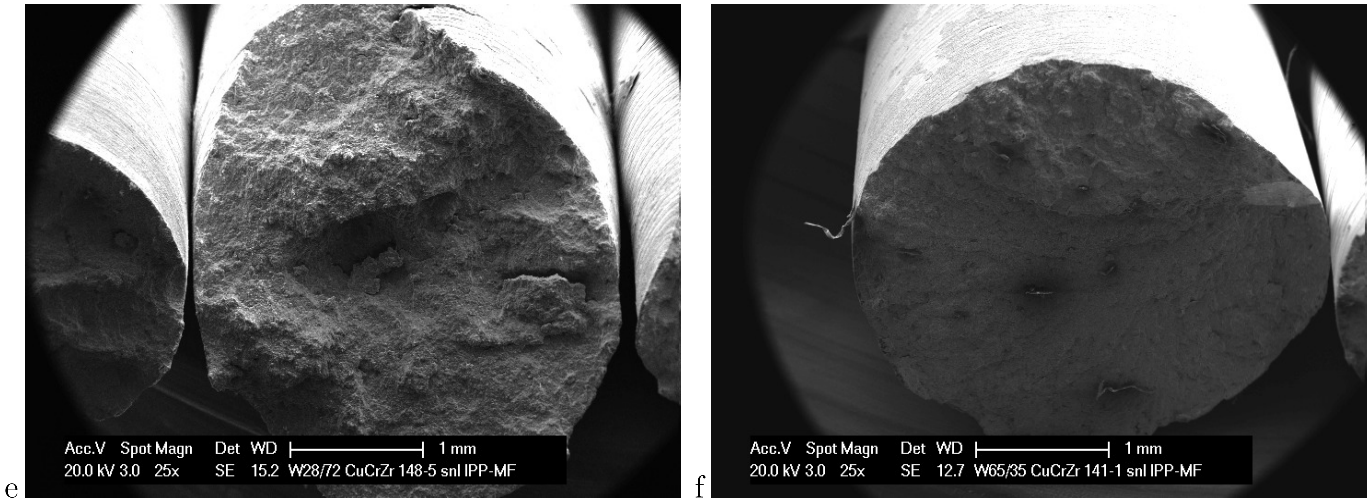

550 °C

Figure 5.7: *Fracture surface overview of W30[%vol] specimens (left) and W70[%vol] specimens (right) after total failure occurred at RT (a,b), 300°C (c,d) and 550°C (e,f).*

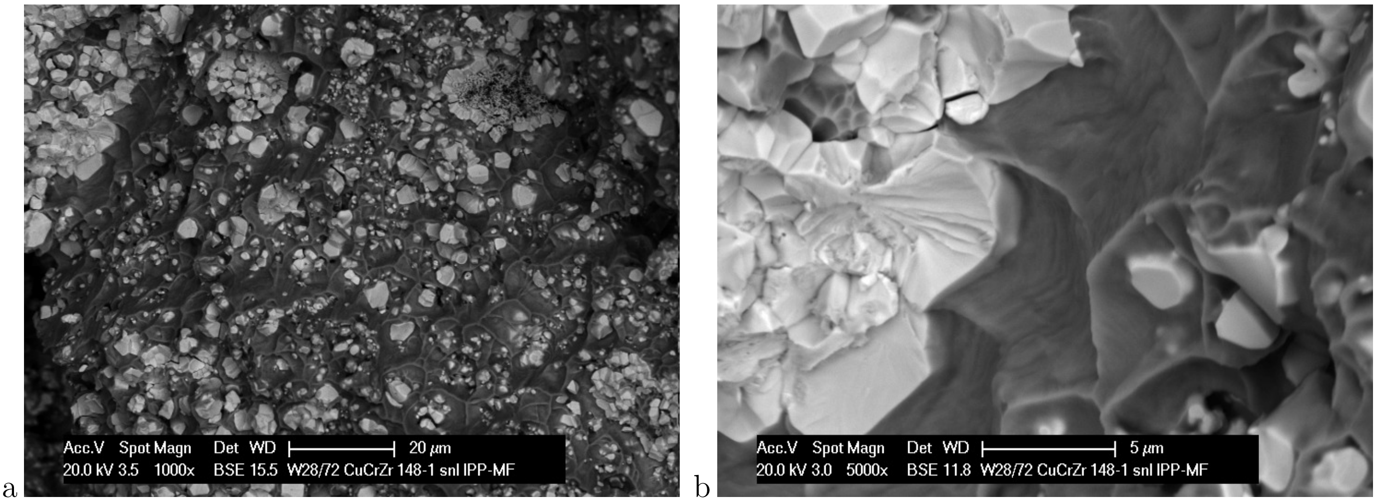

RT

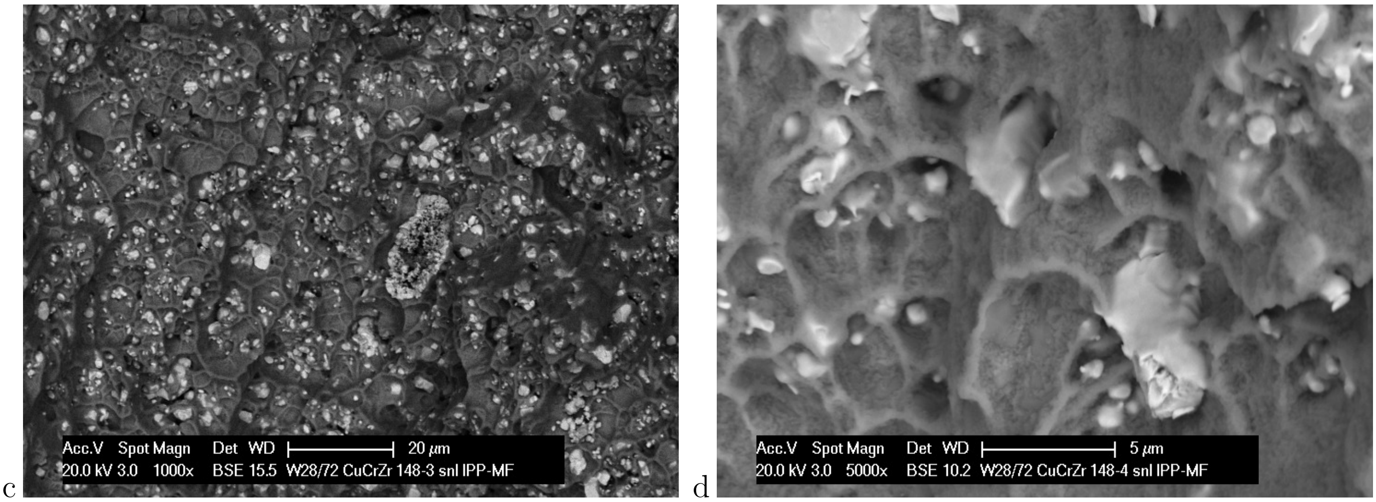

300 °C

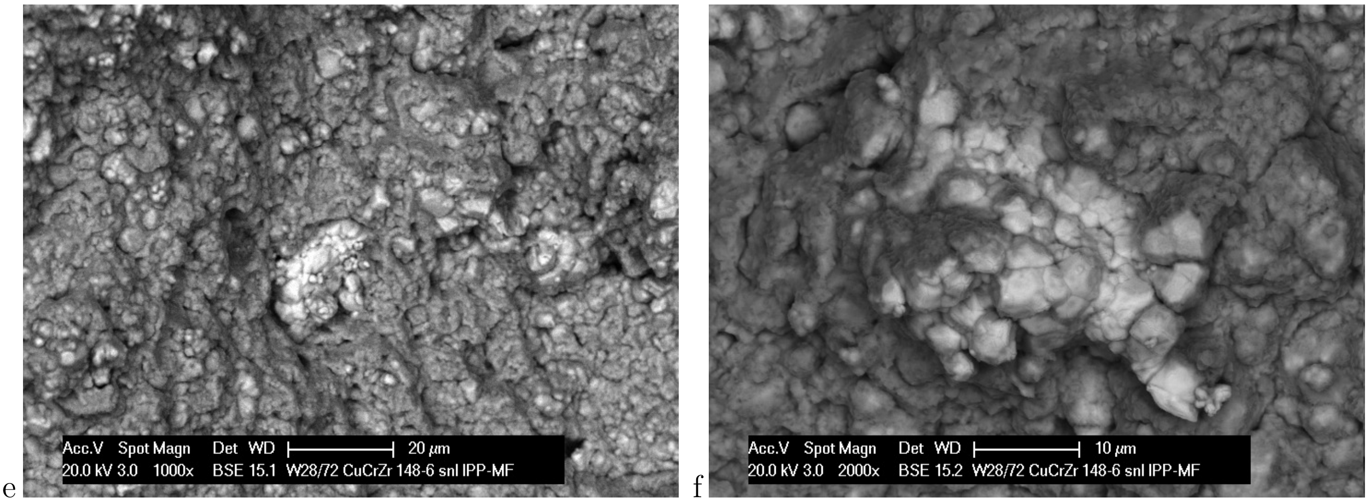

550 °C

Figure 5.8: *Fractographs of W30[%vol]/CuCrZr at different temperatures. One can notice a different shape of the W grains at 550°C suggesting larger irreversible deformation and probably some spots of plastic flow.*

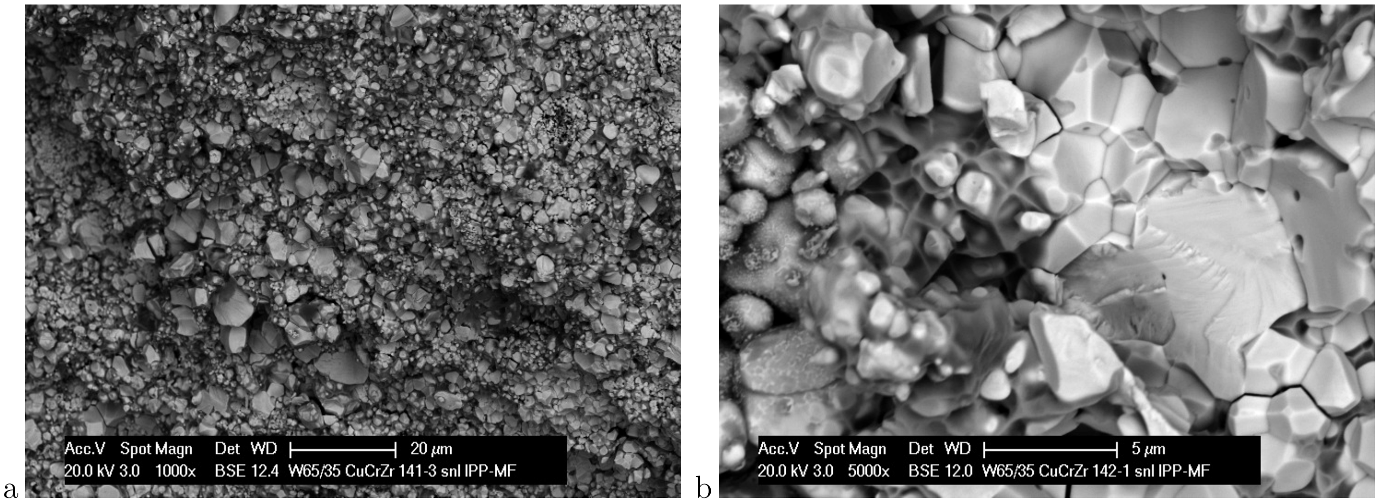

RT

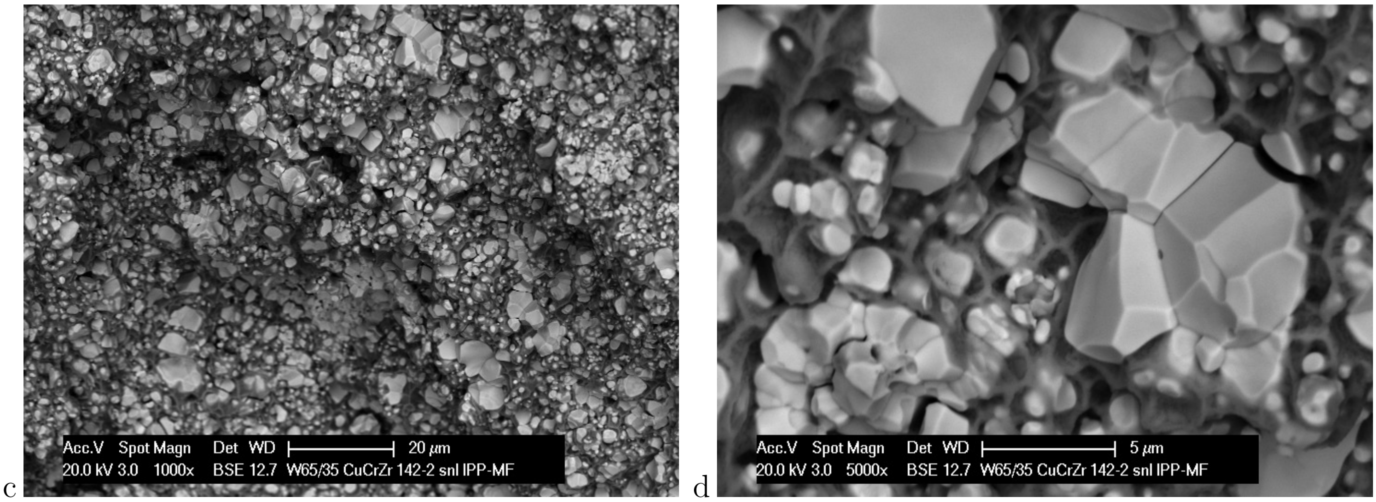

300 °C

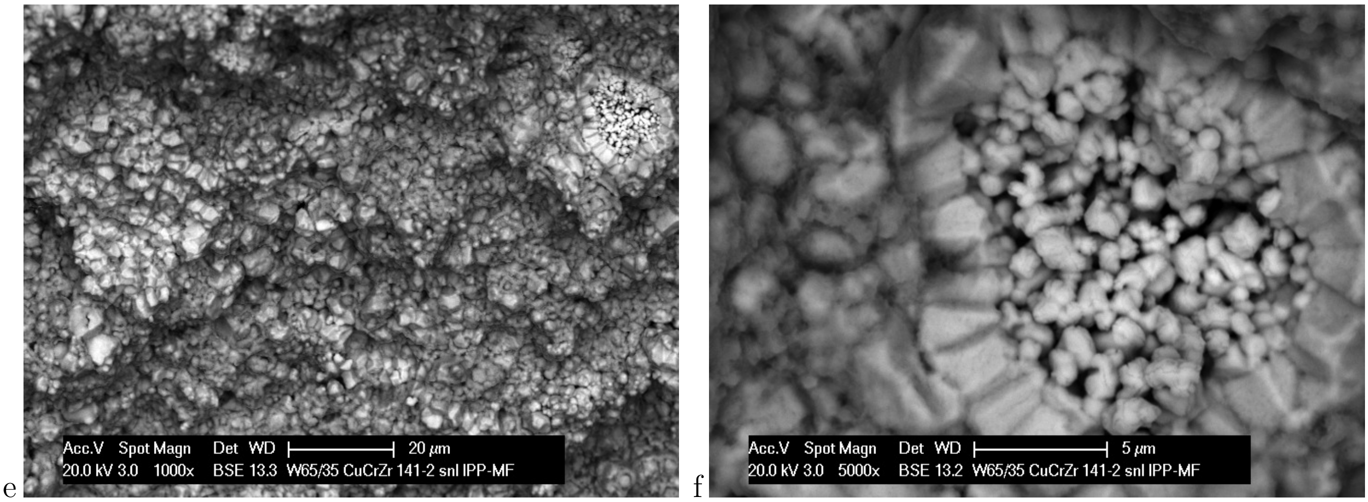

550 °C

Figure 5.9: *Fractographs of W70[%vol]/CuCrZr at different temperatures.*

fractographical inspection indicates a DBTT for our W certainly above 300 °C, but at 550 °C the fractographs are of dubious interpretation and some ductility in tungsten cannot be excluded (Fig.5.8f and 5.9f).

Recrystallization

Other phenomena which may affect grain structure like recrystallization and related embrittlement seems to play a minor role or to be even negligible at such relatively low temperatures for W. While fractographs with limited magnification cannot produce reliable information on the grain structure, recrystallization in W can nevertheless be excluded, since the activation temperature is well known to range from 1300 °C (non pure W) to 1100°C (pure, cold worked W) [6]and our specimens are kept at the maximum temperature of 550 °C for only 10-12 minutes during tensile test. Recrystallization in CuCrZr can be neglected as well, since its activation temperature is mostly found above 700°C in the literature [119].

Yielding and Failure

For CuCrZr it appears well motivated to assume a temperature evolution of yield stress and maximum elongation which follows that of a reference CuCrZr from literature [117] with the same thermomechanical history of the copper alloy in our composite (annealed at ~1000 °C and aged at 480 °C). The stress-strain curves are shown in Fig. 2.7. The YS of the CuCrZr-phase was also changed at 300°C to show the influence of this parameter on the overall stress-strain curve (see later paragraph 5.6.3).

As for the softening and failure behaviour of CuCrZr, a *continuum damage model* (CDM) with element removal based on equivalent (accumulated) plastic strain thresholds ($\bar{\varepsilon}_{pl}^{D}$ or PEEQ-th) has been adopted. The choice of a damage evolution model for ductile materials is well founded in the literature [121, 124, 122] and its implementation in ABAQUS has been already tested and extensively bench-marked on *homogeneus* models [92].

Details of the damage evolution model have been already given in section 3.3. The PEEQ-thresholds are in principle temperature dependent, but they are difficult to be directly estimated from empirical macroscopic stress-strain curves since they are local model parameters which describe ductility as an average effect of microscale phenomena (dislocation movement, formation and growth of microvoids) occurring in a localized region of the homogeneous specimen. We will therefore investigate parametrically the effect of different PEEQ-th on the global composite response at a fixed temperature (Fig. 5.16).

As for modeling failure of the W phase, since we could not include in simulation an explicit calculation of brittle crack propagation, we considered two options:

A. modeling W as perfect elastic with conditions for crack onset based on the maximum principal stress criterion (Section 3.3.2) with decreasing ultimate tensile strength for increasing temperature (checking at each simulation step if the strength limits were satisfied locally).

B. modeling W as *perfect plastic* with decreasing yield stress for increasing temperature, approximating the ultimate tensile strength with the local yield stress.

As we will see in the discussion of simulation results, the assumption B will lead to a much better approximation for the overall failure behaviour than the assumption A (pure elasticity without crack propagation). Furthermore, B appears even more justified at 550 °C since we could reasonably assume after fractographical inspection to be closer to the effective DBTT of the W-phase.

5.6.2 Microstructural Response

Starting from the previous assumptions on the local behaviour of tungsten, we describe the two resulting scenarios for each phase composition (W30% and W70%) looking first at the mesoscale FE-solution. The two main failure mechanisms at microstructural level are brittle cracking in tungsten (below DBTT) and ductile fracture in CuCrZr at all temperatures. Since the tungsten skeleton is completely connected in the real 3D case and it was completely infiltrated by CuCrZr with negligible residual porosity, none of these mechanisms can lead alone to total failure. A mixed failure mechanism is therefore necessary. Depending on some parameters, however, one process can dominate the other.

Internal debonding as third failure mechanism could in principle take place too. However, because of the good wettability and good adhesion between W and CuCrZr and because of the relatively limited temperature range considered, debonding seemed to play a minor role and it was not considered in simulations.

Strain Localization in W30%

The local state of plastic deformation is given by the Equivalent Plastic Strain (PEEQ). Its integration over the simulation steps (accumulated plastic strain) enters the definition of the element removal criterion in the ductile damage model as defined in 3.3.1. Fig. 5.10 shows the evolution of local plastic deformation at 300 °C at four different stages of deformation (as indicated by average strain in the vertical direction): ductile crack onset (a), ductile front propagation (b), and total failure shown in two different samples (c,d). It is noted that no preliminary crack location is prescribed during this simulation: both crack initiation and propagation are calculated. The location of crack onset is random as the microstructure. This is better evident from simulation conducted on different specimens of W30% showing each a different crack location (compare for instance Fig. 5.10c and d).

Fig. 5.11 shows mesoscopic arrangement of stress and plastic strain under the two different assumptions for W: A. elastic and B. elastic perfect plastic (shown on the top and bottom micrographs of Fig.5.11, respectively). For the comparison, the same geometrical model and the same stage of macroscopic stress-strain evolution is represented. This stage has been conventionally set when the first damage element has been removed from the FE-model, i.e. shortly after the top of the macroscopic stress-strain curve has been reached. At this stage of overall

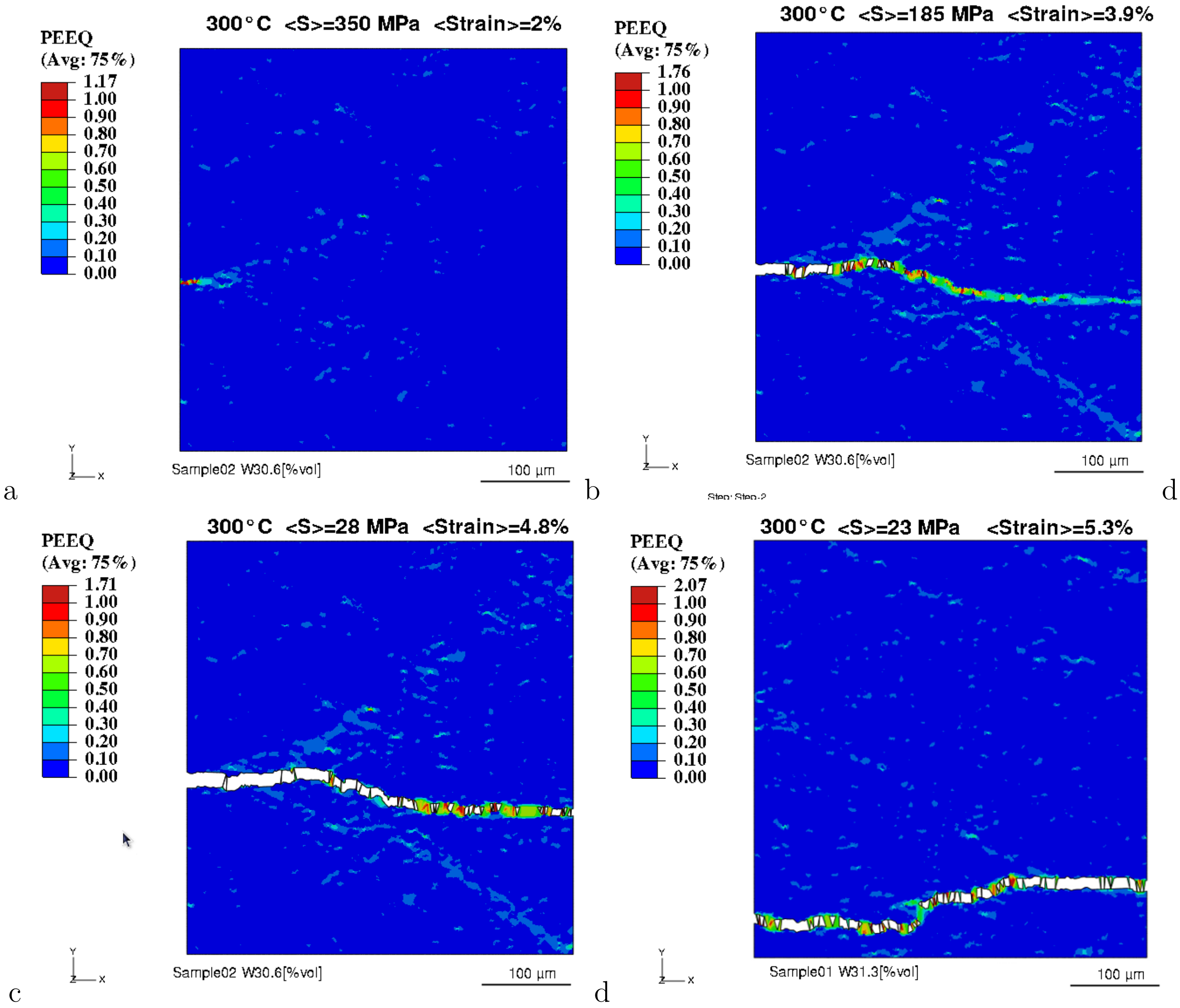

Figure 5.10: *Example of crack evolution pattern following the concentration of Equivalent Plastic Strain (PEEQ) along CuCrZr. In (a,b,c) it is shown the evolution of local plastic deformation and the ductile fracture front in a W30[%vol]/CuCrZr70[%vol] specimens. In (d) the final stage as in (c) for a different W30% sample under the same constitutive assumptions (perfect linear elasticity for W). showing a different crack propagation path as effect of the random microstructure.*

deformation the stress status inside the material is still quite high. A remarkable difference is noted first concerning stress-fields. While in the first case stress accumulated separately within the two phases, under the assumption B (activated plasticity in W) it already localizes in a trans-phase pattern.

As for plastic strain fields, one can notice the interesting phenomenon of *PEEQ concentration patterns (plastic strain localization)* occurring before crack initiates (b and d in Fig. 5.11). This fact has been systematically observed in W30% at all temperatures and regardless of model assumption on the local behaviour of tungsten. It is certainly caused by the activation of yielding into the ductile phase (CuCrZr). An important co-factor is certainly the particular phase arrangement in W30%: in cross-sections, the ductile phase becomes an effective ductile matrix with embedded tungsten particles, randomly distributed. This allows morphological patterns in the ductile phase to percolate from one side of the specimen to the other.

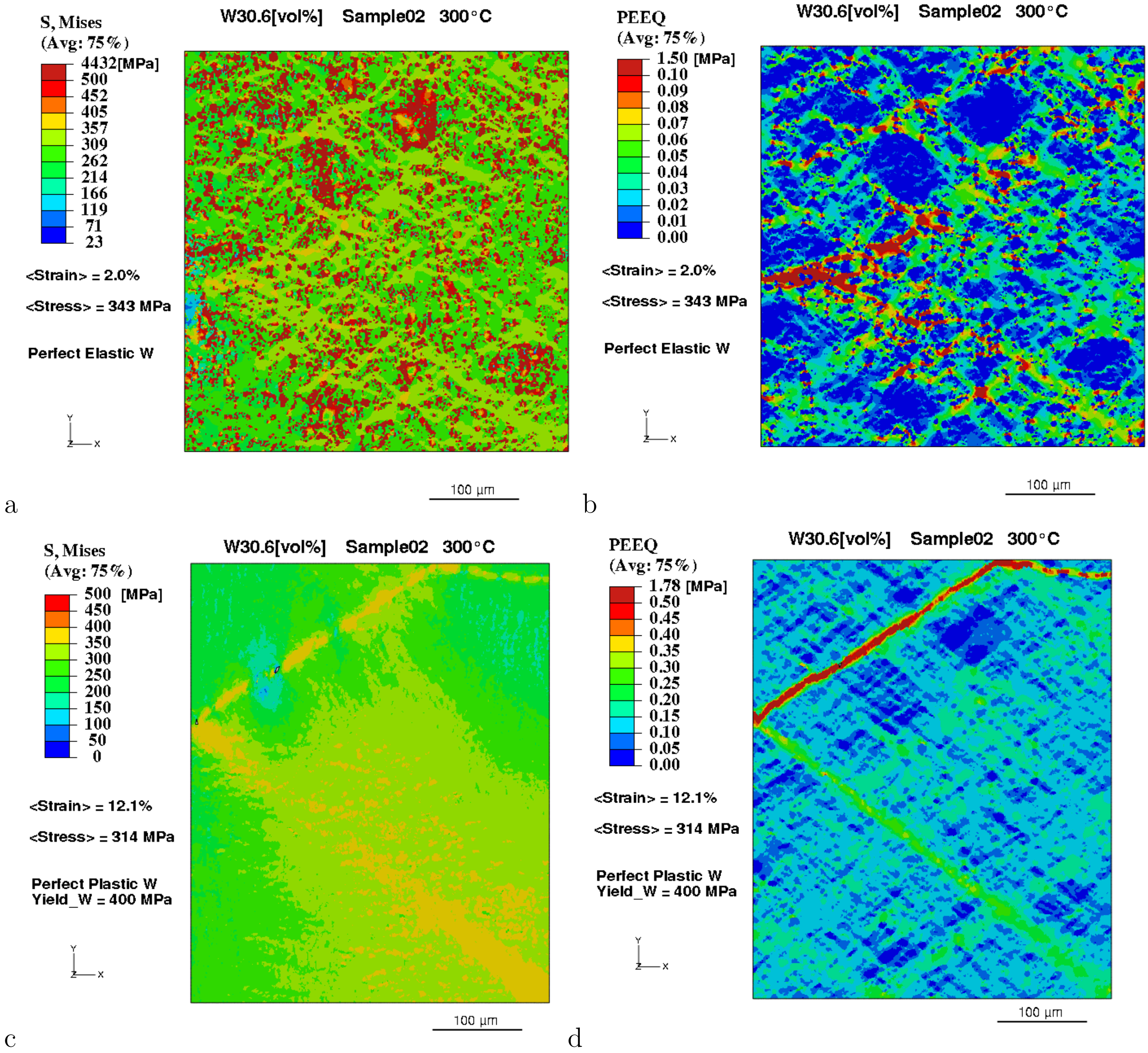

Figure 5.11: *Microstructural arrangement of stress and plastic strain in W30[vol%]/CuCrZr comparing two different assumptions on the local behavior of W when the overall stress was close to its maximum. Top raw: W perfect plastic. Bottom raw: W elastic-perfect plastic with yield stress of 400 MPa. Left column: V.Mises Stress field, Right column: PEEQ field (Equivalent Plastic Strain). The localized band (in red) is oriented at 35° with respect to the vertical axis.*

Once the threshold value for the first element removal is reached within a localized strain pattern, an enlargement of the fracture front follows, showing its fundamental ductile nature. This happens through further element removal ahead of the initiated crack front but not necessarily adjacent (Fig.5.10). Only later (when the average stress drops of 30-40% from its top value) a defined crack front propagation develops, until total failure is reached (Fig. 5.13).

Important differences characterize the assumption B (perfect plasticity activated in W). First, the global strain localization pattern develops much later (in Fig.5.11 at 12% overall strain instead of only 2% in the corresponding elastic case[4]) and second, the pattern looks more defined

---

[4] it has been also noticed that this gap decreases for increasing yield stress of the W phase

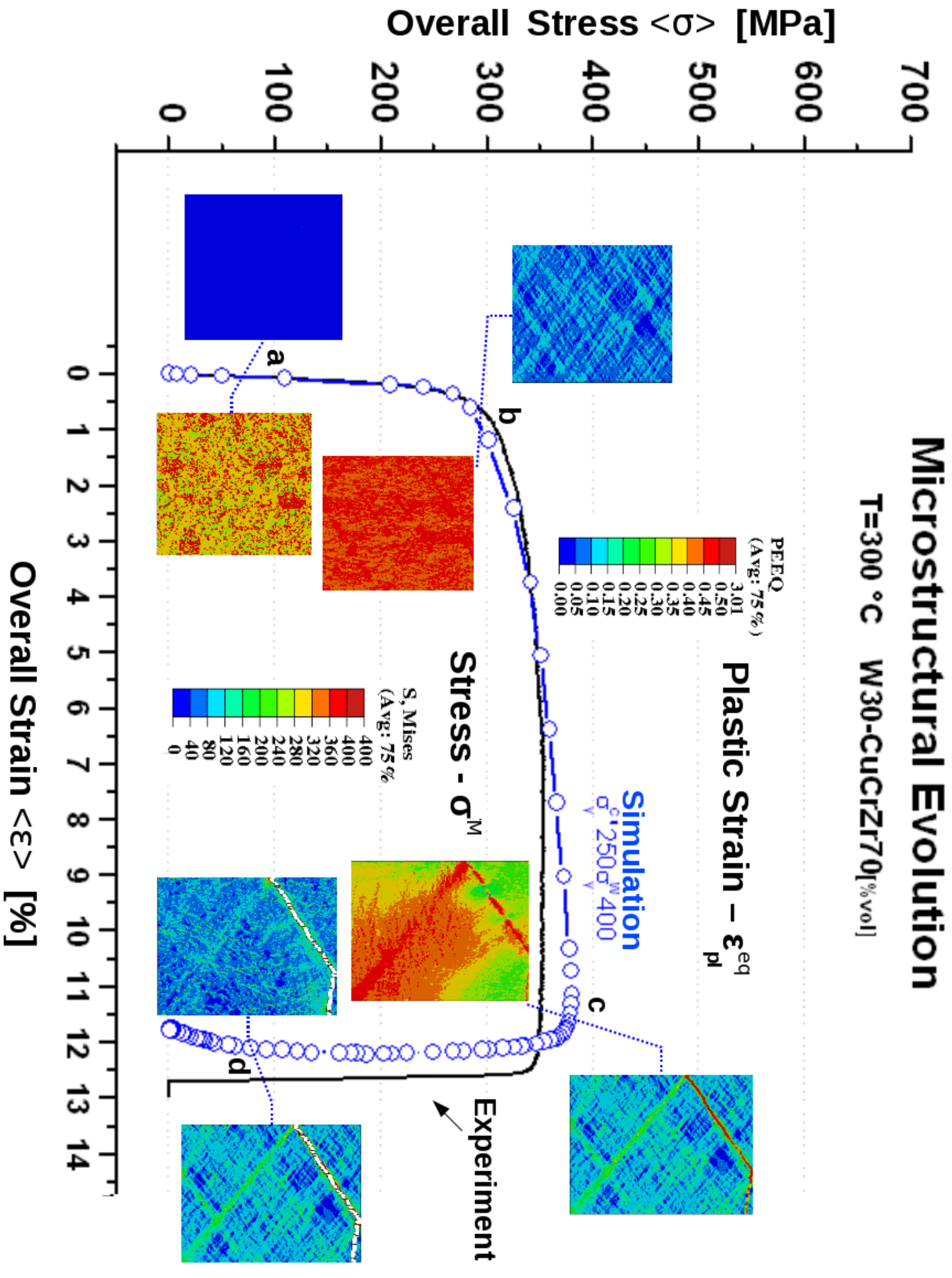

Figure 5.12: *Evolution of macro- and mesoscale stress-strain fields under the assumption of W-perfect plasticity with yield stress of 400MPa at 300°C. Four critical stages of composite deformation are shown: elastic deformation (a), yielding (b), plastic-strain localization at maximum overall stress (c) and failure (d).*

and sharp. A third important difference is about the main orientation of the subsequent crack front: approximately horizontal with significant deviations when W is considered elastic and

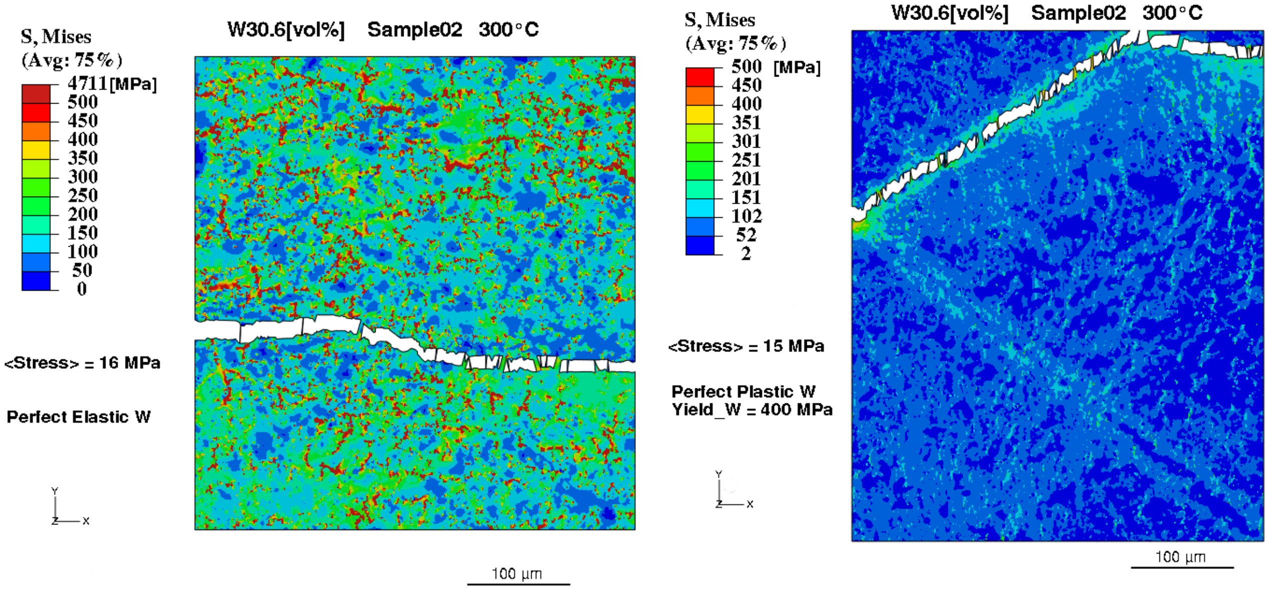

Figure 5.13: *Total failure in W30[vol%]/CuCrZr under perfect elasticity (left) and perfect plasticity (right) assumption on W.*

almost straight with slope of about 35-37° in the full plastic case. This fact remembers the well known phenomenon preceding failure in pure homogeneous ductile metals: strain localization and formation of shear bands oriented at 45 ° (as consequence of activated slip planes at atomic level and a maximum at 45° of the shear component). The small discrepancy of about 10 degrees is probably due to a microstructural effect, i.e. the particular phase arrangement of this particular sample. Furthermore it was observed that among the stress variables which localizes most the shear stress play a minor role here and a more pronounced localization patterns were found for the Mises invariant and the Equivalent Plastic Strain (PEEQ), an indication that all components contribute to the observed localization. However, the phenomenon was not fully clarified and further investigation are needed to better understand the linkage between microstructure and localization in W30%.

Strain Localization in W70%

In W70% the geometrical phase arrangement looks symmetrical to the W30% case: the ductile phase is now entrapped within a tungsten brittle matrix (in planar section). The lack of a brittle crack propagation model is mostly affecting the simulation of total failure in composite at room temperature since here brittle failure in tungsten has certainly taken place (and is well supported by fractographical evidence). However, simulation up to crack onset are still meaningful if an elastic model for tungsten and a brittle crack initiation criterion is checked locally at all simulation steps. In doing this we adopted a simple criterion based on maximum principal stress (when values of ultimate strain are difficult to be measured) or maximum principal strain (when significant deformation occurs) as explained in 3.3.2.

At 300 °C, while fractographs seem to support brittle fracture in W, a larger total elongation in composite (from 0.3% to 2%) results from experimental curves. This would suggest that the

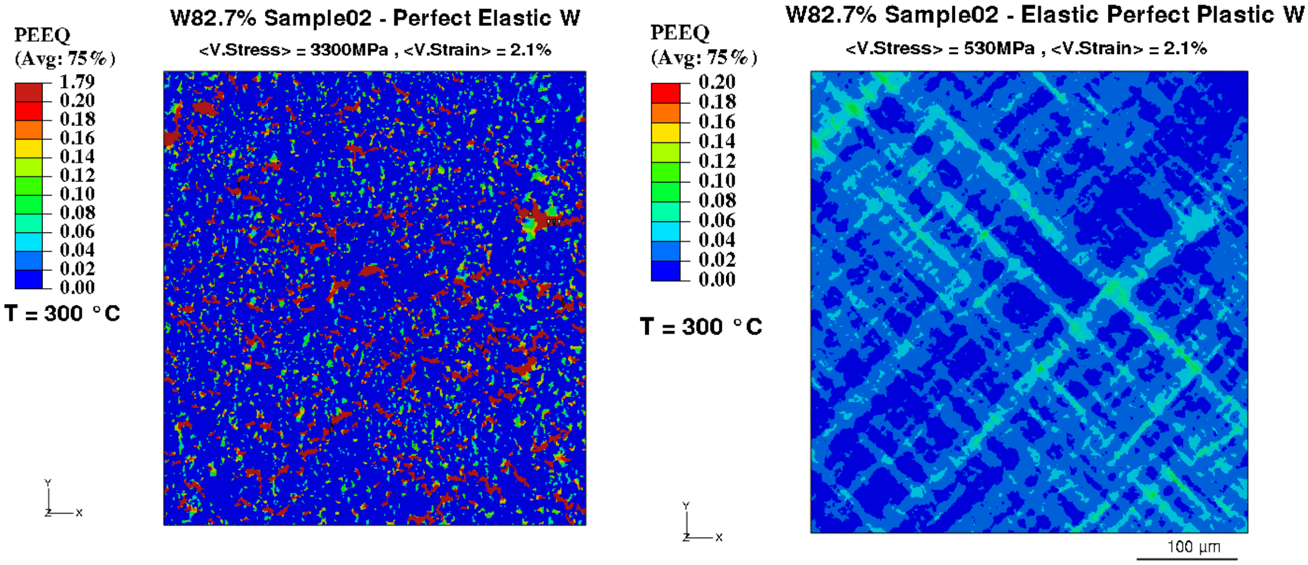

Figure 5.14: *Difference plastic response between the two assumptions on W in W70%CuCrZr20%. Left: a pure elasticity assumption on W causes plastic strain accumulation in isolated spots of CuCrZr (which were connected in a real 3D model) preventing the formation of a localization pattern. Right: activating plasticity in W allows for localized bands of plastic strain oriented at 45° (with respect to the vertical axis).*

tungsten skeleton possibly underwent (at least partially) small localized plastic deformation before rupture. However, caution is mandatory in proposing this interpretation and further experimental evidences are required (other phenomena like the neglected debonding at the phase interface could play a role eventually resulting in an equivalent global effect). In Fig. 5.14 two microscale scenarios are compared (by equal temperature, sample and overall strain) with the usual different assumptions on tungsten. When this is modeled as perfectly elastic, there is no way for the strain to localize in transphase patterns, because the ductile phase remains entrapped in closed regions of the tungsten skeleton. This causes a tremendous increase in local and average stress values (Fig. 5.19) which lead to total failure much before the experimentally observed overall strain (~2% at 300°C) has been reached. On the other hand (assumption B), when yielding is allowed in tungsten, transphase strain localization bands develop again and an overall yielding behaviour for the composite allows for more reasonable lower values of the overall stress.

5.6.3 Macroscopic Response: Stress-Strain Curves

The simulation results described at the mesoscale so far, are revisited here from the macroscopic point of view. In the following paragraphs we will often abbreviate "ultimate strain" as UE.

Influence of Damage Model Parameters

The influence of the ductile damage model parameters are firstly discussed. Changing the softening material data of the ductile phase like the shape of the softening function (from linear

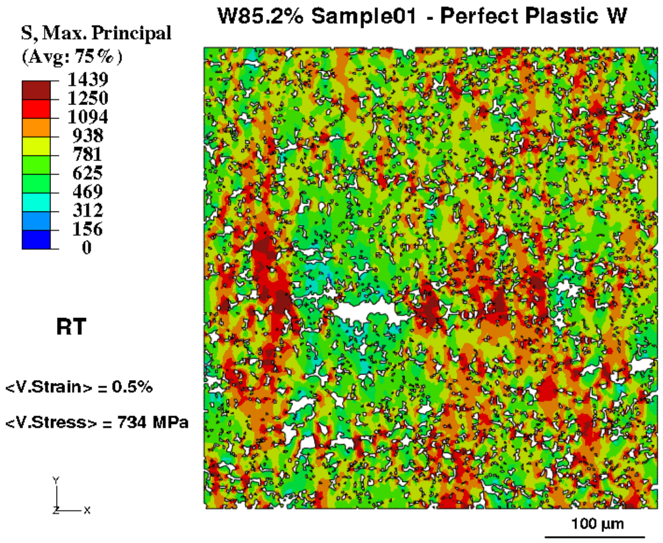

Figure 5.15: *Principal stress field distribution at RT in W70%. A horizontal concentration pattern (above W-UTS) develops in the central area of the micrograph, indicating imminent total failure.*

to exponential) and the damage evolution coefficients (varied of two order of magnitude) had a minor impact on the failure behaviour (green, orange and pink curve of Fig. 5.16). The most critical parameter of the ductile damage model is the accumulated plastic strain threshold (PEEQ-th) for element removal. Fig. 5.16 clearly shows that a reduced PEEQ-th of factor 10 from a reference value of 1 reduces to half the UE, without considerable change in the shape of the stress-strain curve. By contrast, an increment of factor ten improves the ultimate strain of only half its original value with a minor impact on the shape of the curve. This clearly indicates for the UE a saturation effect between for PEEQ-th towards 1 (Fig. 5.16). The shift in UE due to increased PEEQ-th can be a co-factor for explaining the first transition in UE from RT to 300°C, since the same behaviour was noticed in the stress-strain curves of pure CuCrZr from literature (Fig. 2.7).

Influence of Single Phase Yielding

The influence of local yield stress (YS) values on the macroscopic stress-strain response for both phases is shown in Fig. 5.17 (once plasticity is activated in W the trends are qualitatively representative also for the W70% case). In W30% *the YS of CuCrZr is dominating the overall yield values of the composite and also influencing its ultimate elongation* (UE), while tungsten-YS has an impact only on the UE. One can also notice how a decrease in CuCrZr-YS of 25% implies also an almost equivalent decrease in composite UE. Since the damage threshold was kept the same, this fact could play a role in explaining the second transition in UE from 300 to 550 °C (Fig. 5.18). The graph in 5.17 also shows how a perfect elastic W (which can be viewed as the limit case of infinite W-YS) causes the lowest limit in UE, progressively decreasing for increasing YS values of the tungsten phase.

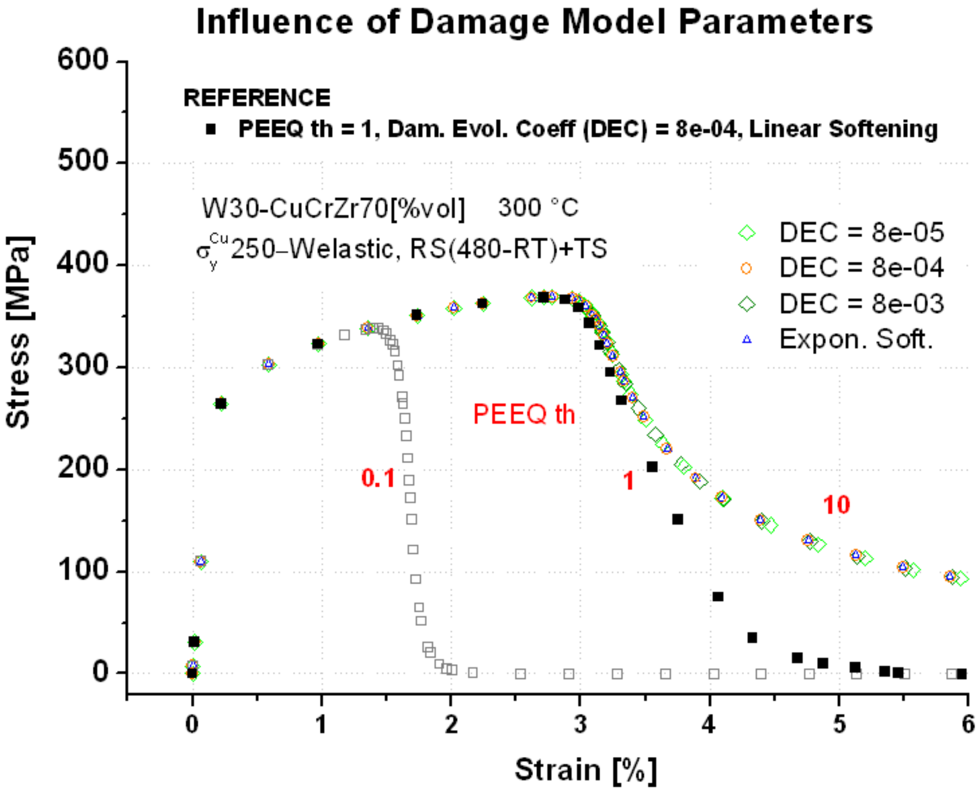

Figure 5.16: *Influence of different cumulative PEEQ thresholds on the activation of the damage evolution law in W30%. This has been also varied with negligible macroscopic effect.*

Ultimate Strain

In Fig. 5.18 and 5.19 the calculated full stress-strain curves for W30% and W70% are compared to experimental ones at all temperatures. For both compositions two scenarios are presented, corresponding to the assumptions A and B as explained in section 5.6.1. The impact of these assumptions on the composite UE and its temperature dependency is strong.

W30% - Hyp. A (W purely elastic at all T): the resulting UE as shown in Fig. 5.18-top is relatively low at all temperatures and the mismatch with experimental curves quite large.

W30% - Hyp. B (perfect plasticity activated in W at all T, Fig.5.18-b): the resulting UE is larger than in Hyp. A at 300°C and 550 °C, with maximum elongation at 300°C. The calculated curves are generally much better aligned with experimental ones.

W70% - Hyp. A: Only at RT the simulated curves can well reproduce the experimental trend. At higher temperatures the model fails.

W70% - Hyp. B: An overall good agreement between experiment and simulations can be observed at all temperatures. Even the calculated slops at failure at 300°C and 550°C seem to be well aligned to the measured ones.

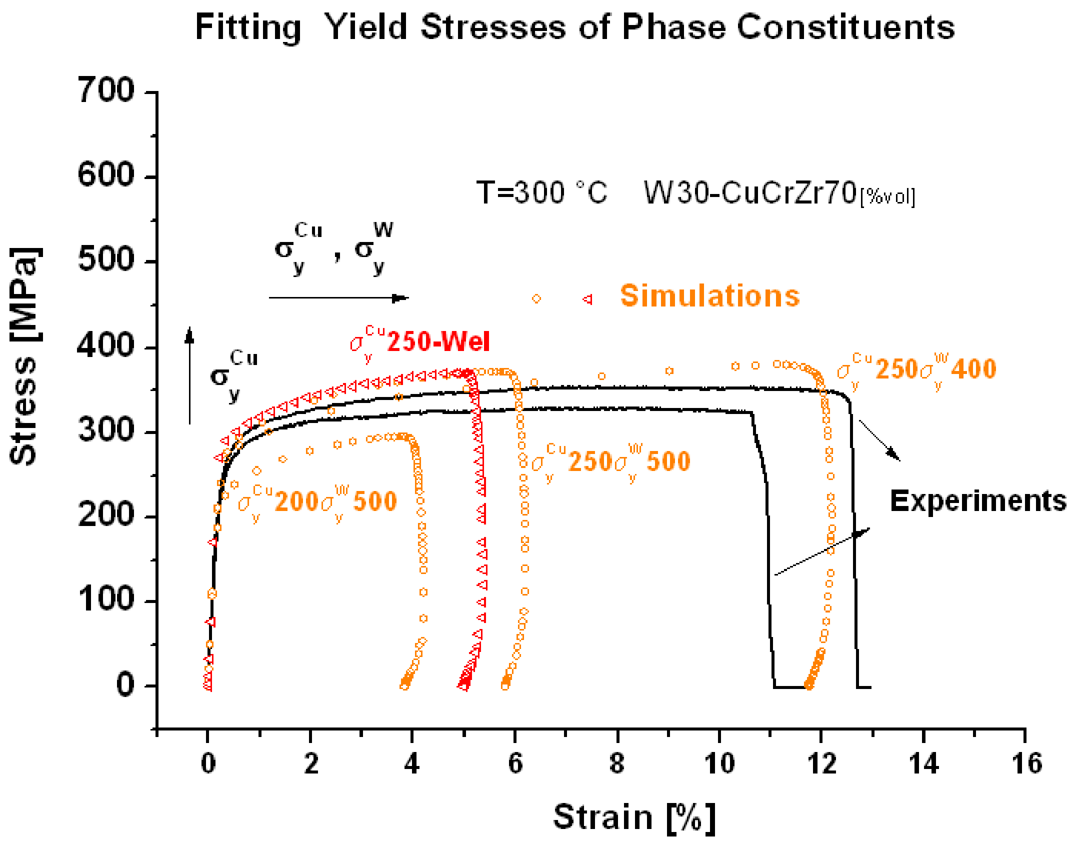

Figure 5.17: *Influence of local elastoplastic models on the macroscopic stress-strain response at 300 °C. The red curve indicates a pure elastic model for W, while orange ones assumes perfect plasticity with different yield thresholds (labels of each calculated curve indicate the reference values of the local yield stress for both phases assumed during simulation).*

A final remark is given:

- simulated *scatter of the UE between samples* becomes important only when plasticity is activated in W30%. Limited to this situation, simulation can also reproduce (qualitatively) the increase in scatter from 300 to 550°C (from less than 10% to about 30%).

In the coming section we will try to consolidate all the results presented so far (numerical results at the mesoscale, comparison between calculated and experimental curves, fractography).

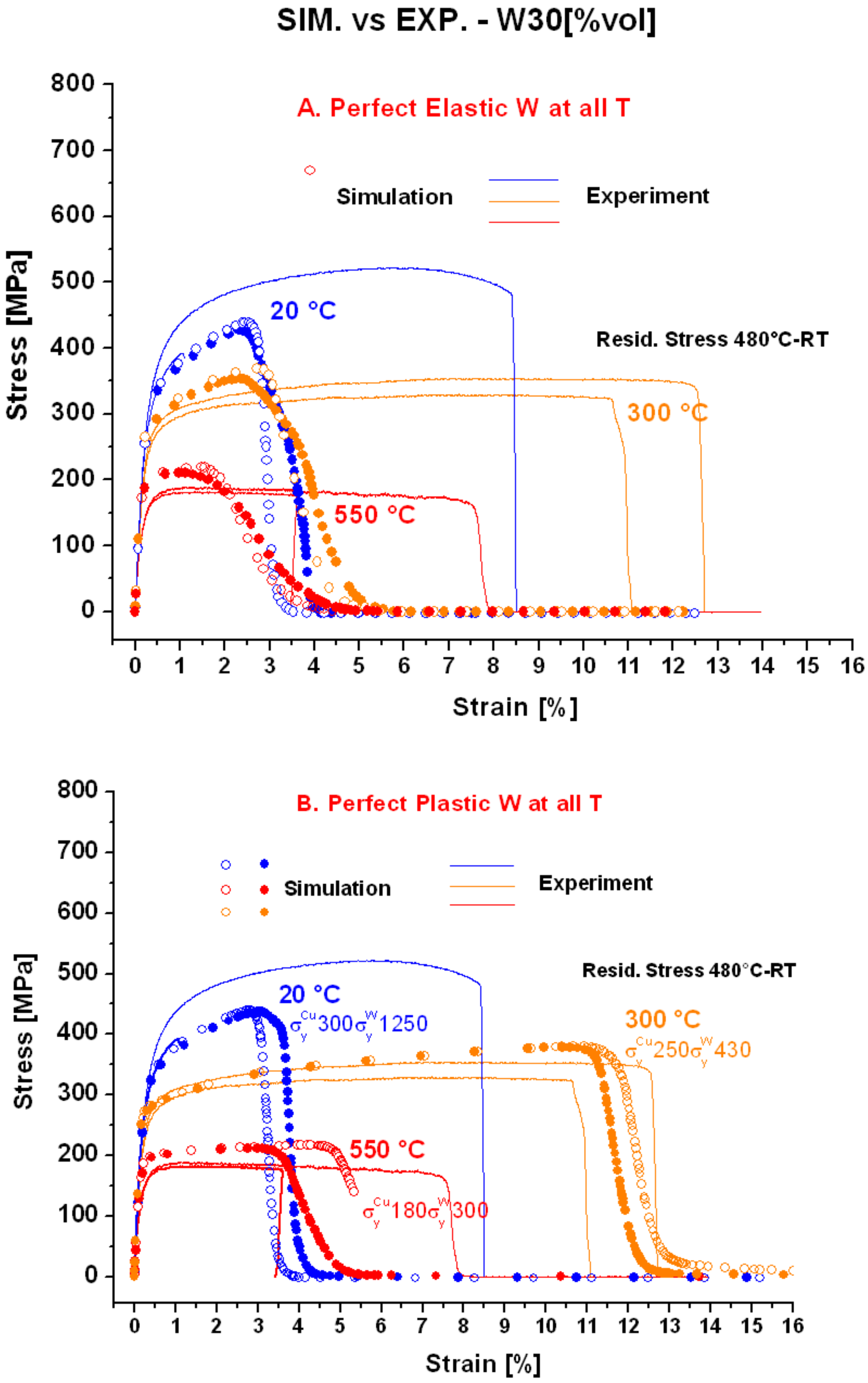

Figure 5.18: *The two resulting scenarios for W30% when changing the assumption on the local behaviour of W: perfect linear elasticity (top) and perfect plasticity (bottom). The indicated YS of the phase constituents* ($\sigma_y^{Cu/W}$) *is given for the bulk case at 0.2% plastic strain.*

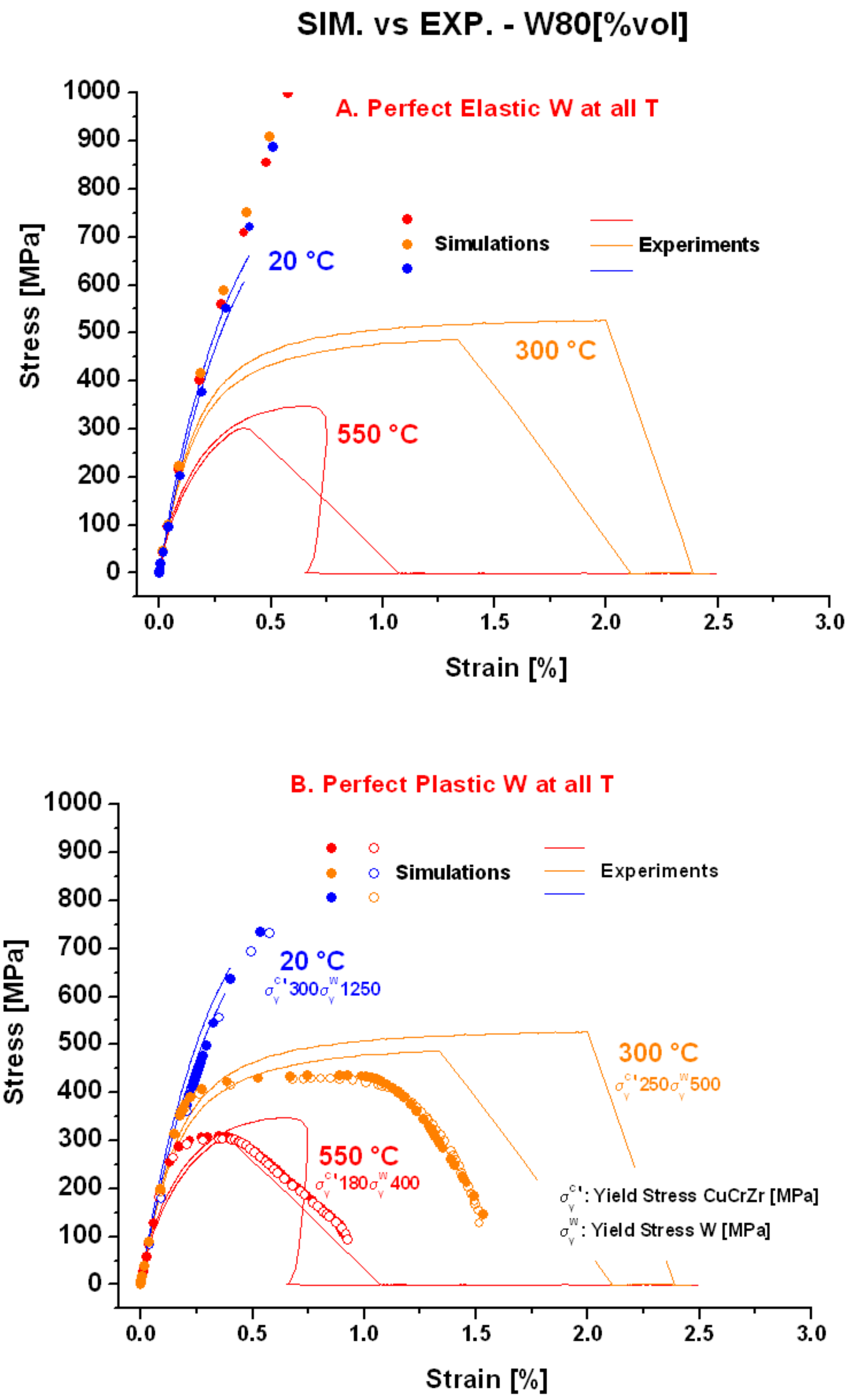

Figure 5.19: *The two resulting scenarios for W70% when changing the assumption on the local behaviour of W: perfect linear elasticity (left) and perfect plasticity (right).*

5.7 Discussion and Interpretation of Results

Table 5.2 summarizes the interpretation figure given for deformation and failure behaviour of the two compositions of W/CuCrZr for all the temperatures considered.

Table 5.2: *Summary of the deformation and failure behaviour of particulate W/CuCrZr Composites at different temperatures.*

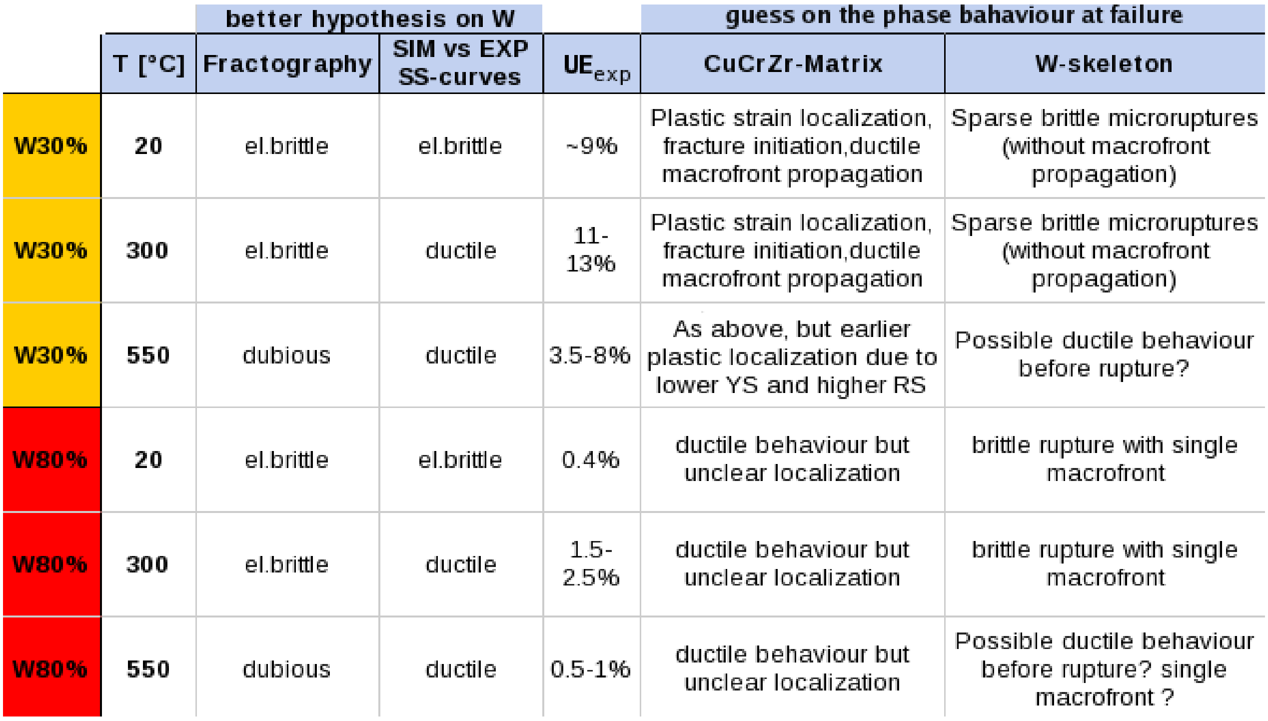

		better hypothesis on W			guess on the phase bahaviour at failure	
	T [°C]	Fractography	SIM vs EXP SS-curves	UE$_{exp}$	CuCrZr-Matrix	W-skeleton
W30%	20	el.brittle	el.brittle	~9%	Plastic strain localization, fracture initiation,ductile macrofront propagation	Sparse brittle microruptures (without macrofront propagation)
W30%	300	el.brittle	ductile	11-13%	Plastic strain localization, fracture initiation,ductile macrofront propagation	Sparse brittle microruptures (without macrofront propagation)
W30%	550	dubious	ductile	3.5-8%	As above, but earlier plastic localization due to lower YS and higher RS	Possible ductile behaviour before rupture?
W80%	20	el.brittle	el.brittle	0.4%	ductile behaviour but unclear localization	brittle rupture with single macrofront
W80%	300	el.brittle	ductile	1.5-2.5%	ductile behaviour but unclear localization	brittle rupture with single macrofront
W80%	550	dubious	ductile	0.5-1%	ductile behaviour but unclear localization	Possible ductile behaviour before rupture? single macrofront ?

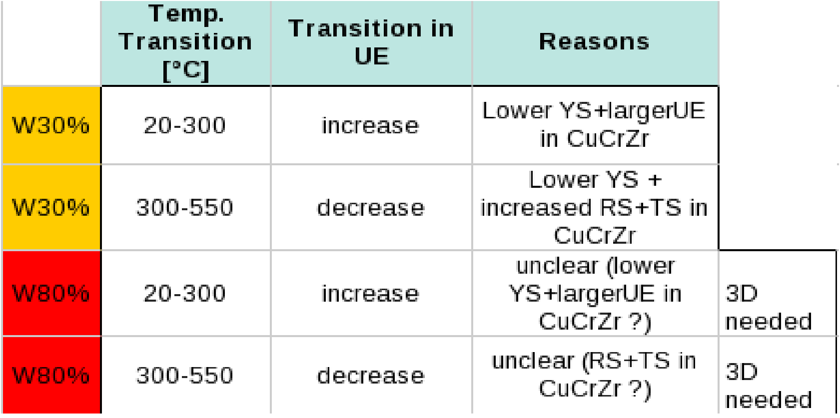

	Temp. Transition [°C]	Transition in UE	Reasons	
W30%	20-300	increase	Lower YS+largerUE in CuCrZr	
W30%	300-550	decrease	Lower YS + increased RS+TS in CuCrZr	
W80%	20-300	increase	unclear (lower YS+largerUE in CuCrZr ?)	3D needed
W80%	300-550	decrease	unclear (RS+TS in CuCrZr ?)	3D needed

First a note about statistical representativity of the results. Important scatters were observed in both experiments and simulation (Fig. 5.18and5.19) and a very limited amount of samples was employed. The simulation unit cells, however, included hundreds of micro inclusions and could well catch the mesoscopic deformation process. However, the large scatters in UE observed even on experimental curves suggest that instabilities originating from random structures are amplified at failure because of the intrinsic non-linearity and multiscale nature of this phenomenon. An improved statistics of both experimental and simulated tensile curves (left to future development of this work) is therefore necessary in order to achieve more quantitative and conclusive statements.

The Link between Localization and Ultimate Strain (UE)

We first recall the observations of the local field analysis in 5.6.2: plastic strain localization in CuCrZr could account for experimental stress-strain curves of W30% at every temperature and regardless of hypothesis on W, since the phenomenon develops entirely in CuCrZr. In W70%, plastic strain localization must interest also the W-phase in order to allow the formation of a tranphase pattern. Therefore, non negligible UE is observed only under plasticity assumption on W (Hyp. B). We also observe how peaked plastic localization develops close to the maximum overall stress[5] (of the overall stress-strain curve, cf. Fig. 5.12). A larger macroscopic UE (measured *after* the maximum overall stress) means therefore a *retarded* formation of the peaked plastic pattern at the mesoscale (the region where the ductile crack fronts ultimately develops, cf. Fig. 5.12c and d). The observed reduction in sample scatter from 300 to 550°C

When tungsten perfect elasticity (Hyp. A) is assumed, the stress saturates soon to high values in W itself, which means, a further strain increase in W would cost much more energy. For this reason, the system prefers to allocate stress into the ductile phase. Then, in W30% the connected ductile phase can plastically elongate causing an UE in the order of some percents (up to 3% at 300°C). Shortly after, the strain localization pattern can develop eventually releasing fracture energy. This phenomenon however, does not occur in simulated W70% *since the ductile phase is constrained in 2D islands* (cf. Fig. 5.14-a) and the plastic localization pattern cannot develop. As a consequence the resulting UE results very small at all temperatures, even smaller than the measured values (Fig. 5.19a). The assumption A of W-elasticity combined with the planar approximation results for W70% in a dramatic mismatch with experimental curves at 300 and 550 °C, leading to a wrong scenario.

On the other hand, when yielding is activated in both CuCrZr and W (Hyp. B), the simulated curves fit better the experimental curves in both cases (W70% and W30%). This because the system has much more ways to arrange local stress/strain fields in more homogeneous configurations before peaked localization develops. Plastic pattern localization becomes energetically convenient only after overall yielding occurred, resulting in larger overall strains. Depending on the yield-stress value assigned to the W-phase (Fig. 5.17) the UE can reach the very high values observed experimentally in W30% (>10%).

However, what explained so far (tungsten plasticity better fits the experimental data for T>=300°C) seems to contradict an important evidence from fractographical inspection: brittle fracture of the W-phase still occurred at 300°C, that means, tungsten DBTT seems to lie above 300°C. How can we explain this apparent inconsistency ?

---

[5] localization of a single peaked pattern should be distinguished from localized bands without peak already observed in the early stage of yielding, see Fig. 5.12b

Accounting for Large Strains with a Brittle W-Skeleton

A possible explanation starts from the observation that in the real case a W-skeleton could deform elastically much more than in the corresponding bulk form. As a spring deforms much more than its constituent material, so the skeleton of an even brittle material can allow for larger deformation before rupturing, since the “skeleton branches” can allow internal micro-rotations. Of course this phenomenon depends on the extent of “void” within the skeleton: for a “thicker” three dimensional arrangement with higher density of “branches” the overall response will be stiffer. This observation would imply a reduction in overall strain for increasing amount of W. On the other hand, below DBTT strain values of W before rupture are so low that they cannot be even measured. We can therefore exclude that the 3D-spring effect alone could account for an overall strain close to 12% (at 300°C)! Second, a spring still needs an increased force to continue deformation, but we noticed extended plateaus in the experimental curves. And third, a planar model of W30% cannot account properly for the skeleton collective spring effect since the skeleton is not connected in 2D. We must therefore suppose that other phenomena occurred inside the material to explain the large observed UE.

The first of them, well supported by fractographs (Fig.5.8-b and Fig.5.9-b) is *intergranular fracture* occurring sparse between branches of the W-skeleton in the W30% case at the W/W sintered interfaces acting as weakest points of the skeleton structure. Sparse ruptures in W with local micro-drops in stress would still allow large composite elongation, before mesoscale plastic localization develops into a macroscopic crack front. This can happen since the composite is still well connected by the surrounding ductile phase. In fact, a brittle failure sparse in the W-skeleton would imply further incoming stress to be transferred to the “ductile neighborhood” *which would dilate further without increasing much the local stress status* (since it already yielded). The resulting effect is also compatible with the slightly convex plateau in the experimental stress-strain curves, particularly evident at RT, while to some extent also visible at 300°C and 550°C.The second phenomenon which could play a role in allowing large total strains is *phase debonding* between W and CuCrZr. Once the stress debonding limit is locally activated in composite and a critical “sliding” stress is reached for a given critical value of overall stress, only a small increase in stress would be necessary to sustain this mechanism.The important conclusion is that the cumulative effect of internal skeleton micro-fractures and interphase debonding is *numerically* well approximated from the a perfect plastic behaviour assumed for the W phase (as indicated from the better matching of experimental curves with this scenario). Real micro-stress drops in W are certainly underestimated from stress-transitions at the local elastic limit in simulation, resulting in overestimation of the overall stress. This fact is confirmed by the mismatch in overall stress of W30% between predicted and experimental curves close to the ultimate strain zone (Fig. 5.18-b).[6]

At 550°C it remains unclear whether real plastic deformation occurred in W (W-DBTT <

---

[6] Such mismatch is probably mitigated by a dimensionality effect, since it has been reported that a 3D model with yielding activated in both phases (and a background ductile matrix) would produce a stress-strain curve lying further above that one calculated in plane-stress approximation [95].

550°C) or an equivalent stress-strain effect was caused by micro-ruptures and debonding.

Explaining the Temperature Transitions in UE

Fig. 5.16 shows the influence of the PEEQ-threshold for damage activation in CuCrZr as an important parameter determining a shift in composite UE. We may think that temperature dependence of this phenomenon could play a role in explaining the experimental UE-shifts (RT-300°C) and (300-550°C) since we observe temperature driven shifts also in the bulk CuCrZr (Fig. 2.7). However, an alignment with the trends observed in our W-CuCrZr composite is missing. Only a slight difference in UE from RT to 300°C in the bulk case cannot account for the large shift in UE observed for the same temperature transition in both W30% and W70%. Furthermore, as shown in Fig. 5.16, the calculated maximum shift in composite UE changing the PEEQ-threshold is about 2% (in absolute value), as the trend saturates (probably due to a microstructural effect).

It seems that we cannot explain the large shift in UE from RT to 300°C only through a temperature effect for the activation of damage in the CuCrZr phase. On the other hand, simulated curves in Fig. 5.18-bottom better account for the large observed transition in UE (about 4%) by allowing plastic deformation of the tungsten phase with a low YS (~400MPa). Combining this result with fractographs at RT and 300°C, we have shown that even if no-ductile behaviour of the tungsten phase occurred, approximately the same evolution of *composite stress-strain* would result from brittle micro ruptures occurring sparse along the W-skeleton. Temperature can certainly affect such phenomenon by influencing the ultimate strength at the interface W/W of sintered grains (W/W-US). During the transition RT-300°C of both compositions the W/W-US has been probably reduced. Since the local W/W-US would correspond roughly to the YS in W used in simulations, the closer such value becomes to the YS in CuCrZr the higher the probability for plastic localization to develop *later* in CuCrZr allowing for *larger* composite UE. The variation of the ratio $r(T) = YS_W/YS_{CuCrZr}$ at different temperatures seems therefore the driving force behind the first observed temperature transitions in UE, with an inverse proportionality of this type: $\frac{\triangle UE}{\triangle T} \div -\frac{\triangle r}{\triangle T}$ (easily verifiable on the the first transition of Fig. 5.18-bottom). However, while r decreases from 4.2 to 1.7 during the first transition, it remains approximately unvaried during the second transition to 550°C, whereas a new increase would be actually expected (since the UE decreases of about 50%!). This apparent inconsistency can be explained looking at the large difference in *residual and thermal stress* (RS and TS) at 300°C and 550°C (cf. Table 5.1). The total stress along the CuCrZr phase at 550°C (before starting the external load is more than 10 times higher than the corresponding RS+TS at 300°C. This implies an higher probability to initiate ductile damage before large values of composite elongation are reached, since the ductile phase is already experiencing high tensile stress before applying external tensile load to the whole specimen. These considerations, while reasonable for the W30% case (where the planar approximation seems to appropriately described the material behaviour) cannot be directly transferred to the W70% case which requires a full 3D approach to show the role of the ductile phase, otherwise artificially entrapped in planar models.

Limits of the model

The postulated equivalence between sparse micro-ruptures and overall yielding of the tungsten skeleton, while partially justified for the W30% case, seems to be hazarded for the W70% case at temperatures below DBTT. Fractographical overviews at low magnification in Fig 5.7 suggest rather a single crack front rapidly propagating across the material, without being much disturbed by ductile “hurdles”. Such brittle behaviour is actually expected from the high connectivity and the high volume fraction of the microstructural configuration. But then we should explain why an overall yielding with non-negligible UE is still measured in W70% at 300°C and 550°C (cf. Fig.5.19-top). First, we may think that the spring effect of the skeleton could be active in simulations this time, since the W-skeleton is well connected and micro-rotations would be in principle allowed. However, due to the high modulus of W, we are beyond failure conditions already at quite low values of composite-UE (~0.5%, as shown in Fig. 5.15). Therefore, we cannot explain ultimate strains up to 2% (4 times larger) with an elastic collective deformation of the W-skeleton. An explanation for these large UE for the high W composition cannot be given here. It would require at least a full 3D model of the microstructure in order to verify possible activation of collective plastic deformations in CuCrZr before stress in W reaches limit levels. [7]Another important limitation is given by the absence of a brittle crack propagation model for the W-phase, which has been partially mitigated studying conditions for brittle failure *onset*. Regardless of composition, an embedded propagation model in the IB-FEM framework (based for instance on energy criteria calculated locally and updated at each time-step) would predict the stress re-arrangement after initiation and allow more quantitative statements about the competition of the different failure phenomena involved. It will also allow to simulate the overall extent of the micro-ruptures phenomenon along the tungsten skeleton in 3D and ultimately demonstrate the equivalence with the perfect plasticity assumption.

Finally, since it remains unclear whether the W phase really behaved in a ductile manner at 550°C or not, further experimental investigations are required to identify the effective W-DBTT in composite, the extent of ductility of the W-skeleton and the temperature dependence of the UTS at the W/W sintered interfaces.

---

[7] the temperature effect of the PEEQ-th in CuCrZr could be also verified

Chapter 6

Synchrotron Tomography of Plasma-Sprayed Tungsten

This chapter describes tomography on plasma-sprayed tungsten, which has been carried out with the purpose to generate three-dimensional models of the coating microstructure suitable for finite element (FE) simulation.

Passing through large regions of highly absorbing tungsten while collecting an acceptable signal to noise ratio (S/N) was a demanding experimental task. The generation of 3D models suitable for finite elements calculation was a further major problem to solve requiring advanced signal processing. Large reconstruction volumes (at least [200 µm]^3) were required since the average size of the globular pores was about 50 µm and the volume fraction was highly variable at the mesoscale (one purpose was indeed to allow future investigation of the three-dimensional representative volume element). The very strong absorption of X-rays by tungsten atoms restricted the possible choice among available experimental methods to high-energy *Synchrotron Tomography* (ST). Destructive methods like progressive cutting with focus ion beam (FIB), while offering an even higher spatial resolution in combination with scanning electron microscopy (tens of nm per voxel) are not suitable to reconstruct large volumes (only volume sizes in the order of [10µm]^3 are achievable nowadays in reasonable timescale).

The result is a set of fully reconstructed and segmented volumes of VPS-W coating (including the W/Steel interlayer) at the spatial resolution of 1.4 µm/vx for a total volume of approximately 3 mm^3. While the mayor achievement is in fact the first successful tomographic reconstruction of a PS-W coating system, the mayor limitation is still a relatively poor image quality and a much lower resolution compared to equivalent SEM images, ultimately leading to the exclusion of interlamellar micro-porosity from the final 3D FE models.

The experiment has been performed at the high-energy micro-tomography beam-line ID-19 of the European Synchrotron Radiation Facility (ESRF). Details about the instrumentation and the complex experimental setup are given in [133]. The post-processing analysis has been carried out cooperatively with the staff of the beam line ID-19.

In the following, some basic concepts of computed micro-tomography (µCT) are first intro-

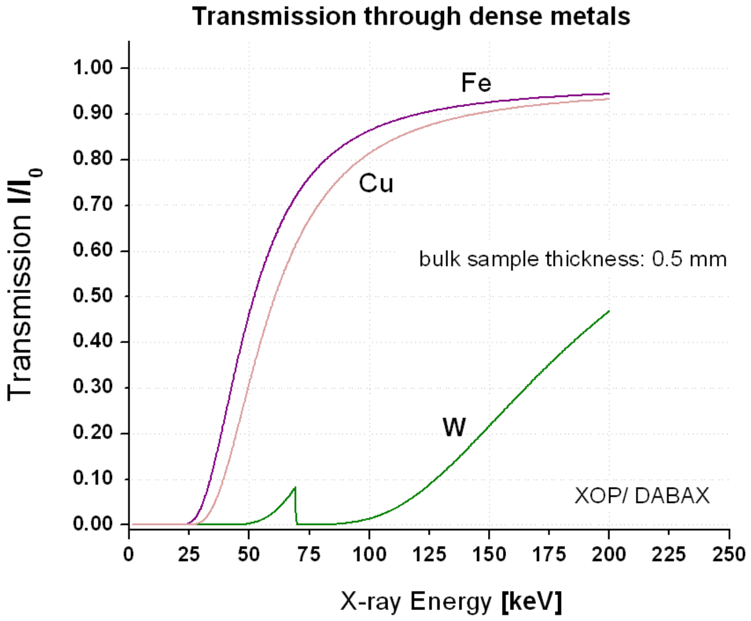

Figure 6.1: *X-ray transmission curves (calculated with the modul XPOWER of XOP [140], using data from the Windt-Database in DABAX) for dense tungsten (W), iron (Fe) and copper (Cu) in the energy window 0-200 keV (low energy K edges are not visible for Fe and Cu because of the sample thickness). One can notice the very low transmission of W below 100 keV, which makes high resolution microtomography on materials with high amount of W particularly challenging.*

duced with a brief theoretical background. For more details the reader is referred to dedicated texts, like [137, 139, 138].

6.1 Basic Principles of Computed Micro-Tomography

Computerized tomography (CT) is a non-destructive imaging technique capable of producing accurate three-dimensional reconstructions of the real microstructure of heterogeneous materials. The principles of CT were firstly developed in the early 1970s [134, 135] for biomedical purposes on biological tissues mainly made of low absorbing elements like carbon and hydrogen. Since then the technique has been constantly improved in spatial resolution and penetration capability.

Micro-Computerized Tomography (µCT) or simply Microtomography is the extension of CT to spatial resolutions lying substantially below 100 µm. It was developed from the early 1980s onwards and greatly benefited from the availability of modern "third-generation" synchrotron sources since the mid-1990s. Synchrotron radiation microtomography (SRµCT) gives access today to spatial resolution down to sub-micrometric length scales [136] and is widely used in materials science and other scientific domains. Nowadays, as we will see with our target material, even for highly absorbing media a detailed tomographic reconstruction of their microstructure is possible.

Tomographic imaging is based on the concept that the distribution of an unknown object function f(r) might be calculated from the ensemble of parallel projections of such function detected at different orientations. In the case of X-ray imaging this unknown object function is usually the spatial distribution of the attenuation coefficient μ(r) (absorption tomography) or the refractive index decrement δ(r) (quantitative phase-contrast tomography).

We will consider here only the first approach based on the absorption of radiation from solid matter. In metallic composites contrast between different topological phases is indeed usually obtained by the strong variation of the absorption coefficient across the different phase constituents.

The attenuation of X-rays in matter is based on several interaction processes at atomic scale between the photons and the electrons in the material, whose global effect, averaged over a large number of atoms, is contained in the *absorption coefficient* μ [1] Hence, μ is in the end strongly dependent on the element atomic number Z [141]. For an ideally homogeneous bulk material μ does not vary spatially and it becomes only a function of the incident beam energy E.

In case of a 3D object with different atomic elements (including void as non absorbing entity) arranged in heterogeneous morphological phases, the spatial function $\mu_E(x, y, z)$ as given for a fixed energy E, corresponds to a geometrical fingerprint of the 3D internal structure of the object. [2]

In can be easily shown that for a fixed energy, the relation between the incoming (I_0) and transmitted (I) beam intensity and the object function $\mu_E(x, y, z)$ is (z being parallel to the beam axis):

$$-ln\frac{I}{I_0} = \int \mu_E(x, y, z)dz \tag{6.1}$$

The solution of this equation for μ_E (or simply μ) from the knowledge of a single measurement of I/I_0 is not possible. However, it becomes possible when several different measurements of such kind are performed at different angles until the full spatial information on$\mu(x, y, z)$ can be derived from its partial 2D projections. In mathematical form the relation between the object function μ and its projections $F(\phi, p)$ can be written as (considering the cylindrical symmetry of the problem[3]):

$$\mu(\mathbf{x}) = \frac{1}{(2\pi)^2}\int_0^\pi \mathrm{d}\phi \int_{-\infty}^{+\infty} \tilde{\mathrm{F}}(\phi, \mathrm{h})\mathrm{e}^{-\mathrm{iu}\mathbf{n}\cdot\mathbf{x}} \left|\mathrm{h}\right| \mathrm{dh} \tag{6.2}$$

---

[1] Such processes are known as *photoelectric effect* and *incoherent (Compton) scattering.*

[2] The medium and the function μ are here approximated as continuous. This is valid up to a certain spatial scale fairly above the atomic scale.

[3] and assuming a continuous variation of the projection angle ϕ , i.e. an infinite number of projections

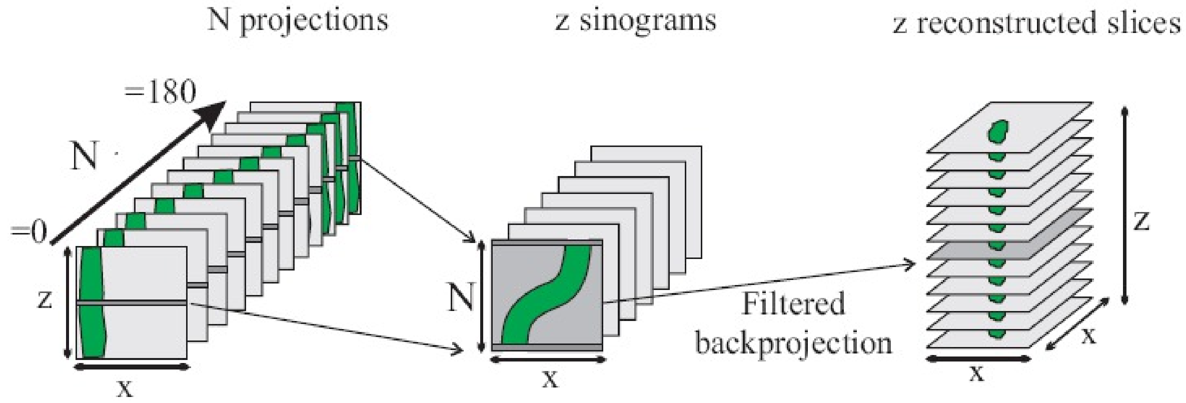

Figure 6.2: *Reconstruction of a three-dimensional object: N two-dimensional projections are recorded while the sample is rotated stepwise over 180°. Each projection contains z lines and x columns. The projections are reorganized into z sinograms (Radon transform of one object layer), containing N lines and x columns and the volume (z slices) is then reconstructed slice by slice. Here, an homogeneous material with the same attenuation coefficient across its volume (in green) is assumed. Image taken from [139].*

where $\tilde{F}(\phi, u)$ means Fourier transformation in the frequency space of the projection function $F(\phi, p)$, and $\mathbf{n}$ indicates the normal vector of components $[sin(\phi), cos(\phi)]$, such that the first integral is solved along a line $u\mathbf{n}$ in the frequency space. The variableϕ indicates the projection angle while p the distance from the origin of the projection line in the space domain. This is the famous *filtered back-projection* equation [138]. We note here that behind this there are several mathematical steps, involving an important operator, the so called *Radon transform* $F(\phi, p)$, and the *projection slice theorem* which assures the equivalence between $F(\phi, p)$ and the slice function $\mu(x, y)$ in the frequency space.

In practical terms, tomographic reconstruction involves basically three steps, as shown in Fig. 6.2 :

1. Acquisition of N two-dimensional figures of transmitted intensity I at different angles (projections of the object function µ), while the sample is rotated stepwise for 180° around an axis perpendicular to the X-ray beam.

2. Generation of z images (so called sinograms[4]) from stacking up projection lines extracted over the N projections at a fixed height z.[5]

3. Tomographic reconstruction performed slice by slice from application of the inverse Fourier transformation (back-projection equation 6.2) on the sinograms.

---

[4] also called “Radon transform”

[5] some modern numerical techniques as implemented in the most recent reconstruction softwares actually skip this step, however it is shown for clarity.

6.2 Tomography of Plasma Sprayed-Tungsten (PS-W)

6.2.1 Low Transmission of W

High-Z metals like tungsten strongly absorb X-rays [141]. This means that the radiation containing the information necessary for the reconstruction (in the form of the above mentioned projections) is collected with low intensity and the generated reconstruction is affected by the poor signal to noise (S/N) ratio, eventually degrading in spatial resolution.

The strong absorption of tungsten compared to the other metals is clearly demonstrated in Fig. 6.1, which shows the comparison of the tungsten transmission curve with that of iron (main constituent of steel). Transmission across a homogeneous material is related to the attenuation coefficient μ(E) by the Lambert-Beer's law:

$$T(E) = \frac{I}{I_0} = e^{-\mathrm{\mu(E)^{*}t}} \tag{6.3}$$

Since mechanisms of absorption/transmission strongly depend on the energy E of the incoming X-ray beam, transmission curves are shown as function of E for a given thickness t of the sample. The energy interval shown (0-100 keV) is that of the high resolution synchrotron beam-line; higher energies are not considered, since they imply a considerable loss in spatial resolution. One can immediately notice the very poor transmission of W for 0.5 mm sample thickness: the suitable energy window is restricted between 50 and 70 keV with a peak in transmission of about 8%, almost a factor of 10 lower than for the iron in the same energy range and for the same sample thickness.

Limited Sample Thickness

The dependency of the transmission coefficient on the sample thickness follows an exponential rule (Lambert-Beer's law, equation 6.3). The simple intuitive interpretation is: at a given energy, the higher the sample thickness, the lower the intensity of the signal detected behind the sample. This trend is evident in Fig. 6.3 where different transmission curves are calculated for different thicknesses of a bulk-W specimen. When doubling the sample thickness from 0.25 to 0.5 mm, the transmission peak is reduced from 30% to nearly 10%. Then it dramatically drops to only 3% at 1 mm.

The calculated curves in Fig. 6.3 refer to 100% dense tungsten. For tungsten with a porosity around 20% the exact upper limit in thickness was unknown, but expected to be not far above 0.5 mm. This eventually resulted in a strong limitation on the sample size and geometry. The exact size value was planned to be found during the preliminary campaign in order to optimize the sample design for the real measurement. Using a multi-step conical geometry (shown in Fig. 6.7 and 6.4) we were able to test for diameters continuosly increasing from 0.25 to 1 mm, searching for the limit sample thickness (by which the transmission was still sufficient for the tomographic data to be of an acceptable quality). The value found turned out to be between

0.60 and 0.65 mm (depending on sample porosity which, after segmentation was varying in the range of 21 to 24%).

The Monochromator

When the synchrotron beam comes out from the wiggler or undulator source in the storage ring, it has a wide spectrum of frequencies (corresponding to a spectrum of photon energies and X-ray wavelengths). This spectrum firstly needs to be filtered to a small bandwidth by a *monochromator*. Monochromatization is necessary to ensure high quality of the data. Generally, the spatial resolution of X-ray images will improve as the energy bandwidth is narrowed down. In the present case, the center of the energy distribution had to be chosen between 50 and 70 keV in order to get some non-zero transmission, as previously mentioned. On the other hand, narrowing the spectral bandwidth means reducing the photon flux, which may severely affect the signal-to-noise ratio of the images. In this study, a multilayer monochromator was used to reduce the spectral bandwidth to approximately 1%.

The Suitable Energy Window

Unfortunately, because of the efficiency and spatial resolution of the detector, we had to operate in the 50 keV region (gray zone in Fig. 6.3) with an upper limit of 52 keV. The scintillator used in the detector loses both efficiency and spatial resolution quite rapidly if the energy is increased beyond that limit. This fact further decreased the suitable transmission level to a factor of 6 (compared to the peak values at 70 keV). Hence, the suitable range in thickness was between 0.25 mm and 0.5 mm. The lower limit was caused by sample cutting feasibility and the requirement of relatively large volumes.

The Scattering Problem

A strong *internal scattering* of the beam associated with low transmission and strong absorption at 52keV occurred at the material internal boundaries (between tungsten and pores). In the end scattering was the most serious problem affecting the quality of the reconstruction. Its visible effect was that voids in tungsten appeared gray rather than completely black with a strong dependence on their size. Scattering also affected spatial resolution. This factor caused the smallest pore structures to be undetectable and the other structures to be difficult to segment (see later). Without providing details of the complex scattering phenomenon itself, we believe that the effect was mostly probably caused by small-angle coherent scattering of the X rays on the smallest pore structures (whose thickness goes down to the sub-micrometer scale). However, an inelastic scattering may also play a role and further investigation are needed to better understand this phenomenon in porous tungsten.

In this study we limited ourselves to try *a posteriori* solutions to eliminate “scattering artifacts” in the reconstructed volumes through the application of special signal processing filtering during segmentation (Section 6.3).

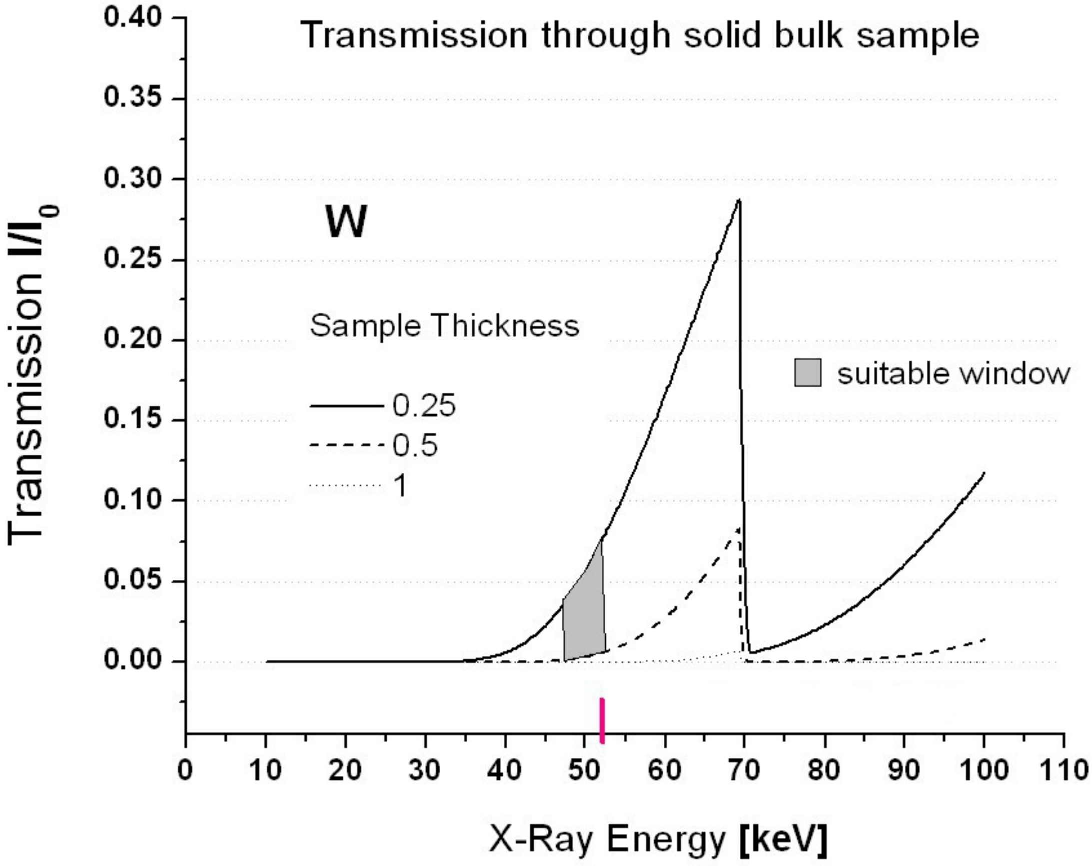

Figure 6.3: *Different transmission curves for different sample thicknesses in case of 100% dense tungsten. In gray it is indicated the accessible transmission region for the experiment. The pink line indicates the selected energy channel after monochromatization (52 keV +-1%).*

The Beam Hardening Problem

After the beam monochromatization, the frequency profile is sharper but still has a bandwidth of about 1%. Within this energy window X-rays of lower energy are absorbed stronger than those of higher energy. They are also progressively removed from the beam by increasing penetration depth across the material: the beam inside the material becomes progressively "harder" and the reconstructed attenuation coefficient is affected by dependency on the thickness of material, ultimately causing undesired “beam hardening” artifacts in CT images. Depending on the exact experimental setup there may also be a substantial fraction of radiation outside the expected bandwidth, which aggravates the phenomenon. In particular, when a multilayer monochromator is used lower-energy photons can be present in the beam because of total external reflection on the surface of the multilayer mirror.

For tungsten samples with thickness between 0.25 and 0.75 mm and photon energies in the range between 50 and 70 keV, beam hardening was expected to be a serious problem because of the low intensity transmission of the samples. A careful choice of attenuator sheets in the X-ray beam path ensured minimal presence of low-energy photons in the beam. Moreover, the low

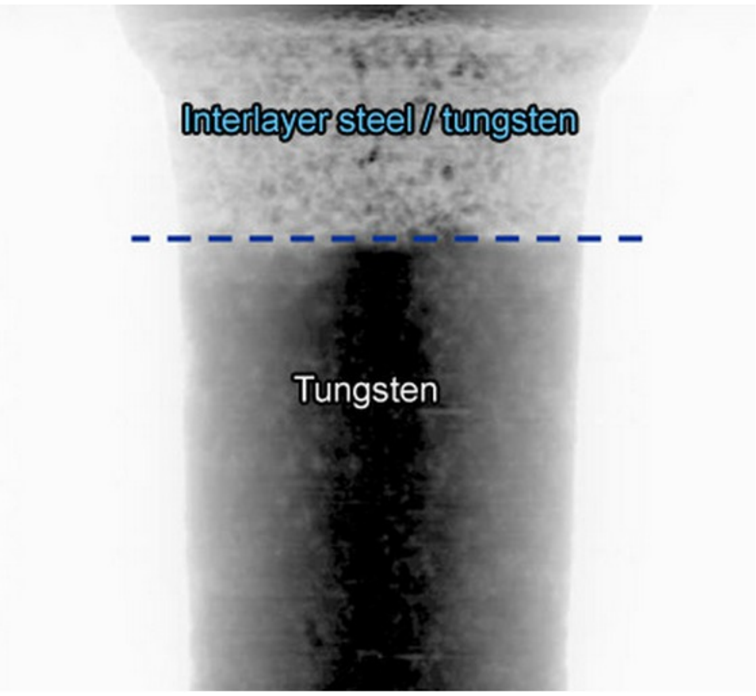

Figure 6.4: *Projection radiograph of a VPS-W sample. The beam hardening effect is visible (dark areas correspond to strong absorption in logarithmic scale). The dashed line indicates the transition zone between the porous tungsten and the interlayer zone, consisting of steel with tungsten precipitates.*

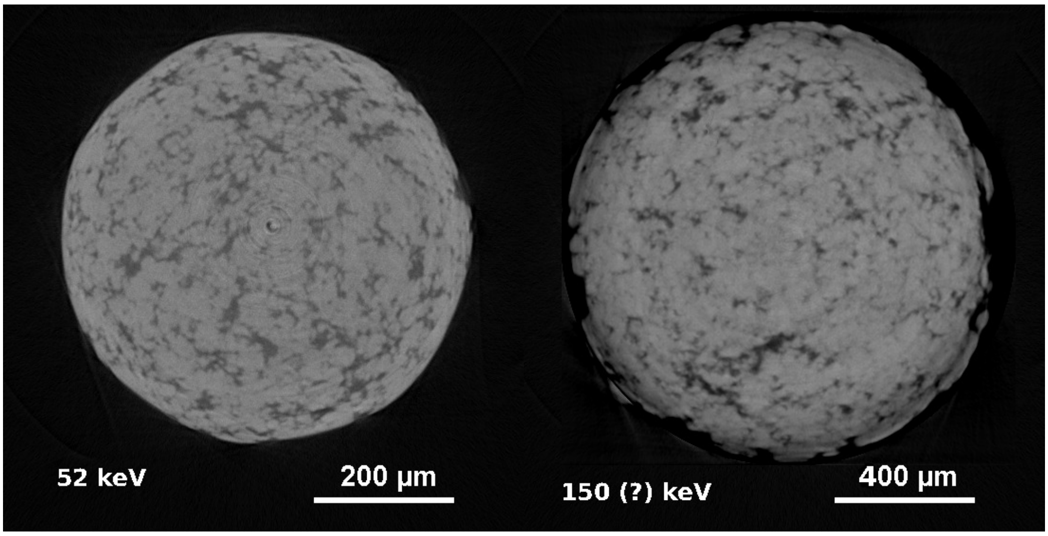

Figure 6.5: *Comparison of the preliminary reconstructions at two beamlines ID-19 (left) and ID-15 (right). A larger penetrable diameter (factor of two in the magnitude) obtained at ID-15 at very high energy implies a decreased final image resolution. While a more precise comparison should be made on the segmented slices, this gap is about 35% (2.2 µm/px instead of 1.4 µm/px). The overall image quality becomes improved at 52keV with pores being better defined without concentric degradation of contrast (thanks to reduced beam hardening)*

sample thickness (already reduced as much as it was compatible with manufacturing technology in order to allow sufficient transmission) further helped in limiting the beam hardening artifacts which could be largely if not fully eliminated.

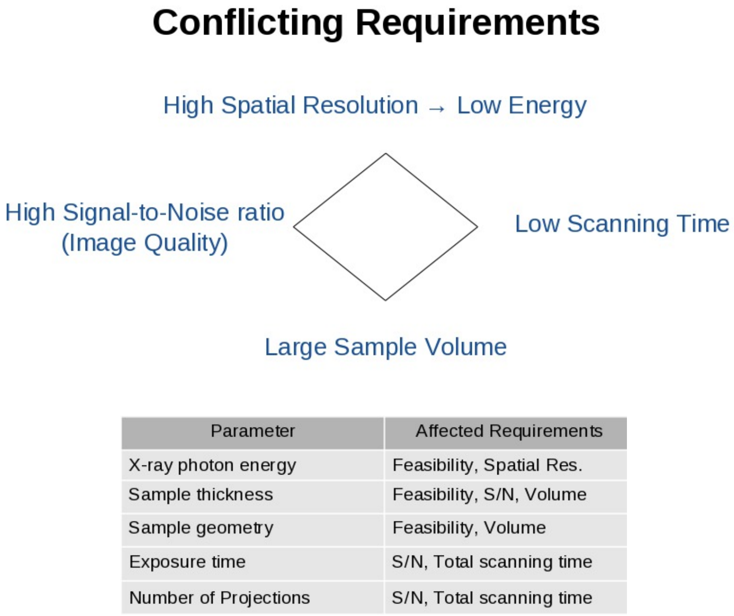

Parameter	Affected Requirements
X-ray photon energy	Feasibility, Spatial Res.
Sample thickness	Feasibility, S/N, Volume
Sample geometry	Feasibility, Volume
Exposure time	S/N, Total scanning time
Number of Projections	S/N, Total scanning time

Figure 6.6: *The schematic representation of the conflicting requirements (a) and the parameters governing such requirements (b) during a CT-measurement on plasma-sprayed tungsten. The parameters firstly constrained to certain limits by experimental feasibility should then be optimized to improve the outcome of tomography in terms of the image quality and RVE.*

6.2.2 Optimizing Beam Parameters and Sample Geometry

The challenging task of µCT on plasma-sprayed tungsten was to maximize image quality and total reconstructed volume while dealing with the limitations previously explained. This ultimately caused *conflicting requirements* (Fig. 6.6).

As for image quality, high resolution was required in order to catch morphological details of the porous network of VPS-W at the micrometer scale. This requirement was actually conflicting with that of operating at the highest possible energy to maximize transmission, and eventually lead to choose an intermediate energy beam-line (ID-19, 10~100keV) instead of a very high energy beam-line (ID-15, 100-300keV). A comparison on preliminary reconstructions on both beamlines (Fig. 6.5) clearly shows the effect of better resolution at 52keV (1.4µm/px) in terms of improved level of morphological detail. However, a decreased beam energy has an impact on the maximum sample thickness and the size of the reconstructed volume (approximately the half of that accessible at very high energy).

Another important requirement was to keep the signal to noise ratio (S/N) as high as possible in order to allow later a better segmentation of the porous phase (see section 6.3). The S/N is mainly influenced by the exposure time at a given angle which should be maintained sufficiently high to assure a good statistics at the detector (the higher the exposure time, more photons can be collected, up to detector saturation). On the other hand, a fairly limited total time per scanned sample was also desired to allow several preliminary attempts and to maximize the total reconstructed volume (over different scanned samples).

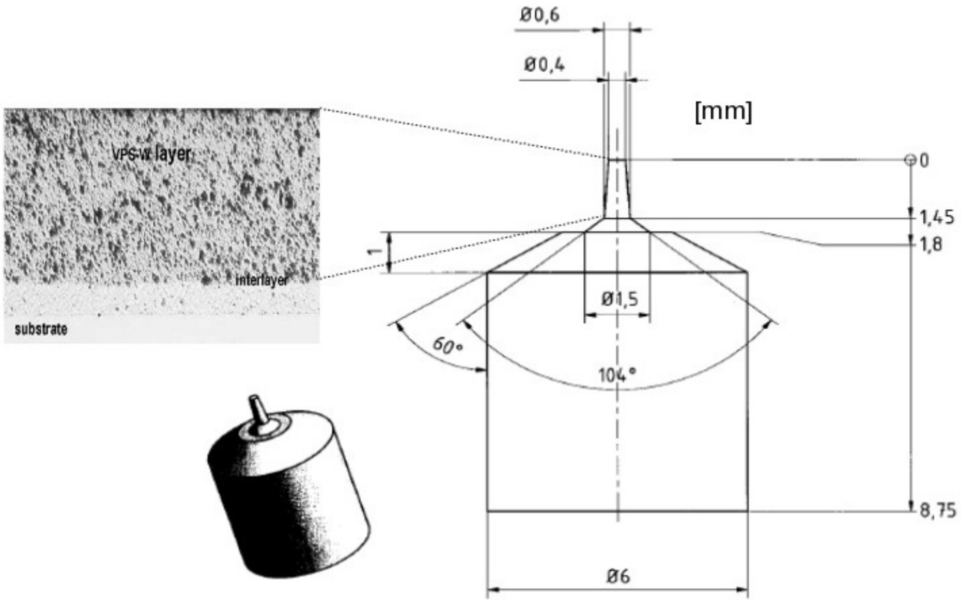

Figure 6.7: *Sample geometry of PS-W for the CT measurement (PS coating on top, interlayer in the middle and large steel substrate on bottom). The whole sample was cut top-down continuosly with Wire Cut Electrical Discharge Machining by Stangl&Co, Germany. The original coating was provided by PLANSEE, Austria.*

Sample Geometry

The only chance to scan a representative region of plasma-sprayed tungsten was to keep the sample size (parallel to beam direction) sufficiently low. As previously mentioned this limit turned to be around 0.5 mm for dense tungsten, but for 20% porous tungsten it could be higher and it was difficult to predict precisely. At the same time the sample geometry should allow the largest possible volume to be accessible by that constraint. Moreover, in order to simplify post-measurement processing, full axial symmetry was preferred.

The sample geometry should not only satisfy measurement requirements but the feasibility of sample preparation itself. The chosen metal cutting technique (see later) could achieve a precision of 0.1 mm. Avoiding brittle failure across the sample implied a minimum outcoming sample diameter (in the upper part of the sample) of 0.25 mm. However, since PS-W is only manufactured as a coating, a further stringent limitation was dictated by the coating thickness (1.8 mm).

The sample should be finally designed to allow montage on the rotating support (Ø=6mm) to be easy and stable, possibly avoiding direct contact to fragile tungsten.

All these requirements were fulfilled with a multi-stage conical geometry, as shown in Fig. 6.7. The conical geometry with diameter continuosly varying with the height of the sample allowed to test the maximum penetration depth[6] at 52keV. This limit turned to lie between 0.6 and 0.65 mm (as previously mentioned).

---

[6] after which only noise (no signal) was detected behind the sample

Sample Preparation

In the first step of the sample preparation a cylindrical blank was cut out of the material. This was realized by a wire cut electrical discharge machining, which ensures the required precision. Subsequently, the conical cross-section was achieved by profile grinding. To this end, a purpose-built *grinding disc* with the required conical profile was created. Thus, it was possible to grind conical cross-sections of PS-W up to 0,25 mm in diameter while avoiding brittle failure across the sample. During the profile grinding process the most critical stage was grinding across the interlayer zone (made of tungsten, steel and large voids) while keeping a very thin conical section (Ø~0.6mm). A large amount of samples were broken when brittle fracture propagated at the interlayer or along the tungsten region slightly above it. Only 10 specimens were successfully prepared over more than 70 attempts.

Volume Rendering

Volume renderings[7] of tomographic reconstructions of PS-W coating and W/Steel interlayer are shown in Fig. 6.9 and 6.9 respectively. The pictures were obtained with the rendering software VGStudioMax v2.0. The complex porous network of PS-W coating as well as of the three phases (pores, W, Steel) of the interlayer region between PS-W coating and steel substrate are clearly visible. In Fig.6.9 the three morphological phases have been separated in order to better visualize their 3D arrangement. Surprisingly, a relatively high amount of porosity (estimated to be about 8%) was discovered at the interlayer. This clearly indicates a mechanical weak point of the coating system (coating+interlayer+substrate), which would eventually lead to delamination under thermomechanical load. While future investigations will comprise 3D finite element models of the full coating system we will limit our investigation in the present work to the stand-alone PS-W coating.

6.3 Tomographic Segmentation of PS-W

By *image segmentation* (or *phase image segmentation*) we mean an unambiguous identification of morphological phases inside a digital image (2D or 3D). A digital image corresponds to a discretization of space, structured by a regular grid of basic elements (voxel in 3D) to which a certain value (color) has been assigned. An unambiguous identification means a quantitative identification, i.e. that a numerical value (usually an integer) uniquely corresponding to a certain phase is assigned to each pixel which is supposed to belong to that phase. This operation completely defines the spatial phase arrangement of the material phases.

In tomographic images of Plasma-Sprayed Tungsten there are basically two morphological phases to be identified: pores and tungsten (since spatial resolution and S/N was too low to

---

[7] with “volume rendering” we mean here image generation from a tomographic model by means of algorithms which optimize the boundary surfaces of a volume for visualization purposes only. It also includes selecting the proper viewpoint, texture, lighting and shading effects. Rendering does not output any quantitative information about the phase arrangement but it is useful to visualize the 3D phase arrangement.

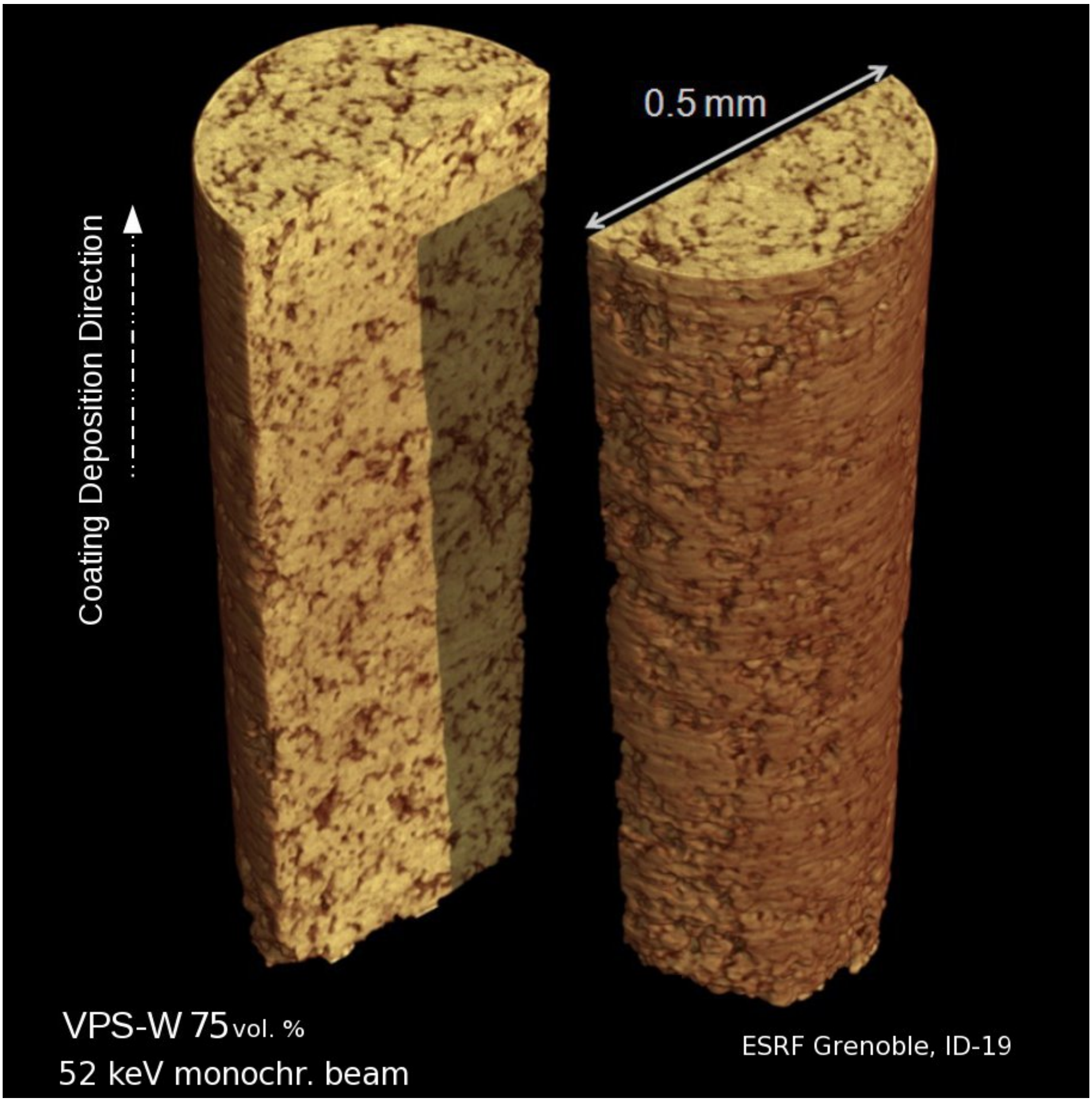

Figure 6.8: *Volume rendering of the 3D microstructure of vacuum plasma-sprayed tungsten (VPS-W) as reconstructed from a synchrotron tomography measurement at 52 keV with monochromatic beam (spectral width ~1%). One can distinguish the highly irregular porous network (in brown) and its random arrangement in space.*

allow identification of the contact-zone as third phase). Since a tomograph consists of piling up planar slices, this operation is also performed slice by slice. Before segmentation takes place each pixel of the starting tomographic slices gets a color value the gray scale: to pixels corresponding to the pores, for instance, are assigned several slightly different values of the gray-scale interval close to dark-gray and black. After segmentation, all pores get an unique integer value and the same happens for the spatial domains of tungsten so that it becomes possible to quantitatively analyze their volume fraction and measure other morphological parameters. As it has been shown in the previous chapter a segmented image is also the requirement for the further adaptive mesh generation in order to get FE models suitable for simulations.

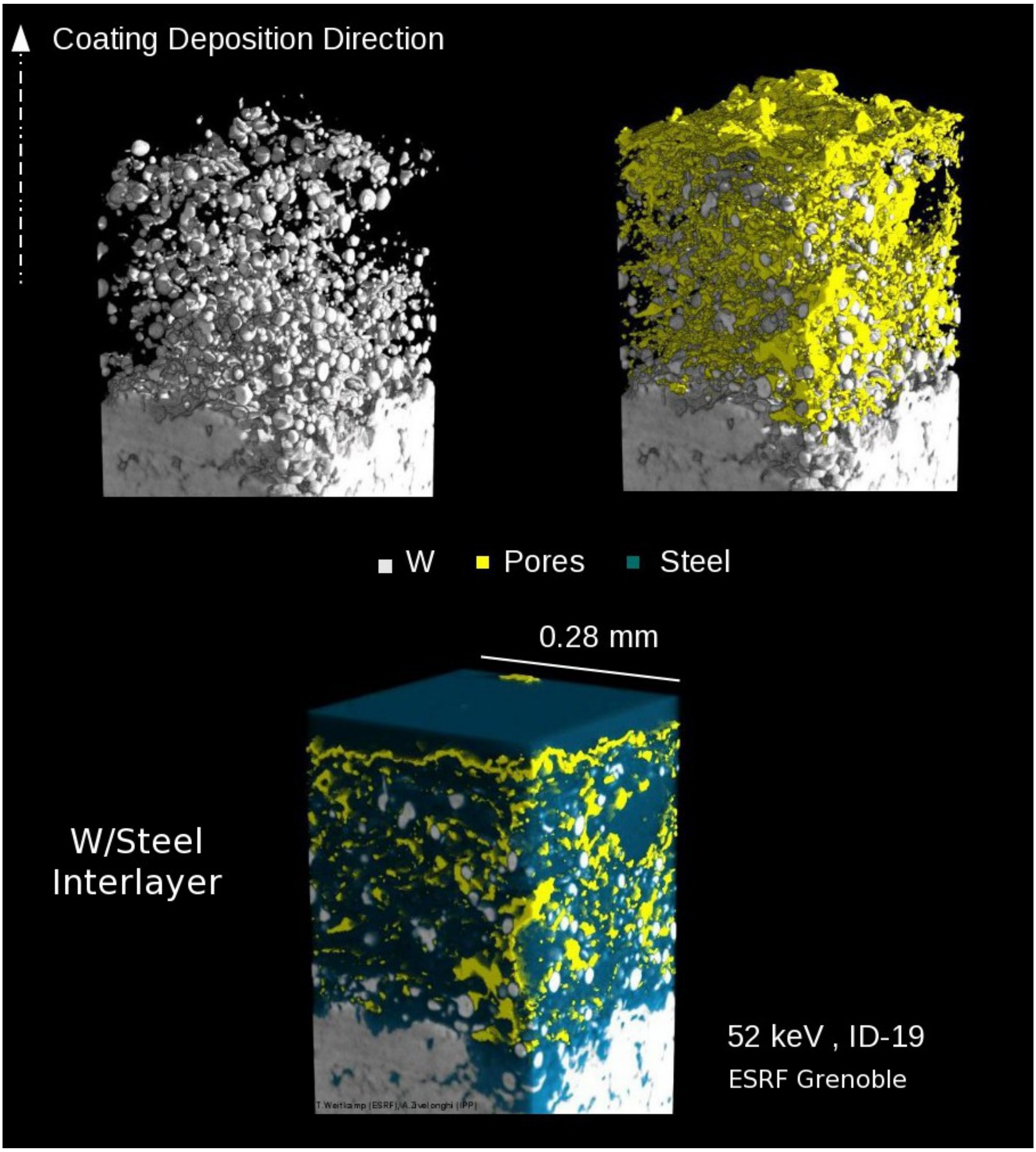

Figure 6.9: *Tomographic renderings of the W-Steel interlayer region. Top-left: the W-phase in the interlayer and part of the VPS-W coating. Top-right: the porous phase (yellow) of the interlayer region. Bottom: all the phases of the reconstructed interlayer region where the W particles and the porous phase are surrounded by the EUROFER-steel matrix (in blue)[143].*

Image filtering

Usually segmentation consists of two steps: *image filtering* and *thresholding*. The first operation aims at preparing the image so that it becomes possible to set a unique threshold value on the gray-scale pixel/voxel distribution in order to produce the segmented image. In other words, the original gray-scale distribution reduces the number of color values to the number of phases. Filtering can be skipped only in the case of very good image quality, where segmentation can be performed directly from the original pixel distribution. However, as in the case of PS-W, the low S/N ratio and the presence of artifacts in the original tomographic reconstruction required the application of several digital image processing algorithms (filters) to prepare the image. In the most challenging cases an alternative to filtering is a manual segmentation, extremely time consuming and possibly affected by human error. This option can only be considered for limited volumes (or a limited number of slices) and was therefore discarded.

The special filters used to handle the problematic segmentation of plasma-sprayed tungsten were developed in cooperation with beam-line ID-19 at ESRF Grenoble.

Even with an optimized beam parameters (section 6.2.2) the quality of the images was relatively poor compared to standard tomographic reconstructions on less absorbing materials. Scattering and beam hardening, as previously described, caused a number of artifacts affecting the tomographs which should be removed or at least reduced before thresholding. The most important ones were:

a. *Ring artifacts* (Fig. 6.10), which are most probably caused by the punctual defects in the optics. These features, whose contrast and thickness are highly variable, are typical of SRµCT.

b. Concentric variation of the average gray-scale intensity caused by beam hardening

c. Deviation of the value assigned within the porous phase from the average gray scale value assigned (actually it should be black for zero-density non-absorbing medium, but it was dark-gray because of the scattering). This deviation was not homogeneous across the whole porous phase mostly affecting thin pore structures. This kind of artifact was an effect of internal beam scattering at the pores/tungsten interfaces.

d. Variation of the slice grayscale distribution along the z-axis (independent of the local fluctuations of porosity) due to the beam inhomogeneities along the same axis.

The global effect of b and c on segmentation is shown in Fig. 6.11. The contrast of thin pores can be so low that their pixels get values usually belonging to the tungsten phase. This makes segmentation of such pores only possible at high threshold levels (central picture of Fig. 6.11) but at the expense of an incorrect subtraction of pixels to the tungsten phase and with the spreading of additional noise.

Artifacts removal has been handled by dedicated image processing algorithms, which helped to substantially reduced all the mentioned problems. In particular b,c, and d required non-standard “splitting” filters, operating in the frequency domain, splitting each slice into a low and high band signal and hence applying independent filtering. The accurate description of the splitting filters requires advanced mathematics from the signal processing theory and is not given here; for further details the reader is referred to [142].

Setting the proper threshold value

Even after the artifacts were removed the issue of choosing an appropriate threshold value remained unsolved. Slice pixel distributions were still too spread to allow the determination of the threshold value only from their shape (sum of the unknown phase sub-distributions

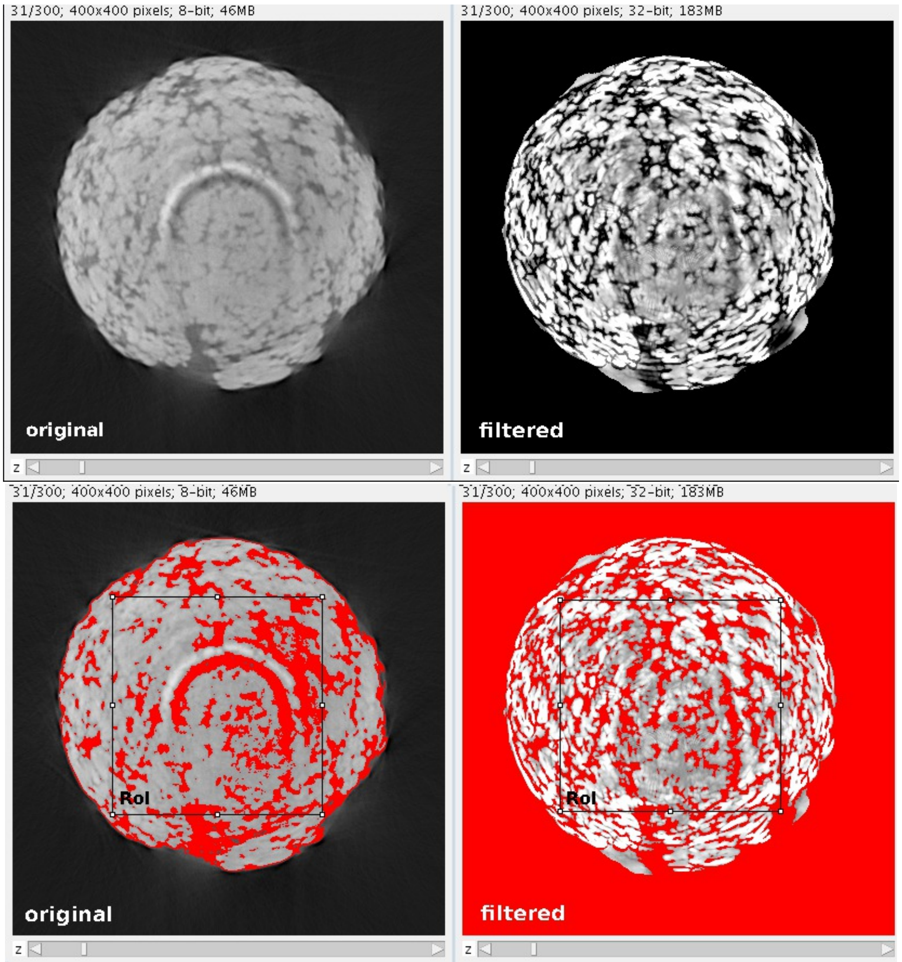

Figure 6.10: *Example of ring artifacts removal by post-processing filtering on tomographic slice. The red zone inside the region of interest (RoI) indicates the segmented porous zone within tungsten. In the original picture a nearly central thick ring is affecting the correct segmentation of pores, while after filtering it has been successfully removed.*

of pores and tungsten). The reason behind this is that sub-distributions were still not well separated in a bimodal total distribution and the overlapping zone between them was too high even after filtering. As a consequence of this only a *variable* grayscale interval with a fixed lower boundary (black value) and an variable upper limit (in the dark gray zone)[8] could be identified for the final segmentation of the porous phase. Such variable interval resulted in a non-negligible uncertainty of the phase boundaries. In order to reduce this uncertainty and assure an acceptable segmentation additional inputs from independent measurements were needed. To this extent we compared the tomographic slices with the corresponding cross-sectional images from scanning electron microscopy taken at a similar resolution[9] (Fig. 6.12). As evident, a much better contrast and S/N ratio characterizes the SEM image. The idea was therefore to take the volume fraction calculated from SEM images as reference parameter to set a precise

---

[8] such large interval was found by slice inspection after thresholding, looking at the macropores boundaries

[9] SEM specimens were independently prepared but extracted from the same coating of the tomographic samples.

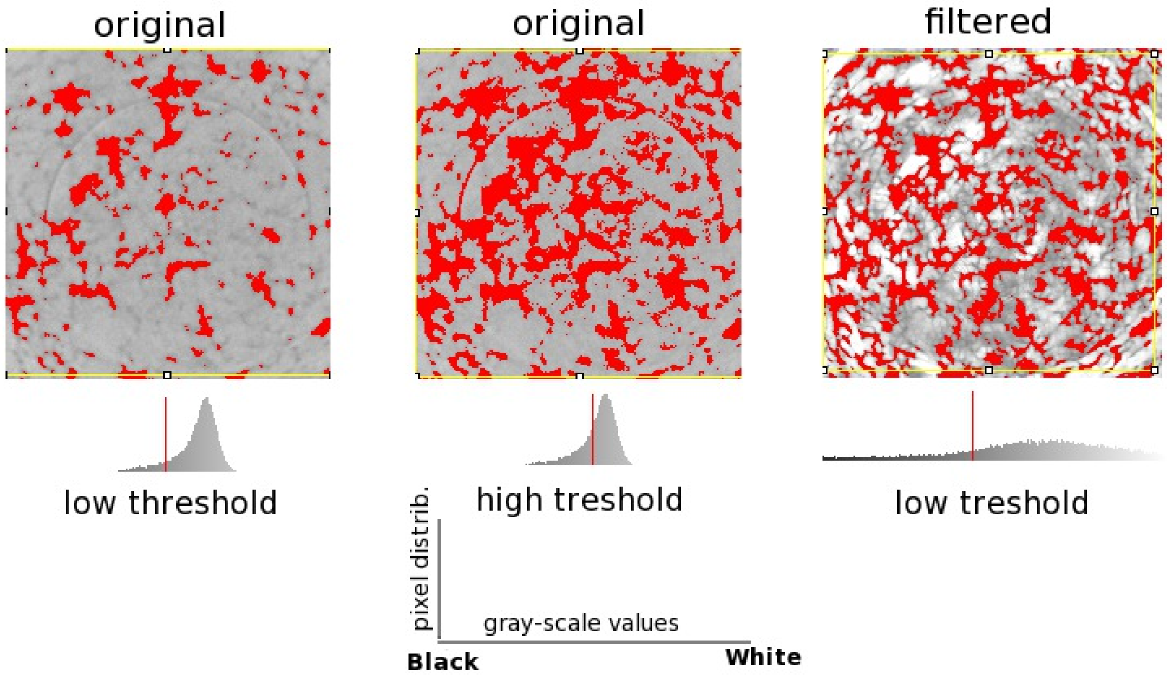

Figure 6.11: *Effect of the split frequency filter on the removal of beam hardening and scattering effect. Because of these phenomena thin pores and pore boundaries cannot be properly segmented from the original picture: either some of them are missing (by choosing low threshold levels) or, when trying to include them (towards higher threshold levels) other pores are overestimated in size and noise develops across the section. After the filter has been applied, a suitable threshold level can be found which includes almost all pores detectable, while limiting artifacts (rings and overestimation of boundaries).*

threshold on (filtered) tomographs[10].

As for the morphological comparison, the most important difference is about the crack-like interlamellar porosity, which is clearly visible (and segmentable at higher magnification) in the SEM image but barely detectable in the tomographic slice (Fig.6.12). Despite the efforts in beam optimization and image processing it was not possible with the present experimental setup to include such feature in the final segmented tomographs of PS-W. On the other hand, thanks to the special segmentation filters, macropores could be well segmented despite the poor tomographic quality. Reference porosity should therefore be calculated from the high quality SEM images, through an isolation of the globular pores. To achieve this, the small interlamellar porosity was first removed from the SEM images through a sophisticated image processing procedure [11]. After adjusting the threshold, the segmented models were then suitable for the subsequent mesh generation (FE models). This final step required 3D image-based mesh generation techniques, which were explained in the section 4.2.

---

[10] with the implicit assumption, that 2D and 3D porosity of the same random structure must have the same value. This assumption is valid when 2D porosity is calculated as average over a number N of slices of the same 3D structure, for N sufficiently high.

[11] identification of all connected objects and removal of those objects with a low ratio between principal moment of inertia and whose area was below the average area estimated for small crack-like structures.

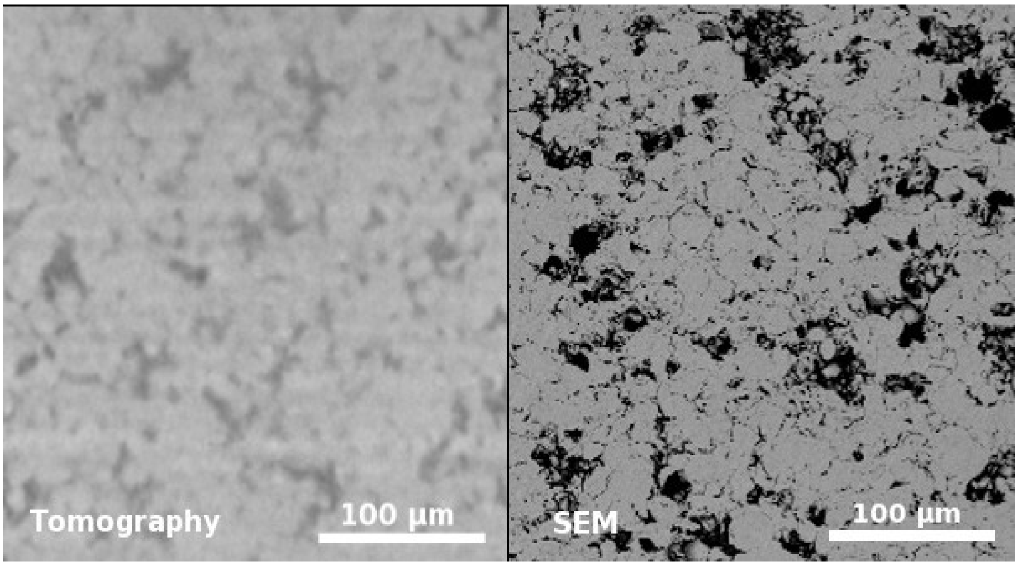

Figure 6.12: *Comparison between a tomographic slice (left) with an image taken at approximately the same resolution with a Scanning Electron Microscopy (right). Thanks to a better S/N ratio in SEM, small interlamellar porosity is also visible between macro-pores. Both images are showing an equivalent material region (300µm*300µm).*

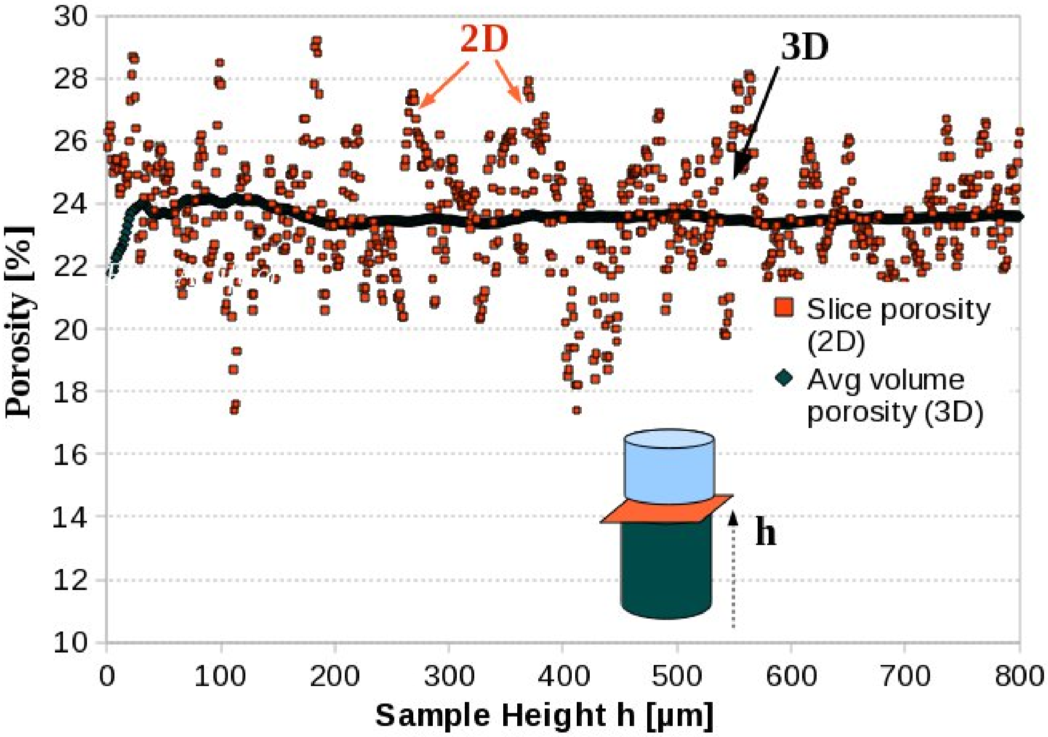

Figure 6.13: *Local fluctuations of slice porosity compared to volumetric sample porosity as function of the sample height h.*

Chapter 7

Image-Based FEM on Plasma-Sprayed Tungsten

This chapter illustrates the results of thermal and mechanical analysis on models of vacuum plasma sprayed tungsten (VPS-W) acquired via the image-based (also referred here as direct mapping (DM) technique. Two dimensional models were generated from high resolution SEM images (Section4.1), while 3D models were generated from computed microtomography at high energy (Section4.2). The original material stem from a previous VPS-W deposition campaign on Eurofer-Steel substrate conducted at PLANSEE (Austria).

Results of mechanical analysis are presented with emphasis on the comparison between different models and stress concentration at failure. Results of thermal analysis focus on morphological decomposition and statistical analysis of the representative volume elements (RVE). Due to the extremely complex random morphology of VPS-W and the critical absorption of tungsten for the generation of 3D models, the results can be considered an innovative application of the image-based finite element method (IB-FEM).

7.1 Models

The type of direct mapping models used are illustrated in Fig. 7.1. As previously discussed in chapter 4, the main differences between 2D and 3D models, apart from dimensionality, is to be found in the mapping resolution (0.2µm/px for planar models versus 1.4µm/vx - 7 times lower - for the 3D case). For this reason the planar model are named image-based high Resolution - IBHR.

As for 3D models, because of the low resolution and the limited tomographic quality due to high X-ray absorption of W, it was unfortunately impossible to include important morphological features like interlamellar gaps and Contact Zone (for more details about 3D segmentation, cf. 6.3).

The number of spatial dimensions is not the only parameter characterizing different models. As illustrated in Fig.7.1, within 2D models we further distinguished standard ones (2D

IBHR) from those including the Contact Zone (2D IBHR-CZ). Here internal boundaries between lamellas (partially in contact) were identified as an independent morphological phase with its own material properties. To the CZ mesh elements a reduced stiffness and a reduced thermal conductivity (with reference to bulk W) have been assigned (reduction coefficients q and k respectively, see section 3.3.3).

As for 3D model generation, due to mentioned computational constraints, we considered only low mesh-density models based on smoothing and simplification of the starting isosurface (3D-DMS models in Fig. 7.1).

7.2 Mechanical Analysis

7.2.1 Elastic Regime

The elastic part of computed stress-strain curves under tensile load is shown in Fig. 7.3. Here, planar IBHR models derived from SEM images were used. Since the material is transversely isotropic in statistical sense, two sets of BC were separately implemented to compare the response along the principal directions of the coating: parallel (OY) and perpendicular (OX) to coating deposition direction. The first BC (with reference to Fig. 7.1a) is obtained prescribing the y-component of the strain at TOP-nodes while fixing BOTTOM-nodes in the same OY direction; the second BC is implemented prescribing the x-component of the strain at RIGHT-nodes while fixing LEFT-nodes in the same OX direction.

In Fig. 7.3, one can first notice a high scatter in the elastic slope of the curves over the 6 samples considered (about ±35% for both directions, referring to the average value). The average Young's modulus values (55 and 66 GPa along OY and OX axis respectively) are well aligned to previous experimental estimations [97] via three and four-points bending tests (54 GPa for the horizontal component). The mismatch between our predictions and the experimental value is mainly to be ascribed to the different modeling approach used for evaluating the results of experimental bending test. While bending obviously induces both compressive and tensile stress fields along the coating, two different stiffnesses (for compression and tension respectively) should have been considered. While this distinction is observed with the IBFEM approach (here only limited to estimations of tensile stiffness), this was not considered in [97].

During IB-FEM calculations residual stress (RS) was neglected, although this feature is supposed to occur in any plasma-sprayed coating as result of quenching and CTE's mismatch between coating and substrate [97]. However, since the average RS is a constant to be added to or subtracted from the total average stress and strain fields, it does not really affect the estimation of Young's modulus, as long as deformation occurs within the elastic regime. Estimation of residual stress is of interest to assess the elastic limit of the coating. In [97] we can find an estimation of the average residual stress for PS-W deposited on steel substrate ranging (across the coating) from -40 to 50 MPa (depending on coating thickness, quenching stress values and cooling temperature during manufacturing). Since this values are fairly below the ranges of

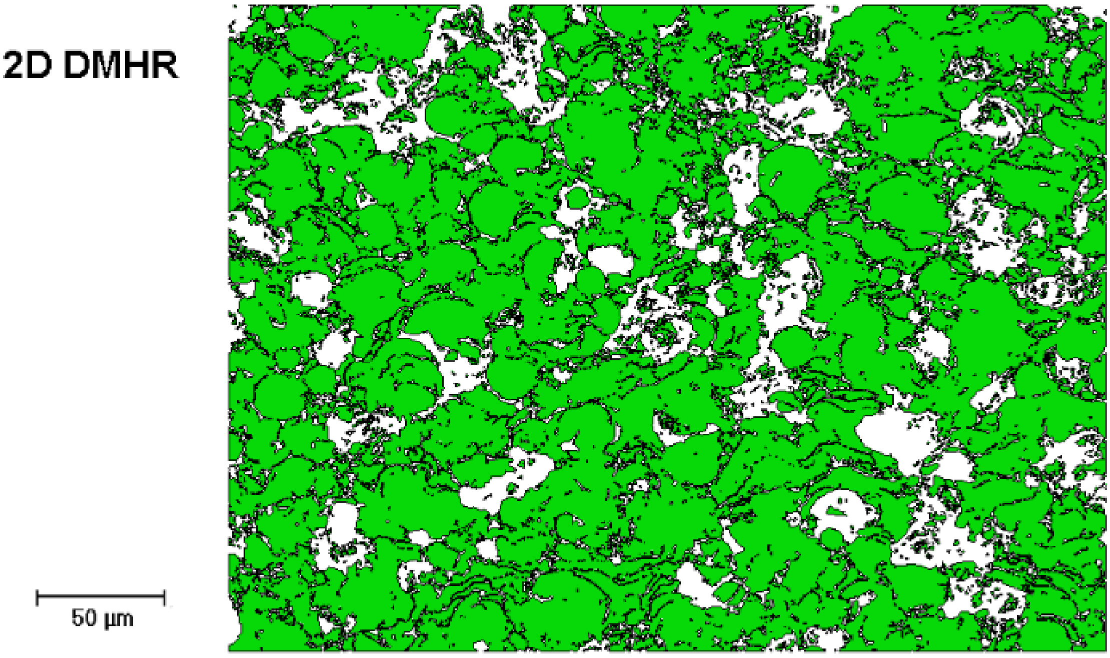

2D Direct Mapping High Resolution Model

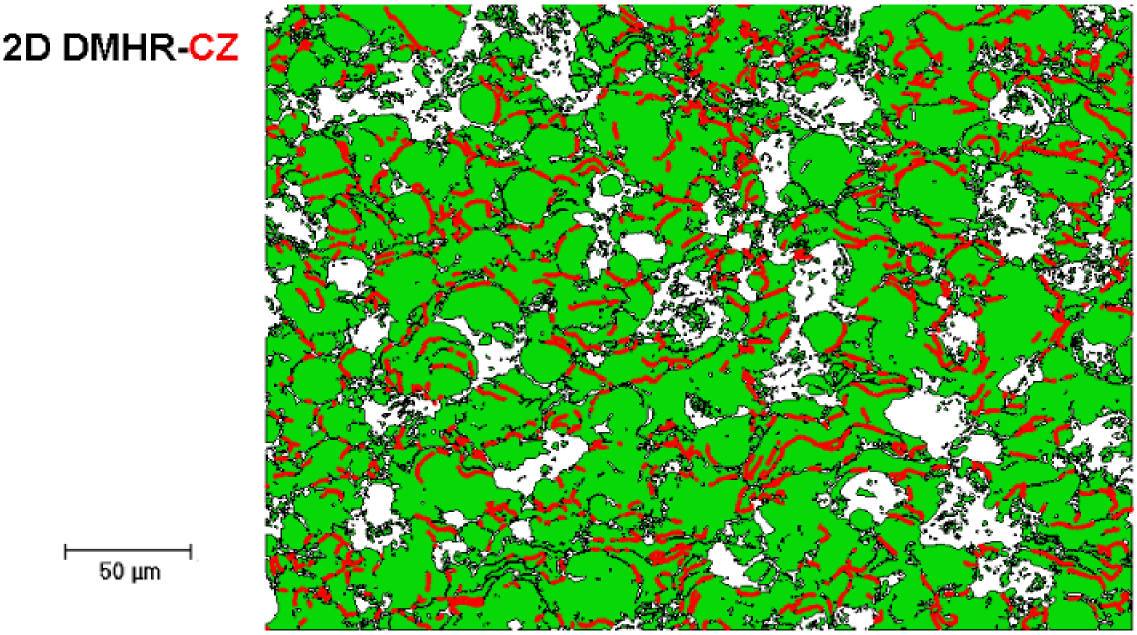

2D Direct Mapping High Resolution Model with Contact Zone

Figure 7.1: *The planar image-based high resolution (IBHR) models used for FE-simulation of plasma sprayed tungsten. Both type of models are generated from SEM images with spatial resolution of 0.2μm/px. Top: IBHR with two morphological phases, solid tungsten (in green) and pores (in background color, with slim elongated interlamellar voids also included into the porous phase). Bottom: IBHR-CZ with Contact Zone (CZ, in red) as third morphological phase representing internal boundaries between lamellas in contact. To the CZ-elements reduced stiffness or reduced thermal conductivity has been assigned.*

tungsten ultimate strength and yield stress (1200-1300 MPa at RT and 500-1000 MPa above

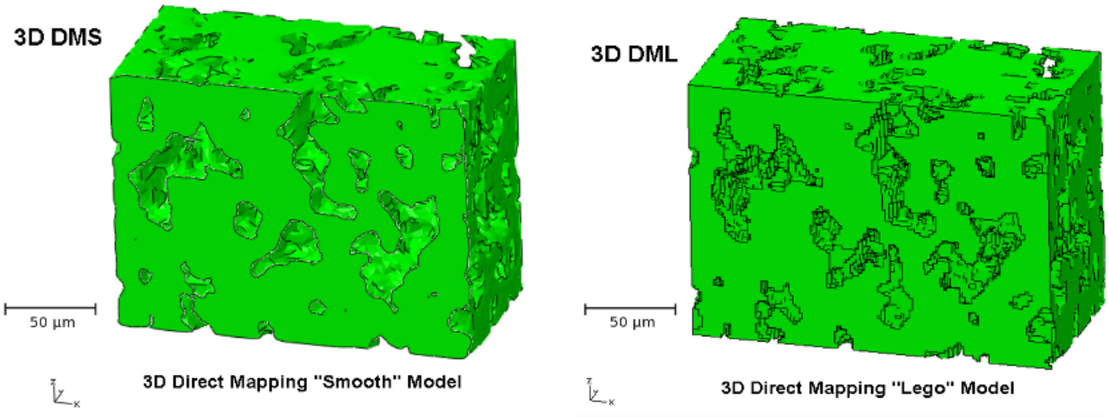

Figure 7.2: *3D Direct Mapping models of VPS-W used in FE-simulations. Left: with smoothed boundaries at the interface between solid and porous phase. Right: with pores boundaries matching the voxel structure of the original tomographic image. Length and height of the model are half those of the planar models of Fig. 7.1).*

Table 7.1: *Comparison of average stress values at 0.02% average strain between full 3D models and their corresponding slice reconstructions (100 slices along the X axis). Both the "smooth" (DMS) and the "lego" (DML) 3D models have been compared.*

	3D DMS	2D HRDM
$<E_{yy}>$ [MPa]	303± 5	63 ± 7
<por> [%]	17± 0.5	24± 2

DBTT respectively, cf 3.3.2), it seems correct to assume perfect elasticity for the local behavior of the tungsten phase at room temperature.

Comparison 2D/3D

So far we showed results only from 2D models. They seem the only ones suitable for a correct description of the thermomechanical response of the coating since they include essential morphological details (like the Contact Zone) which are missing in tomographic models. On the other hand, they suffer of another important restriction: the lack of the third spatial dimension.

An important question to be addressed is: can we quantify the effect of a missing dimension between models representing the same random structure ? Thanks to the IB-FEM approach the answer is yes, once we provide an overall reference parameter (for instance the average stress) and once we perform the comparison between "morphologically equivalent" models. Because of the previously mentioned limitation affecting 3D models (they do not include thin interlamellar "cracks" and Contact Zone), only a comparison with 2D models with a similar level of morphological detail and mapping resolution is appropriate. This fact is proven by the first comparison between 3D DMS and 2D HRDM models, which are not morphologically equivalent, with the first ones completely lacking thin cracks and CZ. As immediately evident, 3D models extremely overestimate the modulus (by factor 5!). Apart from possible numerical

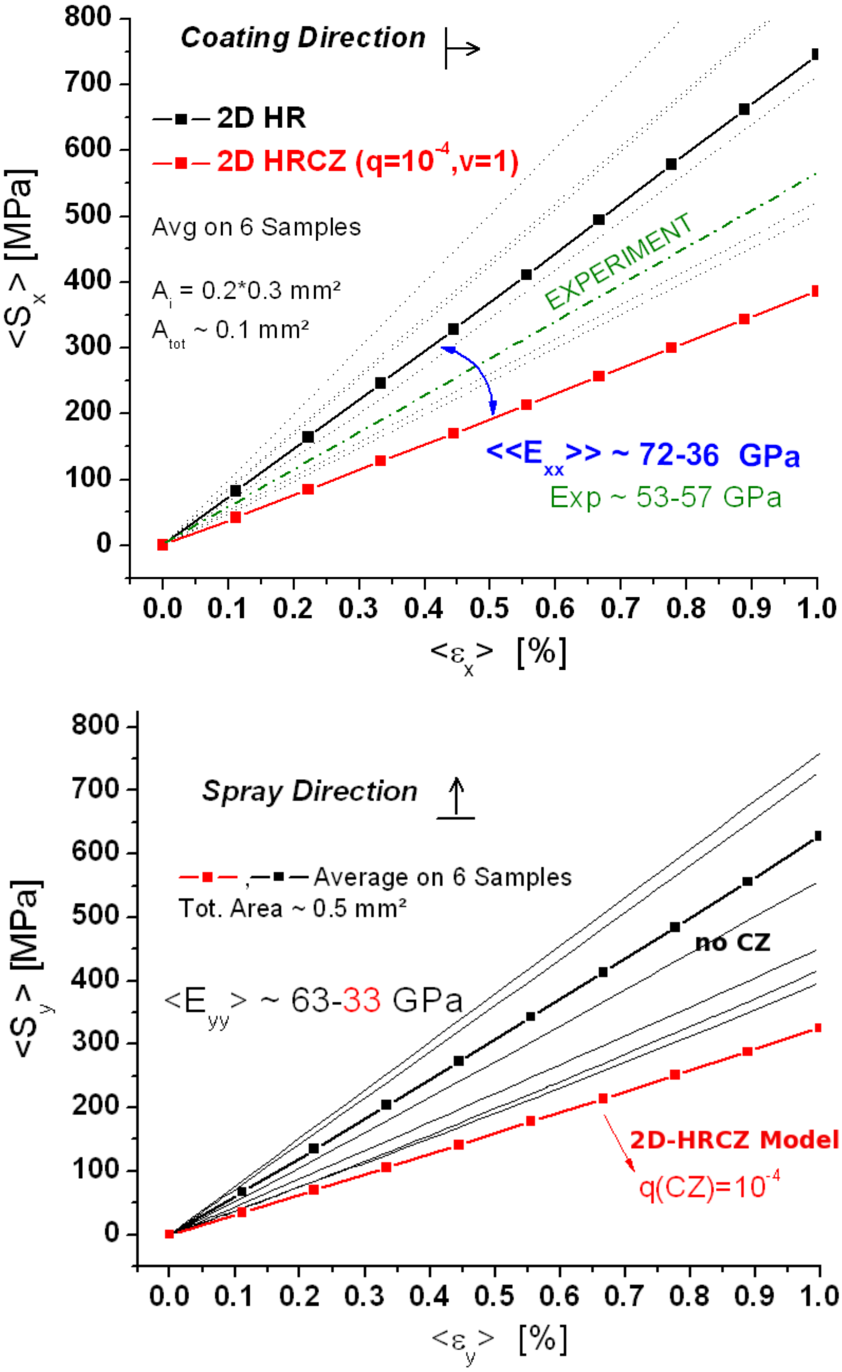

Figure 7.3: *VPS-W: calculated stress-strain plots after prescribed tensile elongation up to 1% in both directions (parallel and perpendicular to coating growth direction). The model used here were of type 2D-IBHR (bold black) and 2D-IBHR-CZ (bold red). For this latter type a reduced stiffness has been assigned to CZ-elements (q=E_CZ/E_W=10^-4) The bold curves are obtained averaging over 6 micrographs (in background is only shown the set without CZ). One can notice the large scatter in Young's modulus ($\Delta E/E \sim 35$ % in both cases).*

artifacts [1], the principal factor behind the mismatch is certainly the lack of crack-like porous inclusions in 3D models. These, having small thickness and being planarly extended have

---

[1] prescribing the strain at the boundary nodes of a 3D DMS model could have caused artifacts, due to the low final mesh resolution. The sometime excessive smoothing of pores boundaries could have caused missing TOP or BOTTOM model regions to be properly constrained (cf. Fig. 7.1c)

Table 7.2: *Comparison of average stress values at 0.02% prescribed tensile strain between full 3D models and their corresponding slice reconstructions (100 slices along the X axis). Both the "smooth" (DMS) and the "lego" (DML) 3D models have been compared.*

[MPa]	3D DMS	3D DML	%Δ	2D DMS	%Δ	2D DML	%Δ	%Δ
$\langle\langle\sigma_{eq}\rangle\rangle$	66	65	1%	46 ± 7	-30%	40 ± 7	-38%	27%
$\langle\langle\sigma_{y,z}\rangle\rangle$	68	63	7%	40 ± 8	-41%	35 ± 8	-55%	34%

certainly a large impact on the overall elastic property.

The proper quantification of the 2D/3D gap can only be done between models of the *same* random structure, once mapped in 2D and once in 3D. In this regard, we generated 2D models extracting them directly from a reference 3D model, previously generated. We could then perform an "intrinsic 2D-3D comparison", which allowed to isolate and quantify the dimensionality effect. Unfortunately, due to the segmentation problems of 3D tomographic images explained in 6.3, this comparison was limited to macro-porosity (globular pores).

"Planarization" of a 3D model was performed dividing the original tomographic image into N parallel planar sections (slices), generating a mesh on each of them with a proper OOF2 algorithm and solving the reference 3D mechanical problem with equivalent planar Boundary Conditions (BC) on the N independent slices[2]. The global parameters chosen for the comparison were the average equivalent (von Mises) stress ($<\sigma_{eq}>$) and the average stress tensor component aligned to the prescribed tensile elongation ($<\sigma_y>$ in 2D and $<\sigma_z>$ in 3D). The results are shown in Table 7.2.

A general underestimation of stress values (causing a loss of stiffness) is evident for all the planar models. This fact has been already found in previous works on metallic foams [144]and theoretical studies on elastoplastic composites.

Remarkably, the difference between the DMS ("smooth") and DML ("lego") models in overall stress is fairly limited (up to 7%) but concerning the 2D-3D gap within the same model (Δ) this difference is much larger (up to 34%), with 2D DMS models approximating better the corresponding 3D model.

Fig. 7.4 illustrates the 2D-3D comparison at the level of local fields (limited to the smooth model, but also including the plane strain case). This is useful to understand, at least qualitatively, the source of the mismatch 2D/3D. The planar models show large "stress-free" regions (in blue) along the solid phase, while the same regions get values up to 50 MPa (in indigo-light green colors) on the equivalent cross-section of the 3D model. In this latter case, the fields are only projected on a 2D cross-section but we should keep in mind that they are the result of a three dimensional interaction within the material. This produced a 3D stress-strain arrangement along the solid matrix which is connected in all the three spatial dimensions. The whole 3D solid structure looks indeed more "connected" than its equivalent "slice reconstruction". Here, each slice is geometrically independent and there is no "elastic connector" between them

---

[2] in order to keep reasonable the total computational time, while assuring a fairly good morphological equivalence between the N slices and the original 3D model, we set N=100. This implied a step of 1.6 µm between slices, close to the tomographic resolution.

(in the out of plane direction). The stiffness component between slices is therefore zero while it remains equal to that of tungsten in 3D. The real 3D model results therefore stiffer and, for a certain prescribed strain, the stress values are higher (when considered as averaged over the whole solid volume).

When looking at the local stress peaks, we notice more frequent and higher peaks in planar models (cf. Fig. 7.4). This because stress/strain fields have less "spatial possibilities" in 2D to arrange in a more "energetically" favourable configuration[3].

As for plane-stress/plane-strain comparison, as expected, higher local stress values are observed for the plane-strain case (representing a situation where inclusions extend indefinitely in the out-of-plane direction).

We finally remark that the 2D/3D comparison was limited to the globular porous structures. Until a 3D model with sufficiently high mapping resolution will become available[4], the effect of dimensions on the full microstructure, in particular on the thin crack-like inclusions, cannot be quantified.

7.2.2 Probabilistic Assessment of Failure (2D)

The failure analysis presented here is based on the analysis of static stress field at the onset of cracking (without modeling dynamic crack propagation). The general aim was to link the microscale condition for the local onset of crack with an overall total failure condition at the mesoscale (crack entirely crossing a micrograph). Some strong hypothesis on the propagation phenomenon had to be introduced, like assuming a link between a mesoscale parameter characterizing the micrograph stress distribution *before* cracking and the actual total failure.

The local criterion for crack initiation

The random location of the pores and their irregular shapes make it impossible to use the classical fracture mechanics approach based on stress intensity factors, since these are defined for the much simpler situation of a single crack in a homogeneous material, assuming ideal shape of the crack and load applied far away from the crack tip. In other words, we cannot calculate "local stress intensity factors" to define crack onset and propagation across this material.

The local variable observed is the Maximum Principal Stress (MaxPS), since it is believed that brittle crack usually initiates perpendicular to its maximum component. A brittle failure criterion developed on this indicator appears the most simple and indicated choice for start modeling local crack onset in VPS-W. Criteria based on yielding are not suitable for W at RT and criteria involving shear components appear mostly indicated to model different brittle media like concrete (es. the Mohr-Coulumb criterion). A criterion based on strain was discarded as well, since the ultimate elongation at RT of bulk-W (to be taken as reference) is extremely

---

[3] since the equilibrium configuration of stress and strain is always that which minimizes the overall model energy.

[4] (average element size of at least $1\mu m^2$)

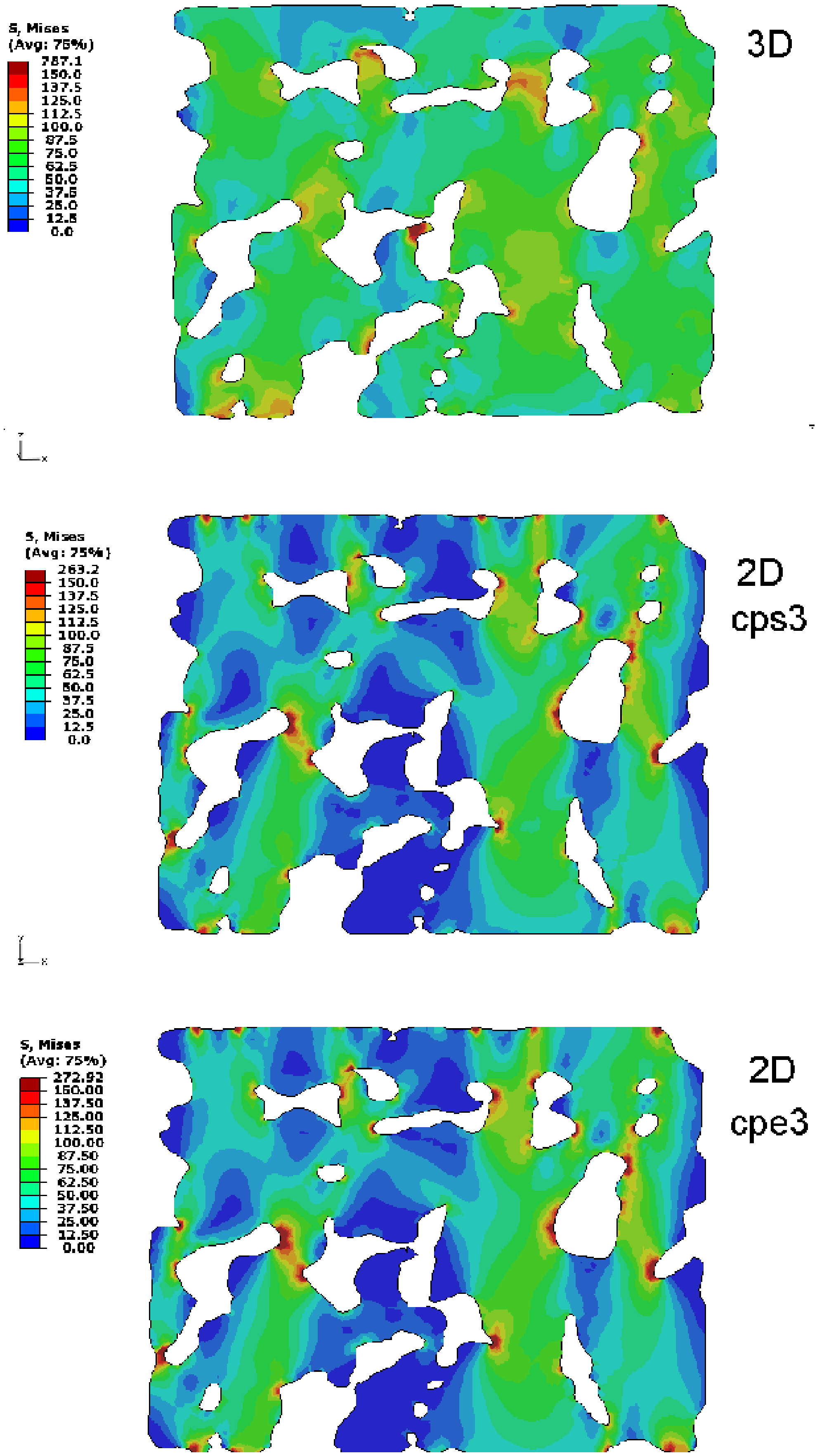

Figure 7.4: *2D/3D comparison of stress micro fields (v. Mises invariant). Extrapolated values on a planar cross-section of the full 3D "smooth" model are compared to the same cross-section meshed as independent 2D model. For the planar model both plane stress and plane-strain elements (CPS3 and CPE3 respectively) have been used, with slightly higher values obtained for the latter case.*

difficult to be measured or to be found in the literature. The last category, the energy criteria, certainly deserve to be tested, but it was not considered here.

Unfortunately, an important information needed to quantitatively set the local criterion is missing: we don't know precisely (and we cannot know) the local value of ultimate strength $\sigma_{CZ}^{ult}(x,y)$ of internal interfaces in contact (Contact Zone, CZ). This because the underlying detachment phenomenon between lamellas strongly depends on the local quality of the contact, which varies across the material and further depends on a number of parameters (sintering temperature, quenching stress, interfaces impurities - just to mention some of them). Eventually, we can only make a reasonable guess on the upper limit of σ_{CZ}^{ult} (which certainly lies quite below σ_{W}^{ult}) and imagine its phase average value $\bar{\sigma}_{CZ}^{ult}$ as homogeneously distributed across CZ.

From the average local value $\bar{\sigma}_{CZ}^{ult}$ and the average local ultimate strength of the whole solid phase $\bar{\sigma}_{VPS-W}^{ult}$ (which includes both tungsten and CZ).

Then, we have two possibilities: either we explicitly consider the Contact Zone as morphological phase using CZ models (2D IBHR-CZ) or we make use of standard models (2D-IBHR) including the CZ contribution as implicit one in the local onset criterion (which should then be based on $\bar{\sigma}_{VPS-W}^{ult}$ and not on $\bar{\sigma}_{CZ}^{ult}$). Explicitly including the CZ means to deal in principle with two free parameters instead of one: the reduced local stiffness E_{CZ} and the ultimate strength in CZ $\bar{\sigma}_{cz}^{ult}$ (even considering both phenomena, cracking at the Contact Zone and cracking across the W-phase, only $\bar{\sigma}_{cz}^{ult}$ remains unknown, since $\bar{\sigma}_{w}^{ult}$ is already known). On the other hand, IBHR models without CZ require only one free parameter: the onset crack threshold across the whole solid phase $\bar{\sigma}_{VPS-W}^{ult}$.

Because the first option requires much higher computational costs (and the problematic definition of CZ-elements during segmentation), we will stay on models without explicitly defined CZ making use of a single criterion for the whole solid phase.

Hence, our guess for local crack onset reads:

$$MaxPS(x,y) \geq \bar{\sigma}^{ult};\ 0 < \bar{\sigma}^{ult} < \sigma_{W}^{ult} \tag{7.1}$$

On the other hand, guessing $\bar{\sigma}^{ult}$is not enough for the definition of a *total* failure criterion. Let's suppose the crack onset criterion is satisfied on a certain localized region of VPS-W, say at the CZ. The crack develops, propagates and then eventually stops at the next pore surface. Although damaged, the whole material remains connected. Further stress coming from increased external load will redistribute on a less connected region, a next CZ-crack will develop and so on, until a defined macrocrack front develops and the specimen ultimately fails. The progressive crack growth is fast, since the basic constituent is very brittle and the internal stress status increasingly higher at each further detachment.

A tentative method for total failure prediction

The question is then: how can we predict total failure ? Certainly, the microstructure plays the most important role, since it determines the spots of stress concentration and the possibility for

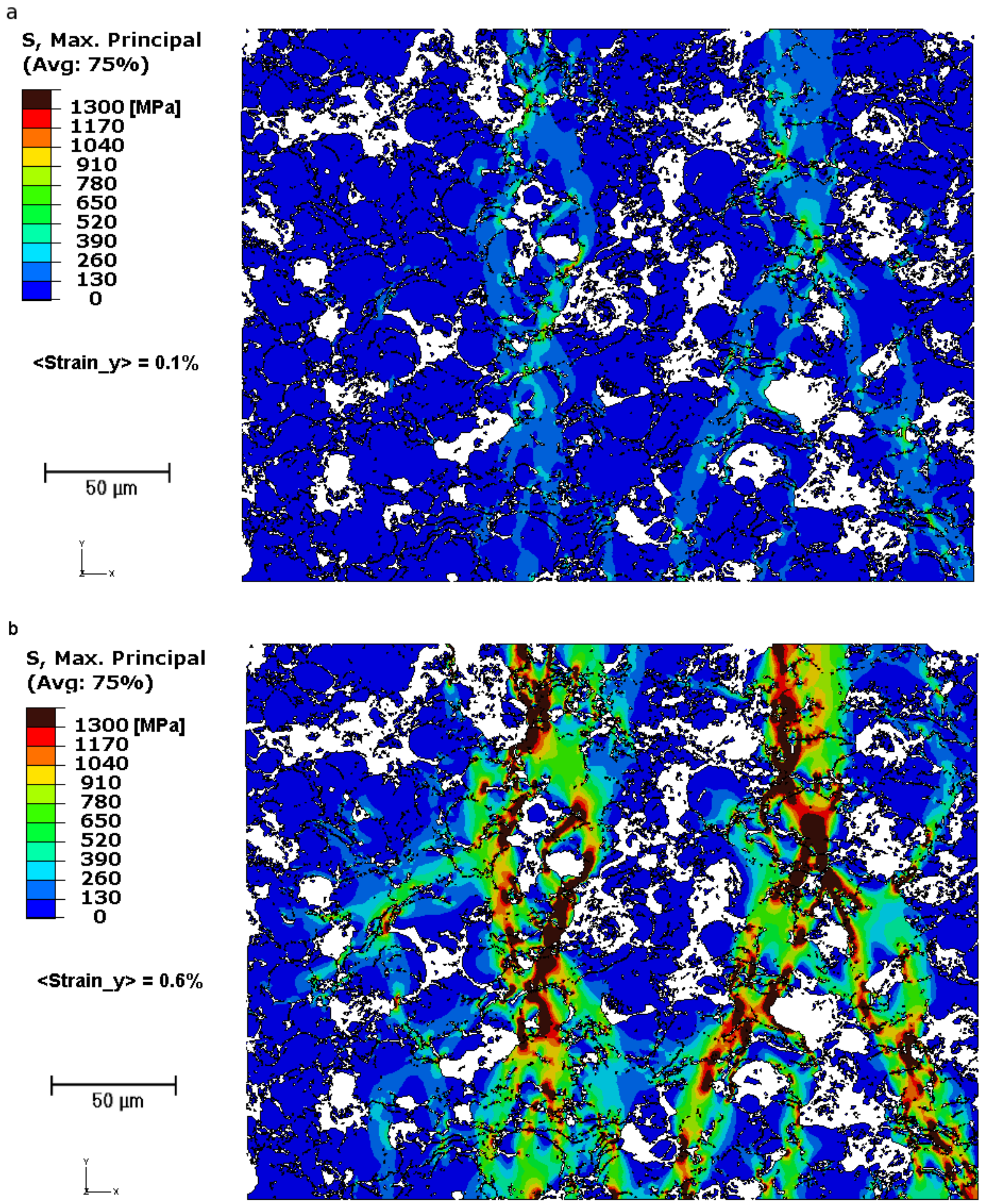

Figure 7.5: *Evolution of the maximum principal stress (MaxPS) field inside VPS-W. Two stages of the simulated tensile test are shown (corresponding to point a and b in Fig. 7.6). The "dark brown" region (only visible in b) indicates MaxPS exceeding the ultimate strength of tungsten at RT (σ_W^{ult} = 1300 MPa). The "green-dark brown" and the "light blue-dark brown" regions indicate MaxPS exceeding 650 MPa and 130 MPa (corresponding to $0.5\sigma_W^{ult}$ and $0.1\sigma_W^{ult}$ respectively). No Contact Zone was activated in this model.*

them to become a growing crack. The resulting criterion must therefore be based on inspection of the stress-fields on the micrographs. A way to inspect the stress-fields "quantitatively" is given by the analysis of their stochastic distribution across the simulation domain.

Since we deal with a *deterministic* process (the estimation of stress values at a certain point of the micrograph) on a *random* spatial domain (the porous material), the stress function over the micrograph s = s(x,y) becomes itself a random variable. Hence, it makes sense to define the probability for s to lie within a certain interval across the simulation domain (at a given stage of mechanical load). It appears also natural to measure such probability by the relative micrograph area containing such interval of stress values. Finally with these instruments we will set the total failure criterion (here also referred as micrograph or mesoscale criterion, to be distinguished from the local or microscale onset criterion represented by equation 7.1).

We can formally define the probability $P(s\epsilon I)$ for s to get values in the interval I=$[s_1, s_2]$ through the probability density function $p(s)$ as:

$$P(s\epsilon I) = \int_I p(s)ds = \int_{s_1}^{s_2} p(s)ds \tag{7.2}$$

where for $p(s)$ holds:

$$\int_0^\infty p(s)ds = 1 \tag{7.3}$$

The function$p(s)$ is therefore a probability distribution (or density). The shape of $p(s)$ (and its evolution at different stages of load) is strictly related to the particular random morphology considered (in our case that of VPS-W). Among the possible components or invariants of the stress tensor to be assigned to s, we focus on the maximum principal stress (MaxPS), as we assume that this is the critical variable driving the onset of brittle crack under tensile load.

We can also define the *cumulative distribution function* $P^{\overline{s}}$ as:

$$P^{\overline{s}} = P(s < \overline{s}) = \int_0^{\overline{s}} p(s)ds \tag{7.4}$$

and its *complementary cumulative distribution function* $P_c^{\overline{s}}$as:

$$P_c^{\overline{s}} = P(s > \overline{s}) = 1 - P^{\overline{s}} = 1 - \int_0^{\overline{s}} p(s)ds$$

Once the micrograph stress function $s = s(x, y)$ is known at a certain stage of the loading history (as result of the Finite Element solution at a certain time step of the simulation), we can “measure” the probability in terms of normalized micrograph area. Since the domain is discretized by the finite elements mesh, we can measure the probability function $P(s\epsilon I)$ by summing the area of all grid elements $A_i^{s_I}$interested by the stress values $s\epsilon I$ and normalizing over the total area (the value s should have been previously averaged over the element integration points or extrapolated at the element centroid). In order to carry out such calculation we should first discretize the stress domain with n regular intervals (bins) s_j of size $\triangle_j = s_{j+1} - s_j$. Once we get the frequencies f_j of the discrete values s_j, these generate the discrete probability density function which approximates the function $p(s)$ as:

$$p(s) \approx f_{s_j} = \frac{1}{A}\sum_i A_i^{s_j}; \sum_{j=1}^{n} f_j = 1 \tag{7.5}$$

In the same way$P(\overline{s})$ can also be estimated as:

$$P^{\overline{s}} = P(s < \overline{s}) \approx \frac{1}{A}\sum_{s_j<\overline{s}} \triangle_j \sum_{i=1}^{N} A_i^{s_j} \tag{7.6}$$

We can finally estimate $P_c(\overline{s})$ as:

$$P_c^{\overline{s}} = P(s > \overline{s}) \approx 1 - \frac{1}{A}\sum_{s_j<\overline{s}} \triangle_j \sum_{i=1}^{N} A_i^{s_j} = \frac{1}{A}\sum_{s_j>\overline{s}} \triangle_j \sum_{i=1}^{N} A_i^{s_j} \tag{7.7}$$

$$\overline{s} = \tau\sigma_w^{ult} \tag{7.8}$$

For the sake of clarity, we simplify notation renaming $P_c^{\overline{s}}$ into $P_\tau(\langle\epsilon\rangle)$ (which is a two variable function in $\langle\epsilon\rangle$ and τ), expliciting the mesoscopic load variable$\langle\epsilon\rangle$. Fig. 7.6 plots the values (as obtained from simulations) of sections of the two variable function $P_\tau(\langle\epsilon\rangle)$ in $P-\langle\epsilon\rangle$ planes for two different values of τ which means having set three different local criteria from equation 7.8 ($0.5\bar{\sigma}^{ult}$ and $0.1\bar{\sigma}^{ult}$) where $\langle\epsilon\rangle$ is the value of prescribed micrograph strain and the observed variable is MaxPS, the plotted functions are actually

The physical meaning of this function is better understood looking at the graphs of Fig. 7.5, which show the stress field $s(x, y)$ at two stages of the loading evolution. The first one has colors which correspond to relatively low stress values, while the second one, at higher prescribed strain, shows large zones of stress exceeding the threshold. The plots $P_\tau(\langle\epsilon\rangle)$ show the relative micrograph area where $MaxPS(x, y)$ is *exceeding* a certain extremal stress value $\tau\sigma_w^{ult}$. Any point of the graph represents the answers to the question: what portion of the VPS-W micrograph is *now* above the tensile limit that such material can tolerate ? This function is therefore a useful indicator to track the global evolution of that part of the stress distribution relevant for crack initiation. One can notice how the extremal magnitude of the curves is strongly dependent on τ , while the general shape remains similar.

The influence of τ on the ultimate strain interval $\triangle\langle\epsilon\rangle_f$is also strong: a large interval at 1300 MPa becomes much tighter at 130 MPa as the slope of the P curves gets increasingly stiffer. At higher strain values a saturation effect is visible, as expected from the definition of P. However, this part of the curve, while interesting from a theoretical point of view is lacking physical meaning, since total failure at this stage has most probably already occurred.

Another important trend can be found in Fig. 7.6 while tracking the values of P for different values of micrograph porosity (indicated in the legend): at higher porosity levels the value of P and so the probability of total failure increase (small deviation from this trend by single micrographs may occur, since micrograph porosity cannot be considered an unambiguous morphological parameter). This trend is also in accordance with the observation that an higher porosity of the kind of VPS-W implies an higher probability to develop stress concentrations which eventually lead to failure.

Between the three cases studied, the scenario we believe to be the closest to the real situation is that for the smallest value of τ (Fig. 7.6b), where the average ultimate strength across VPS-W is supposed to be one tenth the strength of bulk tungsten.

It appears now natural to link the probability function $P_\tau(\langle\epsilon\rangle)$ to another one measuring the probability for total micrograph failure. Total failure will be naturally described also through a cumulative distribution function $F = F(\langle\epsilon\rangle_f)$, which associates to a certain value of mesoscale ultimate strain $\langle\epsilon\rangle_f$ the probability for values above it to cause total failure. Since P raises monotonically from zero (at zero strain) to 1 and so must behave F: the larger the micrograph area above the local failure threshold, the larger the probability for total failure to occur. The difference however is that F = 1 is obtained much before P reaches 1 (in terms of total mesoscale strain). In other words, there exist a limit value$\langle\epsilon\rangle_f^{lim}$ after which we are sure the material will fail at the mesoscale level. We can therefore assume F to be directly proportional to $P_\tau(\langle\epsilon\rangle)$:

$$F = kP_\tau(\langle\epsilon\rangle_f) \tag{7.9}$$

The value of k could then be easily found after setting a limit value of $P_\tau^{\overline{Max}}(\langle\epsilon\rangle_f)$ after which total failure will occur with probability equal to one (F=1).

A reasonable value of $P_\tau^{\overline{Max}}(\langle\epsilon\rangle_f)$ lies fairly below 50%, however the choice of an exact limit remains arbitrary at this stage of the work (through further empirical inputs and an inverse procedure, it could be more precisely estimated). Qualitative inspection of the micrograph suggests to set the extremal values of P at 10-15%. It has been verified in the whole ensemble of micrographs that th interval proposed corresponds to a situation where stress zones above threshold are enough extended to build bridges between globular pores (see 7.5). It appears reasonable to assume as first approximation that the corresponding accumulated energy, once released, could give rise to a macro crack crossing the entire micrograph.

We remark once again the approximate nature of the total failure criterion derived without including crack propagation into the model. The criterion is therefore acceptable for this tentative numerical study, but certainly needs to be improved and further validated through experiments. Once it will become possible to accurately measure the ultimate strength and strain of the porous coating (and their interval of variation), the two free microscopic parameters (reduced stiffness$< E >_{CZ}$ in contact zone and ultimate strength of the contact zone$\bar{\sigma}_{CZ}^{ult}$) could be inferred via inverse methods.

A possible approach to the solution of this inverse problem is proposed. First, $< E >_{CZ}$ could be guessed from a parametrical variation of $q = \frac{<E>_{CZ}}{E_w}$ included in 2D-HRIB-CZ models (as in Fig. 7.3). Then, a numerical estimation of the curve $P_\tau(\langle\epsilon\rangle)$ could be obtained from mesoscale simulations (as given in Fig. 7.6) and hence an estimation of the function F_τ through equation7.9. From the definition of F_τ, one could then derive the failure probability distribution f as:

$$f_{\tau_{CZ}}(\langle\epsilon\rangle_f) = \frac{dF_\tau}{d\,\langle\epsilon\rangle_f} = k\frac{dP_\tau}{d\,\langle\epsilon\rangle_f} \tag{7.10}$$

Provided a sufficiently large statistic on the experimental ultimate strain (for instance through bending tests) the function f could be fitted having τ_{CZ} as parameter and hence an estimation for $\bar{\sigma}_{CZ}^{ult}$ could be provided.

A natural extension of this work will be integration of crack propagation analysis using the same HRIB unit cells. Possible approaches should be based on modeling the Contact-Zone either with *cohesive elements* (COH) or with *extended finite-elements* (XFEM).

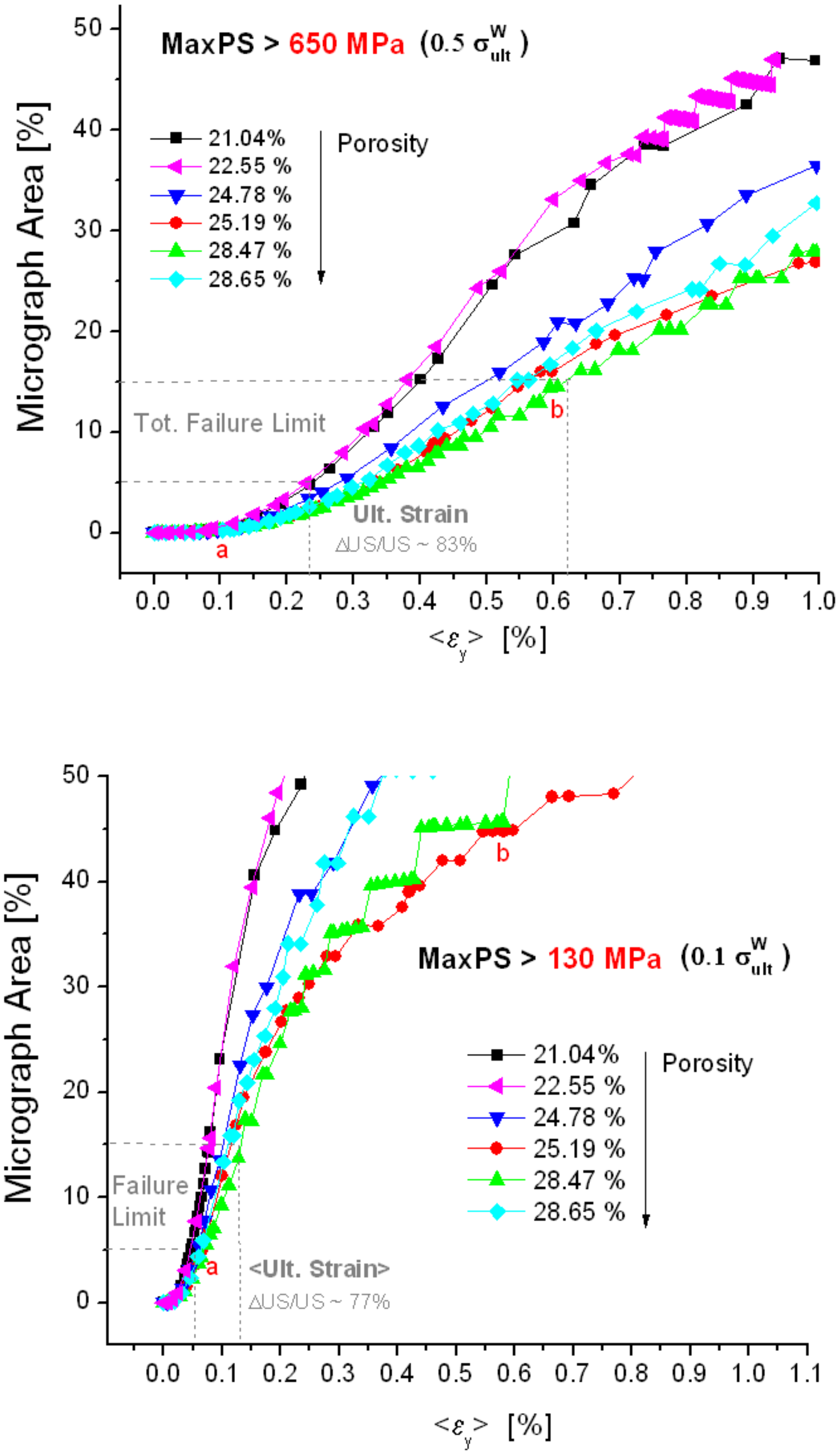

Figure 7.6: *Complementary cumulative distribution function* $P_{\tau}^{\overline{Max}}(\langle\epsilon\rangle)$ *as function of prescribed strain during simulated tensile test (in deposition direction). It represents the fraction of the micrograph area exceeding a maximum principal stress value. The threshold value has been set to* σ_{W}^{ult} *(1300 MPa),* $0.5\sigma_{W}^{ult}$ *and* $0.1\sigma_{W}^{ult}$*. The stress fields across the micrograph at point a and b are shown in Fig.*

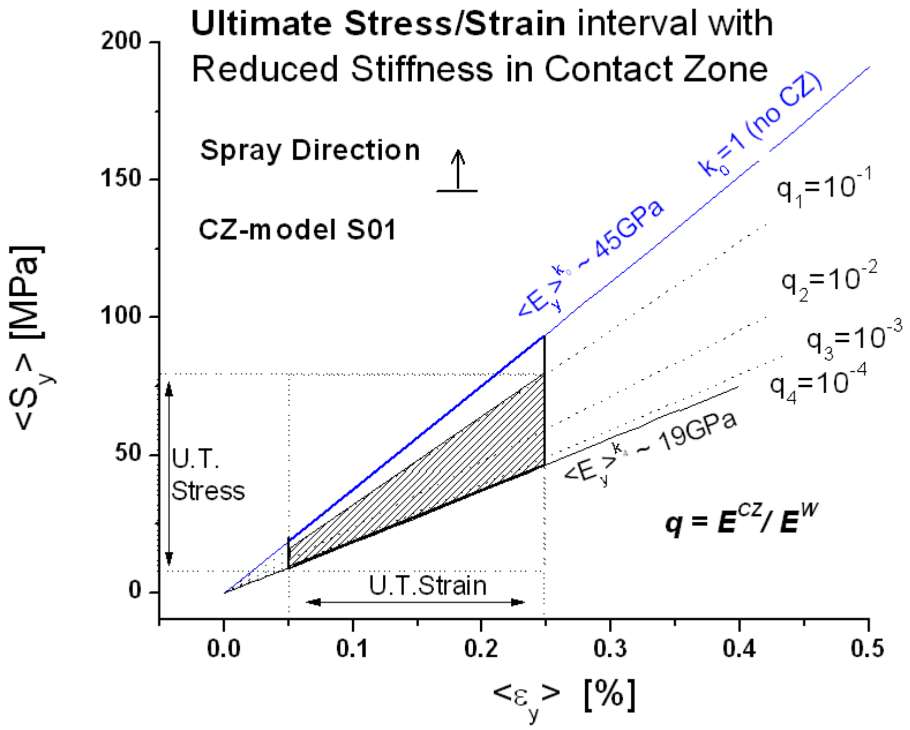

Figure 7.7: *The estimated interval of VPS-W Ultimate Tensile Stress as resulted combining the probabilistic failure model with the contact-zone (CZ) model. A starting guess on the ultimate strain resulted from varying the threshold for crack onset in the range 130-200MPa (which corresponds to* τ *= 0.1-0.3, cf. Fig. 7.6). The interval is determined by the uncertainty of the parameter q representing reduced stiffness in CZ. The saturation effect for very low q values is also shown. Please note only one micrograph was used for this estimation.*

7.3 Thermal Analysis

Thermal analysis aimed at the estimation of steady-state thermal properties stressing the influence of the random morphology. Finite element solution of the heat equation in steady-state have been calculated on planar models with contact-zone (2D IBDM-CZ) and uniform gradient of temperature (UGT) boundary condition. Results of FE simulations were compared with measurements from a laser flash apparatus (LFA, described in Appendix) on real VPS-W specimens, finding an overall good agreement.

7.3.1 Mesh Dependency Study

Benchmark on Homogeneous Tungsten

First, a benchmark for the numerical estimation of thermal conductivity through FE-simulations was conducted on planar models of homogeneous tungsten, testing different simulation parameters like average element size and temperature gradients. Results of the benchmark (Table 7.3) show the reliability of the simulation method. The parameter calculated was $<\lambda>^y$ in each case (average thermal conductivity in the direction parallel to the thermal gradient). The model was 0.31 mm * 0.26 mm (the same size of a full size VPS-W micrograph), meshed once at low and once at high mesh density (in Table 7.3 the inverse of the average mesh density is indicated, which corresponds to the average element size). Input material data for tungsten were taken from the ITER Material properties handbook [114].

Calculated thermal properties for the homogeneous case were in excellent agreement with literature material data, showing no dependency from mesh refinement and only a negligible influence from the applied thermal gradient.

Table 7.3: *Benchmarks on bulk-tungsten for thermal conductivity calculated via steady-state analysis on planar micrographs of homogeneous tungsten. The micrographs were meshed at two different refinements. The case with average element size<el.size> = 0.3 μm^2 is comparable to that used for real DM models of VPS-W. The negligible influence of different boundary conditions is also shown.*

Sim. Material	Method	<el.size> [μm^2]	ΔT^{SS} [°C]	$< \lambda >^y$ [W/mm°C]	$\Delta[\%]^{sim-lit}$
Bulk-W at RT	Liter. Data	-	-	0.173	-
Bulk-W at RT	Steady-State	3.7	1	0.17295	0.03
Bulk-W at RT	Steady-State	3.7	0.5	0.17298	0.01
Bulk-W at RT	Steady-State	0.3	1	0.17295	0.03

2D Image Based Models of VPS-W

A mesh dependency test was also performed in order to investigate the influence of mesh features (in particular local refinement) on the numerical results. Both global and local convergence have been checked in order to investigate the conditions for mesh independent results.

As global parameter we choose the average flux $< \phi_y >$ (since calculations of conductivity and diffusivity depends on it, see eq.4.10). Five increasing levels of refinement (average element size of 0.9, 0.7, 0.5, 0.3 and 0.2 μm^2 respectively) have been considered on a test micrograph, corresponding to different levels of mesh adaptation to the underlying microstructure. From the test results (Fig. 7.8), we noticed a remarkable element size dependency for coarse refinements up to 0.31 μm^2 (blue graph in Fig.7.8). We therefore set this value as lower limit during mesh generation of the whole simulation ensemble. This choice, which implied high level of local refinement on large domains (0.3 mm* 0.25 mm) implied also high computational cost already during the mesh generation process (several hours pro micrograph, since the mesh generation program, OOF2, cannot run on multiple CPUs). Targeting for instance an average element size of 0.25μm^2, we ended up with planar meshes of about half a million elements, whose nodes had to be moved several times from the adaptive optimization algorithm (section 4.1.2).

In general the smaller the average element-size the better the mapping of irregular boundaries with high curvature gradient (see for instance the mesh regions shown in Fig. 7.9). On the other hand, a too small element size (usually at the boundaries solid/void) could also affect results with pixelization artifacts (section 4.1.2). In order to prevent pixelization artifacts a constraint on the smallest element size was also imposed to 0.05 μm^2 (due to the high image resolution of [0.2 μm]^2/px),

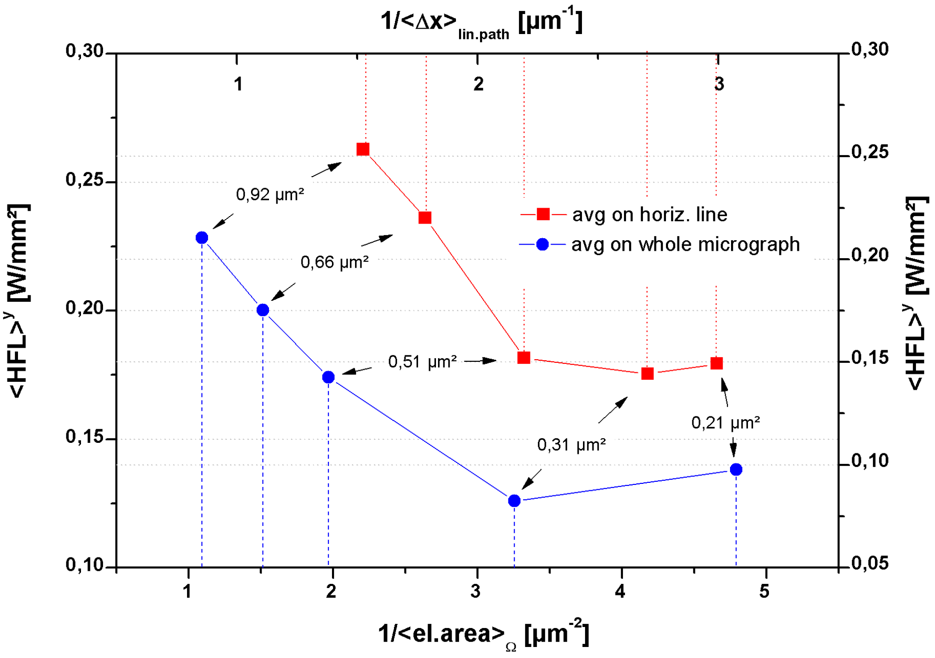

Figure 7.8: *Average Heat Flux (vertical component, parallel to thermal gradient) from a steady state simulation with constant temperature gradient ($\Delta T_{bottom}^{top} = 1°C$) calculated for increasing level of mesh refinement on the same location. In red the average is computed on a straight horizontal line with linear interpolation at the mesh intersection points and plotted as function of the average intersection length between the line-path and the mesh. (see Fig. 7.9). In blue the average heat flux has been computed on the whole 2D micrograph extrapolating at the element centroids and plotted as function of the average element mesh density. The simulated domain was a large region of VPS-W (0.31*0.24 mm^2) scanned at high-resolution (0.219 μm/px).*

Local values of the heat-flux field have been also compared for different levels of mesh refinement (Fig. 7.9). Flux profiles along a straight line crossing the mesh in direction perpendicular to the temperature gradient become almost coincident for sufficiently small average element size (blue and cyan symbols corresponding to 0.31 μm^2 and 0.21 μm^2 respectively). The mean value of the flux along the linear path also showed a satisfactory convergence (red curve in Fig. 7.9).

7.3.2 Thermal Diffusivity

Thermal diffusivity at RT was estimated starting from homogenization of the vertical heat flux component as result of the steady-state solution with prescribed thermal gradient of 1°C between top and bottom nodes of the simulation cells. From the knowledge of the average flux, average thermal conductivity and diffusivity follows. Details of this calculation can be found in 4.3.2.

Results of estimated average diffusivity are in good agreement with experimental data (Fig. 7.10) and confirm the observed drop (close to a factor of 8) for VPS-W compared to the bulk case. The excellent agreement between simulation and literature data for the bulk case (green/yellow lines in Fig.7.10a) is also reported. The relatively high variance on simulated

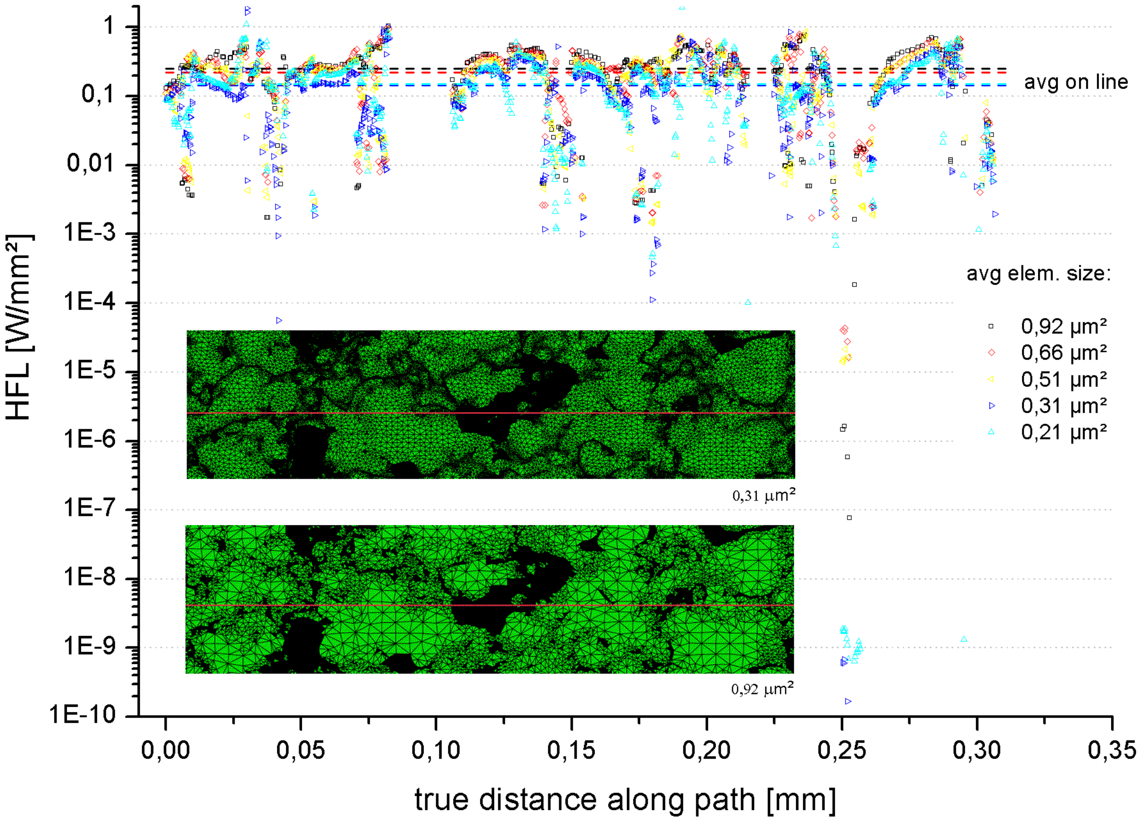

Figure 7.9: *Magnitude of the heat flux (from a steady state simulation with constant temperature gradient* $\Delta T_{bottom}^{top} = 1\,^{\circ}C$ *) along a straight path crossing the mesh for increasing level of mesh refinement (decreasing average element size). Two refinement levels are also shown.*

samples is due the limited simulation cell size and to fluctuations of the random morphology (this further motivated the general estimation of the representative volume element, see later section 7.3.3). Unfortunately, due to the very limited amount of experimental samples available, experimental standard deviation could not be estimated. Nevertheless, experimental deviation is expected to be much lower than simulated deviation since the volume of real samples is much larger than the total simulation volume. Furthermore, experimental diffusivity on VPS-W with the same device already reported in [8], while conducted on different coatings (15% porosity instead of 23%), showed negligible deviation.

Influence of the Contact-Zone

The heat transfer process across internal boundaries in contact substantially degrades compared to the case of continuous homogeneous medium (perfect conduction). This is due to several factors, like non ideal contact between tungsten interlamellar boundaries, possible presence of oxides at interlamellar surfaces and entrapped gas molecules from the deposition process or after subsequent diffusion processes.

Because we cannot know the exact value of the average thermal conductivity at the contact-zone, similarly to the mechanical case, we adopted a parametrical approach. Details of the

CZ-model are reported in section 3.3.3.

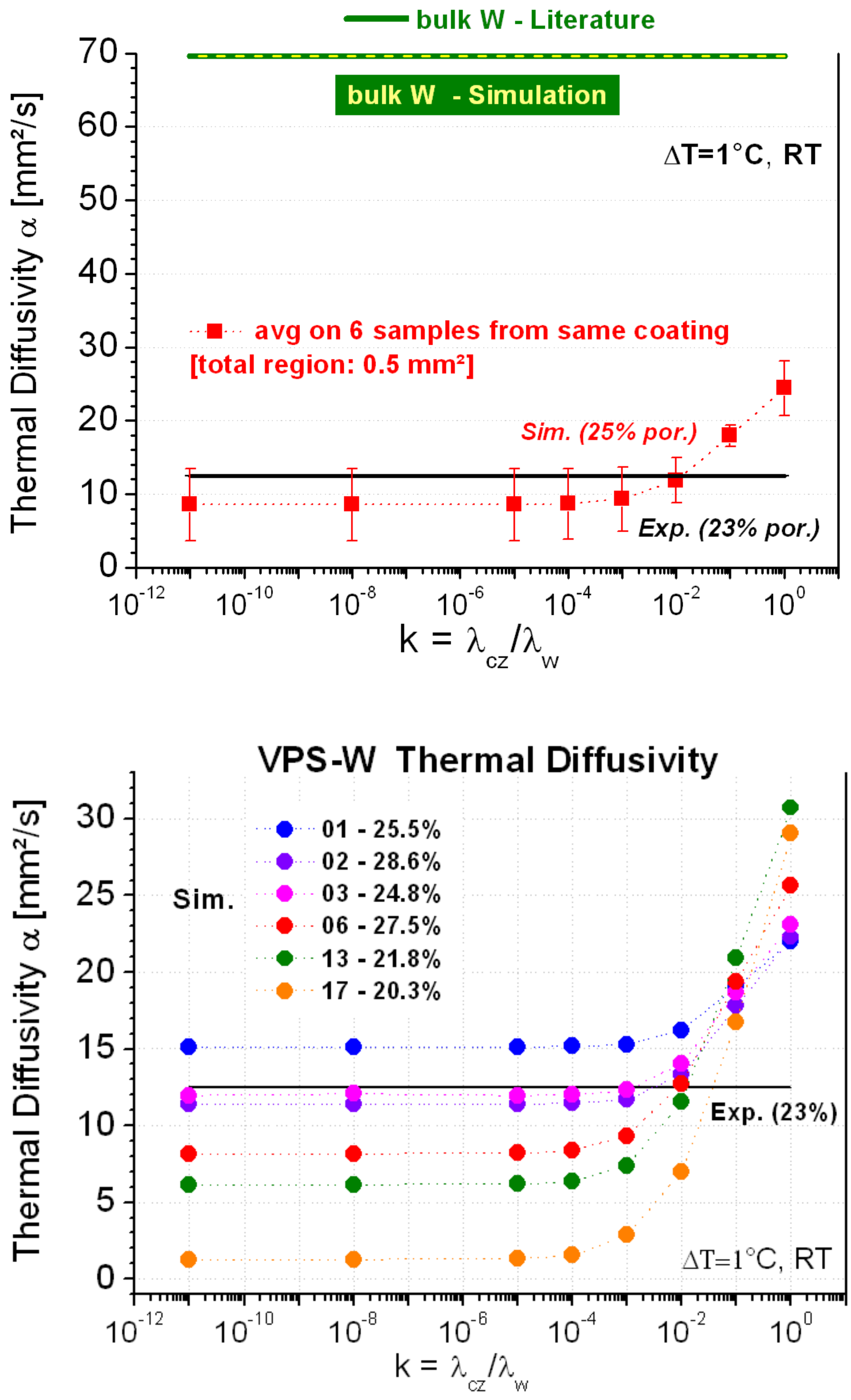

Figure 7.10: *Comparison between experimental data and simulations for the global thermal diffusivity of VPS-W calculated from steady state 2D-IBHR-CZ models. In a) is shown the gap between bulk-W (simulation results in yellow and literature data in green) and VPS-W 25% porous (as average on 6 micrographs representing a total region of 0.5 mm²). In b) the results from the individual micrographs are shown in detail. On the x-axis the parameter k indicates the reduction of thermal conductivity in contact zone. No experimental error bars are plotted since only one sample was measured (with a negligible error of 0.2% over ten pulses).*

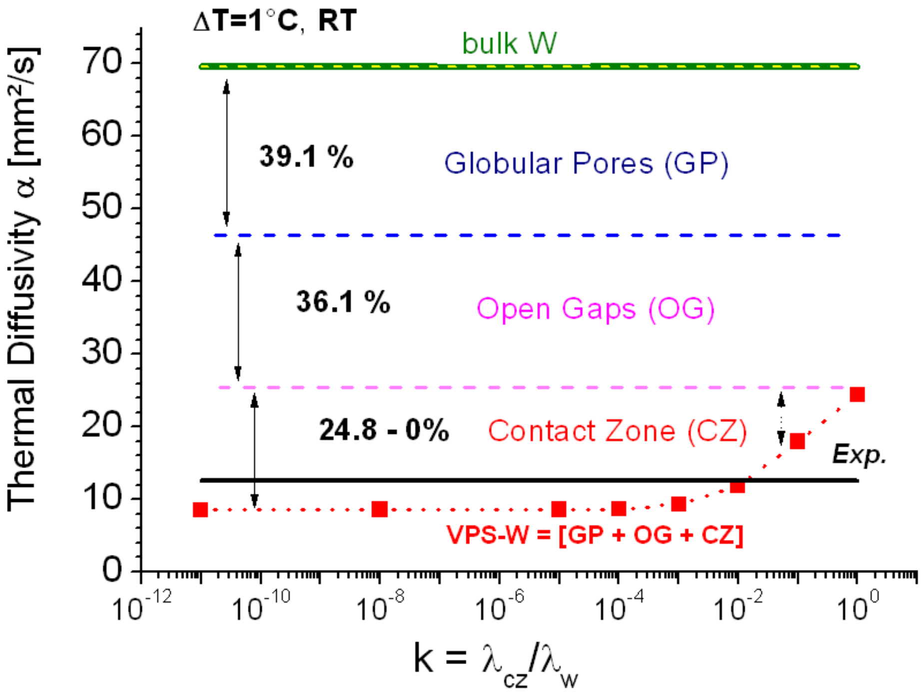

Figure 7.11: *Decomposition of the reduction of thermal conductivity in VPS-W Three contributions (globular pores, open gaps and contact-zone) have been quantitatively isolated via image processing and direct mapping FEM simulations*

A wide range of values for the reduced thermal conductivity in contact zone has been explored, from perfect conduction (k=1) towards perfect isolation ($k=10^{-11}$). This approach led to identification of a saturation effect for $k > 10^{-4}$, when the CZ acts as an insulator and heat „prefers" faster bulk channels. In saturation zone we could estimate the highest possible contribution of the CZ to the reduction of the average thermal diffusivity, which was close to 25%.

The big drop of factor 8 compared to the homogeneous W is due to additive microstructural effects which act as "hurdles" to the heat transfer: first globular pores, then elongated "crack-like" pores with small thickness (0.1-1µm) and finally interlamellar boundaries in contact (CZ). The IB-FEM approach allows to quantify each contribution, through quantitative "morphological decomposition". During image segmentation planar models were also generated with isolated globular pores (applying special Gaussian and blurring filters). Simulation were then performed once with globular pores only, once with globular and "crack-like" porosity together and finally with the full VPS-W microstructure (including the contact-zone). Results of the quantitative phase decomposition are shown in Fig. 7.11. If one considers the total contribution of interlamellar boundaries (open gaps plus CZ) , the partial decrease lies between 50 and 60% (depending on k), which is higher than the reduction caused by globular pores only.

As for comparison between numerical predictions and measurements, an overall good match was found. Only at high k-values (close to 1) the mismatch was relatively high (17%, referring to bulk-W), but such levels of k are certainly unrealistic (they would correspond to the scenario of perfect conduction at interlamellar boundaries). For more realistic values of k, say between

10^{-1} and10^{-4}, the mismatch ranges from +7% to -5%).

A negative mismatch was actually expected due to the planar approximation of the three-dimensional microstructure. Given a planar section of a 3D random porous medium, for the same applied gradient of temperature, average planar conductivity should be always lower or equal than average 3D-conductivity, because in 3D it is always possible to find heat conduction patterns across the pores which are at least as fast as those of the particular cross-section considered. Furthermore, in 3D there are always *different possible* heat-transfer patterns and among them it is highly probable to find faster patterns (except for very symmetrical cases, like a spherical hole in the middle of a cube).

The Laser Flash Apparatus

Experimental measurement of thermal diffusivity were obtained with a laser flash apparatus (LFA). An LFA is a laser-based device for measuring the thermal diffusivity of homogeneous and heterogeneous materials (with sufficiently small heterogeneities, because of the limited size of LFA-samples). Indirect estimation of thermal conductivity λ are also possible (through the basic relation $\lambda = \alpha \rho C_p$). An LFA measurement is based on the time dependent temperature evolution detected on the top external surface of a sample. The sample is hit from rear with a short laser pulse. The well known formula of Parker [145] relates thermal diffusivity α with the time $t_{1/2}$ required for the temperature on the top face to reach half of its recorded maximum:

$$\alpha = \frac{1.38 L^2}{\pi^2 t_{1/2}}$$

where L is the height of the sample. The Parker's formula is valid assuming one dimensional heat propagation and infinitesimal pulse length. It is usually corrected after measurement according to the Cape-Lehman's model [146] which considers radiation losses and finite pulse length. Modern devices use further corrections based on even more sophisticated numerical models for three dimensional heat propagation (however, limited to the homogeneous case). The device employed for this measurement was an LFA machine from NETSCH based on the improved Cape-Lehman model from Blumm [147]. The device is based on a Nd:YAG laser with pulse length of 0.8ms, pulse energy of 20 J/pulse and an InfraRed-InSb detector. LFA-measurements can be performed at different temperatures in a furnace under controlled gas or air atmosphere. Samples used for this measurement were cut from the same coating used to generate IB-FEM models. Due to the very limited material available (most was consumed for the preparation of tomographic samples), only one sample (Ø=12.63 mm, h=1.45mm) could be successfully measured with a serie of 10 pulses. The measurement reported was performed at RT under vacuum conditions (10^{-5} mbar) in order to neglect possible gas contribution to diffusivity, allowing a more precise comparison with IB-FEM calculations (which neglected the gas contribution across macro pores, as the VPS-W coatings were deposited in vacuum).

7.3.3 Estimation of 2D RVE for VPS-W

In our numerical investigation we had to face the computational challenge of mapping a complex morphology on large regions of our material in order for them to be sufficiently representative while, at the same time, keeping a high level of morphological details (i.e. mapping lower scale “crack-like” porosity). Moreover, we had to be compliant with the requirement of sufficiently high local refinement and good element shape in order to limit numerical artifacts. This turned into a technical “upper limit” for the size of the mapped regions and also implied restrictions on the total number of realizations.

A natural question arose: how representative for the whole material are the results derived on a limited number of finite size unit cells ? This question introduces the general micromechanical issue about the representative volume element (RVE) as discussed already in section 3.4.1.

In order to get a quantitative estimation of the RVE for VPS-W we followed the procedure based on the theoretical model of Kanit and Jeulin. Mathematical details of this method were resumed in section 3.4.1 and can be found in [107, 106].

The procedure is based on the study of the *size effect of the variance* of a given property (in our case thermal conductivity - λ).

To perform this study we need different “samples sets” Ω^{V_i} (= collection of meshed unit cells of size V_i) of different size representing the microstructure of VPS-W and calculate the average conductivity $\langle\langle\lambda\rangle\rangle_{\Omega^{V_i}}$ for each sample set (where the double-bracket symbol indicate a double average first on the single micrograph and then on the set).

Starting from the largest mesh set generated with OOF2 (6 samples of area 0.074 mm^2 each), we then generated smaller size realizations making use of a “splitting algorithm”, specifically developed for this scope. This algorithm takes meshes of the largest size and “split” them into smaller domains, keeping the same local refinement level and avoiding expensive re-meshing. It is based on the idea of small adjustment of nodes close to the “cutting-axis” (with a prescribed tolerance) in order to align those nodes which deviates from the axis before splitting them. Since the split axis can be any any desired (sub)-domain size can be obtained. In order to maintain the realizations as statistically independent as possible we tried to limit superposition between the new sub-micrographs by setting their centers as distant as possible each other. However, for sub-domain sizes greater than 25% of the original micrograph, a small superposition was unavoidable.

Table 7.4 resumes our realizations ensemble (6 sets covering approximately the same total volume indexed by percentage size with respect to the original set: 25%,33%,44%,50%,100%). Apparent thermal conductivity λ^{app}has been calculated for the 5 different sample-sets together with their associated variance (for a fixed value of k). The chosen value has been k = 1E-02 which gave a fair estimation of global diffusivity close to the value experimentally measured (Fig. 7.10). The sample aspect ratio L/H (L is the length and H the height of the micrograph) has been kept constant through the sets except for the half-size 50%-H and 50%-V obtained

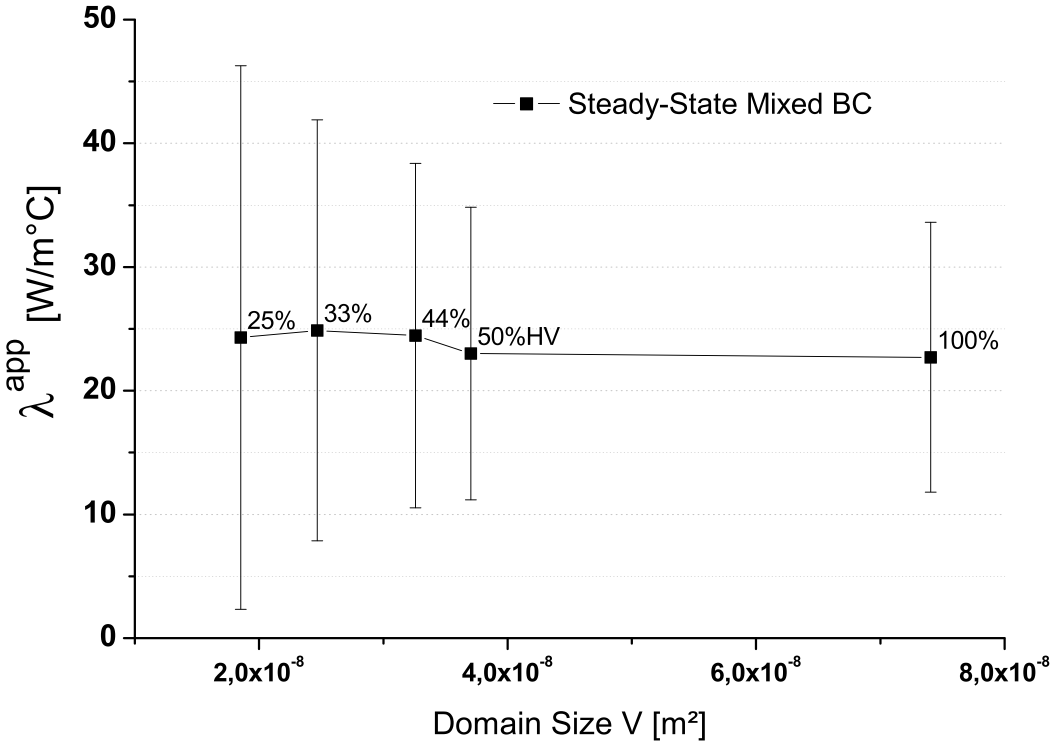

Figure 7.12: *Mean values and intervals of variation of the apparent conductivity, as a function of the domain size*

by splitting the original mesh with the vertical and horizontal median axis respectively; we then averaged on both series in order to limit aspect-ratio artifacts. The thermal gradient $\triangle T_{bottom}^{top}/H$ has been also kept constant among all the different sample-sets.

Results used for the RVE estimation are shown in Fig. 7.12 and 7.13. Monotonic convergence of the apparent property appears from the 44% set. The average value at the largest set ($\lambda_{100\%}^{app}$ = 22.70 W/m*K) has been taken as good estimation of effective thermal conductivity. With the variances of the domain sets we were then able to fit the data in Fig. 7.13with equation 3.27 and get an estimation of the parameter ξ to be used in relation 7.11. After estimating the point variance as indicated in [107] eq. 43, the found value for the second order integral range A_2 was about 3.7E-04 mm, fairly below the smallest volume size used (1.85E-02 mm for the 25% set). This would justify γ=1 and the use of eq. 3.27.

The general RVE relation found for the thermal-conductivity of our VPS-W finally reads:

Table 7.4: *The domain size sets (n is the number of realizations, V the volume of a single realization) considered for the RVE study*

V [%]	V [mm^2]	n	V$_{tot}$[mm^2]
25%	1,85E-02	24	4,44E-01
33%	2,47E-02	18	4,44E-01
44%	3,26E-02	18	5,87E-01
50%	3,70E-02	12	4,44E-01
100%	7,41E-02	6	4,44E-01

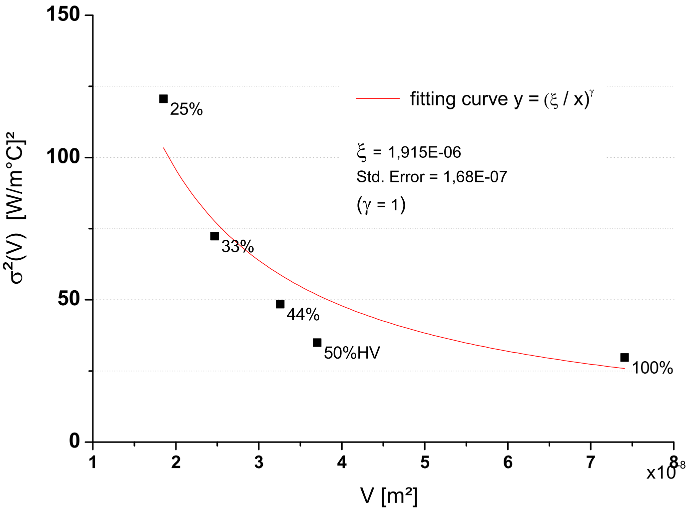

Figure 7.13: *Fitting of the variance behaviour for increasing volume of the sample sets. The points indicate the calculated variance on average values of thermal conductivity calculated for a given sample set. The 50%HV set (calculated splitting the original unit cell horizontally and vertically) shows the most deviating point probably due to a different aspect ratio and related boundary effects. All other sets had the same aspect ratio.*

$$V_{\lambda}^{RVE} = \frac{4\,\xi}{\bar{\lambda}^{2}\,\varepsilon^{2} n} = \frac{k}{\varepsilon^{2} n} \tag{7.11}$$

where the constant k has been estimated to be 1.47E-08. A visual representation of this formula is given in Fig. 7.14, where we plotted the relative error ϵ in the interval 1-100%.

The relative error of our data-set turned to lie close to 20%. However, as shown in Fig. 7.12 convergence of the average value was achieved within a good tolerance (~ 5%). We should also consider that the statistical definition of RVE is actually a parametrical one which *depends on* ϵ (the *prescribed* relative error to be satisfied for a given cell size to become an RVE). The tolerance value for a proper RVE is usually set in the range of 1 to 10% [107]. In our case we can therefore conclude that the ensemble chosen was still insufficient to be a proper RVE in strict sense. Considering the high variance of the volume fraction at the magnification used for the analysis, the result is not surprising. Nevertheless, the performed RVE calculation is a general characterization of the VPS-W morphology, (theoretically) independent from the particular set used for its estimation. It also remains an useful indicator to predict the minimum volume required to achieved a prescribed accuracy (in principle also valid for experimental measurements[5]). As evident from Fig. 7.14, to ensure a better statistical accuracy with the same sample size, e.g. targeting a relative error of10%, we should compute only 5 realizations more. Since the plot is in logarithmic scale, higher accuracy levels would be thinkable only with a major increase of the volume size, for a much higher computational price.

---

[5] of course with a certain approximation, since measurements refer to 3D samples and the calculated RVE to planar models

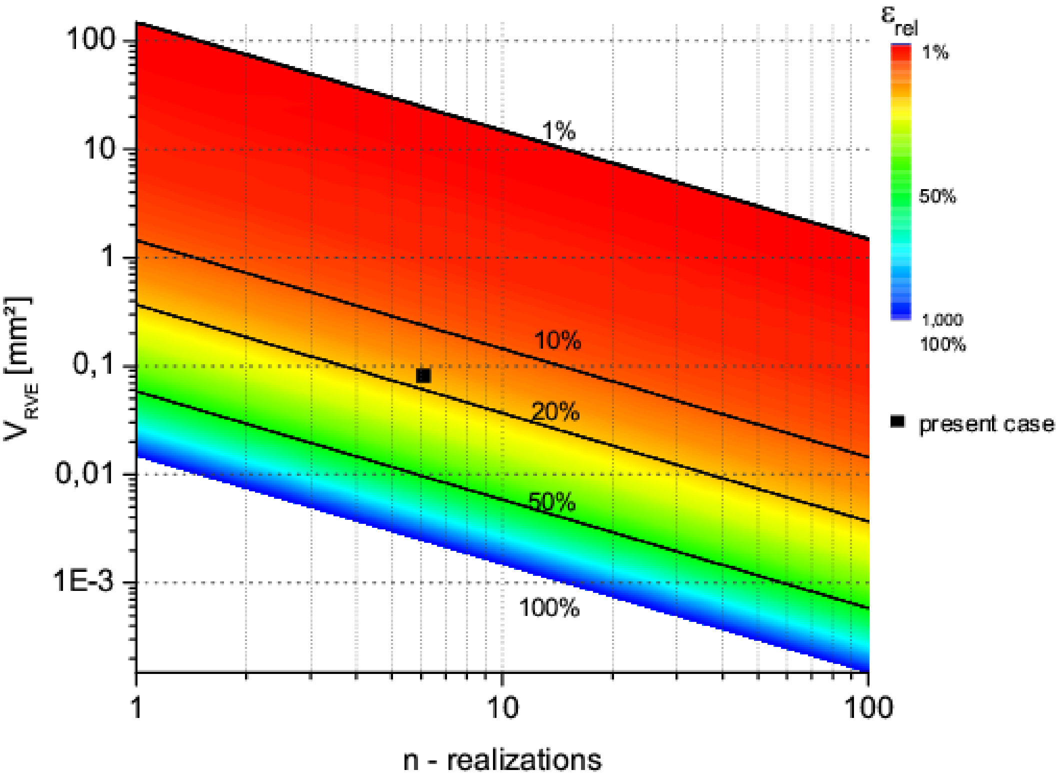

Figure 7.14: *Logarithmic RVE-plot showing the general relation between domain size V, number of realizations n and relative error ε when estimating the thermal conductivity of VPS-W (equation 7.11). The black square indicates the highest accuracy obtained with the largest unit cell size available (0.2mm*0.3mm, full size 2D-HRIB models, cf Fig. 7.1).*

Chapter 8

Summary and Conclusions

An advanced numerical technique has been presented for modeling the thermomechanical behaviour of heterogeneous materials for fusion applications. This technique, referred to as image-based finite element method, combines the finite element method with imaging of the real microstructure of heterogeneous materials.

The main focus of this work was to model *multiscale random* microstructures with inclusions of arbitrary shape. The two materials chosen for our investigation were W/CuCrZr composites and VPS-W coating.

In particular we focused on the following issues:

- damage evolution and failure
- RVE and stochastic accuracy
- heat transfer
- comparison between 2D and 3D models

Results were validated with experimental measurements in most cases.

8.1 W/CuCrZr Composites

Image-based FEM simulations were implemented to investigate the complex thermoelastoplastic deformation and failure mechanism of W/CuCrZr composites to be used for functionally graded interlayers of plasma-facing components for the future fusion reactors. Two material compositions, W30[%vol] and W70[%vol] were considered for the analysis.

To this end, we extended the image-based-FEM technique integrating a damage evolution model on large unit-cells. These were produced from high-resolution SEM images [2µm/px] of the random microstructure. We validated simulation findings through an extensive experimental campaign based on tensile tests at RT, 300 and 550 °C combined with fractographical inspection. Scope of the simulation campaign was to set up a numerical experiment close to the real one. Residual and thermal stresses developing during composite manufacturing and pre-heating during tensile tests were calculated during simulation.

The two phase-symmetric microstructural configurations (in planar section: ductile CuCrZr matrix with W-inclusions and brittle W-matrix with ductile CuCrZr inclusions) showed strong differences in their thermomechanical response, especially in ultimate strain and as expected in failure mode. The complex failure mechanism of the composites exhibited both ductile and brittle fracture. The numerical challenge was to develop a micro-mechanical numerical procedure able to capture both these aspects. Thanks to the direct calculation of mesoscale stress-strain fields on image-based domains, we could describe the mixed-failure mechanism. To this end, we combined simulation of damage initiation and evolution across the ductile phase with conditions for brittle crack onset in tungsten. Simulation could predict the starting location of failure on the simulation domain without specifying a predefined crack position.

Using this approach on large domains of the random microstructure, we could observe collective macroscale phenomena arising from the evolution of characteristic stress-strain fields at the mesoscale. The most significant phenomenon was spontaneous localization of plastic strain into characteristic patterns over the random morphology. These localization patterns preceded the onset of ductile failure and were remarkably oriented at 35° and 45° to loading direction (in W30[%vol] and W70[%vol] respectively). Mesoscale plastic strain localization within the ductile matrix was identified as the main failure mechanism in W30%.

Combining both simulation results at meso- and macroscale with experimental data, we could also qualitatively explain complex phenomena like the temperature dependence of composite ultimate strain and produce some well founded interpretations of the internal failure mechanisms. We could show, for instance, that only the assumption of a ductile local behaviour of the W-phase could account for large overall strains, in good agreement with experimental stress-strain curves at 300 and 550 °C. However, because fractographs suggested a rather brittle failure at 300°C and since crack propagation was not included in the model, we were not allowed to claim a ductile behaviour for the W-phase in the real case at this temperature. In this regard, we suggested an alternative interpretation: a yielded tungsten skeleton in composite seems numerically equivalent, in terms of macroscopic stress-strain response, to the collective effect of brittle micro-ruptures occurring sparse across the W-skeleton. However, further theoretical and numerical investigations are needed to confirm this statement.

During this investigation we also showed an important possible application of the IB-FEM technique. From the comparison of calculated stress-strain curves with experimental ones, we could guess meso-structural parameters otherwise difficult to be measured (like local yield stresses at different temperatures).

As future development of the present work, we finally suggest:

- to extend both the simulation and experimental ensembles to achieve an improved statistics
- further experimental investigations to shed light on open issues like the effective DBTT of the tungsten phase in composite and the internal failure mechanism of the W-skeleton
- tomographic 3D-models to overcome the structural limitations of planar models (particu-

larly affecting the W70% composition).

8.2 VPS-W

In this work, we showed how basic thermomechanical properties of VPS-W could be successfully predicted with an extensive use of the image-based finite element method starting from 2D as well as from 3D images of the real material microstructure. The complex random morphology of this material, characterized by multiscale random inclusions of non-elementary shapes, is a challenge for micro-mechanical material modeling, since the global material response is influenced by all kind of micro-heterogeneities (in particular globular pores up to hundreds of micrometers, interlamellar gaps up to some micrometers in thickness and internal boundaries in contact or partially in contact).

One of the main problem was to find an optimal combination of model size and image magnification. The ensemble of simulation cells had to be sufficiently extended to be statistically representative -or an RVE - for the whole material, while possessing at the same time high spatial resolution to resolve all the critical morphological features. This intermediate goal was achieved generating image-based models on cross-sectional SEM images of 1.5 mega-pixels at resolution of 0.2 µm/px. Mesh generation on such images required an extension of state-of-the-art in planar discretization of morphology. A very high adaptive mesh density was eventually used in combination with special segmentation techniques for the isolation of globular pores and interlamellar boundaries in contact (Contact-Zone).

As for 3D model generation, due to the very strong X-ray absorption by W, we must look to the very edge of feasibility of tomographic techniques. After optimizing the specimen geometry and several beam parameters, a high-energy synchrotron microtomography was successfully performed on the VPS-W coating system (coating layer and coating/substrate interlayer). This measurement produced the first three dimensional reconstruction of a porous microstructure entirely made of tungsten. Together with the coating, the plasma-sprayed W/Steel interlayer was also reconstructed. Due to poor contrast and presence of several kind of artifacts, special segmentation filters were tailored for the coating part. Quality of coating reconstruction was satisfactory. Globular pores could be well segmented while micro-porosity features below 2µm in size could not be included in the final reconstructions. On the other hand, the interlayer region was reconstructed in much higher quality thanks to the lower amount of tungsten. Unexpected high porosity was found at the interface coating/interlayer .

As for elastic properties, estimated Young's modulus for the coating transverse direction from 2D models was in good accordance with previous experimental measurements. The numerical calculation could also predict the component parallel to deposition direction, where no experimental data was available to date. On the other hand, 3D-unit cells were in the end less accurate than planar ones due to the lower spatial resolution. Nevertheless, they could be useful to assess the 2D/3D mismatch limited to the random arrangement of macro pores.

A probabilistic failure criterion based on and the cumulative probability function of planar stress-fields on planar image-based models was also proposed. We showed how this approach could be employed for deducing critical microscopic failure parameters like the ultimate strength in contact-zone from macroscopic experimental measurements. Experimental validation however, which would require an extended statistics on broken samples, is left to future development of the present work, together with an extension of the present simulation capability for predicting dynamic crack propagation across the complex microstructure.

As for thermal properties, coating conductivity was predicted from the only knowledge of tungsten conductivity and the application of the IB-FEM technique. The drop from homogeneous W of almost one order of magnitude was correctly predicted and validated by comparison with LFA diffusivity measurements. Moreover, we could quantify each morphological phase-contribution to the heat transfer reduction, showing in particular the influence of the Contact-Zone and the related saturation effect.

Finally, through an inverse mesh splitting algorithm developed to the scope, we could successfully apply the method of Jeulin and Kanit for the quantitative estimation of the RVE, assessing statistical accuracy of the ensemble used for thermal calculations. In this regard, a general predictive estimation of the RVE size (expressed as relation between variance, micrograph size and number of realizations) was obtained. As for the case considered, while the sample set was large enough to allow converged average predictions, it was insufficient to be considered a proper RVE of the material in strict sense, due to an insufficient number of samples.

8.3 Concluding Remarks

While already established as numerical technique in micromechanics, the image-based FEM approach is new in modeling materials for fusion applications. As we have seen, it can be a valuable instrument to investigate the material behaviour and the link between microstructure and macroscopic response even in case of very complex random morphologies.

Several ways to improve and extend the present contribution are obviously possible.

The first one we may think is the use of full dimensional tomographic models of W/CuCrZr. The extent of the accuracy of the planar approximation used in this work could be evaluated through numerical experiments on 3D models with real morphology. However, feasibility of this measurement could be an issue for compositions with high amount of W.

An improvement in spatial resolution for the present 3D models of VPS-W is also desirable in order to include the missing morphological micro-features. However, this very demanding requirement seems hard to be fulfilled by improvement of tomographic techniques. Integration of existing tomographic data with SEM or FIB imaging appears a more feasible scenario.

Concerning the micromechanical framework for modeling both materials, an extension in upscaling direction is also desirable. Stochastic FEM and iterative computational homogenization could be employed to extend the macroscale to macroscopic regions of the reactor vessel, taking into account its real geometry on a larger macroscale.

As for extending the simulation capability, the most important challenge to face in the coming future is the implementation of a *brittle fracture propagation* model on the complex 2D and 3D domains of VPS-W and W/CuCrZr (in the mixed ductile-brittle material, such a model should coexist with the local ductile damage model, already implemented for the planar case). In order to tackle both these numerical problems the most promising approach appears the extended finite element method (X-FEM) based on enriched functions and phantom nodes at the crack-tip zone preventing re-meshing [149, 150, 151]. This technique has been gaining favour from the fracture mechanics modeling community since more than ten years [152]. However, while some works have been published recently using tomographic data to validate predicted crack patterns[69, 68], these XFEM calculations were performed on homogeneous models (without meshing the heterogeneities). It appears therefore natural to extend the X-FEM approach on tomographic models of complex random microstructures generated via direct mapping meshing. Fig. 8.1 shows a preliminary study on tomographic models of VPS-W, where crack initiation and propagation was limited to the very early stage due to strong numerical instabilities. However, the results is still interesting as it shows the capability of the XFEM to calculate the location of the crack onset (without a predefined path) and it also shows how this location differs substantially in 3D models from equivalent 2D models .

A final important remark is given. In future, we could think to employ the IB-FEM to *optimize material properties* in order to achieve particular thermomechanical performances at component level. We can think for instance at the W/CuCrZr FGM multilayer and the related problem of heat transfer optimization avoiding failure under very high heat-fluxes (and also the recent issue of limiting the amount of copper used in order to reduce neutron embrittlement [148]). A multi-parametric model should relate structural parameters (like the set h_1, h_2, h_3 of the single layer heights) to macroscopic quantities like the overall thermal conductivity of the full FGM structure, to be maximized. At the same time, the optimized set should be compliant with safety bounds, like limits on the local stress peaks in order to avoid local failure spots. One may think to employ the IB-FEM and its very accurate local solution to check these limits in a iterative numerical optimization scheme where the local solution of a proposed optimized configuration could be controlled and re-adjusted at each optimization step. Since the FGM-multilayer structure and other component design parameters can be well controlled during manufacturing, we could think to perform a*n IB-FEM driven multiscale optimization* of the real component.

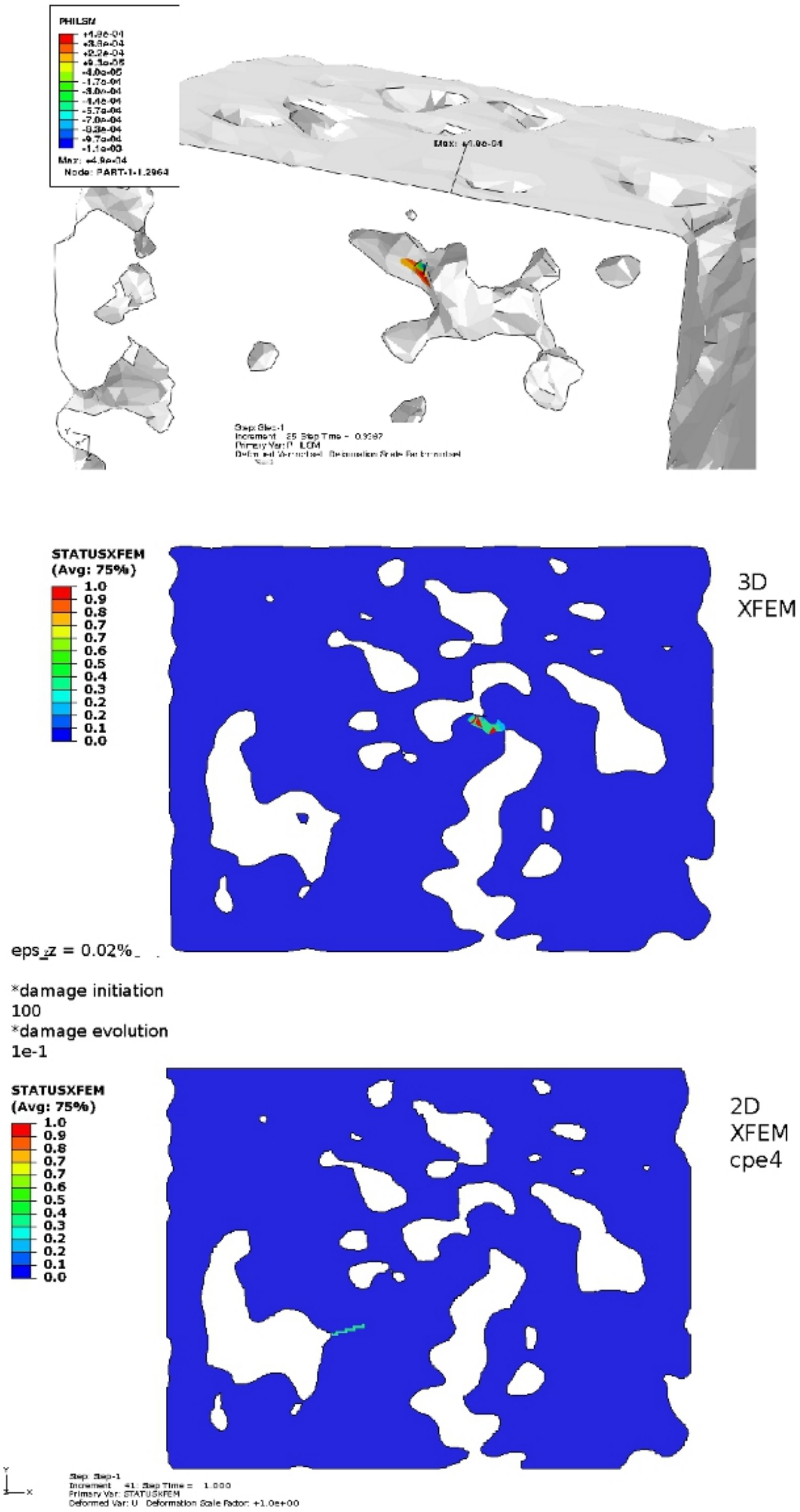

Figure 8.1: *Preliminary result of an XFEM simulation of crack initiation and propagation across 3D and 2D models of VPS-W.*

Appendix A - Elementary Equations

Thermoelasticity

Within the small strain assumption we can decompose the total strain in elastic, plastic and thermal part:

$$\varepsilon_{ij} = \varepsilon_{ij}^{el} + \varepsilon_{ij}^{pl} + \varepsilon_{ij}^{th} \tag{8.1}$$

The general constitutive law relating stress and strain in a elastic anisotropic media in three dimensions reads (Hook's law):

$$\sigma_{ij} = E_{ijkl}\varepsilon_{lk} \tag{8.2}$$

where σ_{ij} is the second rank stress tensor and E_{ijkl} is the fourth rank elasticity tensor.

Assuming isotropy of response in both the deformation and dilatation phenomena one can write the basic constitutive equation of thermoelasticity as (where ε_{ij}^{pl} is zero in 8.1):

$$\varepsilon_{ij} = \frac{1+\upsilon}{E}\sigma_{ij} - \frac{\upsilon}{E}\sigma_{kk}\delta_{ij} + \alpha(T - T_0)\delta_{ij} \tag{8.3}$$

which expresses the sum of the elastic and thermal terms in equation 8.1.

When considering a variation of temperature without stress, one obtains the isotropic coefficient of thermal expansion :

$$\alpha = \frac{\varepsilon_{ij}}{(T - T_0)\delta_{ij}} \tag{8.4}$$

Plasticity

The classical flow theory of plasticity is based on the work of Tresca and Von Mises. Formally, the general equations of a flow theory model are[1] :

$$The\,yield\,surface\,condition: \qquad f(\sigma_{ij}, H_\alpha, T) \leq 0 \tag{8.5}$$

$$The\,flow\,rule: \qquad \dot{\varepsilon}_{ij}^{pl} = \dot{l}\frac{\partial g(\sigma_{ij}, H_\alpha, T)}{\partial \sigma_{ij}} \tag{8.6}$$

$$The\,hardening\,model: \qquad \dot{H}_\alpha = \dot{l}\dot{h}_\alpha(\sigma_{ij}, H_\beta, T) \tag{8.7}$$

where a dot over a symbol denotes differentiation with respect to a formal parameter in rate-dependent models, g is the flow potential (whose gradient in stress space give the direction of the plastic strain rate), l is called plastic multiplier, H_α and$h_\alpha$are the hardening parameters and function respectively.

The behavior of most metals can be well described using a flow rule where the direction of the plastic strain rate is normal to the yield surface (associated flow rule). Under uniaxial loading the stress transmitted by a yielding material may increase, known as hardening, or decrease, referred to as softening. During hardening or softening, the elastic domain undergoes a certain modification. This evolution of the yield surface during plastic flow is described by equations 8.6-8.7. For most rate-independent plasticity models the direction of flow is the same as the direction of the outward normal to the yield surface:

$$\frac{\partial g}{\partial \sigma_{ij}} = c\frac{\partial f}{\partial \sigma_{ij}} \tag{8.8}$$

where c is a scalar. Such models are called "associated flow" plasticity models. The behavior of most metals can be well described using an associated flow rule. However, this is generally not accurate for materials in which the inelastic deformation is primarily caused by frictional mechanisms. A more general plasticity model can involve a set of yield surfaces f_i, flow potential functions g_i and hardening evolution functions$h_{i\alpha}$. In complex plasticity models—for example, models used to describe the cyclic behavior of metals used for high temperature applications—these evolution laws have complicated forms, since such complexity is required to match the experimentally observed behavior.

For an isotropic material, the elastic region can be defined in the space of the principal stresses. In the case of metallic materials, it has been observed experimentally that yielding is not affected by hydrostatic loads. In other words, the yield criterion is function only of the deviatoric stress tensor. And as the first invariant of the stress deviator tensor, $j(1)(\sigma_{ij}^{dev})$, is zero, it can be deduced that the general form of the yield criterion must be:

---

[1] The yield condition does not contain enough information to obtain the whole plastic strain tensor, which has six independent components. Therefore, an additional rule governing the evolution of the plastic flow, the flow rule, must be postulated.

$$f(j(2)(\sigma_{ij}^{dev}),\, j(3)(\sigma_{ij}^{dev}),\, H_\alpha) \leq 0 \tag{8.9}$$

From this general formulation the theory of isotropic and kinematic hardening follows (not treated here). Isotropic hardening is generally considered to be a suitable model for non-cycling problems without unloading, where no Bauschinger effect appears. Due to the nature of MMCs' matrices, only criteria for isotropic pressure independent materials should be considered. There exist several yield criteria for different materials. The usual suitable criteria for metals are the Mises and Tresca criteria. In modeling the early stage of elastoplastic behaviour of W/CuCrZr composites, we assumed isotropic hardening for CuCrZr with and perfect plasticity for W, both with Mises criterion for yielding.

Heat Transfer

The general time-dependent heat transfer equation in two-dimensions for an heterogeneous material reads:

$$\frac{\partial T}{\partial t} = \alpha_{ij}(x,y,T)\nabla^2 T(x,y) \tag{8.10}$$

where $\alpha_{i,j}$ is the local tensor of thermal diffusivity generally temperature and position dependent, while the corresponding steady-state heat transfer equation (derivable from 8.10) is described by the Fourier's law:

$$q(x,y) = -\lambda_{ij}(x,y,T) \cdot \nabla T(x,y) \tag{8.11}$$

where $\lambda_{i,j}$ is the local tensor of thermal conductivity (also temperature and location dependent in multiphase materials).

For the characterization of a microstructured heterogeneous material the parameters to be found are the effective homogenized macroscale properties (which are function of the local ones):

$$\alpha_{ij}^{eff} = f(\alpha_{ij}(x,y,T)) =? \;;\; \lambda_{ij}^{eff} = f(\lambda_{ij}(x,y,T)) =? \tag{8.12}$$

Bibliography

[1] C.M.Braams and P.E.Stott. *Nuclear Fusion: Half a Century of Magnetic Confinement Fusion Research*, 2002.

[2] W. Hofer, J. Roth (Ed.). *Physical Processes of the Interaction of Fusion Plasmas with Solids*, San Diego, 1996.

[3] R. Behrisch and D. E. Post (Ed.). Physics of Plasma Wall Interactions in Controlled Fusion, *Proceedings of a NATO Advanced Study Institute*, New York, 1985.

[4] K. Ehrlich. Materials research towards a fusion reactor, *Fusion Engineering and Design*, 56-7:71-82, 2001.

[5] S. J. Zinkle and N. M. Ghoniem. Operating temperature windows for fusion reactor structural materials, *Fusion Engineering and Design*, 51-52:55-71, 2000.

[6] N. Baluc. Assessment report on W, *Final report on EFDA task* TW1-TTMA-002 Deliverable 5, 2002.

[7] Karlsruher Institut für Technologie (KIT) - Divertor Development for Fusion Reactors, http://www.iam.kit.edu/wpt/english/313.php

[8] H. Bolt, V. Barabash, W. Krauss et al. Materials for the plasma-facing components of fusion reactors, *Journal of Nuclear Materials,* 329–333:66–73, 2004.

[9] E.Lassner and W.D.Schubert. *Tungsten: Properties, Chemistry, Technology of the Element, Alloys, Chemical Compounds*, Kluwer Academy, 1998.

[10] D. Pettifor. *Bonding and Structure of Molecules and Solids.* Clarendon Press, Oxford, 1995.

[11] J.R. Davis. *Handbook of thermal spray technology*, Thermal Spray Society Training Committee, ASM International, 2004.

[12] R. Neu, M. Balden, V. Bobkov et al. Plasma wall interaction and its implication in an all tungsten divertor tokamak, *Plasma Physics and Controlled Fusion*, 49-B59, 2007.

[13] R. Neu, V. Bobkov, R. Dux et al. Final steps to an all tungsten divertor tokamak, *Journal of Nuclear Materials,* 363–365:52–59, 2007.

[14] R. Neu, H. Maier, E. Gauthier et al. Investigation of tungsten coatings on graphite and CFC, *Physica Scripta*, 128:150, 2007.

[15] H. Greuner, H. Bolt, B. Böswirth, S. Lindig, W. Kühnlein and T. Huber. Vacuum plasma-sprayed tungsten on EUROFER and 316L: Results of characterisation and thermal loading tests, *Fusion Engineering and Design*, 75-79:333, 2005.

[16] F.L. Chong, J.L. Chen, J.G. Li et al. Failure behaviors of vacuum plasma sprayed tungsten coatings for plasma facing application, *Journal of Nuclear Materials,* 386–388:780–783, 2009.

[17] A.S. Kukushkin, H.D. Pacher, G. Federici et al. Divertor issues on ITER and extrapolation to reactors, *Fusion Engineering and Design*, 65(3):355-366, 2003.

[18] G. Federici, C.H. Skinner, J.N. Brooks et al. Plasma-material interactions in current tokamaks and their implications for next step fusion reactor, *Nuclear Fusion*, 41(12):1967-2137, 2001.

[19] M. Merola, W. Dänner, J. Palmer, G. Vielder, and C. H. Wu. European contribution to the development of the ITER divertor, *Fusion Engineering and Design*, 66-68:211217, 2003.

[20] J. H. You, H. Bolt. Analysis of singular interface stresses in dissimilar material joints for plasma facing components, *Journal of Nuclear Materials,* 299 1-8, 2001.

[21] D. Maisonnier. Plant models for DEMO, *Burning Plasma Diagnostics*, Volume 988 of AIP Conference Proceedings, 52-59, 2008.

[22] D. Maisonnier, I. Cook, P. Sardain et al. *EFDA Final Report of the European Fusion Power Plant Conceptual Study (PPCS)*, Technical report, EFDA, 2004.

[23] Thin S. Kuroda and T.W. Clyne. The quenching stress in thermally sprayed coatings. *Solid Films*, 200(1):49 66, 1991.

[24] Yin, H. M., Sun, L. Z., and Paulino, G. H., 2004, “Micromechanics-Based Elastic Model for Functionally Graded Materials With Particle Interactions,” Acta Mater., 52, pp. 3535–3543.

[25] A. Kawasaki and R. Watanabe. Concept and P/M fabrication of functionally gradient materials, *Ceramics International,* 23(1):73-83, 1997.

[26] B. Kieback, H. Bolt, A. Brendel. W/Cu-Gradientenstrukturen für Komponenten mit unmittelbarem Plasmakontakt in Fusionsreaktoren, accepted proposal for the German Research Council (DFG), 2008.

[27] A. D. Ivanov, A. K. Nikolaev, G. M. Kalinin, and M. E. Rodin. Effect of heat treatments on the properties of CuCrZr alloys, *Journal of Nuclear Materials*, 307:673-676, 2002.

[28] S. Nawka, B. Kieback, T. Schubert et al. Synthesis, characterization and FEM-simulation of W/CuCrZr composites for extreme thermal applications, *Proceedings of the PM2010 World Congress*, 2010.

[29] W. Schatt, K.-P. Wieters, B. Kieback (Eds.). *Pulvermetallurgie / Technologien und Werkstoffe*, Springer-Verlag, Berlin, Heidelberg, 2007.

[30] B. Kieback, A. Neubrand, H. Riedel et al. Processing techniques for functionally graded materials, *Materials Science and Engineering* A362:81, 2003.

[31] G. Pintsuk, S.E. Brünings, J.-E. Döring et al. *Fusion Engineering and Design,* 66-68:237, 2003.

[32] U. Birth, M. Joensson and B.Kieback. Centrifugal Powder Forming (CPF) – Possibilities and limits of a special powder compaction process. *Proceedings of the Powder Metallurgy World Congress* 375, Granada, Spain 1998.

[33] C.-C. Ge, J.-T. Li, Z.-J. Zhou et al. Development of functionally graded plasma-facing materials, *Journal of Nuclear Materials* 283-287:1116, 2000.

[34] R.M. German. A model for the thermal properties, *Metallurgical Transactions A*, 24A:1745, 1993.

[35] M.Takahashi, Y.Itho, H.Takano, T.Okuhata. Fabrication of tungsten/copper graded material, *International Journal of Refractory Metals & Hard Materials*, 12:243-250, 1994.

[36] Y. Itoh, M. Takahashi, H.Takano. Design of tungsten/copper graded composite for high heat flux components, *Fusion Engineering and Design,* 31 279-289, 1996.

[37] Z.Y. Zhong, H. Saka, T.H. Kim, E.A. Holm, Y.F. Han and X.S. Xie. Research on W/Cu Functionally Graded Materials as Divertor Material in China, *Materials Science Forum,* 475-479:1371-1376, 2005.

[38] H. J. Böhm. *A short introduction to continuum micromechanics.* In "Mechanics of Microstructured Materials", volume 464, pages 1–40. Springer–Verlag, Vienna, CISM Courses and Lectures, 2004.

[39] T.Nakamura, S. Suresh, Effects of Thermal Residual Stresses and Fiber Packing on Deformation of Metal–Matrix Composites, *Acta metall.mater.* 41, 1665–1681, 1993.

[40] W. Voigt. *Lehrbuch der Kristallphysik*, Teubner, Leipzig, 1928.

[41] O. Wiener. Die Theorie des Mischkörpers für das Feld des stationären Strömung. *Abhandlungen der mathematisch physischen Klasse der königlich sächsischen Gesellschaft der Wissenschaften*, 32, 509–604, 1912.

[42] A. Reuss. Berechnung der Fliessgrenze von Mischkristallen auf Grund der Plastizitätsbedingung für Einkristalle, *Zeitschrift für Angewandte Mathematik und Mechanik*, 9, 49–58, 1929.

[43] Z. Hashin and S. Shtrikman. A variational approach to the theory of the effective magnetic permeability of multiphase materials, *Journal of Applied Physics*, 33, 3125–3131, 1962.

[44] Z. Hashin and S. Shtrikman. Conductivity of polycrystals, *Physical Review*, 130:129–133, 1963.

[45] R. Hill. Elastic properties of reinforced solids: some theoretical principles. *Proceedings of the Physical Society of London,* London A 65, 349– 354, 1952.

[46] B. Lu, S. Torquato. General formalism to characterize the microstructure of polydispersed random media, *Physical Review A*, Vol 43, N 4, 2078-80, 1991.

[47] S. Torquato. *Random Heterogeneous Materials*, Springer Verlag, New York, 2002.

[48] T.W. Clyne and P.J. Whiters. *An Introduction to Metal Matrix Composites*, Cambridge Solid State Science Series, Cambridge University Press, 1993.

[49] J. D. Eshelby. The determination of the elastic field of an ellipsoidal inclusion and related problems, *Proceedings of the Royal Society of London A*, 241:376–396, 1957.

[50] H. Hatta and M. Taya. Equivalent inclusion method for steady state heat conduction in composites, *The International Journal of Engineering Science*, 24(7):1159–1172, 1986.

[51] T. Mura. *Micromechanics of Defects in Solids*, Martinus Nijhoff, Dordrecht, Netherlands, 1987.

[52] T. Mori and K. Tanaka. Average stress in the matrix and average elastic energy of materials with misfitting inclusions, *Acta Metallurgica,* 21:571–574, 1973.

[53] Y. Benveniste. Some remarks on three micromechanical models in composite media, *Journal of Applied Mechanics,* 57:474–476, 1990.

[54] M. L. Dunn and H. Ledbetter. Elastic–plastic behavior of textured short–fiber composites, *Acta Materialia*, 45:3327–33404, 1997.

[55] H.E. Pettermann. *Derivation and Finite Element Implementation of Constitutive Material Laws for Multiphase Composites based on Mori–Tanaka Approaches,* VDI–Verlag (Reihe 18, Nr.217), Düsseldorf, Germany 1997.

[56] H.E. Pettermann, H. J. Böhm and F. G. Rammerstorfer. Some direction dependent properties of matrix–inclusion type composites with given reinforcement orientation distributions, *Composites Part B*, 28B:253–264, 1997.

[57] E.N. Gilbert. Random subdivisions of space into crystals, *The Annals of Mathematical Statistics*, 33:958–972, 1962.

[58] S.H. Chan and A.H.W. Ngan. Statistical distribution of forces in stressed 2-D low-density materials with random microstructures, *Mechanics of Materials*, 38:1199–1212, 2006.

[59] D. Jeulin and M. Ostoja-Starzewski. *Mechanics of Random and Multiscale Microstructures*, Springer, 2001.

[60] M.J. Pindera, J. Aboudi. Limitations of the uncoupled, RVE-based micromechanical approach in the analysis of functionally graded composites, *Mechanics of Materials,* 20:77-94, 1995.

[61] J.Y. Li. Thermoelastic behavior of composites with functionally graded interphase: a multi-inclusion model, *International Journal of Solids and Structures*, 37:5579-5597, 2000.

[62] J.R. Cho and D.Y. Ha. Averaging and finite-element discretization approaches in the numerical analysis of functionally graded materials, *Materials Science and Engineering A*, 302:187-196, 2001.

[63] V. Birman and L.W. Byrd. Modeling and Analysis of Functionally Graded Materials and Structures, *Applied Mechanics Reviews,* 60(5):195216, 2007.

[64] S.B. Biner. Thermo-elastic analysis of functionally graded materials using Voronoi elements, *Materials Science and Engineering A*, 315:136-146, 2001.

[65] P.R. Marur, H.V. Tippur. Numerical analysis of crack-tip fields in functionally graded materials with a crack normal to the elastic gradient, *International Journal of Solids and Structures*, 37:5353-5370, 2000.

[66] J. Abanto-Bueno and J. Lambros. Parameters controlling fracture resistance in functionally graded materials under mode I loading, *International Journal of Solids and Structures*, 43(13):3920-3939, 2006.

[67] T. Wiederkehr et al. An image morphing method for 3D reconstruction and FE-analysis of pore networks in thermal spray coatings, *Computational Materials Science*, 47(4):881-889, February 2010.

[68] E.Ferrié, J-Y.Buffière, W. Ludwig et al. Fatigue crack propagation: In situ visualization using X-ray microtomography and 3D simulation using the extended finite element method, *Acta Materialia*, 54(4):1111-1122, 2006.

[69] J. Rannou, J. Limodin, J. Réthoré et al. Three dimensional experimental and numerical multiscale analysis of a fatigue crack, *Computer Methods in Applied Mechanics and Engineering,* 199(21-22):1307-1325, April 2010.

[70] J.F. Despois, A. Marmottant, L. Salvo et al. Influence of the infiltration pressure on the structure and properties of replicated aluminium foams, *Materials Science and Engineering A,* 462:68–75, 2007.

[71] C. Requena, H.P. Degischer, E. Marks, E. Bolleret. Microtomographic study of the evolution of microstructure during creep of an AlSi12CuMgNi alloy reinforced with Al2O3 short fibres, *Materials Science and Engineering A,* 487:99–107, 2008.

[72] Leon L. Mishnaevsky Jr. Automatic voxel-based generation of 3D microstructural FE models and its application to the damage analysis of composites, *Materials Science and Engineering: A,* 407(1-2):11-23, October 2005.

[73] P. G. Klemens. Thermal Conductivity of Inhomogeneous Media, *High Temperatures – High Pressures*, 23(3):241-248, 1991.

[74] S. Raghavan, H. Wang, R. B. Dinwiddie, W. D. Porter, and M. J. Mayo. The Effect of Grain Size, Porosity and Yttria Content on the Thermal Conductivity of Nanocrystalline Zirconia, *Scripta Materialia*, 39(8):1119-1125, 1998.

[75] W. Schlichting, N. P. Padture, and P. G. Klemens, Thermal Conductivity of Dense and Porous Yttria-Stabilized Zirconia, *Journal of Materials Science*, 36:3003-3010, 2001.

[76] R. McPherson, A Model for the Thermal Conductivity of Plasma- Sprayed Coatings, *Thin Solid Films*, 112:89-95, 1984.

[77] S. Boire-Lavigne, C. Moreau, and R.G. Saint-Jacques. The Relationship Between the Microstructure and Thermal Diffusivity of Plasma-Sprayed Tungsten Coatings, *Journal of Thermal Spray Technology*, 4:245-251,1995.

[78] C. Moreau, P. Fargier-Richard, R.G. Saint-Jacques et al. Thermal Diffusivity of Plasma-Sprayed Tungsten Coatings, *Surf Coat. Technol.,* 161:67-71, 1993.

[79] R. Bolot, G. Antou, G. Montavon, C.A. Coddet. A two-dimensional heat transfer model for thermal barrier coating: average thermal conductivity computation, *Numerical Heat Transfer Part A: Applications,* 47-49:875-898, 2005.

[80] A.C.E. Reid, S. A. Langer, R. C. Lua et al. Image-based finite element mesh construction for material microstructures, *Computational Materials Science,* 43:989–999, 2008.

[81] S. A. Langer, A.C.E. Reid, S.I. Haan, R.E. Garcıa et al. The OOF2 Manual, http://www.ctcms.nist.gov/~langer/oof2man/, 2008.

[82] S.A. Langer, E.R. Fuller Jr. and W.C. Carter. OOF: an imagebased finite-element analysis of material microstructures, *Computing in Science & Engineering,* 3(3):15-23, 2001.

[83] C.H. Hsueh, E.R. Fuller Jr., S.A. Langer et al. Analytical and numerical analyses for two-dimensional stress transfer, *Materials Science and Engineering A,* 268(1-2):1-7, 1999.

[84] A. Saigal and E.R. Fuller Jr. Analysis of stresses in aluminum– silicon alloys, *Computational Materials Science*, 21(1):149, 2001.

[85] V. Cannillo, C. Leonelli and A.R. Boccaccini. Numerical models for thermal residual stresses in Al2O3 platelets/borosilicate glass matrix composites, *Materials Science and Engineering A,* 323:246–250, 2002.

[86] V.Cannillo, T.Manfredini, M.Montorsi et al. Characterisation of glass matrix composites reinforced with lead zirconate titanate particles, *Materials Science and Engineering A,* 399(1-2):281 291, 2005.

[87] V. Cannillo, L. Esposito, G. Pellicelli, A. Sola, and A. Tucci. Steel particles-porcelain stoneware composite tiles: An advanced experimental-computational approach, *Journal of the European Ceramic Society*, 30(8):1775 1783, 2010.

[88] N. Chawla, B.V. Patel, M. Koopmana et al. Microstructure-based simulation of thermomechanical behavior of composite materials by object-oriented finite element analysis, *Materials Characterization*, 49:395-407, 2003.

[89] Y. Dong, D. Bhattacharyya, P.J. Hunter. Experimental characterisation and object-oriented finite element modelling of polypropylene/organoclay nanocomposites, *Composites Science and Technology* 68:2864-2875, 2008.

[90] G. Bolelli, V. Cannillo, L. Lusvarghi et al. Glass–alumina composite coatings by plasma spraying. Part II: Microstructure-based modeling of mechanical properties, *Surface & Coatings Technology,* 201:474-486, 2006.

[91] A.D. Jadhav, N.P. Padture, E. H. Jordan et al. Low-thermal-conductivity plasma-sprayed thermal barrier coatings with engineered microstructures, *Acta Materialia,* 54:3343-3349, 2006.

[92] Abaqus Analysis User's Manual, Release 6.9 (Providence, RI: 2009), Figure 21.2.3-1

[93] G.F.Matthews, P. Coad, H. Greuner et al. Development of divertor tungsten coatings for the JET ITER-like wall, *Journal of Nuclear Materials*, 390-391(15):934-937, June 2009.

[94] DIN EN 2002-002 Luft- und Raumfahrt - Metallische Werkstoffe - Prüfverfahren - Teil 2: Zugversuch bei Hochtemperatur; Deutsche und Englische Fassung EN 2002-002:2005, Beuth Verlag 2006.

[95] H. J. Böhm and W. Han. Comparisons between three-dimensional and two-dimensional multi-particle unit cell models for particle reinforced metal matrix composites *Modelling Simul. Mater. Sci. Eng.* 9:47-65, 2001.

[96] T. Hirai, N. Bekris, J.P. Coad, C. Grisolia, J. Linke, H. Maier, G.F. Matthews, V. Philipps, and E. Wessel. Failure modes of vacuum Plasma-Sprayed tungsten coating created on carbon bre composites under thermal loads, *Journal of Nuclear Materials*, 392(1):40 44, 2009.

[97] J.H. You, T. Höschen, S. Lindig. Determination of elastic modulus and residual stress of plasma-sprayed tungsten coating on steel substrate, *Journal of Nuclear Materials,* 348:94–101, 2006.

[98] N. El-Kaddah, J. McKelliget and J. Szekely, Heat transfer and fuid flow in Plasma-Spraying, *Metallurgical and Materials Transactions B*, 15:5970, 1984.

[99] A.-F. Kanta, M.-P. Planche, G. Montavon, and C. Coddet. In-flight and upon impact particle characteristics modelling in Plasma-Sprayed process, *Surface and Coatings Technology,* 204(9-10):1542 1548, 2010.

[100] Böhm H.J., Han W.: Comparisons Between Three-Dimensional and Two-Dimensional Multi-Particle Unit Cell Models for Particle Reinforced MMCs; Modell.Simul.Mater.Sci. Engng. 9:47–65, 2001.

[101] Ch. Geuzaine and J-F. Remacle, Gmsh: a three-dimensional finite element mesh generator with built-in pre- and post-processing facilities, http://geuz.org/gmsh/, 1997-2010

[102] S. Kuroda, J. Kawakita, M. Watanabe et al. Warm spraying—a novel coating process based on high-velocity impact of solid particles, *Science and Technology of Advanced Materials*, 9: 033002, 2008.

[103] R. Suryanarayanan. *Plasma Spraying: Theory and Applications*. World Scientific Pub Co Inc. 1993.

[104] G. Matheron. *The theory of regionalized variables and its applications*, Paris School of Mines Publications, 1971.

[105] C. Lantujoul. Ergodicity and integral range, *Journal of Microscopy*, 161:387–403, 1991.

[106] T. Kanit, S. Forest, I. Galliet, V. Mounoury, D. Jeulin. Determination of the size of the representative volume element for random composites: statistical and numerical approach, *International Journal of Solids and Structures*, 40, 2003.

[107] T. Kanit, F. N'Guyen, S. Forest, D. Jeulin, M. Reed, S. Singleton. Apparent and effective physical properties of heterogeneous materials: representativity of samples of two materials from food industry, *Computer Methods in Applied Mechanics and Engineering*, 195:39–60, 2006.

[108] K. Sab. On the homogenization and the simulation of random materials, *European Journal of Mechanics A/Solids*, 11, 585–607, 1992.

[109] I.O. Golosnoy, S.A. Tsipas, and T.W. Clyne. An analytical model for simulation of heat flow in plasma-sprayed thermal barrier coatings, *Journal of Thermal Spray Technology*, Vol.14(2), 2005.

[110] T.J. Lu, C.G. Levi, H.N.G. Wadley and A.G. Evans. Distributed Porosity as a Control Parameter for Oxide Thermal Barriers made by Physical Vapor Deposition, *Journal of the American Ceramic Society*, 84:2937-2946, 2001.

[111] I.M. Gitman. *Representative Volumes and multi-scale modeling of quasi-brittle materials*, PhD Thesis, T.U. Delft, Nederlands, 2006.

[112] Z. Hashin and S. Shtrikman. A variational approach to the theory of the effective magnetic permeability of multiphase materials, *Journal of Applied Physics*, 33:3125–3131, 1962.

[113] A. Cipitria, I.O Golosnoy, T.W. Clyne. A sintering model for plasma-sprayed zirconia TBCs. Part I: Free-standing coatings, *Acta Materialia*, 57:980–992, 2009.

[114] J. W. Davis revised by V.Barabash, ITER Document No. S74 RE1 and G74 MA16, *ITER Material Properties Handbook (IMPH)*, 2005.

[115] J. W. Davis, V.R. Barabash, A. Makhanov, L.Plöchl and K.T.Slattery, *Journal of Nuclear Materials*, 308:258-263, 1998.

[116] *Wolfram*, company brochure, Metallwerk PLANSEE, Reutte, Austria, 1980.

[117] J. W. Davis, S. Zinkle, P. Fenici and C. Vinche. Document No. S 74 MA 2, *ITER Material Properties Handbook (IMPH)*, 1997.

[118] S. J. Zinkle and W. S. Eatherly. Effect of Test Temperature and Strain Rate on the Tensile Properties of High Strength, High Conductivity Copper Alloys, *Fusion Materials Semi-annual Progress Report for Period Ending*, DOE/ER-0313/21, pp. 165-174, April 1997.

[119] Deutsches Kupfer Institut. *Datenblatt CuCrZr - Legierung*, http://www.kupferinstitut.de, 2005.

[120] J. Schlosser, F. Escourbiac, M. Merola et al. Technologies for ITER divertor vertical target plasma facing components, *Nuclear Fusion*, 45(6):512-518, 2005.

[121] H. Hooputra, H. Gese, H. Dell, and H. Werner. A Comprehensive Failure Model for Crashworthiness Simulation of Aluminium Extrusions, *International Journal of Crashworthiness*, vol. 9(5):449–464, 2004.

[122] N.Bonora. A nonlinear CDM model for ductile failure, *Engineering Fracture Mechanics*, 58(1-2):11-28, 1997.

[123] J. Lemaitre and J.-L. Chaboche. *Mechanics of Solid Materials*, Cambridge University Press, New York, 1985.

[124] J. Lemaitre. *A Course On Damage Mechanics*, Springer, New York, 44-46, 1992.

[125] J.R. Rice and D.M. Tracey. On the ductile enlargement of voids in triaxial stress fields, *J. Mech. Phys. Solids* 17:201–217, 1969.

[126] Gurson, 1977 A.L. Gurson, Continuum theory of ductile rupture by void nucleation and growth: Part 1 – Yield criteria and flow rules for porous ductile media, ASME Trans. *J. Eng. Mater. Tech.* 99:2–15, 1977.

[127] A. Needleman; V.Tvergaard, An Analysis of Ductile Rupture in Notched Bars. *J. Mech. Phys. Solids* 32:2 1984.

[128] N. Metropolis, A. Rosenbluth, M. Rosenbluth, A. Teller, E. Teller. Equation of state calculation by fast computing machines, *Journal of Chemical Physics*, 21:1087–1092, 1953.

[129] Amira - User´s Guide v5.3, http://www.amira.com/, Visage Imaging GmbH and Konrad-Zuse Zentrum für Informationstechnik (ZIB), Berlin, Germany, 2010.

[130] B.W. Clark. *Proceedings of the 18th International Meshing Roundtable in Heidelberg*, Springer-Verlag, Berlin, 2009.

[131] W. Lorensen and H. Cline. Marching cubes: a high resolution 3D surface construction algorithm, *Computers &. Graphics*, 21(4):163–170, 1987.

[132] D.Stalling, M.Westerhoff, H-C. Hege. *Amira: A highly interactive system for visual data analysis*, The Visualization Handbook, 749-767, Elsevier, 2005.

[133] T. Weitkamp, P. Tafforeau, E. Boller et al. Status and evolution of the ESRF beamline ID19*, Proceedings of the 20th International Congress on X-ray Optics and Microanalysis (ICXOM20),* edited by M. E. Denecke, AIP Conf. Proc. 1221:33-38, 2010.

[134] A.M. Cormack. Early Two-Dimensional Reconstruction and Recent Topics Stemming from IT (Nobel Lecture), *Journal of Computer Assisted Tomography,* 4(5):658-664, 1980.

[135] G.N. Hounsfield. Computed medical imaging (Nobel Lecture), *Science,* 210(4465):22-28, 1980.

[136] S.R. Stock. Recent advances in X-ray microtomography applied to materials, *International Materials Reviews,* 53(3):129-181, 2008.

[137] F. Natterer. *The mathematics of computerized tomography*, John Wiley sons, New York, 1986.

[138] M. Born and E. Wolf. *Principles of Optics, 7th ed*, Pergamon Press, Oxford, New York, 1999.

[139] W. Ludwig. *Development and Applications of Synchrotron Radiation Microtomography*, PhD Thesis, Fakultät für Physik der Ludwigs-Maximilians-Universität München, 2001.

[140] M. Sanchez del Rio and R.J. Dejus. XOP: A Multiplatform Graphical User Interface for Synchrotron Radiation Spectral and Optics Calculations. *SPIE Proceedings* 3152:148-157, 1997.

[141] D.E. Cullen, M.H.Chen, J.H. Hubbell et al. *Tables and Graphs of Photon-Interaction Cross sections from 10 eV to 100 GeV Derived from the LLNL Evaluated Photon Data Library (EPDL)*, Part B: Z = 51 to 100, Lawrence Livermore National Laboratory Report UCRL-50400, Vol. 6, Rev. 4, 1989.

[142] A. Larrue. *Observation et quantification tridimensionnelle de microfissures de l'os trabéculaire par microtomographie Synchrotron*, PhD Thesis, INSA Lyon, Université Lyon, 2010.

[143] A. Zivelonghi, T. Weitkamp, J.-H. You et al. Exploring the pores in a heavy metal: the 3D microstructure of coatings for nuclear fusion reactors is revealed by high-resolution synchrotron microtomography, *Tech. Report on The Spotlight of Science*, European Synchrotron Radiation Facility (ESRF), http://www.esrf.eu/news/spotlight/spotlight113/ August 2010.

[144] S. Thelen, F. Barthelat, L.C. Brinson. Mechanics considerations for microporous titanium as an orthopaedic implant material, *Journal of Biomedical Materials Research*, 69A:601–610, 2004.

[145] W. J. Parker, R. J. Jenkins, C. P. Butler, and G. L. Abbott, Flash method of determining thermal diffusivity, heat capacity, and thermal conductivity, *J. Appl. Phys.* 32, 1679-1684, 1961.

[146] J. A. Cape, G. W. Lehman. Temperature and finite pulse-time effects in the flash method for measuring thermal diffusivity, *J. Appl. Phys.* 34:1909-1913, 1963.

[147] J. Blumm, J. Opfermann. Improvement of the Mathematical Modelling of Laser Flash Measurements, *High Temp.-High Press.*, Vol. 34, 515-5216. 2002.

[148] J. Pamela, A. Bécoulet, D. Borba et al. Efficiency and availability driven R&D issues for DEMO, *Fusion Engineering and Design*, doi:10.1016/j.fusengdes.2009.02.028, February 2009.

[149] N.Moes, J. Dolbow and T. Belytschko, A finite element method for crack e growth without remeshing, *Int. J. Num. Meth. Eng.* 46(1):131-150, 1999.

[150] N. Sukumar, N. Moes, B. Moran and T. Belytschko, Extended finite ele- e ment method for three-dimensional crack modeling, *Int. J. Num. Meth. Eng.* 48 [11] (2000) 1549-1570. [32]

[151] N. Moes, A. Gravouil and T. Belytschko, Non-planar 3D crack growth by e the extended finite element and level sets. Part I: Mechanical model, *Int. J. Num. Meth. Eng.* 53 [11] (2002) 2549-2568.

[152] Y.Abdelaziz and A. Hamouinea. A survey of the extended finite element, *Computers & Structures*, 86(11-12):1141 1151, 2008.

List of Publications and Other Contributions

Articles

A.Zivelonghi, T.Weitkamp, A.Larrue, J.H.You, *Computed Tomography of a Tungsten Coating System for Fusion Applications,* (2011), in revision

A.Zivelonghi, J.-H.You, *On the Damage Behaviour of Ductile-Brittle Random Composites* International Journal of Solid and Structures, (2011), in revision

A.Zivelonghi, J.-H.You, *Influence of Dual-Scale Random Morphology on the Heat Conduction of a Plasma-Sprayed W Coating* International Journal of Solid and Structures (2011), prepared to submit

S.Nawka, T. Schubert, A. Brendel, A. Zivelonghi, J.-H. You, B. Kieback, *Synthesis, characterization and FEM-simulation of W/CuCrZr- composites for extreme thermal applications* Conference Proceedings of Powder Metallurgy World Congress - World PM2010 (2010), accepted

A.Zivelonghi, A. Brendel, S. Lindig, S. Nawka, B. Kieback, J.H. You, *Microstructure-Based Analysis of Thermal- and Mechanical Behaviour of W/CuCrZr Composites and Porous W Coating,* Conference Proceedings of the 14th International Conference on Fusion Reactor Materials (ICFRM-14), Journal of Nuclear Materials (2010), accepted

M.Bogana, L. Ravagnan, C.S. Casari, A. Zivelonghi, A. Baserga, A. Li Bassi, C.E. Bottani, *Leaving the Fullerene Road: Presence and Stability of sp Chains in sp2 Carbon Clusters and Cluster-Assembled Solids* New Journal of Physics (2005), published

Technical Reports

A.Zivelonghi, T.Weitkamp, J.-H. You, Ch. Linsmeier, M. Rasinski, G. Waizmann, M. Schlüter, C. Capuano, *Exploring the pores in a heavy metal: the 3D microstructure of coatings for nuclear fusion reactors is revealed by high-resolution synchrotron microtomography* - The Spotlight of Science, August 2010, http://www.esrf.eu/news/spotlight/spotlight113/

Tomographic Images of the W/Steel Interlayer from the VPS-W coating system were selected for the front page of the Synchrotron Radiation News, July/August 2010, Vol 23 N.4

Posters

A.Zivelonghi, T.Weitkamp, A.Larrue, J.H. You, *2D and 3D Stress Fields Analysis Based on Direct Mapping of the Dual-Scale Porous Network of Plasma-Sprayed Tungsten*, The Fifth International Conference on Multiscale Materials Modeling - Freiburg, Germany, 04-08 October 2010

A.Zivelonghi, A.Brendel, S.Nawka, J.H.You, *Microstructure-Based Finite Element Simulations of Heterogeneous Tungsten Materials,* 14th International Conference on Fusion Reactor Materials (ICFRM-14) - Sapporo, Japan, 06-11 September 2009

A.Zivelonghi, S.Lindig, J.H.You, *Thermal Diffusivity of a Porous Tungsten Coating via 2D Direct Mapping Finite Element Simulation*, 12th International Workshop on Plasma-Facing Materials and Components for Fusion Applications (PFMC-12) - Jülich, Germany, 11-14 May 2009

S.Lindig, A.Zivelonghi, J.H.You, *Thermal Diffusitivity of Plasma Sprayed Tungsten: LFA-analysis and first FE-simulations,* 1st International Conference on New Materials for Extreme Environments (ExtreMat) - San Sebastian, Spain, 02-04 June 2008

Conference Talks

T.Weitkamp, A. Zivelonghi, *Synchrotron Microtomography of Porous Tungsten: How to Plan a Successful Experiment*, invited talkm at the 2nd Workshop on Fusion Energy Materials Science (FEMaS 2010) - Athens, Greece, 13-15 January 2010

J. H.You, A. Zivelonghi, *Materials Issues for Fusion Reactor Components* Contributed Talk at the Workshop Bruch & Gefüge - Leoben, Austria, 22-24 April 2009

J. H.You, J.Du, J. Riesch, A. Zivelonghi, *Tungsten Base Composite Materials for Fusion Application and Needs for Advanced Characterization* invited talk at the 1st Workshop on Fusion Energy Materials Science (FEMaS 2009) - Lisbon, Portugal 12-14 January 2009

Acknowledgment

First of all, I'd like to express my gratitude to Prof. Harald Bolt for placing his trust on me in accomplishing this work. I am also thankful to Prof. H. Baier and Prof. H. Werner for the time they dedicated to the evaluation of the thesis and for stimulating questions during the exam.

The most directly involved person in this work was certainly my supervisor Jeong-Ha You. I am very grateful to him for his immense patience and for the great support I received. I am also thankful to the whole IPP-MF group for supporting me (and bearing me :-) over the years. In particular, I'd like to mention Christian Linsmeier, Annegret Brendel, Hans Maier, Stefan Lindig, Gabriele Matern, Henri Greuner and Udo von Toussaint.

A special acknowledgment goes to Prof. Bernd Kieback and Stefan Nawka from IfWW (TU-Dresden) for providing me with one of the most challenging random material to investigate. On the other hand, I'd like to express profound gratitude to Timm Weitkamp (ESRF, beamline ID-19) for his essential and excellent support during the experimental tomographic campaign and after. Also thanks to the ESRF scientists P. Tafforeau, A. Larrue and M. Herbig (beamline ID-19), M. Sheel and M. di Michiel (beamline ID-15) and to my colleague J. Riesch (IPP). For the great technical support I am also thankful to K. Strahl (Stangl & Co.) and J. Springer (IPP).

For enjoyable discussions and for helping me to move the first steps with Linux I am grateful to Udo von Toussaint, Maya Padivattathu and Klaus Tichmann. For "bereichende Diskussionen" I'd like to credit Prof. Karl Lackner, Wolfgang Jacob, Konstantin Moshkunov, Sergio Nogales, Mathias Reinelt and Christian Hopf. I am also tankful to Fabio Genoese and Leonie Krieger for their support with "Hochdeutsch" and written English, respectively. For the good time spent together at IPP, thank you E. Hinson, M. Rasinski, A. Hermann, V. Paffenholz, Y. Weizhi, M. Köppen, M. Oberkofler and S. Kimmig.

A couple of lines ago I mentioned "random materials“: thank you very much Prof. D. Jeulin and Ch. Peyrega (CMM-Fontainebleau) for introducing me to the marvelous world of Mathematical Morphology.

It is now time to say a big "GRAZIE" to Gebhard Waizmann, Konstantin Moshkunov, Riccardo Nocentini, Massimo Lai, Mario Sempf, Piero Agostinetti, Michael Schlüter, Massimo Poggioli and Alex Ziller for the support they gave me both as friends and open-minded persons. A special mention is dedicated to my Italian friend and colleague Riccardo, for his particular talent in injecting, besides neutral particles in tokamaks, a lot of wisdom in my turbulent life.

Scientific projects only work with the right financial and logistical support: to this regard, I am grateful to the DFG - Deutsche Forschungsgemeinschaft - which funded my PhD study and to the FeMAS coordination act, which allowed the personnel exchange between IPP and ESRF.

Finally, it would be unfair to forget to credit all the bright minds behind the development of the most advanced theoretical and experimental tools I used during my work. Without this silent army of believers, this infinitesimal contribution could not exist.

In this conclusive statement, I desire to credit for the most important psychological support I received, which came from Marta and my Family.

Garching by Munich, 22.05.2011

Alessandro Zivelonghi